

# **Transparent High Barrier Coatings for Electronic Encapsulation**

Nessima Kaabeche

A thesis submitted in partial fulfilment of the requirements of  
Manchester Metropolitan University for the Degree of Doctor of  
Philosophy

Faculty of Science and Engineering  
School of Engineering  
Surface Engineering Group  
Bobst Manchester Ltd

2017

## **RESTRICTION NOTE**

This PhD thesis contains internal and confidential information and data of Bobst Manchester Ltd. Release or duplication in parts or in the whole – also in digital form – without the written consent of the company is not permitted. Furthermore, disclosure of the information to anyone other than the examination board is not authorised.

## **DECLARATION**

This is to certify that the material contained in this thesis has been produced by the author, has not been accepted in substance for any other degree and is not currently submitted in candidature for any other academic award.

## **ABSTRACT**

Barrier coatings are a category of functional films designed to enhance end-use properties to the underlying substrate. When used for electronic applications (such as flexible displays, digital paper, lighting, OLEDs and solar cells), the barrier characteristics are meant to protect the device from environmental influence, especially the permeation of oxygen and water vapour that can degrade and corrode the active layers of the devices (causing mal-functioning).

In this project, silicon oxide barrier layers were deposited onto a non-treated BO-PET via plasma enhanced chemical vapour deposition, using a pilot scale roll-to-roll coater. The aim was to optimise the deposited coatings by understanding the effect of the deposition parameters on the barrier properties (oxygen and water vapour barrier) and the surface properties (i.e. topography, chemistry, structure, thickness, mechanical properties) of the coatings. For encapsulation in electronic devices such as OLEDs and photovoltaics cells, the barrier coatings must remain transparent and flexible, which is one of the challenges of this project.

This project has demonstrated that the moisture barrier performance of silicon oxide coated BO-PET is dependent on film structure (i.e. porosity), which are linked to the plasma conditions of the deposited film. Lower WVTR could be reached ( $10^{-2}$  g/m<sup>2</sup>/day) for film produced at high input power (1.6kW), low webspeed (<0.5m/min) and low ratio oxygen:monomer (between 2 and 3). In these conditions, the coating was rather stoichiometric and exhibited a relatively low carbon content (30% atomic) and similar contents in O and Si (about 30% each).

The film type was found to have an influence on the final barrier level, as coatings on planarised and adhesion treated substrates showed better barrier performances than coatings on standard untreated PET.



## Abstract

---

Despite all the development done, barrier levels did not match the requirements ( $10^{-5}\times\text{g}/\text{m}^2\text{day}$ ) for electronic encapsulation but showed some promising improvement.

Thinner coatings were found to have better barrier against moisture permeation, although a threshold of 800nm was identified as critical thickness above which the WVTR dramatically increased.

As far as changing the plasma composition via the addition of  $\text{CO}_2$  as a reactive gas, a slight decrease in WVTR (improvement in barrier) was observed at low  $\text{CO}_2$  flow rates (up to 200SCCM). WVTR doubled, however, when increasing the amount of  $\text{CO}_2$ . This increase was associated with a decrease in hardness and increase of carbon content.

Alternative power generation, using squared waves instead of sinusoidal, was not successful and deteriorated the barrier performances (higher WVTR).

Finally, the route of topcoats to enhance the barrier by filling the pores showed promising results in the case of  $\text{Al}_2\text{O}_3$  ALD topcoats but didn't show significant improvement in the case of acrylate topcoats, partly due to a lack of adhesion of the acrylate on the surface of the  $\text{SiO}_x$  coating.

## **ACKNOWLEDGEMENT**

Although a PhD is a very personal and individual project, I can certainly say I would not have achieved as much as I did without the help and support of many great persons who I would like to thank.

First, thank you to Prof Peter Kelly for his guidance, reassurance and confidence. I also appreciated his patience during the write-up and at all times. He also contributed in moving the project forward during meetings. I am also thankful to Dr Glen West and Dr Chris Liauw for helping me with various experiments and supporting me in various endeavours related to my scientific and public engagement work. I also greatly appreciated the support and commitment of Dr Stuart Harmer during and after the annual reviews. His professionalism in dealing with difficult situations was very helpful. Then, I would like to thank the industrial partner Bobst Manchester Limited for providing some of the resources. My appreciation goes especially to Lyndon Harland, for helping me to get started and giving me technical support and Nick Copeland for being a good link with the management team. I also appreciated the friendly behaviour of all my colleagues in BML, as it without a doubt helped me keep my head out of the water during tough times. I cannot forget to express my gratitude to Dr Carolin Struller, postdoc in BML/MMU at the time, who has always been keen to help me and give me advice as well as share her knowledge, expertise and experience with me. It certainly has made a difference in my PhD. I also, would like to say a word to thank my colleague Stefan Serednycky, who helped me to get started in the laboratory in BML. His endless knowledge of the equipment was really beneficial to me.

On the university side, there are a couple of people that I am thankful to. I would like to thank Tony Scimone, Dr David Sawtell, Dr Marina Ratova for their technical support at times, and simply for their kind words at others. The technical staff at MMU have been more helpful than I could have asked for, especially Dr Hayley Andrews, who helped me countless times with the SEM and other experiments. Some of my work has also been supported and greatly helped by Lee Harman and Glenn Ferris, who assisted me with some difficult

## Acknowledgement

---

analytical techniques. Mike Green also provided an excellent service and helped me with the mechanical testing of my samples.

A thank you also goes to the admin team in Kristina, Megan, and Francesca who have done a brilliant job supporting the administrative side of the PhD. It helped me to understand and keep track the administrative requirements associated with a PhD. I also enjoyed working with them to organise our Research Symposium held in September 2015.

Throughout my course I also had the opportunity to collaborate with various companies and universities. Therefore, I would like to thank them for providing valuable resources and data for me : Dr Mark Day at Gatan (UK) helped me with ion milling, Dr Anna Wise (Stanford University, CA) provided great support and XRR data, Prof Hazel Hassender and Dr Vincent Tobin (Oxford University, UK) kindly and professionally provided the calcium test equipment and expertise, Dr Natalie Kacket (SSS, UK) and Gnaki (DiAtom, UK) did some very important work on ultramicrotomy, finally Dr Ashvin did some great although challenging work with the AFM.

Last but not least, I wanted to thank all my family and friends, especially my mother, father, sister, brother and great friends in France and Switzerland.

Thank you to the many I could not mention here for every kind word, encouragement or simply for looking at me with a sparkle in their eyes showing respect and support.

---

## TABLE OF CONTENTS

Restriction Note .....	ii
Declaration.....	iii
Abstract.....	iv
Acknowledgement.....	vi
Table of contents .....	viii
Abbreviations .....	xiii
List of tables.....	xv
List of figures.....	xviii
List of equations.....	xxvi
1 Introduction .....	1
2 Fundamentals.....	6
2.1 Photovoltaic modules and solar cell (organic/inorganic) .....	7
2.1.1 Organic and inorganic solar cells: device structure .....	7
2.1.2 Efficiency requirements, moisture and oxygen issues.....	10
2.1.3 Encapsulation of PVs .....	12
2.2 OLEDs.....	12
2.2.1 Device structure and operation .....	13
2.2.2 Device efficiency requirements and durability requirements ....	15
2.2.3 Moisture permeation protection via encapsulation .....	15
2.3 PECVD coatings .....	17
2.3.1 Introduction to chemical vapour deposition .....	18
2.3.2 Plasma enhanced chemical vapour deposition .....	19
2.4 Vacuum web coating.....	23
2.5 Barrier coatings.....	24

## Table of contents

---

2.5.1	Water vapour and oxygen transmission rates .....	24
2.5.2	Permeation through polymers .....	24
2.5.3	Permeation through plastic foils coated with thin film inorganic coatings .....	29
2.5.4	SiO <sub>x</sub> coatings and porous structures .....	31
2.5.5	Barrier requirements .....	33
3	Methods and materials .....	35
3.1	The PECVD roll to roll coater .....	36
3.2	The substrate and precursor .....	42
3.2.1	Detail on the substrate .....	42
3.2.2	Precursor for SiO <sub>x</sub> barrier coatings .....	44
3.2.3	Plasma composition .....	45
3.3	Coating analysis characterisation .....	45
3.3.1	Barrier measurement .....	45
3.3.2	Barrier retention with stretch tests .....	48
3.4	Surface characterization of the samples .....	50
3.4.1	Morphology and roughness via optical profilometry .....	50
3.4.2	Topography scanning electron microscopy .....	53
3.4.3	Defect characterisation via calcium test .....	55
3.5	Optical properties .....	56
3.6	Mechanical properties .....	57
3.7	Coating composition .....	58
3.7.1	X-Rays photoelectron spectroscopy .....	58
3.7.2	Fourier transform infrared spectroscopy (FTIR) .....	61
4	Initial Platform Assessment .....	63

## Table of contents

---

4.1	Substrate characterisation .....	64
4.2	Process parameters vs barrier .....	66
4.2.1	Effect of discharge power on the water vapour barrier .....	67
4.2.2	Relationship between the monomer flow rate and the WVTR ..	68
4.3	Coating characterisation .....	71
4.3.1	Morphology .....	71
4.3.2	Composition and stoichiometry .....	79
4.3.3	Relationship between composition and WVTR .....	84
4.4	Defect observation (calcium test).....	88
4.5	Conclusion on the initial platform development.....	90
5	Platform Characterisation .....	92
5.1	Surface coating properties: topography .....	93
5.2	Influence of power on coatings and barrier performances .....	94
5.3	Barrier performances and coating thickness.....	96
5.3.1	Relationship between web-speed and barrier performances ...	99
5.3.2	Barrier performance with elongation.....	99
5.4	Summary and conclusion.....	102
6	Platform Development and Optimisation.....	103
6.1	Investigation of CO <sub>2</sub> injection.....	104
6.1.1	Methods and materials .....	104
6.1.2	Results .....	105
6.2	Conclusion .....	112
6.3	Investigation of injection of argon and oxygen through GPE .....	114
6.3.1	Methods and materials .....	114
6.3.2	Barrier properties.....	115

## Table of contents

---

6.4	Study on the effect of the power delivery type .....	116
6.4.1	Material and methods .....	117
6.4.2	Initial work .....	117
6.4.3	Full-mode .....	118
6.4.4	Barrier performances .....	123
6.4.5	Conclusions from the study .....	124
6.5	Investigation of double sided coatings .....	125
6.6	Investigation of different substrates .....	127
6.6.2	Coating topography .....	131
6.6.3	Barrier performances .....	135
6.6.4	Summary of the study .....	137
6.7	Investigation of design of the machine .....	138
6.7.1	Internal parameters: modification of the GPE position .....	138
6.7.2	External parameters: dust and cleanliness management .....	142
6.7.3	Conclusion of the study .....	144
7	Top Coats and Hybrid Coating .....	146
	ALD top coats .....	147
7.1	Experimental details .....	147
7.2	Results .....	149
8	Conclusions and Outlook .....	151
8.1	Future work .....	154
9	References .....	156
A.	Appendices .....	167
	Appendix A Investigation of Thickness .....	168
	Ultramicrotome .....	177

## Table of contents

---

Ultramicrotomy with vibrating blade .....	177
Cryo ultramicrotomy .....	179
Ion milling.....	181
Embedding and polishing.....	184
Comparison between techniques.....	185
Conclusion .....	188
Appendix B Study of the morphology with the atomic force microscope ... .....	189
Reference sample.....	190
Sample 02 - 100SCCM of CO <sub>2</sub> .....	197
Sample 03 - 200 SCMM of CO <sub>2</sub> .....	201
Sample 04 - 500SCCM of CO <sub>2</sub> .....	204
Appendix C Study of adhesion .....	209
Motivation .....	209
Methods and materials .....	210
Results.....	211
Summary and conclusion.....	213
Appendix D Study of plasma cure of acrylate.....	214
Motivation .....	214
Methods and materials .....	215
Results.....	215
Appendix E Substrate information.....	217
Appendix F Public engagement and publications .....	218



## **ABBREVIATIONS**

<b>AES</b>	Auger electron spectroscopy
<b>AFM</b>	Atomic force microscope
<b>AIO<sub>x</sub></b>	Aluminium oxide (x is the unknown stoichiometry)
<b>ASTM</b>	American Society for Testing and Materials
<b>BO-PET</b>	Bi axially oriented PET (see PET)
<b>CVD</b>	Chemical vapour deposition
<b>EDAS (EDX)</b>	Energy dispersive atomic spectroscopy (X-ray)
<b>EDS</b>	Energy dispersive spectroscopy
<b>ESPRC</b>	Engineering and Physical Sciences Research Council
<b>FF</b>	Fill factor
<b>GPE</b>	Gas purge electrode
<b>HMDSO</b>	Hexamethyldisiloxane
<b>J<sub>sc</sub></b>	Short circuit current
<b>LCD</b>	Light capacitive device
<b>LED</b>	Light emitting diode
<b>OLED</b>	Organic light emitting diode
<b>OTR</b>	Oxygen transmission rate

## Abbreviations

---

<b>PC</b>	Polycarbonate
<b>PEEK</b>	Polyether etherketon
<b>PEN</b>	Polyethylene naphthalate
<b>PES</b>	Polyether sulfone
<b>PET</b>	Polyethylene terephthalate
<b>PEVCD</b>	Plasma enhanced CVD (see CVD)
<b>PI</b>	Polyimide
<b>PNB</b>	P-nitro phenyl butyrate
<b>RH</b>	Relative humidity
<b>SEM</b>	Scanning electron microscope
<b>SIMS</b>	Secondary ion mass spectroscopy
<b>SiO<sub>x</sub></b>	Silicon oxide (x stoichiometry to be determined)
<b>TEM</b>	Transmission electron microscope
<b>TOF-SIMS</b>	Time of flight SIMS
<b>V<sub>oc</sub></b>	Open circuit voltage
<b>WVTR</b>	Water vapour transmission rate
<b>XPS</b>	X-ray photoelectron spectroscopy
<b>XRF</b>	X-ray fluorescence
<b>ZnO</b>	Zinc oxide

## LIST OF TABLES

Table 3-1 Identification and role of the different zones in the roll-to-roll PECVD coated shown in Figure 3-1 .....	37
Table 3-2 Name and role of each labelled element in Figure 3-4 .....	40
Table 3-3 Table summarising the main properties of the HMDSO used to produce the SiO <sub>x</sub> barrier coatings.....	44
Table 4-1 Process parameters for the reference run .....	66
Table 4-2 Summary of the process parameters used to produce sample A and sample B.....	71
Table 4-3 Summary of the main data of the samples analysed via XPS: Oxygen flow rate, WVTR, %transmission. ....	80
Table 4-4 Summary of the composition and stoichiometry of the samples analysed by XPS (the composition is reported in atomic percentage (%) of each element Si, C, O) .....	86
Table 4-5 Process parameters used to produce the coating tested on the calcium corrosion test.....	88
Table 5-1 Process parameters used for the reference sample in the initial platform characterisation study.....	93
Table 6-1 Process parameter used to deposit SiO <sub>x</sub> onto 120µm thick PET with and different flow rates of CO <sub>2</sub> .....	105
Table 6-2 Moisture barrier performance results comparing the barrier performance of the reference samples with helium and the samples produced with the injection of CO <sub>2</sub> .....	108
Table 6-3 Measured R <sub>a</sub> and R <sub>q</sub> roughness parameters for the different samples deposited with 100SCCM, 200SCCM and 500SCCM flow rate of CO <sub>2</sub> , the reference sample and the PET substrate. ....	109

## List of tables

---

Table 6-4 Results of hardness tests performed on samples produces with different flow rates of CO <sub>2</sub> (pencil hardness decreases from 6H to F). The values are an average for 5 tested samples .....	112
Table 6-5 Process parameters used to produce and the sample with injecting the O <sub>2</sub> and Ar through the GPE.....	114
Table 6-6 Barrier performance of the reference run and sample produced with feeding the oxygen through the GPE .....	115
Table 6-7 Power equalisation parameters investigated in full mode .....	118
Table 6-8 Main electrical parameters used during the investigation of PECVD deposition in full mode with the 4040 PSU.....	119
Table 6-9 Barrier performances of the coating deposited in full-mode at 40 kHz, 60 kHz and 80 kHz . Reference sample (AC Advanced Energy power supply unit).....	123
Table 6-10 Barrier performances of double sided coatings (Sample 01 and sample 02) compared to the reference sample.....	125
Table 6-11 Summary of the technical data of the substrates used for the study .....	128
Table 6-12 Table indicating which side was coated for each DTF film used .....	129
Table 6-13 Barrier performances and barrier improvement factor of the coated PEN films (DTF) and the commodity grade PET.....	136
Table 6-14 Detail of the locations number and name.....	141
Table 6-15 Barrier performances of coatings produced with various GPE positions.....	141
Table 6-16 Barrier performances of samples produced without the dust cleaning rollers (Coating 01) and with the dust cleaning rollers (Coating 02) .....	144

## List of tables

---

Table 7-1 Barrier performances of the SiO <sub>x</sub> coating with and without Al <sub>2</sub> O <sub>3</sub> topocoant.....	150
Table A-1 SiO <sub>x</sub> coating thickness measurments. Comparison of thicknesses measured using different techniques.....	187
Table A-2 Roughness measurement done on the 20µm x 20µm and 5µm x 5µm topography scans of each sample (reference sample, produced with 100SCCM, 200SCCM, 500SCCM of CO <sub>2</sub> injected into the plasma).....	208

## LIST OF FIGURES

Figure 2-1 Schematic of the structure of a PV module [13].....	9
Figure 2-2 Photo of 20 year old photovoltaic panels that suffer from discoloration due to exposure to high humidity and changing temperature outdoor environment in Mexico [17, 18]. .....	11
Figure 2-3 Schematic showing the structure of the encapsulated photovoltaic module. ....	12
Figure 2-4 Schematic showing the structure of an OLED, adapted from [9] and [24].....	13
Figure 2-5 Structure of the pin- OLED adapted from [23] .....	14
Figure 2-6- Schematic of encapsulated OLEDs, adapted from [8] .....	16
Figure 2-7 Schematic illustrating the principle of PECVD[35]. .....	20
Figure 2-8 Schematic of vacuum web coating Mechanism. ....	24
Figure 2-9 Schematic illustrating the gradient of pressures of the permeant on both sides of the solid that is taking place during permeation. $p_1$ is the partial pressure of permeant on the entrance side and $p_2$ is the partial pressure at the exit side of the solid.[3] .....	25
Figure 2-10 Permeation through pinhole model (top view and cross-section) [3].....	31
Figure 2-11 Barrier performance requirements for some technological applications including organic electronics and photovoltaic encapsulation. .	34
Figure 3-1 Photo of the pilot scale roll-to-roll PECVD coater used for $\text{SiO}_x$ deposition onto PET. (BML property).....	36
Figure 3-2 Illustration of the webpath in the roll-to-roll coater and the conductance seals between the different zone. ....	38

## List of figures

---

Figure 3-3 Pictures of the different zones of the roll-to-roll PECVD coater (BML). Number 1 to 17 are labelling the different rollers. The arrows indicate the winding direction.....	39
Figure 3-4 Insight view of the process chamber with each element labelled. (see .....	40
Figure 3-5 Semi-developed formula of the PET showing the main monomer unit that is repeated n times in the polymer. ....	43
Figure 3-6 Cram representation of the HMDSO molecule .....	44
Figure 3-7 Schematic of the cross section of the cell explaining the principle of the measurement of the water vapour transmission rate in the Systech 7001 analyser [74].....	46
Figure 3-8 Schematic of the cross section of the analyser's cell showing the principle used to measure oxygen transmission rate on the Systech 8001[75] .....	48
Figure 3-9 Tensile equipment used to perform the stretch tests.(Hounsfield H10KS with QMat 5.52 software) .....	49
Figure 3-10 Optical densitometer Macbeth TD-404.....	57
Figure 3-11 Hardness pencil tester.....	58
Figure 4-1 SEM micrographs showing the morphology of the PET substrate : area 1 (a) and area (b), x10000 magnification.....	64
Figure 4-2 SEM micrograph showing the morphology of the PET substrate in the area 1: x800 magnification (left) and zoom on the scratch left by the antiblock x20k magnification.....	64
Figure 4-3 Graph showing the evolution of the WVTR with the input power for samples produced using the parameters of the reference run 13_05_28_01.....	68
Figure 4-4 Graph showing the evolution of the WVTR with the monomer flow rate for coatings produced using the reference run 13_05_28_01. Each data	

## List of figures

---

point is an average of the WVTR measured on two samples from the same run. Each data point is related to one discrete experiment. ....	69
Figure 4-5 Picture of the burned insulating plate on the back of the drum. ...	70
Figure 4-6 SEM micrographs of the surface of the SiO <sub>x</sub> coating deposited onto PET for two low WVTR samples of Sample A (top image, (0.049+/-0.003 g/m <sup>2</sup> /day), sample B (bottom image, WVTR= 0.014±0.003 g/m <sup>2</sup> /day). ....	73
Figure 4-7 SEM micrograph of Sample A showing the dicolored areas. ....	74
Figure 4-8 SEM micrograph showing the morphology of the dark region (top picture) and clear region (bottom picture) at x20000 times magnification ....	75
Figure 4-9 Photograph of the samples of SiO <sub>x</sub> coating onto PET revealing hazy regions. The machine direction is vertical to the images.....	77
Figure 4-10 SEM micrographs of the dark side area of the coating (a) and the hazy white area of the SiO <sub>x</sub> coated PET (b).....	78
Figure 4-11 Depth profile of sample 03 (a), sample 09 (b), sample 10 (c), sample 12 (d). Black line for carbon content, red line for oxygen content and blue line for Si(2p) content. ....	83
Figure 4-12 Evolution of the content of silicon, oxygen and carbon content in the coating with ratio oxygen:monomer .....	85
Figure 4-13 Photos of calcium coating on top of the SiO <sub>x</sub> coated samples taken after 0h, 2h, 26h, 365h exposure to 90% RH and temperature controlled atmosphere (37°C).....	89
Figure 5-1 SEM micrographs of the coating deposited of coating deposited using the same parameters except input power. Sample a: P=1.1kW, sample b: P=1.6kW. The ratio oxygen: monomer for both samples was 6. The WVTR rates for the samples (a) is, 0.230 g/m <sup>2</sup> /day and sample (b) 0.053 g/m <sup>2</sup> /day. ....	94
Figure 5-2 Graph showing the relationship between the input power and the WVTR/BIF.....	96



## List of figures

---

Figure 5-3 Graph showing the relationship between WVTR and ratio oxygen:monomer and associated barrier improvement factor when the oxygen flow rate remains constant (1100 SCCM) and the oxygen flow rate is varied from 88 to 264 SCCM.....	97
Figure 5-4 Graph showing WVTR and associated BIF as a function of the ratio oxygen:monomer . In this case the monomer flow rate was kept constant at 179SCCM and the oxygen flow rate was varied from 200SCCM to 1100 SCCM.....	98
Figure 5-5 Graph showing the relationship between the web speed and the WVTR/BIF .....	99
Figure 5-6 Graph illustrating the change in barrier induced by elongation of the coated film in the machine direction. WVTR measured after relaxation. ....	100
Figure 6-2 FTIR spectra of coated films produced with 100, 200 and 500SCCM of CO <sub>2</sub> injected into the plasma and the spectrum of the reference sample. ....	110
Figure 6-3 Waveform recorder on the advanced energy power supply unit. ....	116
Figure 6-4 Picture of the 4040 TruPlasma power supply unit .....	117
Figure 6-5 Graph representing the waveform of delivered by the PSU in Full-Mode .....	119
Figure 6-6 Screenshot showing waveform delivered by the PSU during the trial carried out at 40 kHz (U=960V, I= 3A).....	121
Figure 6-7 screenshot of the waveform recorded when running the power supply unit in Full mode at 60 kHz and 1.6kW .....	122
Figure 6-8 SEM micrographs of the surface of the substrate DuPont Teijin Film ST504, Side A is the planarised side B and Side B is the surface treated for adhesion.....	131

## List of figures

---

Figure 6-9 SEM micrographs of both sides (coating on planarised side A) and non-planarised (Side B) of the base substrate PQA1 and the coating deposited on the planarised side.....	132
Figure 6-10 SEM micrograph of the SiO <sub>x</sub> coating applied onto the planarised base substrate (Side A coated).....	133
Figure 6-11 SEM micrograph of the SiO <sub>x</sub> coating deposited onto the Teonex® Q65HA.....	135
Figure 6-12 Schematic showing the three GPE experimental positions.....	139
Figure 6-13 Photograph showing the location of the GPE on the process zone for different experiments. Positions referred as 1, 2 and 3.....	140
Figure 6-14 Roller located before the drum to clean the substrate before being exposed to the plasma. ....	142
Figure 6-15 Cleaning rollers positioned in the rewind zone before the rewind roller.....	143
Figure 7-1 Schematic representing the surface prior to ALD when the OH are adsorbed onto the surface .....	147
Figure 7-2 Schematic and equation describing the reaction occurring during the first half-cycle of the deposition of Al <sub>2</sub> O <sub>3</sub> via ALD.....	148
Figure 7-3 Sketch and equation illustrating the second part of the half cycle of deposition of Al <sub>2</sub> O <sub>3</sub> by ALD .....	149
Figure A-1 White light interferometer scan of the stepedge created on the SiO <sub>x</sub> coating onto PET for thickness measurement .....	170
Figure A-2 Screenshot of the tools used in the Gwydion software to measure the profile along the step edge.....	171
Figure A-3 Photograph of the cryo microtome LEICA CM 1800(a) and inside of the microtome (b, used to cut the sections. ....	173
Figure A-4 Configuration and positioning of the frozen sample prior to cutting the slice.....	174

## List of figures

---

Figure A-5 SEM micrographs of the cryosection and raw section of the reference sample.....	175
Figure A-6 Photograph of microtome Leica RM2235 and the additional stage used to section the samples in order to measure the coatings' thickness. .	176
Figure A-7 Photograph of the ultramicrotme used at DiAtom to create cross sections of the SiO <sub>x</sub> coatings.....	178
Figure A-8 Schematic showing the sample held in AFM sample holder after cross sectioning with the ultramictome and vibrating knife. ....	179
Figure A-9 SEM microcraph of the same sample. Cross section 1 was done by ultramicrotomy with vibrating knife and cross section 2 was done by cryo ultramicrtomy. ....	180
Figure A-10 Photograph of PECS II ion milling device used in the work(Gatan). .....	181
Figure A-11 Schematic showing the sample holder used for ion milling.....	182
Figure A-12 Schematic showing the sample inserted in the ion milling device and the argon ion beam hitting the top surface of it.....	182
Figure A-13 SEM microcraph othe sample treated via ion milling. ....	183
Figure A-14 Embedded sample to be polished to reveal the interface between coating and substrate. ....	184
Figure A-15 SEM micrographs showing of a sample after embedding and mechanical polishing. ....	185
Figure A-16 Picture of the Solver Nano on a table top active vibration isolation system use for the study of prophology. ....	189
Figure A-17 AFM scan of the reference SiO <sub>x</sub> sample. Scan size 90µm x 90µm. The top image is the topography scan and bottom image is the phase scan. .....	192

## List of figures

---

Figure A-18 AFM scan of the topography of the reference SiO <sub>x</sub> sample. Scan size 20μm x 20μm (a) and 5 μm x 5μm (b). The length of line L1 is 6.46μm and the length of line L2 is 9.80μm. ....	194
Figure A-19 Profiles measured along the green lines S1 (top image) and S2 (bottom image) shown in Figure A-18. ....	196
Figure A-20 AFM topography (a) and phase (b) scan of the SiO <sub>x</sub> x sample deposited with injecting 100SCCM of CO <sub>2</sub> into the plasma. Scan size 90μm x 90μm. ....	198
Figure A-21 AFM topography scan of topography the SiO <sub>x</sub> sample deposited with injecting 100SCCM of CO <sub>2</sub> into the plasma. Scan size 20μm x 20μm. Scan taken in flat region away from the very large particles. ....	199
Figure A-22 AFM topography scan of the SiO <sub>x</sub> x sample deposited with injecting 100SCCM of CO <sub>2</sub> into the plasma. Scan size 5μm x 5μm. ....	200
Figure A-23 AFM topography scan of topography the SiO <sub>x</sub> sample deposited with injecting 200SCCM of CO <sub>2</sub> into the plasma. Scan size 90μm x 90μm. The particles height is annotated next to them. ....	201
Figure A-24 AFM topography scan of topography the SiO <sub>x</sub> sample deposited with injecting 200SCCM of CO <sub>2</sub> into the plasma. Scan (a) is 20μm x 20μm in size and scan (b) is 5μm x 5μm in size . ....	202
Figure A-25 AFM topogorahy scans of SiO <sub>x</sub> sample deposited with injecting 200SCCM of CO <sub>2</sub> into the plasma. Scan (a) is 90μm x 90μm in size and scan (b) is 20μm x 20μm and was takne in the square area highleghted in Scan (a). ....	204
Figure A-26 AFM topgorgrahy scans of SiO <sub>x</sub> sample deposited with injecting 200SCCM of CO <sub>2</sub> into the plasma. Scan size is 5μm x 5μm in size. ....	205
Figure A-27 AFM topography scan of the surface of the 120 μm thick PET bare substrate on which the SiO <sub>x</sub> coatings have been deposited. ....	206

## List of figures

---

Figure A-28 AFM phase scan of the surface of the 120 $\mu$ m thick PET bare substrate on which the SiO <sub>x</sub> coatings have been deposited. Scan size 5 $\mu$ m x 5 $\mu$ m. ....	207
Figure A-29 Cross-sectional view of sample during peel test (from [3]).....	211
Figure A-30 PhOtograph showing results of the test on Sample A. Graph associated with the physical sample after the peel test. ....	212
Figure A-31 Photograph of the acryalte (SR399+3% TPO-L) coated sample (AlO <sub>x</sub> coated 120 $\mu$ m PET). ....	216

## LIST OF EQUATIONS

Equation 2-1 Equation describing Fick's law.....	26
Equation 2-2 Formula of expressing Henry's law of solution .....	26
Equation 2-3 formula describing the  Fick's first law in the steady state .....	27
Equation 2-4 Formula of transmission rate according to Fick's first law in the steady state.....	27
Equations 2-5, 2-6, 2-7 expressing the permeability, sorption and diffusion coefficient.....	27
Equation 2-8 Equation expressing the permeance .....	28
Equation 2-9 Equation expressing the permeance as a Arrhenius-type equation.....	28
Equation 2-10 Equation expressing the permeation according to the laminate theory.....	28
Equation 2-11 Equation expressing the barrier improvement factor (BIF) ...	33
Equation 3-1 Formula of the roughness average $R_a$ .....	52
Equation 3-2 Formula of the root mean square roughness $R_{RMS}$ .....	52
Equation 3-3 Formula of the mean height.....	52
Equation 3-4 Equation describing the reaction taking place during the oxidation of the calcium coating deposited for calcium tests .....	55
Equation 3-5 Formula describing the relationship between the % of light transmitted and the optical density.....	57
Equation 3-6 Einstein relationship.....	59
Equation 3-7 Planck equation .....	61
Equation 3-8 relationship between wavenumber and wavelength .....	61
Equation 3-9 Penetration depth during ATR spectroscopy .....	62

# 1 INTRODUCTION

This work deals with the development of high flexible barrier coatings for encapsulation of electronic devices, such as organic light-emitting diodes (OLEDs) and flexible displays. All electronic devices must be protected from the permeation of any gas or vapour that can alter, corrode and damage them. Most of these devices are nowadays designed to be portable, thus very light. Furthermore, there is a high demand for flexible photovoltaic cells. Therefore, they must be protected from gas permeation by a flexible material, a so-called barrier coating.

Barrier coatings are functional coatings designed to protect the properties of the underlying substrate and enhance the lifetime and durability of the device. They are not needed with rigid glass substrates, but are mandatory to reach acceptable barrier levels on flexible substrates, such as flexible glass or plastics. Flexible glass has the advantage over plate glass in that it is much lighter (it is typically approximately 70 $\mu$ m thick) and offers some degree of flexibility. However, there is a limit to the bend strength and this is critically dependent on the quality of the surface and the edges. Embedded in the flexible glass are potential cracks that form when flaw sizes and stress reach a threshold. Flexible glass is normally coated to minimise contact damage during handling, transportation and later subsequent device manufacturing processes, but it can still be easily damaged.

Vacuum-deposited thin barrier films have the unique property of requiring only a very thin layer (sub-micron), which maintains flexibility. This is potentially a huge mechanical and economic advantage for vacuum coating technology. Several vacuum-based deposition techniques have been developed over the years for producing inorganic, optically clear oxide coatings for various packaging applications, where product transparency is a key requirement. Market size and growth, however, have been restricted, typically due to the high capital costs of the roll-to-roll vacuum coating platform, and the high

associated coating costs due to low line speeds and high consumable costs. While this is a problem for high volume packaging lines with low margins on mass produced quantities of film, it is still well within the acceptable cost realms for electronic applications as the current methods using glasses represents 50-70% of the cost of the end-product. In Japan, South-East Asia and Europe, development of high barrier clear coatings has been underway to provide a cheaper, lighter and more flexible alternative to glass or coated glass[1]. While glass substrates provide excellent barrier, they have disadvantages[2] in that they can be expensive to produce, heavy, rigid and prone to damage. The only alternative to glass currently showing promise for such applications is by the coating of flexible glass using a roll-to-roll method[3].

Clear barrier polyester films coated with both  $\text{SiO}_x$  and  $\text{AlO}_x$  ('x' is used because the stoichiometry is not determined) have been developed by many different routes (including reactive evaporation of  $\text{SiO}_x$  with  $\text{O}_2$

, plasma enhanced chemical vapour deposition of organosilane, electron beam evaporation of  $\text{Al}_2\text{O}_3$  and reactive thermal evaporation of Al with  $\text{O}_2$ ).  $\text{AlO}_x$  coatings have been developed for high rate production of barrier coatings on packaging materials[4]. PECVD (Plasma Enhanced Chemical Vapour Deposition) of  $\text{SiO}_x$  has been developed for similar purposes and has been adapted for creating the higher barrier levels required for electronic applications[5].  $\text{SiO}_x$  multi-layers may be required to provide tortuous barrier paths (i.e. to increase the path length through the barrier layer) for the permeating molecules. Variations of  $\text{SiO}_x$ , e.g.,  $\text{SiO}_x\text{N}_y$  or other additional components may be needed to enhance barrier properties. Various monomer types are available for producing  $\text{SiO}_x$  coatings with HMDSO (Hexamethyldisiloxane) most widely used.

In order to satisfy the requirements for a flexible substrate, several physical, mechanical and chemical properties should be considered when selecting the material to be used. Polyethylene terephthalate (PET) has many good intrinsic key characteristics including high melting point, low density and excellent chemical resistance, as well as the material itself being environmentally



friendly. Unfortunately, although PET offers reasonable water vapour barrier, the oxygen barrier performance is poor, but it is relatively easy to achieve good oxygen barrier through the coating itself. The more important requirement for electronic applications is high water vapour barrier. The optical properties of PET however, are known to be affected due to plasma attack. Other more exotic film types such as Polyethylenephthalate (PEN) cost more but offer a better starting point as the base barrier for O<sub>2</sub> and H<sub>2</sub>O is superior and the optical properties remain stable. Other potential substrate candidates may include PEEK, PC, PES, PNB, and PI (see Abbreviations list for more complete names). Planarisation or acrylate layers on the base substrates may enhance the barrier properties also. The deposited thin film, together with potential surface preparations, need to be optimised to make clear and flexible high barrier a commercially viable process that can be put into large-scale production.

This project is, therefore, focused on PECVD production of SiO<sub>x</sub> coatings with the overall aim of characterising and optimising the coating/substrate properties and understanding their relationship with the barrier properties. Potential challenges exist, because the proprietary equipment used for barrier measurement cannot measure down to the levels required for electronic applications. However, other methods can be used or developed to achieve measurement in that range, the calcium corrosion test is one of them. The calcium test is first a visual test to give an indication to the failure mechanism. Nevertheless, several groups have developed electrical calcium tests that give quantitative results[6]. For barriers required e.g. for OLED encapsulation, the only current way to test is by encapsulating OLEDs and testing the failure rates.

The particular PECVD method of the industrial partner (BOBST) is a unique patented process technology with empirical evidence to suggest it delivers a significant densification effect to the coatings[5]. The mechanisms of densification of the plasma and coating are not well understood yet and require further investigation.

Moreover, most of the current barrier technologies involve multilayer coatings (i.e. alternating organic and inorganic coatings [7]) that are designed to provide a tortuous path to moisture permeation. The methods used to produce these multilayers are complicated and make the optimisation and scaling up of the coating platforms very difficult. Thus, one of the challenges of this project is to reduce the number of layers to as few as possible, while keeping the moisture barrier close to the target of  $10^{-6}\text{g/m}^2/\text{day}$ . The first step in this direction is to understand the process and the relationship between the process parameters (power, flow rates, webspeed) and the coating properties (composition via XPS and FTIR, adhesion, morphology via SEM, roughness via white light interferometry, and barrier properties). Using different types of substrate with better surface properties can lead to further enhancement of the protective properties. The chosen substrate has to be characterised to find the most suitable type for the process; and the barrier mechanism and the relationship between moisture permeation requires investigation[6]. Another route for the optimisation of the single layer deposition process is to improve the properties of the surface of the base substrate (i.e. roughness, adhesion, and covering defects) by adding an acrylate coating as a topcoat. Further characterisation of the mechanical properties of the surface (substrate and acrylate coating) and interface are essential to develop this method. Finally, combining different deposition techniques and coating types is believed may lead to a breakthrough in the design of barrier coatings.

The aim of this project is, therefore, to study the interrelationships between deposition parameters, film properties, substrate properties and barrier performance in an industrial-scale PECVD production process.

This was planned to be achieved via completion of the following objectives:

- Review of the various existing techniques for creating atmospheric and vacuum transparent barriers coatings in the area of electronics on base substrates (PET, PEN, polyamide): described in Chapter 2
- Conduct coating trials and monitoring (deposition and characterization) at MMU and Bobst: Chapters 4 and 5
- Analysis/characterisation of the SiO<sub>x</sub> coatings produced by the PECVD method; investigate stoichiometry, structure and optical transparency of the coatings and identify which parameters influence the barrier level: Chapters 4 and 5.
- Measure the barrier properties of the coated substrates: Chapters 4 and 5
- Investigate other routes to achieve the goal (i.e. different gases, topcoats, different substrates): Chapters 6 and 7
- Perform repeat process trials on hypothesis, theoretical conclusions or assumptions gained from the initial coating trial and analytical study (Future work)
- Use an optimised SiO<sub>x</sub> solution to carry out trials. (Future work)

## **2 FUNDAMENTALS**

## 2 Fundamentals

This section aims to provide a basic theoretical background to help understand the project. As mentioned in the introduction, barrier coatings are complex microsystems. Thus, the permeation mechanisms of molecules, such as oxygen and water vapour are not trivial.

Electronic devices have been proven to be very sensitive to moisture permeation[8, 9]. Long exposure to high relative humidity and temperature environments can cause failures within hundreds of hours, which is not acceptable for devices that are expected to function effectively for up to 20 years.

Therefore, the device requires protection against moisture permeation. In this project, the main devices targeted by the development of barrier coatings were organic light emitting devices, photovoltaics, and solar cells. Even though the need of protection is the same, the sources and effect of permeation varies for each device.[10]

### **2.1 Photovoltaic modules and solar cell (organic/inorganic)**

#### **2.1.1 Organic and inorganic solar cells: device structure**

##### ***Organic solar cells***

In organic photovoltaic devices (OPV), the solar energy is converted into electrical energy. Several types of OPV have been developed over the years:

- Single layer OPV cells
- Bilayer OPV
- Bulk heterojunction OPV cells

More comprehensive descriptions of the devices can be found in the literature[11]. However, the principle of function of OPVs can be explained and extended from the bilayer OPV. A typical bilayer OPV device consists of one or several photoactive materials sandwiched between two electrodes. The main active layers are the donor and the acceptor semi-conducting organic materials. Each photoactive layer has a specific role as shown in Figure 2-1.

The donor material donates electrons and mainly carries holes, whereas the acceptor material withdraws and transports electrons. When the light is absorbed in the material, the donor material harvests photons from the sunlight and produces excitons that are then transported from the lowest unoccupied molecular orbital – LUMO (level of energy in the molecular or valence band) to the highest unoccupied molecular orbital - HUMO (conduction band)[12]. This transfer from the LUMO to the HUMO creates a concentration gradient of excitons that will diffuse at the interface between the donor and the acceptor. When they reach the interface, they are strongly bound as an electron/hole pair, but they will separate. This separation leads to free holes (positive charge carriers) and electrons (negative charge carriers) that will diffuse back, respectively, in the donor and acceptor materials. The photovoltaic process is finalised when the free electrons have travelled to the corresponding electrode, via the acceptor phase and the holes have travelled to the cathode via the donor phase (charge extraction).[10]

### ***Inorganic solar cells***

Inorganic solar cells rely mainly on the use of inorganic semiconductor materials, such as silicon. When the light hits the semiconductor, the photons transfer their energy to the atoms in the semiconductor, allowing electrons to be released and move freely in the material. These electrons create a current and create holes in the material that also move freely.

Silicon is particular in that its structure is made of weak bonds. However, by injecting (doping) other elements in the structure, the silicon can be tailored to hold electrons or holes. That way, it is possible to create a directional flow of electrons and holes, by putting a Si-n material (doped, to be rich in electrons) adjacent to a Si-p (doped to be rich in electron vacancies or holes). Indeed, to recreate the electrical balance, the electrons will move to the Si-p and fill the holes in. Silicon, as a semiconductor can act as both an insulator and conductor and therefore sustain this imbalance[10].

## 2 Fundamentals

Not all the electrons jump to the P side to fill the holes, some stay at the junction between the Si-p type and Si-n type and form an electric barrier. This barrier makes it difficult for electrons to travel across and toward the holes but also forces the electrons to move in only one direction (hole side to electron side). Thus, electric neutrality is disrupted and can be taken advantage of for current extraction. The electron current extraction (electron flow), for external use, is made possible by the contacts placed on the top and bottom of the PV. The electron will naturally move to the P side to fill in the holes. The characteristic power or wattage of the solar cell is defined by the combination of current extracted and the cell's voltage (result of the built in electric field).

The final structure of a solar cell conventionally comprises an antireflective coating such as indium tin oxide (ITO) to prevent the reflection and loss of photons on the silicon. A very important part of the cell is the substrate, which protects the device from moisture ingress. It is generally glass, but there is a desire to replace it with flexible polymers

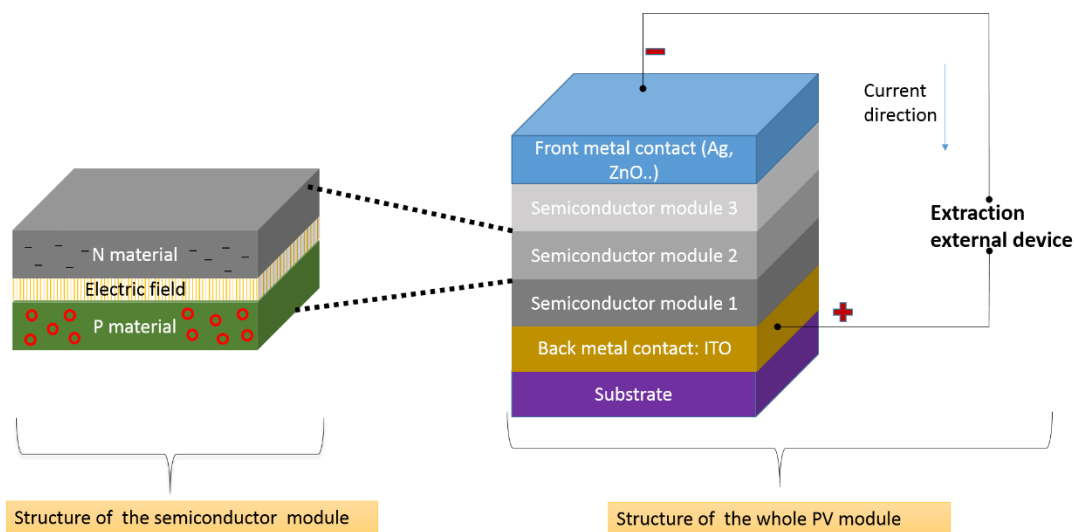


Figure 2-1 Schematic of the structure of a PV module [13]

### 2.1.2 Efficiency requirements, moisture and oxygen issues

PV electrodes (regardless of whether they are organic or inorganic) and active layers are mostly made of metallic materials (e.g. calcium, aluminium, tin, silver). These materials are very reactive to moisture and oxygen. The chemical reactions are generally enhanced by illumination. Two of the main consequences of the combination of moisture/light are photo-oxidation and photochemical reactions.

Moisture and oxygen, when reacting with materials like aluminium and calcium form oxides and insulating areas at the cathode (in OPVs). These insulating areas reduce the overall charge extraction, thus reducing the device performance. Oxidation is further enhanced under illumination. It is known that photo-oxidation changes the polymer chain (by scission or breaking the conjugation along the polymer backbone). This change induces a modification of the colour of the polymer (called photo-bleaching Figure 2-1) and a loss in light absorption. Thus, the efficiency of the device decreases. Photocatalysis is another form of photo-induced chemical reaction, whereby a chemical compound acts as a catalyst and accelerates the chemical reaction and degradation of the material. This has been observed in perovskite (hydride organic/inorganic) solar cells.[14]

The photochemical reaction between the metallic ion and moisture also could initiate the diffusion of metal ions. This creates deep traps in the active layer where the charges recombine, resulting in device performance loss through a reduction in  $V_{oc}$ ,  $FF$  and  $J_{sc}$ . [15]

The permeation of moisture in PV modules has been modelled by Kempe *et al.*[16] . They concluded that, although permeation of moisture depends on the encapsulation structure and materials, it largely happens through the EVA layer, and the edges of the structure. For example, with ‘permeable’ back sheets (plastic foils), equilibrium is reached within a few days to a few weeks. Whereas, in the case of glass it can take up to a couple of years for moisture



## 2 Fundamentals

---

to reach the device. However, in the latter case the main problem can be edge permeation (through the sealant, and its saturation in a rather short time and delamination.



*Figure 2-2 Photo of 20 year old photovoltaic panels that suffer from discoloration due to exposure to high humidity and changing temperature outdoor environment in Mexico [17, 18].*

The loss in efficiency due to moisture ingress can be quite dramatic depending on the device architecture. For instance, the efficiency of CIGS (copper, indium, gallium selenium) cells was found to decrease by almost 100% after 1000 hours exposure to 85% relative humidity at 85°C. Encapsulation with a barrier coating has proved to improve the lifetime of PVs by delaying the loss in power (less than 10% loss in efficiency after 1000 hours).[19]

### 2.1.3 Encapsulation of PVs

Solar cells are encapsulated following the structure presented in

Figure 2-3. The solar cell is placed in a sandwich between the two back and front encapsulant substrates (in our case the polymer barrier material). Ethylvinyl acetate is used to seal the system.

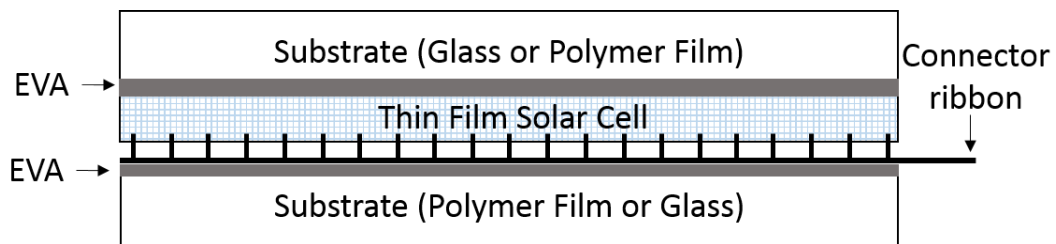


*Figure 2-3 Schematic showing the structure of the encapsulated photovoltaic module.*

Over the years, the structure has evolved to meet the requirements in terms of mechanical resistance. More information can be found in the review published by Czanderna et al[20] and Pern[21]

## 2.2 OLEDs

Organic light emitting devices have been emerging over the last decade as a reliable and interesting solid-state lighting technology. Not only do they find a use in phones displays (flexible displays, Samsung Edge) and TV screens. They are also expected to be implemented in various technologies and applications such as flexible, wearable lights (especially for aerospace), lights for automotive industry, hospitality and architectural purposes. Other market sectors are also known to be using OLEDs, i.e. tablet and notebook displays (flexible tablets), micro displays, etc. The main interesting features in OLEDs are that they are thinner, lighter and offer better colour performances, in comparison to backlit liquid crystal displays (LCDs).

IDtechEx, in 2014 was predicting a growth to 1.9 billion USD by 2025[22, 23]. However, they now estimate the global market value to remain under 200

million USD. This is mainly due to the difficulty for the OLEDs manufacturers to guarantee the lifetime and durability of the components.

### 2.2.1 Device structure and operation

The structure of OLEDs is relatively simple and similar to that of solar cells. The device consists of an anode and cathode both covered by an organic layer as shown in

Figure 2-4.

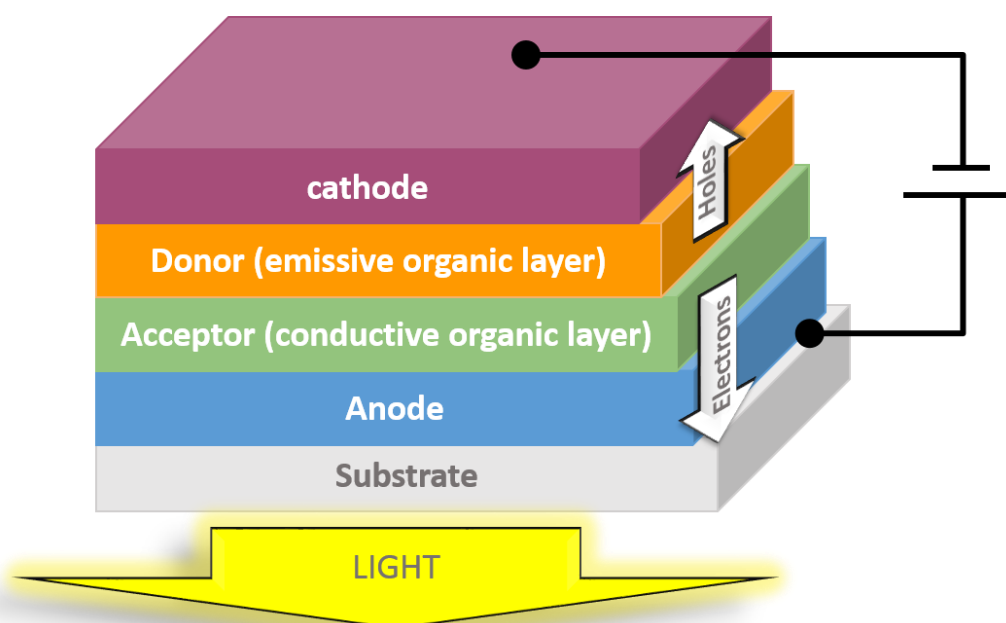


*Figure 2-4 Schematic showing the structure of an OLED, adapted from [9] and [24].*

An electrical voltage is applied between the cathode and the anode. This leads to the injection of free holes in the cathode and free electrons on the anode. These electrons and holes travel through the device under the applied potential and recombine to form excited molecular species, such as excitons. When the excited species decay from the excited to the ground state they emit light.[8]

The typical applied voltages are in the 10<sup>6</sup> V/cm range and the emissive and conducting layer are about 100-200nm thick. The anode is generally a sputter deposited indium tin oxide and the cathode is a low work function metal or alloy that facilitates the injection of electron in the adjacent material (organic emissive layer). The common materials used are lithium, magnesium, calcium and barium. They are mostly deposited via physical vapour deposition methods, such as magnetron sputtering and thermal evaporation.[25, 26]

However, for efficiency reasons, additional layers have been added to the structure over the years. These layers prevent recombination of the excitons.

The most common OLED structure[23], therefore, takes into account a emissive layer sandwiched in between the hole and electron transport layers (both very conductive and transparent). Other additional layers such as electron and hole blocking layers (that do not absorb any light) can be added to prevent the excitons from exiting the emissive layer and hinder their recombination only at the emissive layer. This type of structure is commonly called a pin-OLED and is shown in Figure 2-5. Further information about these structures can be found in the literature.[13, 23, 25].

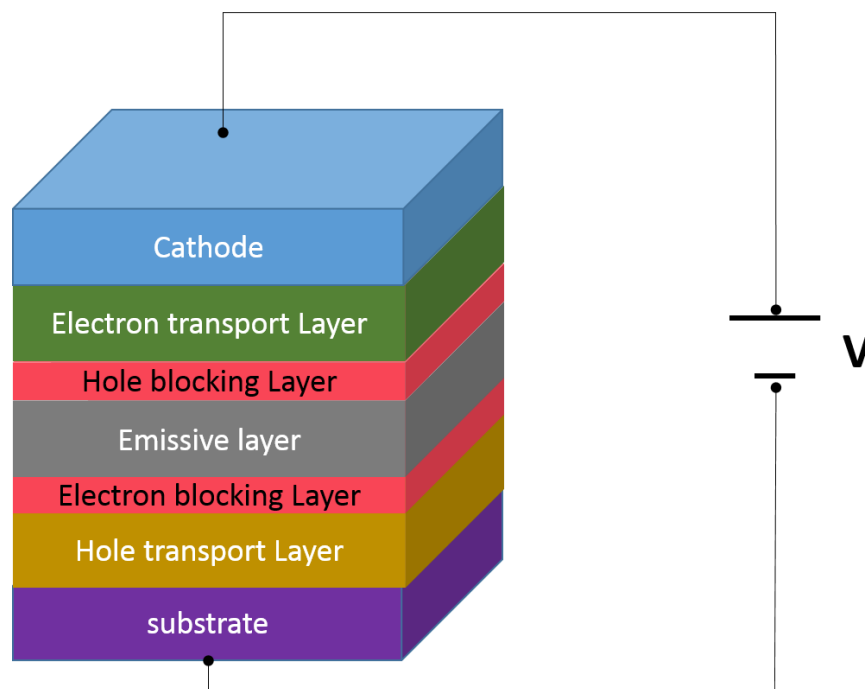


Figure 2-5 Structure of the pin- OLED adapted from [23]

### **2.2.2 Device efficiency requirements and durability requirements**

OLEDs must fulfil specific requirements to be viable commercially. The most important one is stability over time. This is strongly related to the integrity of the different layers. Therefore, the electrodes that are metallic and highly reactive must be protected from any moisture intake that could create corrosion and electrochemical migration, in a similar way to electrodes in solar cells. Chemical resistance is also critical for the materials to be compatible with the encapsulation process and be resistant to corrosion.

Other properties such as good adhesion to the display surface also play a key role, as the system should be one compact block to be hermetic to moisture (i.e. poor adhesion leaves a gap for moisture to permeate between the layers and react).

### **2.2.3 Moisture permeation protection via encapsulation**

With the need to create a moisture barrier product, comes the requirement to make it as compatible to the OLED component as possible. This translates into properties, such as good adhesion with the display surface, similar thermal expansion coefficient as the layer beneath, resistance to any processes used during the fabrication of OLED (e.g. chemical and mechanical resistance during the lithography process).

Moreover, the barrier layer should be robust enough to withstand the user's handling without damaging the component. This leads to the need for high flexibility and retention of barrier with in-flex use over the lifetime of the product. In addition, the substrate on which the device rests should have a high Young's modulus, high thermal and UV stability. All these requirements are expected to be fulfilled while maintaining the cost as low as possible for industrial purposes.[8, 25]

As will be mentioned in Section 2.2.3, one of the main source of damage for electronics devices is due to the permeation of moisture. Burrows *et al*

estimated that the maximum water vapour leakage rate for an Mg cathode without damaging it (less than 10% oxidation of the cathode) should be  $10^{-4}$  g/m<sup>2</sup>/day. This would give the OLED a lifetime of one year. However, it appears clear that in order to protect the device efficiently and increase the operational lifetime, the barrier should be higher. Therefore, it is accepted in the OLED community that  $10^{-6}$ g/m<sup>2</sup>/day is a target figure.[13]

In order to protect the devices from moisture ingress and damage, they are encapsulated with impermeable and moisture resistant materials. This is where moisture barrier materials are needed. Several models exist for encapsulation, and the most widely used are presented in Figure 2-6

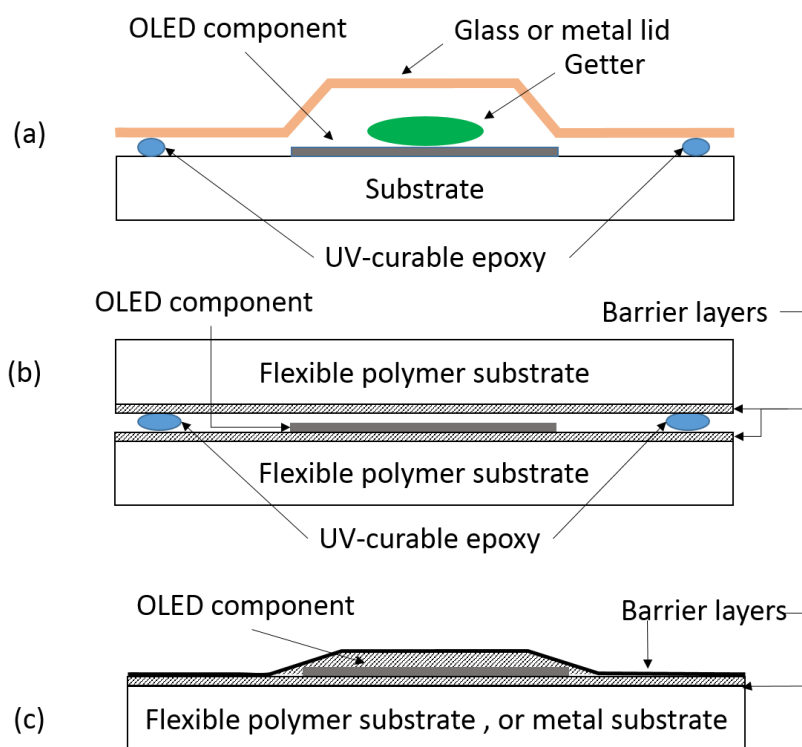


Figure 2-6- Schematic of encapsulated OLEDs, adapted from [8]

In model (a), which is the conventional encapsulation structure, the device is sealed in an inert environment using a metal or glass lid. UV-curable epoxy is used to seal the lid to the substrate, which is most commonly glass in this case. Any by-products from the curing of the UV-curable epoxy or the reaction of the materials with residual oxygen or moisture (or moisture getting in the package over time through the epoxy) is expected to react with the getter material

(generally calcium oxide or barium oxide). This type of structure is however not suitable anymore due to the need to provide a rigid lid, which limits the flexibility of the device.

Alternative structures [8, 25, 27] have therefore been developed in order to gain flexibility of the complete OLED (F-OLED). These structures generally involve a flexible polymer substrate as the base and flexible barrier coated lids to seal the device as shown in Figure 2-6 (b) and (c). Different variations exist; the lids could be sealed with either epoxy or in direct and intimate contact with the polymer substrate (Figure 2-6 (c)). The main advantages of the latter arrangement are the improved flexibility and reduced weight of the completely encapsulated package and less risks of abrasion of the OLED during the in-use flexing of the device. These structures require high quality moisture and oxygen barrier coatings and compatibility of the barrier material with the OLED encapsulation methods. The suitability of deposition techniques for encapsulation and their compatibility with the barrier coating deposited material are still being discussed. However, in recent years, chemical vapour deposition techniques such as ALD and PECVD have proven to be more suitable. Duan et al. have reviewed the techniques and their requirements, which are summarised here: good conformity, good uniformity, accurate thickness over large and complex surfaces, compact, easy controllable process, good adhesion, good coverage, good optical transparency and cost effectiveness[27].

### **2.3 PECVD coatings**

Numerous techniques exist to apply a coating to a polymer substrate. These techniques are divided into two groups: chemical and physical methods.

The chemical methods use a chemical reaction between chosen species (or precursors) at the surface to make the coating. The physical methods are based on physical phenomenon such as evaporation, sputtering and condensation to make a coating.

The principle of the plasma enhanced chemical vapour deposition (PECVD) technique is based around the chemical vapour deposition method, largely used in the microelectronics field. Plasma enhanced chemical vapour deposition of thin films is commonly used to deposit functional coatings in the range of a few nanometres to several microns.

### **2.3.1 Introduction to chemical vapour deposition**

In chemical vapour deposition[28], chemical reactions occur between the reactants near the heated surface of a substrate. The reactive species can be introduced in their solid, liquid or gaseous state. The temperature is typically above 900°C but is lowered for certain specific CVD based processes and provides sufficient energy to activate the chemical reactions. A range of heterogeneous and homogenous reactions occurs in the gas phase.

This coating method has been and remains largely used for a wide range of applications, such as microelectronics, semiconductors, optoelectronics, energy conversion devices and refractory ceramic materials. CVD is also used for hard coatings, protective coatings against corrosion and diffusion barriers. [29]

It is an easy-to-use method to produce uniform, dense, and pure solid materials. It has been proven to provide repeatable and well adherent coatings at high deposition rates. Because CVD has been developed and used for at least fifty years, it is well known that it allows coatings to be deposited with a high control on their uniformity, type and structure.

Nevertheless, as a thermal deposition technique where the substrate needs to be heated, CVD is not applicable to heat sensitive plastic substrates. In addition, it can involve toxic and corrosive gases, which can be especially dangerous at high temperatures. Thus, it can be a dangerous process if not well controlled.

Plasma enhanced CVD processes (PECVD) have evolved over the years to fulfil the requirements of specific innovative applications. Thus, many different



methods based on CVD exist. Some of these are low pressure CVD (e.g. microwave plasma CVD, plasma enhanced CVD, hot filament CVD and remote plasma CVD); others are high pressure CVD based methods (atomic layer epitaxy, combustion CVD or flame pyrolysis, metal organic CVD, rapid thermal CVD, aerosol CVD, etc.). [28-33]

### **2.3.2 Plasma enhanced chemical vapour deposition**

#### **2.3.2.1 Plasma basics**

Plasma exists everywhere and represents more than 99% of the visible matter. Stars and interstellar matter are, for instance, plasmas. Moreover, they are used in many everyday life devices in technologies ranging from the neon lamp, to certain plasma TV displays.

It is the fourth state of the matter, after liquid, solid and vapours. It is a medium with many different types and sizes of particles such as atoms, molecules, ions and electrons. These particles can be found in their ground state or in their excited state. A wide range of reactions including ionisation, excitation, dissociation and relaxation creates the various species. It is a neutral medium overall, although constituted of positively and negatively charged particles. All the reactions occurring in the plasma lead to the emission of light ('glow') of a particular colour. It is the result of the emission of characteristic electromagnetic radiation during relaxation of the excited species.

Extensive literature is available on the phenomenon occurring in plasmas and will not be detailed in this report. [34]

#### ***Principle of PECVD***

In PECVD a mixture of gases, containing the monomer precursor is injected into a chamber between two electrodes (Figure 2-7). The gases are excited using an electrical discharge or magnetic induction. Thus, the reactive gases in the chamber interact and react with the monomer precursor and form the chemical compound to be deposited.

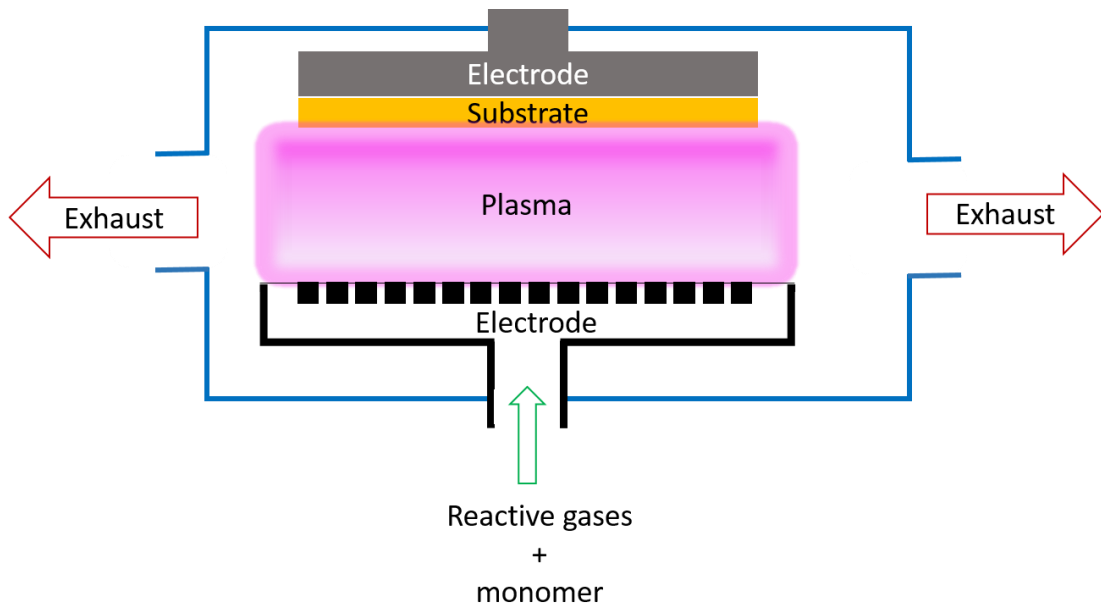


*Figure 2-7 Schematic illustrating the principle of PECVD[35].*

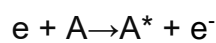
This type of plasma is called cold plasma because it is out of equilibrium and kept at a pressure below atmospheric, usually under 1Pa. This plasma is then used to increase the reaction rate of the gas/precursor mixture. Thus, the mixture does not need to be heated as in the basic CVD technique. Indeed all, the energy is provided by the electrical discharge/magnetic induction supply.

The most common way of supplying energy is by creating an electric discharge between the two electrodes. The discharge can be generated from different types of delivery modes, such as medium frequency (50 kHz), radio frequency (13.56 MHz) microwave frequency (2.45GHz) or by continuous discharge.

### ***Physics of PECVD plasma: kinetics and reactions***

PECVD plasmas are very reactive, particularly in the main reaction zone, where numbers of reactions occur[36].The electrical field provides the electrons with an energy, between 1 and 10 eV[36]. This allows them to travel and collide with atoms from the gaseous reactants injected in the chamber. These collisions are of different kinds and can be divided in four categories:

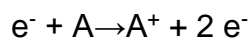
The Inelastic collisions that are described by an excitation of the particle after collision, without change in kinetic energy.



The elastic collisions, during which the kinetic energy of the electron or specie is transferred to the particle. To some extent, some internal energy can be transformed into kinetic energy. This kind of reaction can be described as a super-elastic reaction.



The ionising collisions (inelastic reactions), during which an electron is removed from the atom/molecule. Heavy and charged specie called ions are created.



The reactive collisions that induce a change in chemical nature of the specie. This allows reaction such as



These various collision modes improve the number of chemical and atomic reactions occurring in the plasma [37].

### ***Advantages of PECVD polymerisation***

Plasma polymerisation using the PECVD method presents many advantages, including [37]:

- The low operation temperature of the process: Indeed, the substrate or chemicals do not need to be heated up as they benefit from the high collision rates in the plasma.
- The good dielectric properties of the layers, which makes the coatings good candidates for electronics applications.
- The good step coverage, as the coatings are generally conformal.
- The high density of the coatings that is related to the plasma density.
- Good adhesion, which is promoted by the constant bombardement of the substrate's surface by energetic radiation (such as electron, positive ions, neutrals). This bombardement alters the chemical properties of the substrate's surface as deposition occurs[37, 38].

Plasma polymerisation reactions may be modified by making changes in the deposition parameters and gas mixtures, which is another advantage of the method. Therefore, the composition, chemistry and structure of the coating are also tuneable by controlling the precursor fragmentation.

As a variant of the CVD technique, PECVD has been adapted over the years to suit the requirements of different applications. For example, magnetron PECVD[39] methods and Hollow cathode PECVD[40], along with dual frequency [41, 42] or pulsed PECVD[42] can be cited.

PECVD is suitable for a range of applications. Where conventional CVD can only be performed on glass or heat resistant substrates, PECVD allows the use of flexible substrates such as polymers. This is of interest for the market on flexible devices, such as displays, and solar cells. One of the most obvious advantages of transferring the technologies onto flexible substrates is the reduction of the final device weight.

PECVD has been largely used since the 1980 to produce barrier coatings on plastic flexible substrates. The route of  $\text{SiN}_x$  (and combined with  $\text{SiO}_x$

coatings) has also been explored [43]. Different routes exist with the PECVD process, because it is possible to use different precursors, different gas dilution conditions and various types of power delivery mode. This section will focus on PECVD methods using HMDSO in neutral atmospheres (such as argon and helium) and oxygen gas diluted plasmas.

### **2.4 Vacuum web coating**

Vacuum web coating is based on the use of a process chamber and a winding mechanism, which passes the web from the unwind zone to the rewind zone and through the process chamber as shown in Figure 2-8. The differential pumping taking place between the two zones induces a separation between the winding zone where there is no treatment of the web and the process zone where the film is coated. This process zone is equipped with the gas injection system (source), the electrodes and all the other elements used to make the coating, including a drum (typically 300 to 1000 mm in diameter) webbed up with the film to coat. The pressures are kept at different levels in the process zone and winding zone, in order to keep the process plasma in the process chamber. Rotary and roots pumps are usually used to reach the desired pressures. The web speed through the deposition system can be set and several parameters can be monitored during the process (e.g. thickness, optical density, defect detection, etc.). The drum is cooled down to reduce the heat load on the substrate (which can cause deformation of the substrate and therefore uninform deposition) due to intense bombardment of the surface. This type of coater is commonly called a roll-to-roll coater and can accommodate a wide range processes such as PECVD, magnetron sputtering, electron-beam evaporation, etc.

This type of coater allows the continuous processing of long lengths (several km) of materials, and can be implemented with post or pre-treatment, if needed.[44]

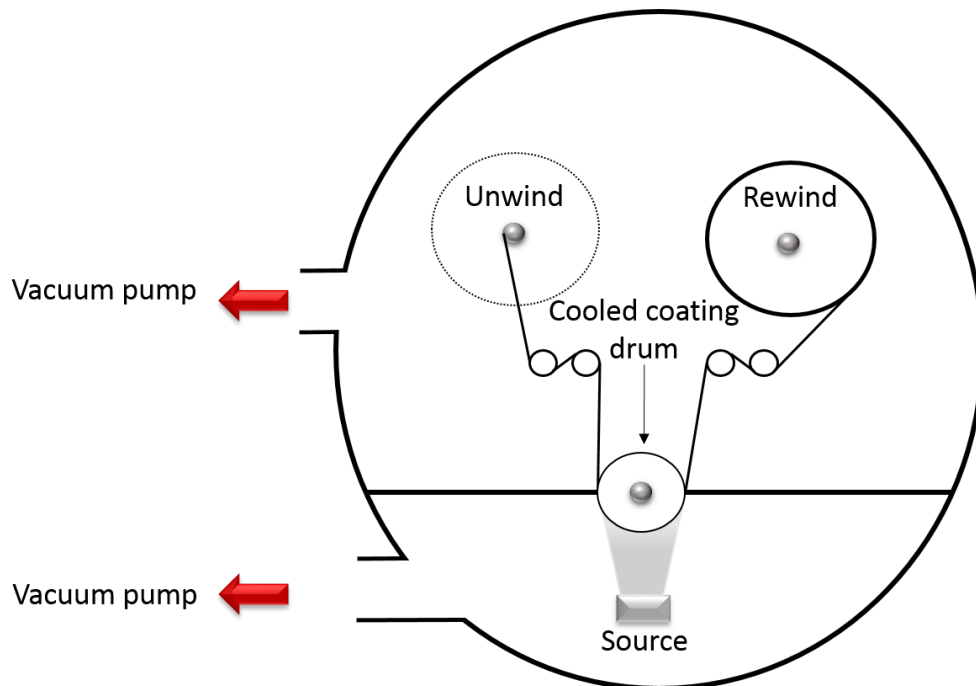


Figure 2-8 Schematic of vacuum web coating Mechanism.

## 2.5 Barrier coatings

### 2.5.1 Water vapour and oxygen transmission rates

Permeation is the physical phenomenon describing the diffusion of molecules and atoms, so-called permeates, through a solid as shown in Figure 2-9. The concentration gradient of the permeate and the solid's intrinsic permeability, along with its mass diffusivity, are the main parameters driving the permeation process.[6, 45-47]

### 2.5.2 Permeation through polymers

**Note:** The following considerations are valid in the steady state in the case of one-dimensional diffusion. In this steady state, a linear concentration gradient takes place, however the diffusion coefficient,  $D$ , and solubility coefficient,  $S$ , are independent of the concentration. [48, 49]

Ideal flawless polymers are not porous materials; therefore, the solution diffusion model describes the transport of ideal gases in these solids. This

## 2 Fundamentals

model states that the gas molecules and atoms dissolve in the solid and diffuse due to a concentration gradient effect. This gradient of concentration in the solid is due to a difference of pressure (quantity of gas molecules) on each side of the solid. In order to equilibrate the pressures, the molecules will start diffusing following four main steps:

- 1) Adsorption: the molecules attach to the surface on the high concentration side of the polymer.
- 2) Solution of the molecule in the volume of the polymer
- 3) Diffusion through the material via Brownian motion due to a concentration gradient
- 4) Desorption on the other side of the material, where the concentration of the permeant is low.

The phenomenon of permeation is shown in the following schematic:

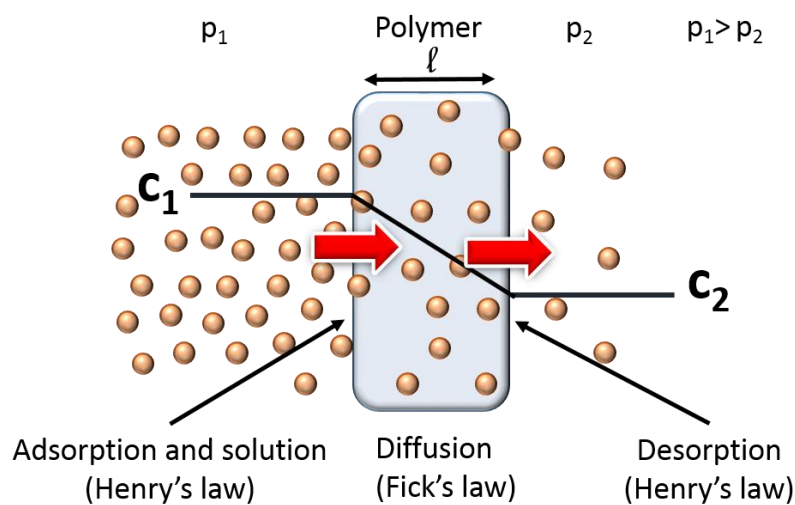


*Figure 2-9 Schematic illustrating the gradient of pressures of the permeant on both sides of the solid that is taking place during permeation.  $p_1$  is the partial pressure of permeant on the entrance side and  $p_2$  is the partial pressure at the exit side of the solid.[3]*

Fick's first law describes the diffusion step

$$J = -D \frac{\partial c}{\partial x}$$

*Equation 2-1 Equation describing Fick's law*

Where:

$J$  is the rate of diffusion [ $mol \cdot m^{-2} \cdot s^{-1}$ ]

$\frac{\partial c}{\partial x}$  is the concentration gradient [ $mol \cdot m^{-4}$ ] (where  $x$  is in  $m$  and the

concentration,  $c$ , in  $mol \cdot m^{-3}$ )

$D$  is the diffusion coefficient [ $m^2 \cdot s^{-1}$ ]

In this model the diffusion step is considered as the limiting step[50]. It states that the concentration of permeant dissolved in solids is proportional to the partial pressure of the component present in this solid. This is expressed in the following formula, which states that the concentration of permeant dissolved in solids is proportional to the partial pressure of the component present in this solid. This is expressed in the following formula:

$$c = Sp_i$$

*Equation 2-2 Formula of expressing Henry's law of solution*

Where,  $S$  is the Henry's solubility constant [ $mol \cdot m^{-2} Pa^{-1}$ ], and  $p_i$  (Pa) the pressure of the gas considered.

As far as the measurement of barrier is concerned, the transmission rate (TR) is mostly used. This transmission rate is obtained by combining the integrated Fick's first law (in the steady state when  $J$  is constant and the concentration does not vary with time, if the diffusion is considered one-dimensional)



## 2 Fundamentals

---

equation and the Henry's law equation. When the steady state occurs, Fick's first law becomes

$$J = D \cdot \frac{C_1 - C_2}{t}$$

*Equation 2-3 formula describing the |Fick's first law in the steady state*

Thus, the transmission rate is defined as follow

$$J = D \cdot S \cdot \frac{(p_1 - p_2)}{t}$$

*Equation 2-4 Formula of transmission rate according to Fick's first law in the steady state*

The product  $DS$  equals the permeability coefficient, expressed in  $\frac{\text{mol} \cdot \text{m}}{\text{m}^2 \text{s} \cdot \text{Pa}}$ .

The permeability ( $P$ ), sorption ( $S$ ) and diffusion coefficient ( $D$ ) are dependent on the temperature and follow the Arrhenius model:

$$P = P_0 e^{\frac{E_P}{R \cdot T}} \quad ; \quad S = S_0 e^{\frac{E_S}{R \cdot T}} \quad ; \quad D = D_0 e^{\frac{E_D}{R \cdot T}}$$

*Equations 2-5, 2-6, 2-7 expressing the permeability, sorption and diffusion coefficient*

Where  $P_0, S_0$  and  $D_0$  are constants unique to the system,

$E_P, E_S, E_D$  are the apparent activation energies specific to each material in

$[J \cdot \text{mol}^{-1}]$

$R$  is the gas constant  $8.314 [J \cdot \text{mol}^{-1} \cdot K^{-1}]$

$T$  is the absolute temperature  $[K]$

Another parameter arises from the combination of Henry's law and Equation 2-8, which is the permeance,  $Q$ , also called transmission rate.

$$Q = \frac{P}{t}$$

*Equation 2-8 Equation expressing the permeance*

Q is expressed in  $[mol \cdot m^{-1} \cdot s^{-1} \cdot Pa^{-1}]$

The permeance, as the other equations state above, can be described by an Arrhenius-type equation as follows [2]:

$$Q = Q_0 e^{\frac{E_Q}{RT}}$$

*Equation 2-9 Equation expressing the permeance as a Arrhenius-type equation*

Where  $Q_0$  is a constant relative to the system

$E_Q$  is the apparent activation energy of permeation (specific to every material)  $[J \cdot mol^{-1}]$

Study of the apparent activation energy is also used to investigate the mechanisms of permeation of vacuum web-coated polymer films such as  $AlO_x$  and  $SiO_x$ . For the permeation of composites or laminates made of several layers of polymers, the overall permeance, Q, can be calculated using the ideal laminate theory[51], as follows:

$$\frac{1}{Q_{total}} = \frac{1}{Q_1} + \frac{1}{Q_2} + \dots$$

*Equation 2-10 Equation expressing the permeation according to the laminate theory*

## 2 Fundamentals

The mechanisms of gas transport into polymers vary with the size and nature of the molecules, which itself differentiates oxygen permeation processes to water vapour permeation. Indeed, water vapour, due to its polarity can interact with the polymer. Other than that, permeation is linked to the chemistry of the polymer, along with its nature, composition (e.g. additives, composites, and copolymers), structure (crystallinity, crosslinking, orientation). This non-exhaustive list of critical parameters also includes the environment and the condition of permeation, such as relative humidity, pressure and temperatures.[48, 49, 52]

### **2.5.3 Permeation through plastic foils coated with thin film inorganic coatings**

Functional thin film coatings can be deposited onto polymers to enhance their barrier properties against water vapour and oxygen permeation. These coatings are mostly inorganic and commonly metal oxides (e.g.  $\text{AlO}_x$ ,  $\text{ZnO}$ ) or ceramics (e.g.  $\text{SiO}_x$ ).

The solution-diffusion model cannot be used to describe the permeation into such materials. Indeed, these films often present specific structures and nature, comprising defects, pores or grains that influence the permeation of gases.

Moreover, the permeability of these thin films is higher than the permeability stated for corresponding bulk materials [53] (e.g. silica for  $\text{SiO}_x$ , and alumina for  $\text{AlO}_x$ ). This can be explained by the difference in density of the bulk material, along with the absence of defects and pores, which makes it impermeable to many gases including  $\text{O}_2$  and  $\text{H}_2\text{O}$ . Following that comparison, it is expected that a bulk-like defect free coating should provide a very good barrier against the permeation of oxygen and water vapour. If the focus is placed on  $\text{SiO}_x$  coatings, the corresponding bulk material (silica) is known to be permeable to He, slightly permeable to Ne and  $\text{H}_2$  and not permeable to Ar,  $\text{O}_2$ ,  $\text{H}_2\text{O}$ ,  $\text{N}_2$ , Kr and Xe [47].

Over the years, permeation of oxygen through barrier coating/plastic substrate composites has been extensively studied. In the last decade, it has been proved that the permeation of water vapour does not follow the same models as the permeation of oxygen, especially not the Fickian models used to describe permeation in polymer substrates. Therefore, this subsection will detail separately the two mechanisms. This is due to the chemical (e.g. chemical reaction) and physical (size) of the two molecules. Ultimately, a final paragraph is dedicated to the mechanisms of permeation through porous structures, as it is not unusual to obtain porous silicon oxide coatings,

### 2.5.3.1 Oxygen permeation

Prins and Hirmans[54] have established that the permeation through metal coated polymers is led by the diffusion through defects (Figure 2-10). Different defects can be found in the coatings, such as pinholes (uncoated area, macro-defects not present in the substrate), micro-cracks, voids, and grain boundaries. Although all these defects contribute to permeation, pinholes contribute the most. Thus, they proved that diffusion is driven by the defects' density and shape (radius and depth) rather than the thickness of the coating.

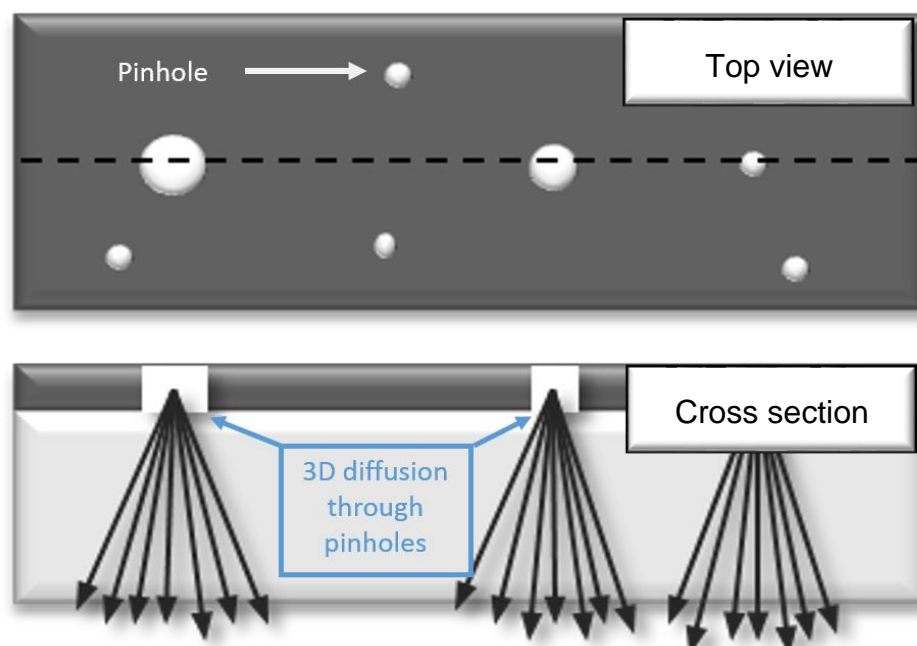


*Figure 2-10 Permeation through pinhole model (top view and cross-section) [3]*

After passing through the defects in the inorganic coating, the permeating substances diffuse out in all directions (lateral diffusion) within the polymer, and a three-dimensional concentration profile (see cross section in Figure 2-10) is created. [55, 56]

### **2.5.3.2 Water vapour permeation**

Water vapour permeation does not follow the Fickian model and is very difficult to predict due to its reactivity.

Elrawemi et al. [57] recently showed that permeation of water vapour through small numbers of large defects dominates over the permeation through small pinholes in metal coated plastic substrates.

### **2.5.4 SiO<sub>x</sub> coatings and porous structures**

Glass and glassy polymers [45, 58] are known to exhibit very good barrier to oxygen at room temperature, due to the low amount of voids and defects in their structures. As it is very dense, it becomes difficult for molecules or atoms to find a path to go through it. This property explains the low permeation rates observed on glass.

Although, silicon based coatings are meant to reproduce the properties of silica glass in terms of permeation, the permeability of SiO<sub>x</sub> coatings is much lower than the ideal silica glass, which tends to prove that silicon oxides are not defect free or fully dense. Another key point to confirm the defect theory is the study of activation energy. Activation energy is defined as the energy necessary for the system (lattice and permeants) to allow the gas to go through the layer/defects. Thus, a defect free layer would exhibit a rather high activation energy in comparison to a layer containing defects like holes (less energy is required to pass through the defects than to go through a very dense layer)[50]. In addition, it appears that the molecule would need more energy to

pass through small defects than through large defects. That way, any observed variation in activation energy can provide information on the size of the defects.

Roberts et al. [59] used the activation criteria to suggest transport mechanisms for oxygen (in its molecular form). Their model states that permeation can take place through three paths. Each path takes into account the measured activation energy, which ultimately is related to the relative size of the defects and the molecule (providing that this molecule is not interactive, i.e., it is an inert gas). The first path for the gas molecules can be through the macro defects, which can be large holes or uncoated areas. As these defects' sizes are several orders of magnitude higher than the size of the permeants, permeation is quite easy through the macro defect ( $>1\text{ nm}$ ). In other terms, only low activation energy is required for that type of permeation. Thus, an unhindered defect does not largely change the energy level in the system. The second possible path for gas molecule is through nano-defects that are about the size of the permeant (or slightly bigger,  $<1\text{ nm}$ ).

The interstice in the lattice ( $<0.3\text{ nm}$ ), which are typically smaller than the size of the permeant molecule represents another path for permeation. A high energy is required for the molecule to get through the interstices; which makes it a much-hindered defect. It is relevant to remind the reader that this model is only valid for non-interactive molecules and cannot be applied to molecules such as water.

Several mathematical models exist to describe each path [59-62] which will not be detailed in this report. In terms of permeability, Roberts et al. [59] also reported that there are two limiting cases for  $\text{SiO}_x$  /polymer composites. Indeed, when the barrier is defect free the global permeability is controlled by the oxide permeability, whereas in the presence of macro-defects in the oxide layer the permeability is mainly related to the properties of the polymer. Although nano-defects and interstices play a role in permeation, they do not allow the transport of large molecules (such as  $\text{H}_2\text{O}$ ), unless the molecule interacts with the material in order to enlarge the defects and go through it. Numerical calculations, taking into account different defect shapes, showed

that small defects play a more important part in permeation than the big defects (for a small density of defects on a considered area). In addition, the polymer adjacent to the defects plays a determinant role in the permeability of the coating.[57, 63]

As far as water vapour transport is concerned, there are still some uncertainties due to the complexity of the interactions (physical and chemical) that can happen between the molecule and the oxide. Indeed, it has been reported that both PET and silicon oxides interact with water, mostly due to attractive interaction and reaction and the high polarity of the molecule[63]. Thus permeation mechanisms [58] are thought to be highly dependent on the water concentration [62]. Although, it is believed that the permeation of H<sub>2</sub>O is led by molecular diffusion through the nano-defects[59] [60].

Another key point in the description of barriers is the barrier improvement factor (BIF). It is a parameter to describe the quality and efficiency of the coating and the contribution of the coating to the barrier performance of the polymer/coating composite. It is defined as the ratio of the permeance (transmission rate) of the plain polymer film,  $Q_0$ , to the coated film,  $Q$  [64]:

$$BIF = \frac{Q_0}{Q}$$

*Equation 2-11 Equation expressing the barrier improvement factor (BIF)*

Since this factor depends on the plain film transmission rate, it is also strongly related to the substrate thickness.

### 2.5.5 Barrier requirements

Functional barrier coatings are needed in a wide range of applications from food packaging to electronic encapsulation. Each application has specific requirements in terms of barrier levels.

As shown in Figure 2-11, electronic devices such as OLEDs LCD/LED and food packaging do not require the same barrier level. Therefore, the

techniques used to produce the coatings vary with the application targeted. In the food packing industry, evaporation is mainly used, whereas PECVD[65] and sputtering fulfil the higher barrier requirements of the electronics industry. Atomic layer deposition of barrier coatings has recently shown very good results reaching barrier performances up to  $4 \times 10^{-3} \text{cc/m}^2/\text{day}$  for oxygen transmission rate and in the range of  $10^{-3}$  to  $10^{-5} \text{g/m}^2/\text{day}$  for water vapour transmission rate.[5, 65, 66]

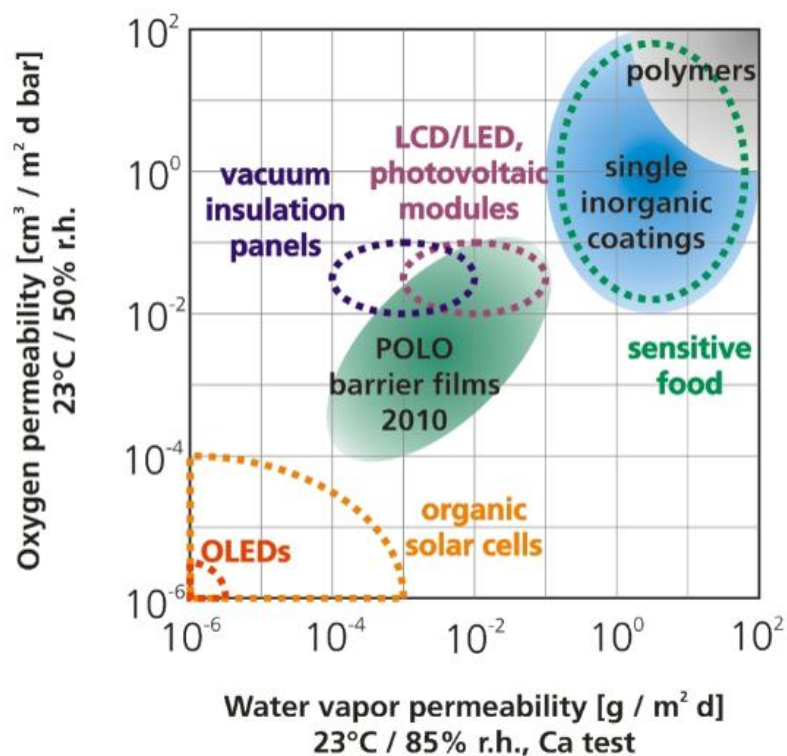


Figure 2-11 Barrier performance requirements for some technological applications including organic electronics and photovoltaic encapsulation.



### **3 METHODS AND MATERIALS**

### 3.1 The PECVD roll to roll coater

The coater provided by the industrial partner, Bobst Manchester Limited (BML), is a pilot scale roll-to-roll coater. It uses the plasma enhanced chemical vapour deposition technique to apply a  $\text{SiO}_x$ , (x to be determined) coating onto a flexible polymer substrate. This equipment is shown in Figure 3-1.

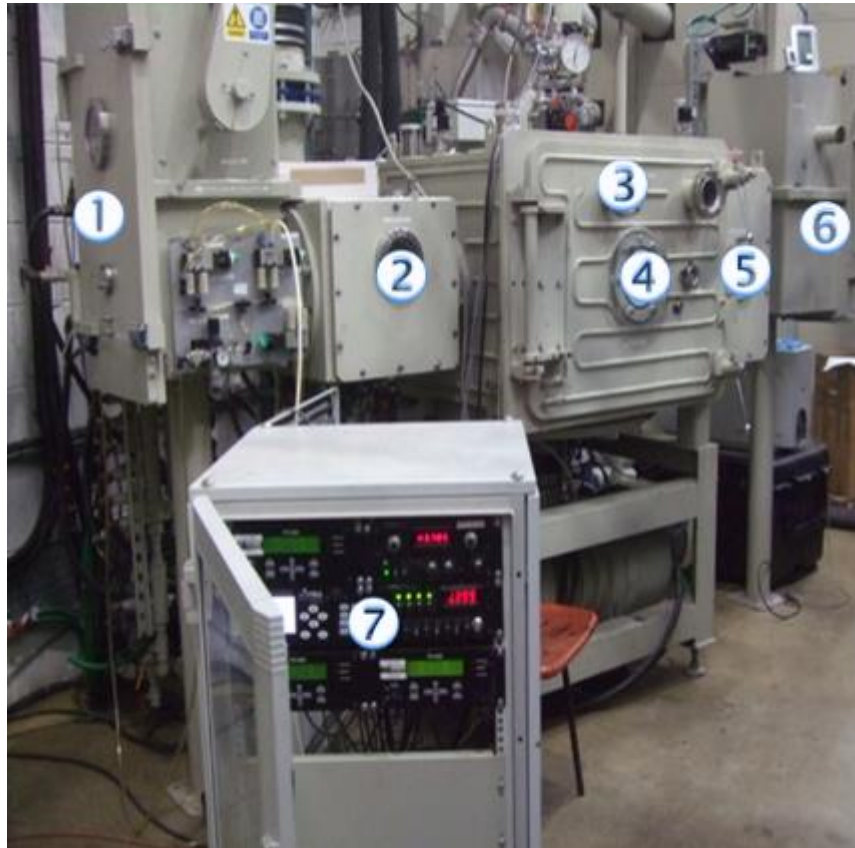


*Figure 3-1 Photo of the pilot scale roll-to-roll PECVD coater used for  $\text{SiO}_x$  deposition onto PET. (BML property)*

### 3 Methods and materials

---

*Table 3-1 Identification and role of the different zones in the roll-to-roll PECVD coated shown in Figure 3-1*

<b>Number</b>	<b>Name</b>	<b>Description</b>
1	Unwind zone	Unwinding of the substrate
2	Pre-treatment zone	No pre-treatment done for this project
3	Main chamber: winding zone	No process
3	Main chamber: process zone	PECVD coating process
5	Post-treatment zone	No process
6	Rewind zone	Rewinding of the coated film
7	Control unit	Control of the gas flows, displaying pressures

This coater consists of six zones that each have a precise role in the process, as mentioned in Table 3-1 and illustrated in Figure 3-2

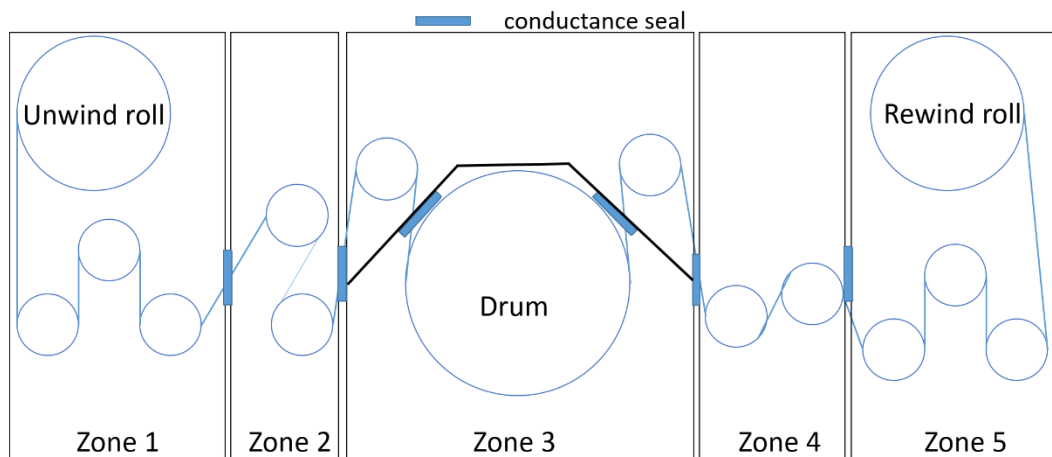


*Figure 3-2 Illustratuion of the webpath in the roll-to-roll coater and the conductance seals between the different zone.*

The first zone located on the left-hand side of the coater is called the unwind zone. This is the where the roll of substrate is located, providing the film to a series of three rollers. Afterwards the film goes through the pre-process zone (2).

At the end of the pre-process zone, the film enters the main chamber, where the coating process takes place. The web is coated and then continues its way to the re-wind zone, passing by the post-treatment zone (no specific post treatment equipment installed). The web path is made possible by a series of rollers (idlers and dancers, shown in Figure 3-3) and a constant control of the tension between the unwind zone and the rewind zone through three drives (three drives controlling, respectively, the drum, the unwind and rewind film rolls). This automatic control system enables the film to move in both directions (forward and backward) as well as to set-up the film speed.

### 3 Methods and materials

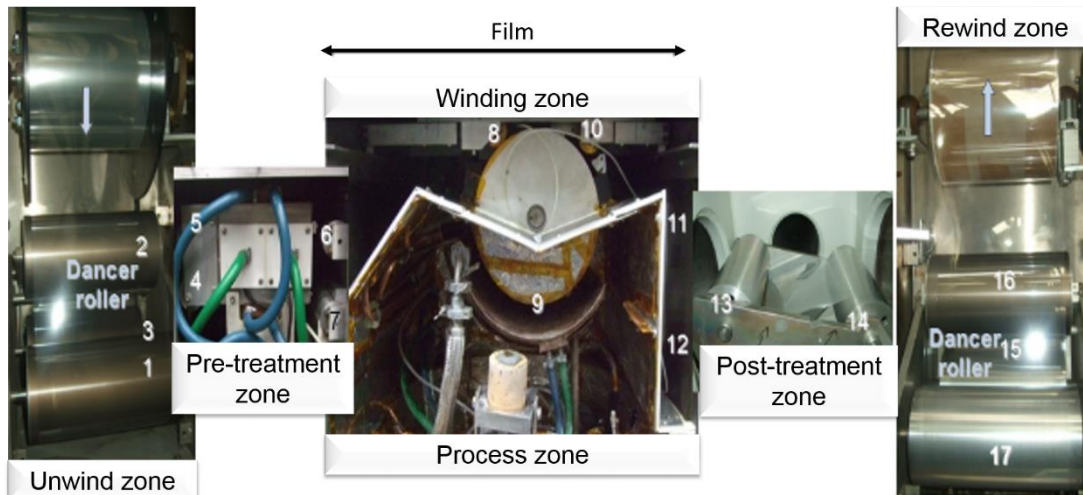


*Figure 3-3 Pictures of the different zones of the roll-to-roll PECVD coater (BML). Number 1 to 17 are labelling the different rollers. The arrows indicate the winding direction.*

Deposition can only take place if the pressure inside the machine is kept at certain levels thanks to a set of pumps (booster pumps, rotary pumps and diffusion pump). The vacuum levels are, respectively, near 3Pa ( $3 \times 10^{-2}$  mbar) in the winding zone and 0.2Pa ( $2 \times 10^{-3}$  mbar) in the process zone<sup>1</sup>.

The process zone, where the deposition takes place is equipped in order to run PECVD, as shown in Figure 3-4:

---

<sup>1</sup> The base pressure is in the low  $10^{-4}$  mbar

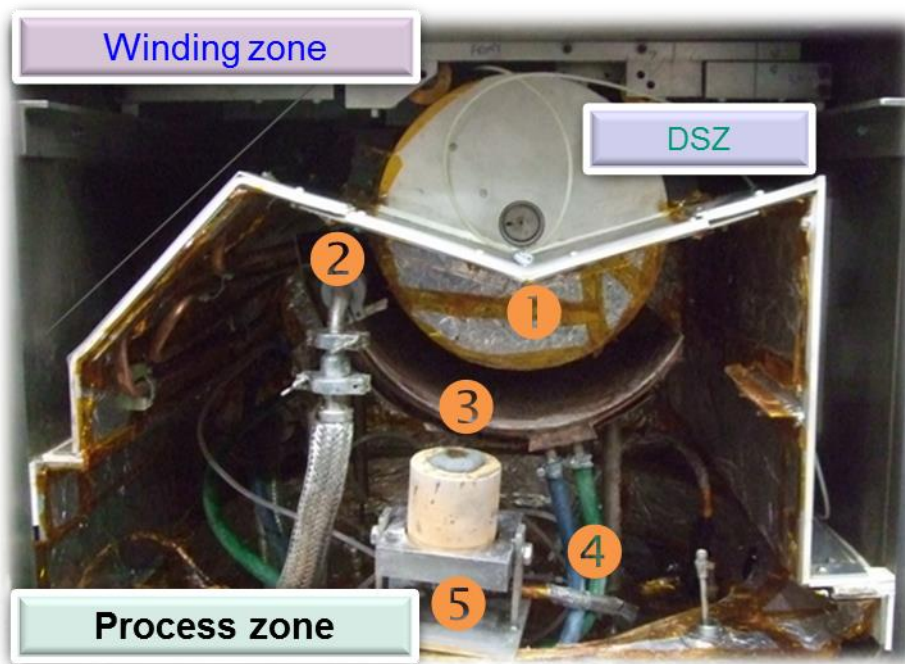


Figure 3-4 Insight view of the process chamber with each element labelled. (see Table 3-2 for more detail)

Table 3-2 Name and role of each labelled element in Figure 3-4

Number	Element
①	Drum
②	Gas delivery bar
③	Magnetic array
④	Water cooling system
⑤	Gas Purge Electrode
DSZ	De-stick zone

### 3 Methods and materials

---

The monomer is vaporised in a vaporiser and injected via the gas delivery bar (copper bar with 10 x 0.1mm diameter holes) along with the process gases. The process gases consist of argon, helium, oxygen and monomer. The mixture is injected between the magnetic array and the drum. As an electric field is applied between the drum and the gas purge electrode, the mixture is excited and the reaction can take place. On one hand, the drum is covered with the substrate which prevents it from being coated and is chilled down to 15°C with glycol diluted in water, in order to limit the substrate heating due to the plasma. On the other hand, the gas purge electrode is flushed with argon that prevents it from being coated. The GPE is a component in which an inert gas stream flows (i.e. argon) and is ionised. It is the counter electrode in the circuit with the drum. The ionised stream exits the GPE into the process zone through a small pinhole (4 mm in diameter). The high-density plasma around the tip of the GPE prevents the dielectric coating forming around the electrode and therefore keeps it clean. Thus, both electrodes are not coated and do not suffer from the disappearing electrode effect, whereby an electrode becomes progressively coated with an insulating layer until it is unable to conduct the plasma current and the plasma cannot be maintained[67].

The distance between the magnetic array (constituted of several linear magnets) and drum can be adjusted, but for this project, it has been kept at a constant value of 54mm, which was previously found to be optimal. The magnets are covered by a water-cooled plate.

The undesirable process gases are exhausted via a pump located underneath the chamber.

The de-stick zone, is part of the winding zone. Its role was to outgas the residual moisture present on the drum that can potentially make the surface stick to the drum and therefore affect the winding. However, it was found that the effect of the plasma in the de-stick zone was not significant. It was therefore not used throughout the project.

The roll-to-roll pilot coated was operated in a manufacturing site and was therefore exposed to relatively high level of contamination. The extrinsic

contamination (mainly dust) could not be controlled throughout the project, but is to be taken into consideration in the formation of defect such as pinholes in the coatings. Thus, the improvement achieved on the coatings moisture barrier was limited by the inappropriate system in place to control contamination for such coatings.

### 3.2 The substrate and precursor

#### 3.2.1 Detail on the substrate

The polymer used as a substrate was 120 $\mu$ m thick PET from Jindal (J500) slit into 150mm width rolls. It is an untreated, ultra-clear bi-axially oriented<sup>2</sup> polyester film. This film is a coextruded, whereby two or more layers are formed simultaneously. One layer may contain a filler to reduce friction or/and increase transparency/reflectivity and the other can promote flexibility of the polymer. Each layer can have a specific set of properties. The substrate is an optical grade with high clarity and a transparency above 85 % (more information on the material can be found in Appendix E).

Polyethylene terephthalate (PET, also named PETE) is a saturated polyester obtained by poly-condensation of terephthalic acid and ethylene glycol. Despite the name, this thermoplastic is not similar to polyethylene and does not contain any phthalate.

---

<sup>2</sup> Bi-oriented: the molten PET film is extruded onto a chill roll, which quenches it into amorphous state. Then the film is stretch in two directions (in the machine direction and in the transverse direction, which creates crystalline regions) by a sequential process, using heated rollers. The semi-crystalline nature of the material plays a role in its flexibility (less flexible), moisture barrier (improved by providing a more tortuous path for water to permeate around the crystalline regions or through the amorphous regions)



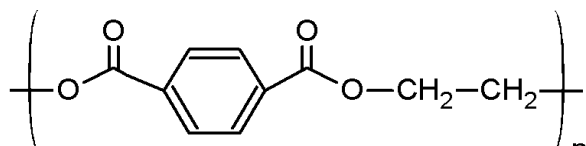


*Figure 3-5 Semi-developed formula of the PET showing the main monomer unit that is repeated n times in the polymer.*

The picture in Figure 3-5 shows the semi-developed formula of PET. It is a repetition of the polymerised unit of the monomer ethylene terephthalate. The repeated unit is made of ten carbons, eight hydrogens and four oxygen atoms. (C<sub>10</sub>H<sub>8</sub>O<sub>4</sub>).

Both semi-crystalline and amorphous (transparent) forms of the polymer can be found. Whilst the amorphous PET is transparent, the semi crystalline structure can appear transparent or opaque, depending on the size of the grains and their arrangement.

For more details on the bi-oriented PET (BOPET) manufacturing process and properties, please refer to literature. [68]

Antiblock particles are commonly added to the polymer to prevent two adjacent layers from adhering to each other during unwinding, which can cause mechanical damage to the substrate. The particles create asperities that minimise the film-to-film surface contact by increasing the distance between these layers. These particles can be either organic or inorganic. However, as the organic particles are often expensive to use, inorganic particles like natural silica are more commonly used. The type of particles can also vary from one application to another. (e.g. food-packaging substrates often contains silica-based additives like Celite for their low interaction with other additives). More information on the additives for plastics have been published [69]. For the substrate used in this work, the main additives are silica antiblock particles.

The PET used here is known to have a high surface gloss, excellent machinability, mechanical properties (e.g. high tensile strength), dimensional

stability and a good flexibility. High clarity and transparency along with dielectric properties are also relevant in many processes. (Appendix E)

#### 3.2.2 Precursor for SiO<sub>x</sub> barrier coatings

Silane/Siloxane compounds are commonly used in the PECVD coating field to produce SiO<sub>x</sub> based coatings. One of the types used is **Hexamethyldisiloxane (HMDSO)**. This is a volatile colourless liquid used for organic synthesis. The chemical formula of HMDSO is O[Si(CH<sub>3</sub>)<sub>3</sub>]<sub>2</sub> the molecule is often represented as shown in Figure 3-6

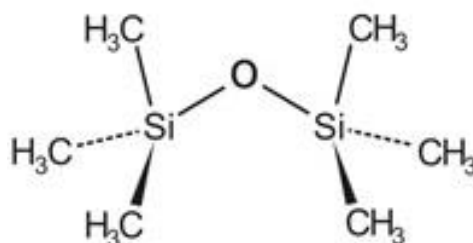


*Figure 3-6 Cram representation of the HMDSO molecule*

The molecule, prepared by the hydrolysis of trimethylsilyl chloride, is similar to polydimethylsiloxane. It is used as a source of the trimethylsilyl functional group (-Si(CH<sub>3</sub>)<sub>3</sub>) in organic synthesis.

HMDSO is also chosen for its easy handling properties, which do not involve any major risks for health and safety, especially when vaporised. The main advantages of the molecule in the liquid form are that it is not pyrophoric and has limited toxicity. The HMDSO used for this project was a high purity material from Dow Corning. The main properties of the liquid are summarised in the following table:

*Table 3-3 Table summarising the main properties of the HMDSO used to produce the SiO<sub>x</sub> barrier coatings.*

Parameter	Value
Boiling point (°C)	100
Melting point (°C)	-68
Flash point (°C)	-3.3
Auto-ignition temperature	352 °C
Vapour pressure at 20°C	4.2 kPa
Viscosity at 25°C	0.65 mm <sup>2</sup> /s

#### 3.2.3 Plasma composition

The plasma is a mixture of argon, helium, oxygen and the monomer. Argon is used to imitate breakdown of the monomer via ionisation. It also decreases the residual stress and increases the crystallinity of SiO<sub>x</sub> based coatings.[70] According to Kim and co-workers[71], argon flow rates also influence the roughness and to some extent can increase the water vapour transmission rate. Thus, argon is an important gas, although not reactive.

Helium acts as a stabiliser of the reactions and limits the incorporation of hydrogen in the coating, which can be useful to produce stoichiometric SiO<sub>2</sub>. [72]

### 3.3 Coating analysis characterisation

#### 3.3.1 Barrier measurement

Both moisture and oxygen permeation were measured during this project.

BML originally used equipment provided by Mocon (i.e. Permatran and Oxtran) to measure barrier for food packaging. However, because the project focused on getting ultra-high barrier or WVTR below 10<sup>-3</sup> g/m<sup>2</sup>/day, it was more relevant to measure the barrier on Systech analysers, which show a lower detection

limit. The measurement principle of each type of equipment is detailed in this following sub-section.

#### 3.3.1.1 Water barrier measurement

The Systech Model 7001 water vapour permeation analyser uses the ASTM F1249 [73] except for the sensor. This equipment uses a coulometric sensor<sup>3</sup> to measure the amount of water vapour that permeates through the membrane or sample, in the case of this project it is the system coating + substrate.

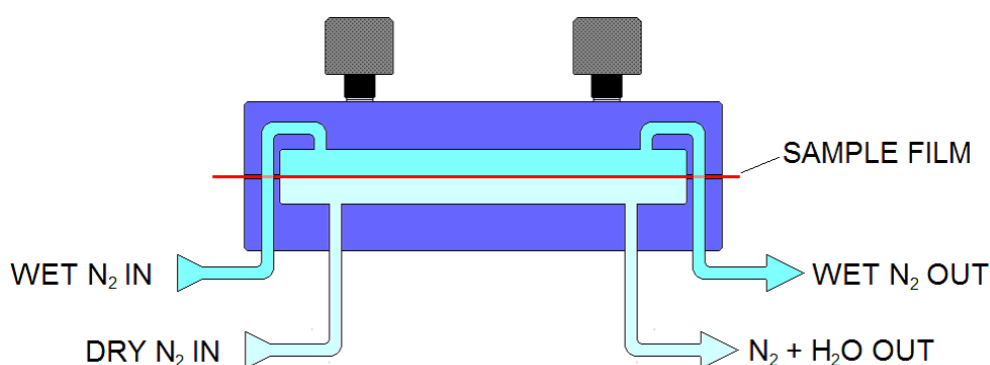


*Figure 3-7 Schematic of the cross section of the cell explaining the principle of the measurement of the water vapour transmission rate in the Systech 7001 analyser [74]*

As shown in

Figure 3-7, a stream of RH adjusted  $N_2$  flows from the top cell through the sample and into the bottom cell. In the meantime, a moisture free  $N_2$  carrier stream flushes the lower cell. The molecules of water vapour (from the top  $N_2$  wet stream) that diffuse through the membrane to the lower chamber are

---

<sup>3</sup> This is a  $P_2O_5$  sensor (phosphorous pentoxide). The change of resistance induced by the passage of the water vapour induces a change in resistance of current. This variation is therefore directly proportional to the amount of moisture in the carrier gas stream. (Faraday's Law)

conveyed to the sensor by the carrier gas. This allows a direct and absolute measurement of the water vapour.

The water vapour transmission rate in  $\text{g/m}^2/\text{day}$  is measured in the standard conditions of  $37.8^\circ\text{C}$  and 90% RH.

The Systech 7001 detector cell is a phosphorus pentoxide sensor (ISO 15106-3). It consists of a quartz tube with two platinum electrodes wound around it. These windings are coated with a thin layer of phosphorus pentoxide, which absorbs all water present in the carrier gas. The constant DC voltage applied between the two electrodes causes an electrolytic decomposition of water into oxygen and hydrogen and the electric current required for electrolysis is a direct measure of the amount of water present in the gas stream.

During all WVTR measurements of coated films, the coating faces the 0 % RH side in order to avoid damage of the barrier layer due to exposure to high RH and potential extensive oxidation.

The Systech Illinois 7001 offers a test range of 0.002 to  $18 \text{ g/m}^2/\text{day}$  for a  $50 \text{ cm}^2$  test area (no further details provided by manufacturer).

#### **3.3.1.2 Oxygen barrier measurement**

The sample is mounted between two chambers (Figure 3-8). A humidified oxygen stream (up to 50%) flushes the top chamber and permeates through the membrane while an oxygen free carrier gas ( $\text{N}_2$ ) flows through the lower chamber. The stream picks up any oxygen molecule that diffused through the membrane and routes it to the sensor. The coulometric sensor measures the amount of oxygen.

The oxygen transmission rate in  $\text{cc/m}^2/\text{day}$  is measured in the standard conditions of  $23^\circ\text{C}$  and 50% RH.

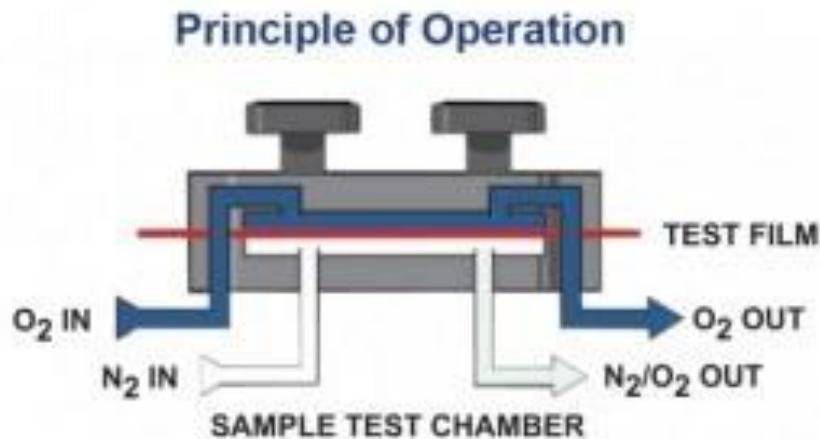


*Figure 3-8 Schematic of the cross section of the analyser's cell showing the principle used to measure oxygen transmission rate on the Systech 8001[75]*

The standard conditions have been fixed to allow a better accuracy of the measurement while avoiding any oxidation of the top layer.

The Systech Illinois 8001 permeation analyser exhibits a measurement range of 0.008 to 432000  $\text{cm}^3/(\text{m}^2 \text{ d})$  over a 50  $\text{cm}^2$  test area. The manufacturer gives no further system specifications for the Systech Illinois 8001 model. A previous assessment in the laboratory with a reference sample demonstrated that the accuracy ( $\pm 10\%$ ) and repeatability of the measurements were acceptable for OTRs above  $10^{-3} \text{cc}/\text{m}^2/\text{day}$ . The main limiting factors for repeatability are the film handling (i.e. damages, operator dependent), the variation in gas flows inside the device and the quality (in terms of barrier) of the samples.

#### **3.3.2 Barrier retention with stretch tests**

During coating, lamination and conversion the films are subject to repetitive strain (due to handling and processing). This can induce defects and potentially affect the barrier. Thus, barrier retention on strain, so called flex-durability, can be investigated to determine the effect of the repetitive strain on the barrier properties of the film. A method called Gelbo flex [76] can be used to simulate the damages caused by repeated twisting and compressing of the film. However, this method is known to be a very aggressive and destructive

### 3 Methods and materials

---

technique for the film and is not comparable to the actual strain induced during the processing and/or handling of SiO<sub>x</sub> PECVD film.

Another method, based on testing the tensile strength, is used instead of the Gelbo flex. This method involves stretching the films in the machine direction to a predefined strain using a tensile testing unit provided by Manchester Metropolitan University. The barrier of the stretched film is then measured to characterise the effect of the strain applied on the barrier properties.

This test should simulate the behaviour of the SiO<sub>x</sub> coated film during film handling (e.g. web tension during winding of the film) and give evidence about the effects of downstream processing on the barrier properties of the SiO<sub>x</sub> coated film.

The unit used to perform the test is shown in Figure 3-9.



*Figure 3-9 Tensile equipment used to perform the stretch tests.(Hounsfield H10KS with QMat 5.52 software)*

The sample is placed between the grips and strain is applied thanks to the QMat 5.52 software. Samples tested were typically 150mm long and 100mm wide (the maximum width of the grips).

The tests performed were between 0.5% and 5% strain. (Simulation of the winding tensions). The barrier was measured on a sample taken in the middle of the stretched area and was measured after relaxation.

### **3.4 Surface characterization of the samples**

#### **3.4.1 Morphology and roughness via optical profilometry**

Various methods can be used to study the morphology and roughness of the organic samples. Among these are atomic force microscopy (AFM) and optical profilometry. On one hand, AFM provides local high-resolution imaging of the surface by probing it using a very fine tip; it is mainly used in contact or intermittent mode. Moreover, the larger the size of the area probed the higher the acquisition time, and when probing a small area, the roughness or reliefs in the coating can lead to probe damage. (A few samples were analysed, and it was found that the quality of probing degraded with the number of samples analysed. This is mainly due to the probe (tip) wearing as it is probing samples that are quite rough in the case of SiO<sub>2</sub> glass-like coatings). Optical profilometry, on the other hand, provides larger scale imaging of the surface by using optical interferences. It does not require any contact and is therefore a non-destructive method.

Due to the long acquisition times associated with AFM, the limited availability of the equipment, and the localised nature of the imaging, optical profilometry was used as the main tool to study the roughness and the morphology of the samples at a large scale (up to 800x800um).

An additional external AFM report (appendices) shows the difficulty encountered with the probing the samples with an AFM.



### 3 Methods and materials

---

Optical profilometry is based on the principles of interference fringes. Interference is caused by the superimposition or combination of two light beams of similar wavelengths. The interference could be of two kinds: constructive or destructive. This manifests as an interference pattern consisting of intermittent 'fringes'. Maximum constructive interference is caused when two waves of identical wavelength in the same phase are superimposed.

As the incident light beam approaches the stage, a beam splitter diverts some of the beam to a flat, highly uniform 'reference mirror'. The distance between the beam splitter and the reference mirror is the same as that between the beam splitter and the focal plane. Therefore, when a sample is in focus (in the focal plane), each 'arm' of the split beam has near identical path length and thus phase. As these beams are reflected towards the digital camera, they are combined; if the sample was in focus, the waves will be in phase and so causes maximum interference, yielding the most intense fringes. Each pixel in the digital camera corresponds to a set of (x,y) coordinates. As the objective is scanned through the vertical, they record the highest fringe intensity detected at their position and correlate it with the z-coordinate at that moment. Software then translates this correlation into height measurements and composes a 3D map of the sample in the field of view.

The thickness of the deposited films was measured via white-light profilometry (WLP). In order to do this, a strip of Kapton® tape was placed at regular intervals (100mm) along the substrate. Thus, the coating was deposited everywhere except on the area occluded by the Kapton® tape. By removing the tape after deposition, a step was left on the surface. The height of this step could then be measured as an indication of the film thickness. A ZeGage system (ZeGage 3D Optical Surface Profiler, Zometrics, Zygo, Middlefield) was used to gather this data. White-light profilometry was also used to determine the roughness of the deposited films. The scan length was set to 50µm and the scan position set to centre. Post-processing operations consisted of subtracting a polynomial fit from the map and subtracting the

### 3 Methods and materials

---

mean value of the plan. Both operations level the sample map (tilt due to the sample preparation or the sample itself).

The acquired WLI surface data were evaluated using the following specific parameters [77]:

Roughness average ( $R_a$ ) value is the arithmetic mean of the height variation:

$$R_a = \frac{1}{n} \sum_{i=1}^n |z_i - \bar{z}|$$

*Equation 3-1 Formula of the roughness average  $R_a$*

Root mean square (RMS or  $R_q$ ) value describes the standard deviation of the height (z-value):

$$R_q = \sqrt{\frac{1}{n} \sum_{i=1}^n (z_i - \bar{z})^2}$$

*Equation 3-2 Formula of the root mean square roughness  $R_{RMS}$*

Where:

$$\bar{z} = \frac{1}{n} \sum_{i=1}^n z_i$$

*Equation 3-3 Formula of the mean height*

(The mean height represents the average z-value of the topography scan.)

$z_i$  height (z-value) for the coordinates  $x_i$  and  $y_i$  of the scanned area

$n_x$  number of points per line (in the scan/area of interest)

$n_y$  number of lines (in the scan/area of interest), usually  $n_y = n_x$

=  $\frac{\text{RMS}}{\sqrt{\text{number of points per scan (or area of interest)}}}$

The RMS value and  $R_a$  value are the most common parameters to describe surface roughness.

#### **3.4.2 Topography scanning electron microscopy**

The scanning electron microscope (SEM) utilises a focused electron beam to image the surface. This type of microscope images samples at high resolution (2nm) even at low voltages (i.e. 1.1 nm at 1kV).

An incident electron beam is generated by the gun and accelerated by applying a fixed (by the user) acceleration voltage varying between 0.1 and 200kV. This beam is directed and focused toward the sample thanks to a series of lenses. The electrons from the incident beam interact with the atoms of the sample. These interactions produce two types of electrons. On one hand, the primary electrons that are reflected electrons coming from the subsurface of the sample. On the other hand, secondary electrons are emitted from a greater depth of the sample.

The SEM is usually used in vacuum to keep a good sharpness of the images with the least noise possible. Indeed, each air molecule present could collide with the electrons from incident beam and create a signal that has nothing to do with the sample.

The secondary electrons (SE) are electrons ejected from the surface of the sample due to impact of the incident electron beam with atoms on the surface. They are at least a thousand times less energetic than the primary electrons and are directed to the secondary electron detector. The Faraday cage at the entrance of the detector is at a positive potential of 300 kV. This positive bias attracts the secondary electrons. The electrons make their way through the Faraday cage up to the target of the detector where they are counted. As their number is not high, a photo-multiplier is used to boost the signal and transmit it to the computer. As the secondary electrons come from the subsurface, they are used to image the morphology.

The backscattered electrons (BSE) are scattered by the atoms in the volume of the sample. This reaction is called elastic scattering, which means that the electrons do not lose energy after interacting with the atoms of the sample. Only a few backscattered electrons can make their way outside of the sample to the detector. Indeed, as they must traverse a certain depth they happen to interact with other atoms before going out of the sample, or be trapped in it. The detector is usually located above the specimen at a certain angle that maximises the detection of the back scattered electrons.

The BSE are used to detect the contrast between areas with various chemical compositions. The light elements (low atomic number) appear darker than the heavier element as they backscatter electrons less strongly. However, in many cases, this only gives a qualitative idea of the element presents, rather than an accurate ratio of the species.

Another detector is commonly used to measure the quantitative composition of the samples, the energy dispersive X-ray analysis detector. When the electrons are emitted from the samples, they sometimes produce a photon that has a specific energy. (Depending on the atom that was hit by the electrons and the excited level of the atom). This photon has an energy in the range of X-rays and is detected by the EDX detector. As the characteristic photon energy of each atom is tabulated, it becomes possible to identify the atoms present in the sample. However, this technique is not suitable for thin materials (sub-micron) and has a resolution depending on the size of the detector (typically a few  $\mu\text{m}$ ).

The SEM was originally designed to observe conducting samples, as it uses an electronic signal. It is easy to understand that the image will be more resolved and sharp when the electrons are conducted by the sample.

Despite this, it is possible to image insulating materials. Two methods can be used to achieve that goal. The first method consists of coating the sample with a gold or carbon coating that will conduct the electrons.

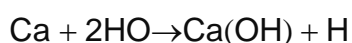
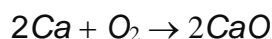
The second method consists of reducing the working distance and decreasing the acceleration voltage to be as low as possible. The working distance will help in focusing the electron beam near the surface, which will ultimately help them penetrate the sample. This work is required to be carried out at low acceleration voltages to avoid damaging the surface by heating it (due to the energy of the electrons and the amount of them near the surface).

The first method suits bulk or thick materials, whereas the second applies to thin coatings or materials. Indeed, covering the surface with another coating could fill in the features and then prevent the user from imaging them.

The microscope used throughout this project to image the samples was provided by Manchester Metropolitan University. It is the Zeiss Supra 40P, equipped with a secondary electron detector, energy dispersive X-ray detector and in-lens detector. This SEM can be operated in variable pressure mode, but this mode was not of interest for the study.

#### **3.4.3 Defect characterisation via calcium test**

Traditional methods to measure the permeation of water vapour through single or multilayer barrier coatings are limited to  $10^{-3}\text{g/m}^2/\text{day}$  (or less but the measuring time can go up to one week)[78]. Thus, new methods have been developed to overcome that limitation, among which is the calcium corrosion test. Calcium is a naturally conductive and opaque metal that is very sensitive to oxygen and water vapour, which makes it relevant for the evaluation of moisture and oxygen permeation. The principle of this method is to monitor the change in oxidation of the calcium deposited on the barrier layers. When exposed to water vapour and oxygen the calcium layer will rapidly oxidise. This oxidation can be expressed by the following equations:



*Equation 3-4 Equation describing the reaction taking place during the oxidation of the calcium coating deposited for calcium tests*

It becomes possible to distinguish the bulk permeation and the defect-based permeation thanks to the change in transparency. This can be done by either visual inspection or optical microscopy.

The conductivity of the calcium-corroded layer is also often measured to determine the effective water vapour transmission rate. This will not be detailed in this section. [5]

The experimental set up used to perform calcium tests is located at the University of Oxford. Calcium is evaporated (thickness and deposition rate controlled by a quartz crystal monitor) onto the barrier and the whole composite is encapsulated (coating facing the glass) with a glass sheet using a UV curable epoxy as a sealant. The whole encapsulated sample is then exposed to a RH and temperature controlled atmosphere. Photographs are taken after encapsulation and at regular intervals to inspect the degradation of the calcium layer.

#### **3.5 Optical properties**

In the coatings industry, the most common parameter used to describe the transparency is percentage transmission (%TR). In the case of this work it was measured using an optical densitometer Macbeth TD 404 [79] shown in Figure 3-10



*Figure 3-10 Optical densitometer Macbeth TD-404*

Optical transmission density is a representation of the materials ability to block the light. Its scale is unit-less and logarithmic. It is widely used to measure the transmission of metallised films. The OD and the % transmission are linked through the formula presented in Equation 3-5

$$\% = \frac{1}{10^{OD}}$$

*Equation 3-5 Formula describing the relationship between the % of light transmitted and the optical density*

### **3.6 Mechanical properties**

The reliability of thin films as moisture and oxygen barriers is influenced by several factors related to either the coating itself or the environment or stress that the coating might be exposed to over its lifetime, processing and conversion. Poor adhesion can cause delamination of the coating, or extreme wear, which should be avoided in the case of protective coatings. [80, 81]

The main properties that must be monitored in relationship to the coating durability are its adhesion to the substrate, its mechanical resistance to abrasion and its hardness.

Coating hardness is a relevant parameter for many applications where the material is exposed to repetitive mechanical stress. Several techniques can be used to assess the hardness, such as nanoindentation, impact, nanoimpact, abrasion[82]. Among these techniques is the pencil hardness test. The main features and advantages of the technique is to provide a rapid inexpensive method to determine the comparative scratch resistance and hardness of coatings. This test is known as the Wolff-Wilborn method.

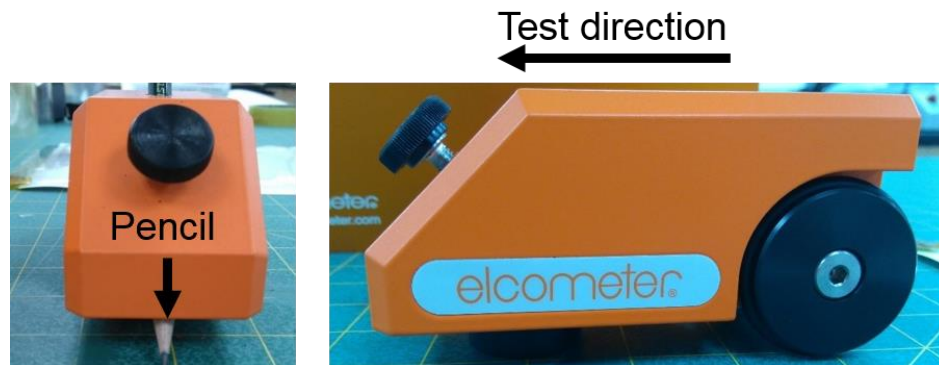


*Figure 3-11 Hardness pencil tester*

The pencil is locked into position in the test device (Figure 3-11) and the device is then pushed away from the operator, across the sample. This standard test allows a constant force to be applied at defined and constant contact angle of 45 degrees between the surface and the pencil.

A series of pencils is available ranging from soft pencils (6B) to hard pencils (6H).

## **3.7 Coating composition**

### **3.7.1 X-Rays photoelectron spectroscopy**

Several techniques can be used to characterise the chemical composition of a coating. Among these is X-ray photoelectron spectroscopy (XPS). This technique is frequently used to obtain qualitative and quantitative information



### 3 Methods and materials

---

on the elemental composition (except for hydrogen) and the atomic binding states of the elements present in a specimen. XPS is generally used to investigate the near-surface region of a sample, i.e., within a depth of 1nm and 10nm and a detection limit around 0.2% for most elements[83].

XPS is based on the analysis of the kinetic energy of the photoelectrons emitted by the atoms when irradiated by a monochromatic photon X-ray beam. If the fixed energy of the incident beam is higher than the binding energy of the core electron of the atom, this electron can be removed. When this electron leaves the atom, a photon is emitted. This photoelectron has a particular kinetic energy that is given by the Einstein relationship:

$$K = h\nu - \phi - BE$$

*Equation 3-6 Einstein relationship*

Where  $K$  is the kinetic energy [eV]

$BE$  is the binding energy [eV]

$h$  is the Planck's constant [ $4.13566733 \times 10^{-15}$  eV]

$\nu$  is the frequency of the incident X-rays [eV]

$\phi$  is the spectrometer work function [eV]

The detector and the analyser measure the kinetic energy of the ejected photoelectrons and calculate the corresponding binding energies using Equation 3-6. Each element has characteristic binding energies associated with each atomic orbital, therefore each element will present a characteristic set of peaks in the XPS spectra.

Each peak of the spectra can be associated to one element present in the specimen and allow the quantification of the atomic fractions of the species present.

The intensity of the peaks relates to the concentration of this element in the material. The chemical state or environment of the elements can also be extracted from the position of the peaks. Indeed, each chemical bond between

two elements affects the core electron binding energy (as a function of the electronegativity of the partner) of the elements and therefore the measured kinetic energy.

In order to optimise the mean free path of the particles (especially the incident beam) the XPS operates in high vacuum, typically between  $10^{-6}$  and  $10^{-9}$  Pa. This helps reduce the number of reactions between the incident beam or the emitted photoelectron and other particles in the environment that can alter the signal, and therefore the analysis.

All the data presented in this report have been obtained at the University of Surrey on a Thermo Fisher Scientific (East Grinstead, UK) Theta Probe spectrometer. XPS spectra were acquired using a monochromated Al K $\alpha$  X-ray source ( $h\nu = 1486.6$  eV). An X-ray spot of  $\sim 100\mu\text{m}$  radius was employed. Survey spectra were acquired employing a pass energy of 300 eV. High resolution, core level spectra for C1s, O1s and Si2p were acquired with a pass energy of 50 eV. Quantitative surface chemical analyses were calculated from the high resolution, core level spectra following the removal of a non-linear (Shirley) background. The Avantage software was used, which incorporates the appropriate sensitivity factors and corrections for the electron energy and analyser transmission function. All spectra were charge referenced against the C1s peak at 285 eV to correct for any charging effects during data acquisition. XPS depth profile data was acquired using the monochromated Al K $\alpha$  X-ray source; while sample etching was achieved, using an Ar ion gun operated at 3 kV and delivering  $\sim 1\mu\text{A}$  of Ar $^+$  etch current. The etch area was  $\sim 1.5 \times 1.5\text{mm}^2$  and an etch time of 500 s (initial) and 50 s (through the SiO/PET interface) was employed. The Ar ion gun was fixed at an angle of  $45^\circ$  to the sample surface. The data were acquired and the peak fitting undertaken at the University of Surrey. The interpretation was done by the author.

### 3.7.2 Fourier transform infrared spectroscopy (FTIR)

Another method of assessing the composition is by attenuated total reflectance Fourier transform infrared spectroscopy (ATR-FTIR). It is a complimentary method to XPS. This technique is used to determine the structure or purity of a compound. When absorbed by a molecule, IR photons are converted into energy of molecular vibration. If the incident energy matched the molecular vibration energy, the molecule/group of atoms will absorb it and will vibrate as a result of the energy absorbed. The Planck equation gives the relationship between the wavelength and the energy. Therefore, the molecular vibration will vary along the light spectrum. FTIR is commonly performed in the medium range of infrareds, which corresponds to the wavenumber between  $4000\text{cm}^{-1}$  and  $400\text{ cm}^{-1}$ .

The raw data collected from the interferometer, over a wide range of wavenumber/wavelengths, are Fourier transformed to obtain a spectrum. Thus, the device can perform several scans for a sample within a short period (since the data is measured for all wavelengths simultaneously and no scanning through the investigated wavelength range is required).

=

*Equation 3-7 Planck equation*

where  $h$  is the Planck constant,  $c$  the light speed and  $\tilde{\nu}$  the wavenumber given by the inverse of the wavelength (Equation 3-8)

$$= \frac{1}{\lambda}$$

*Equation 3-8 relationship between wavenumber and wavelength*

with  $\lambda$  the wavelength in cm

The wavenumber gives information on the functional groups in the molecules. Each wavenumber corresponds to a specific functional group (reported in tables[84]). In order for a molecule to vibrate, its dielectric dipole moment must vary. The molecule can then vibrate (if excited) in different modes. These

### 3 Methods and materials

---

modes indicate a change in either chemical bond (stretching, expansion, contraction) or a change in bond angle (bending, rocking).

The depth of penetration during ATR spectroscopy is wavelength dependent and is defined as the depth at which the intensity of the evanescent wave has fallen to 1/e, i.e. 37 % of its original value. This is described by Equation 3-9

$$d_p = \frac{2 \lambda \sin^2 \theta_1 \left( n_1^2 - n_2^2 \right)^{1/2}}{n_1^2 - n_2^2}$$

*Equation 3-9 Penetration depth during ATR spectroscopy*

Additional information on the FTIR/ATR-FTIR technique is available in the literature. [85]

In this work, FTIR spectra of the SiO<sub>x</sub> coatings were acquired using a Thermo Scientific Nicolet 380 FTIR spectrometer with a Smart iTR ATR accessory (angle of incidence 45°) and Omnic 7.3 software. Here, 32 scans were carried out per spectrum at a resolution of 4 cm<sup>-1</sup>. The clamping pressure/torque could not be accurately adjusted using the Smart iTR. The Smart iTR tool is a single reflection diamond ATR accessory.

## **4 INITIAL PLATFORM ASSESSMENT**

#### 4.1 Substrate characterisation

The PET substrate was found to be quite smooth as shown in Figure 4-1 and Figure 4-2.

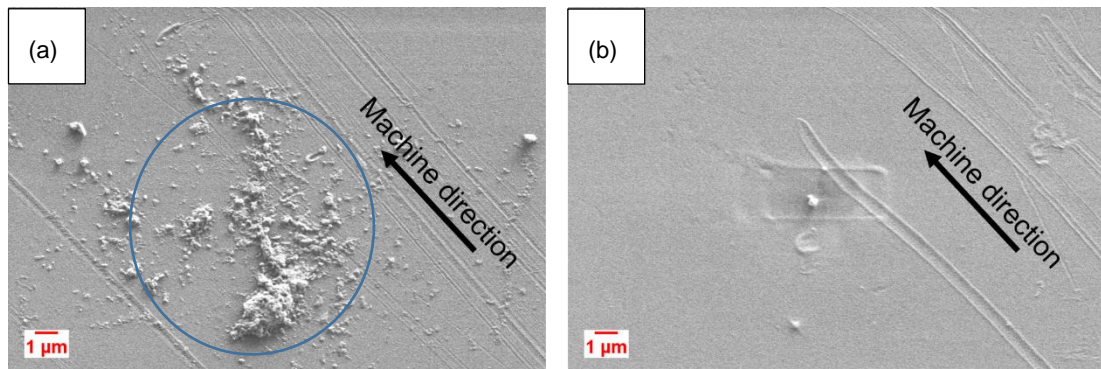


Figure 4-1 SEM micrographs showing the morphology of the PET substrate : area 1 (a) and area (b), x10000 magnification

One can identify some scratches in the machine direction on Figure 4-1(a). These scratches vary in length and width. In the middle of the image, an agglomeration of particles can be seen. These particles are likely to be contamination on the substrate or remaining fragments of the plastic polymer chains. Some scratches Figure 4-1(b) appear in the transverse direction, which could indicate the sliding motion of the substrate over the rollers during winding.

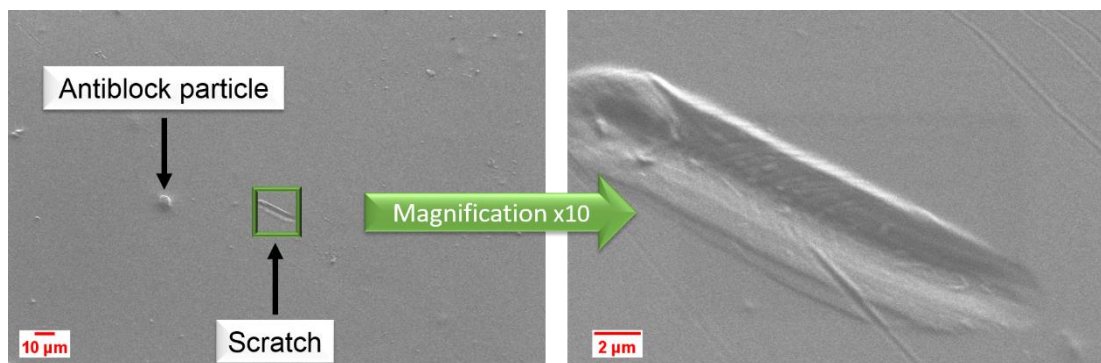


Figure 4-2 SEM micrograph showing the morphology of the PET substrate in the area 1: x800 magnification (left) and zoom on the scratch left by the antiblock x20k magnification

Figure 4-2 both show the contamination remaining on top of the PET substrate and the scratches left on the surface. Those scratches are 0.5 to 2 $\mu$ m wide, which corresponds with the average diameter of the antiblock particles (particle observable in Figure 4-2), and several micrometres in length. They can originate from either winding of the substrate in the machine, or handling. However, those scratches could have originated from the contact of larger particles such as dust particles on the surface with the back surface of the coating or with the rollers. The samples observed under the SEM have been cut just after the unwind roll and has not touched any roller in the machine yet (but may have touched other rollers during the slitting process).

Further analysis of the roughness of the PET along with analysis of the distribution of the antiblock particles (size and number) and their composition could be conducted to further understand the role of the substrate quality on the WVTR. Indeed, Fayet et al.[86, 87] demonstrated that both the oxygen transmission rate and mechanical properties (such as crack on strain) of the SiO<sub>x</sub> coatings deposited on BO-PET were dependent of the density of antiblock particles on the surface. Considering the proportionality found between the OTR and the density of antiblock particles, it is probable that the antiblock particles also have an influence on the WVTR. As only one grade of PET was used throughout this project, the effect of the antiblock particles can't be further discussed in this document.

## 4.2 Process parameters vs barrier

Note: All the results presented in this section are associated with coatings produced prior to the start of the project

In order to optimise the deposition process, it is necessary to understand how each parameter of the process affects different properties of the coating, especially the WVTR (For the purpose of this report, only the water vapour transmission rate is discussed). One way to achieve that is by studying the evolution of the barrier while changing certain parameters, such as the discharge power (delivered to the plasma) and the flow rates (gas and monomer). The main parameters considered are the oxygen flow rate (reactive gas) and the RF power as they were reported to be the main parameters influencing the coatings along with the monomer flow rate[88, 89].

A reference run which resulted in coatings with good transparency (above 85%), good WVTR ( $1.8 \times 10^{-2}$  g/m<sup>2</sup>/day) was obtained after a limited number of passes (single pass in this case<sup>4</sup>) was chosen and repeated. The reference-run, 13\_05\_28\_01, process parameters are summarised in Table 4-1.

*Table 4-1 Process parameters for the reference run.*

<b>Process parameter</b>	<b>Value</b>
Number of passes	1
Speed (m/min)	0.5
Oxygen flow rate (SCCM)	1100

---

<sup>4</sup>Single pass runs are selected to reduce the coating sequence to a simple and easy achievable sequence for the end user. In doing that, one also reduces the costs of production usually associated with multilayer coatings.



Helium flow rate (SCCM)	100
Monomer flow rate (SCCM)	159
Argon in the GPE (SCCM)	110

### 4.2.1 Effect of discharge power on the water vapour barrier

The graph presented in Figure 4-3 shows that the behaviour of the WVTR is not consistent with the increase of power. Indeed, when the power is increased from 1.3 to 1.8kW the WVTR does not show a clear trend due to the wide scatter of results at 1.8kW (the reasons for this wide scatter are discussed in Section 4.2.2). Despite the limited amount of data available that were available at this stage of the project, the average WVTR at 1.8kW appeared to be in the region of  $2.3 \times 10^{-2} \text{g/m}^2/\text{day}$ , whilst the WVTR is slightly higher ( $2.8 \times 10^{-2} \text{g/m}^2/\text{day}$ ) when the input power is reduced to 1.3kW.

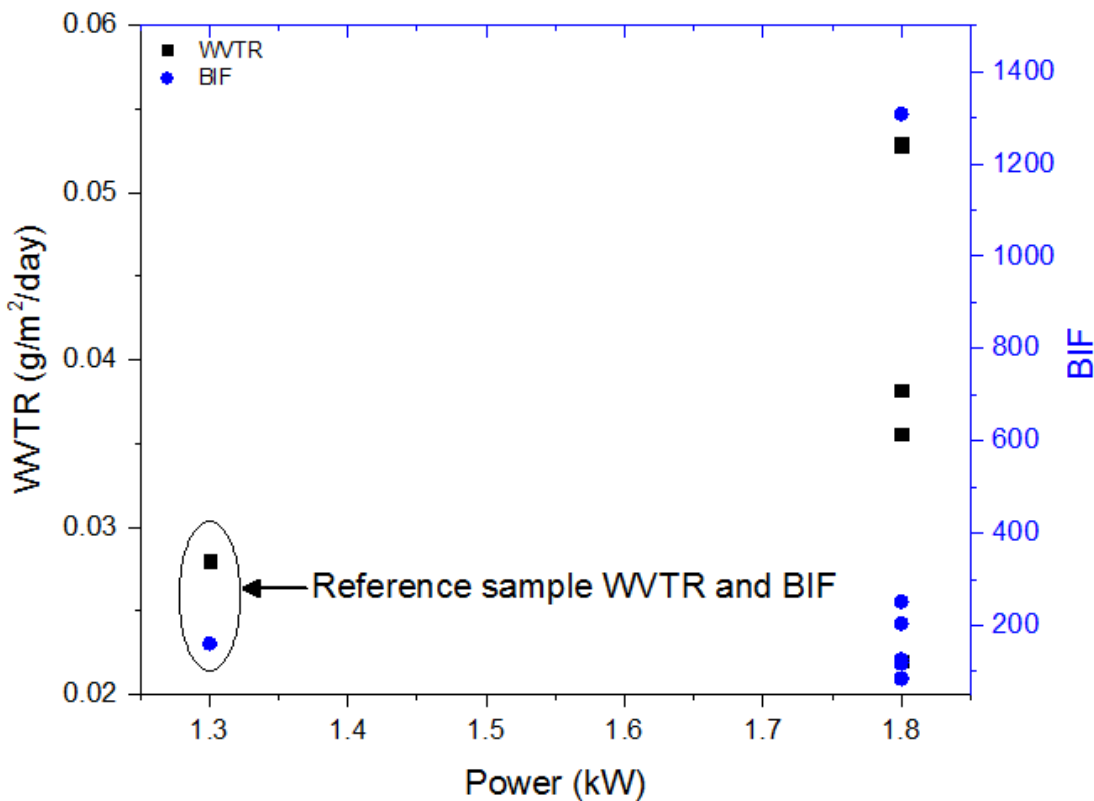


Figure 4-3 Graph showing the evolution of the WVTR with the input power for samples produced using the parameters of the reference run 13\_05\_28\_01.

#### 4.2.2 Relationship between the monomer flow rate and the WVTR

The graph presented in Figure 4-4 shows that the WVTR does not behave consistently with the monomer flow rate, which is not expected, and might confirm that the equipment was not producing repeatable coatings. However, when focusing on the 160 SCCM flow rates zone shown in Figure 4-4, it appears that some of the results are associated with high error bars, which does not allow any conclusion regarding the effect of the monomer flow rate on the moisture barrier.

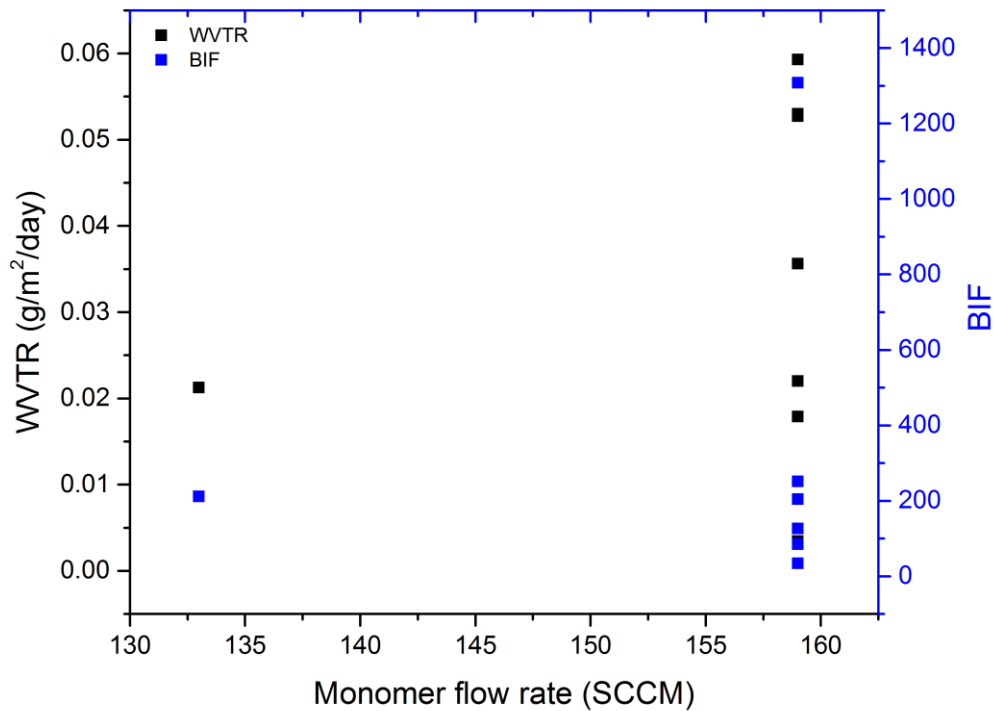


Figure 4-4 Graph showing the evolution of the WVTR with the monomer flow rate for coatings produced using the reference run 13\_05\_28\_01. Each data point is an average of the WVTR measured on two samples from the same run. Each data point is related to one discrete experiment<sup>5</sup>.

The data used to generate in this graph was selected by filtering the data gathered prior to the start of the project. Only the runs with similar process parameters and coating exhibiting above 85%TR were selected and compared. There was, therefore, only a limited amount of data available to plot this graph.

<sup>5</sup> The records showed that, when those samples were produced, the operator was changing the pumping speed to keep the pressure constant. Therefore, the plasma conditions were changed and the gases might have been pumped out, preventing any further polymerisation and coating deposition, which could explain the scattered results at high monomer flow rate

## 4 Initial Platform Assessment

---

To summarise these results, it appears clear that no straightforward relationship between both the process power, monomer flow rate and the water vapour barrier can be seen from these initial trials. The first attempt that was made to repeat the experiments to assess the machine repeatability, presented above, was unsuccessful as the process appeared not to be stable enough. This was mainly due to mechanical and electrical issues<sup>6</sup> (e.g. drum grounded, insulator plates on the drum burned, which changed the electrical path and the impedance of the overall system as show in the Figure 4-5, etc.) which created instabilities in the plasma.

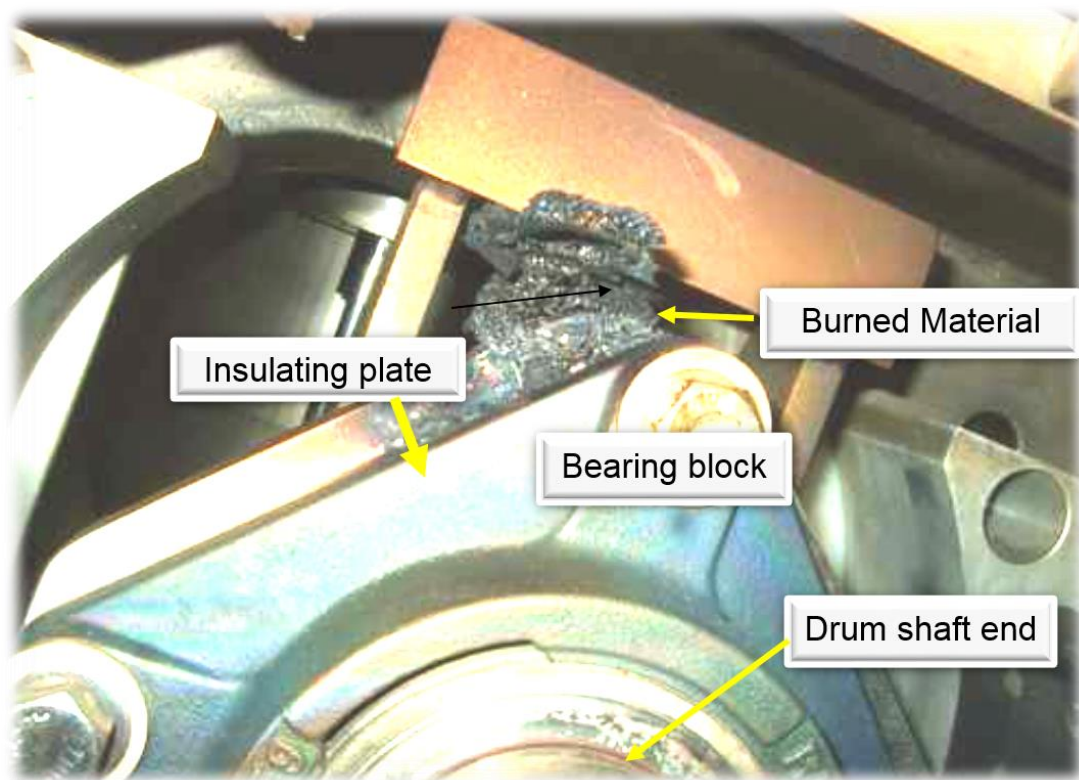


*Figure 4-5 Picture of the burned insulating plate on the back of the drum.*

The work presented in following chapter was done during the project and after repairing this major burn. However, other events were occurring as the

---

<sup>6</sup> Several months were needed to address the issues and fix them.

machine was run (i.e. drum displacement, pump failing, etc.), which compromised repeatability and comparison of results between experiments.

### 4.3 Coating characterisation

Several properties of the coatings have been investigated such as composition, mechanical properties, and morphology. Some of the results are detailed in this subsection.

#### 4.3.1 Morphology

The main method used to characterise morphology was the scanning electron microscope, as it allows images of the topography to be acquired with good resolution and at high magnification. However, as the SiO<sub>x</sub> based coatings and the PET are insulators, it can be difficult to image the surface with minimal charging of electrons on the surface of the sample (charging can cause instabilities of acquisition and difficulties in focusing). This can, though, be reduced by using low working distances, typically below 3mm. At such a low working distance, the acceleration voltage of the electron beam should be lowered in order to avoid melting the surface. The acceleration voltage was kept around 0.5kV, which was found to be a good compromise for keeping a reasonable resolution without damaging the sample. The uncoated PET as well as different coatings were analysed.

The SEM analysis of the SiO<sub>x</sub> coated samples revealed different morphologies. In the first instance, two samples with relatively good barrier were compared. In fact, those two samples presented different visual aspects. Sample A (12\_01\_23\_05) looked homogenous in colour, whereas sample B (12\_10\_31\_01) was found to have a few clear (i.e. colourless and transparent) spots randomly dispersed.

The respective WVTR of sample A and B measured at 37°C and 90% RH were (0.049±0.003)g/m<sup>2</sup>/day and (0.014±0.003)g/m<sup>2</sup>/day. The process parameters used to produce these coatings are shown in Table 4-2

*Table 4-2 Summary of the process parameters used to produce sample A and sample B*

#### 4 Initial Platform Assessment

---

<b>Process parameter</b>	<b>Sample A</b>	<b>Sample B</b>
Number of passes	1	1
Line speed (m/min)	0.2	0.5
Oxygen flow rate (SCCM)	1100	828
Helium flow rate (SCCM)	166	276
Monomer flow rate (SCCM)	166	276
Argon in the GPE (SCCM)	50	80
Power (kW)	1	1.6
Voltage (V)	890	938
Current (A)	1.6	2.1
Mag-to-drum distance (mm)	60	54

The SEM images revealed that the morphologies of these two samples were completely different (Figure 4-5).

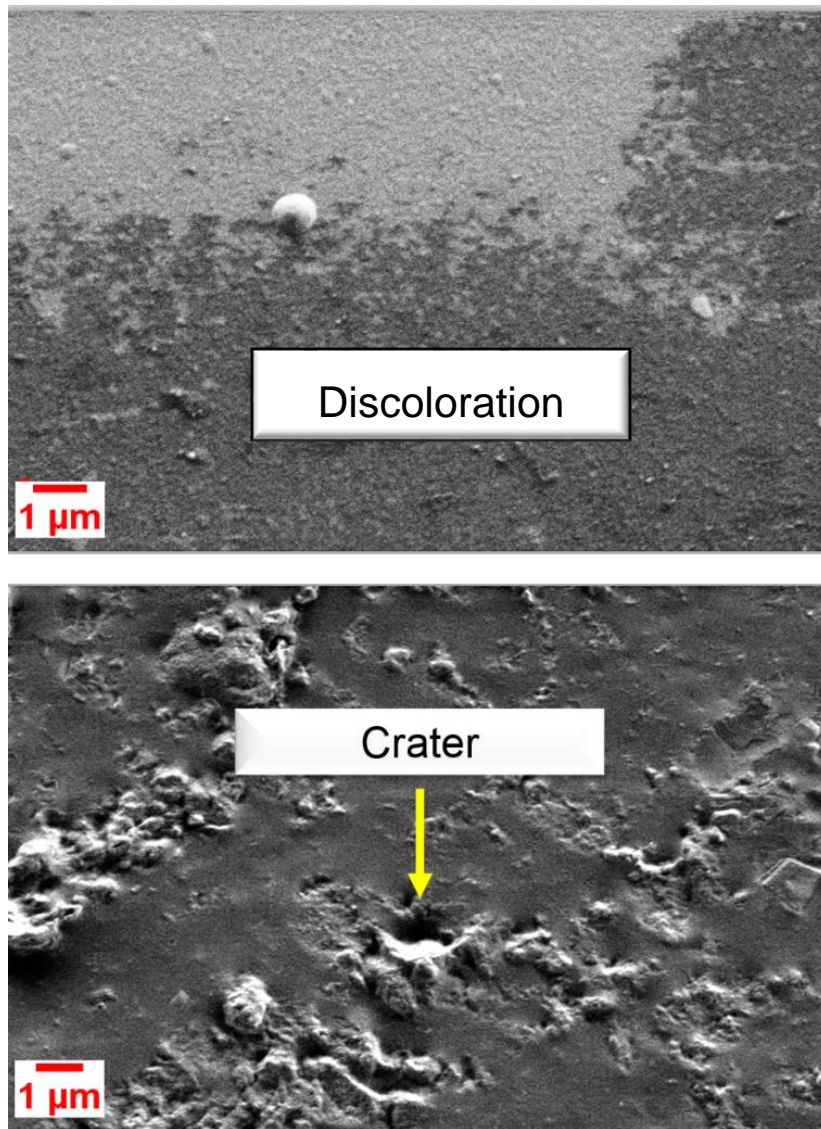


*Figure 4-6 SEM micrographs of the surface of the SiO<sub>x</sub> coating deposited onto PET for two low WVTR samples of Sample A (top image, (0.049±0.003 g/m<sup>2</sup>/day), sample B (bottom image, WVTR= 0.014±0.003 g/m<sup>2</sup>/day).*

On one hand, sample A shows closely packed grains varying in diameter (from approximately 80 to 300nm), which was previously found by different groups working on PECVD SiO<sub>x</sub> coatings[63, 90] [91, 92] and a difference in coloration (which might originate from the reaction between the chemicals migrating from in the underlying polymer and the plasma) that was found in several locations. On the other hand, sample B presents numerous craters and what looks like coating delamination.



The discolouration was noticed on the surface in various places as shown in Figure 4-7.

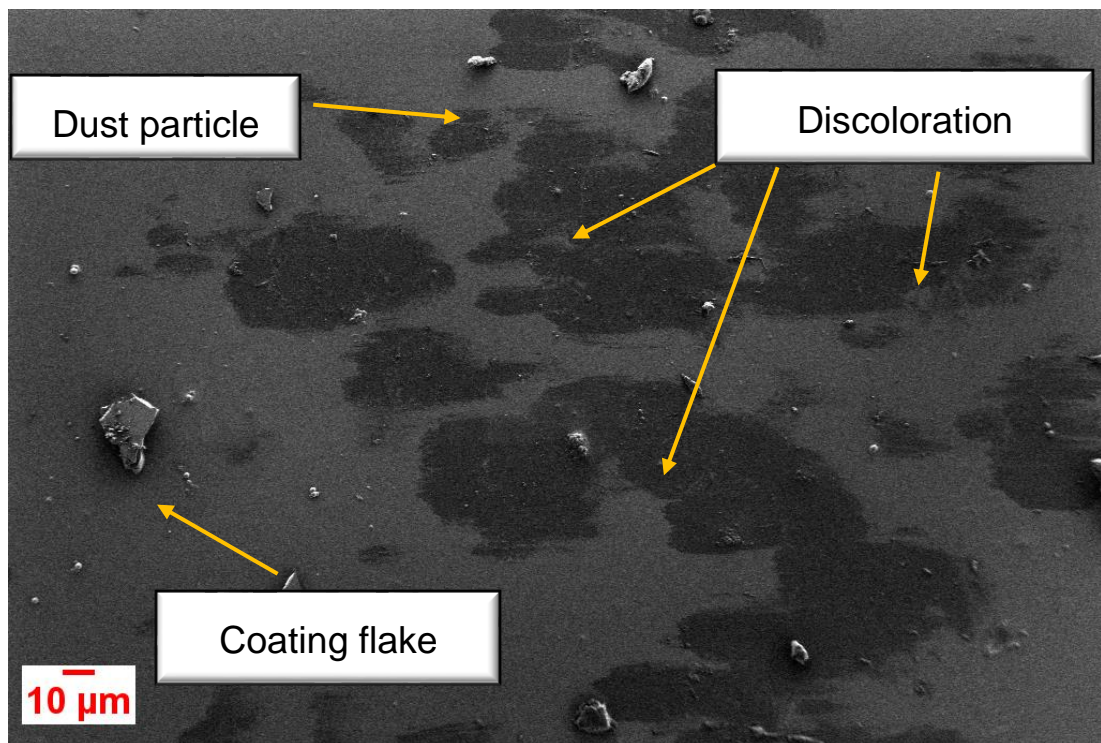


*Figure 4-7 SEM micrograph of Sample A showing the discolored areas.*

The size and shape of the discoloured areas varied. One can also note the presence of dust and flakes of coating on the surface.

Further analysis was done on a clear spot on sample B to determine if the difference in optical property was due to a difference in the topography.

The surface was found to be generally homogenous for both regions but presented defects in some other areas as shown in Figure 4-6 and Figure 4-7

Both the images of the clear spot and the dark areas of the sample are shown in Figure 4-8.



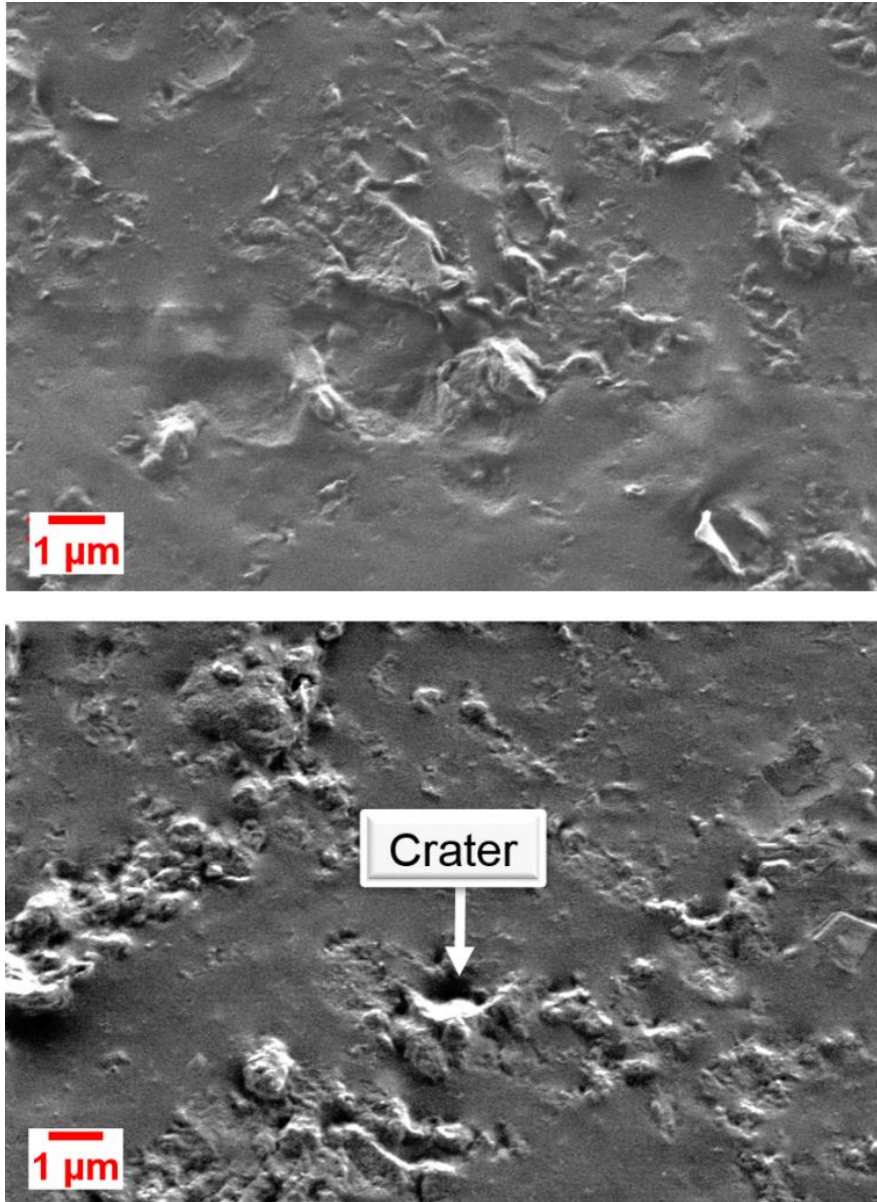


*Figure 4-8 SEM micrograph showing the morphology of the dark region (top picture) and clear region (bottom picture) at x20000 times magnification*

The surface topography of sample B could be explained by the growth of sub-stoichiometric silicon oxide due to a low oxygen flow rate and a higher line speed. This hypothesis needs to be further investigated.

These images show that the topography of the two regions are relatively similar, which suggests that the difference of colour may be a difference in thickness. This difference in thickness is difficult to assess, as the clear spots were only about 1cm<sup>2</sup>. However, this variation might have different sources

## 4 Initial Platform Assessment

---

including the presence of contamination in the area that prevented it from being coated, or instabilities in the plasma that disturbed the deposition (i.e. arcing, power not coupling through the substrate as it should).

The large variation in topography between sample A and sample B suggests a different mechanism of permeation. Whilst sample A would let molecules permeate through the voids between the grains, the dominant permeation through sample B is expected to occur via pinholes and craters, as explained by Henry et al.[93].

The relative barrier performances of both samples would suggest that moisture is more likely to permeate through the voids (in between the grains) than through the craters, providing the craters do not extend all the way through the coating. The origin of the craters has not been identified, but they could be a result of the contact of contamination and dust with the coated surface during rewind of the coated material (causing scratches).

In addition to these variations in topography, another observation was made several other samples at this stage obtained on the coater. Some of these samples were hazy and the coating that was originally expected to be yellow/brown coloured, presented hazy white lines, as shown in Figure 4-9.

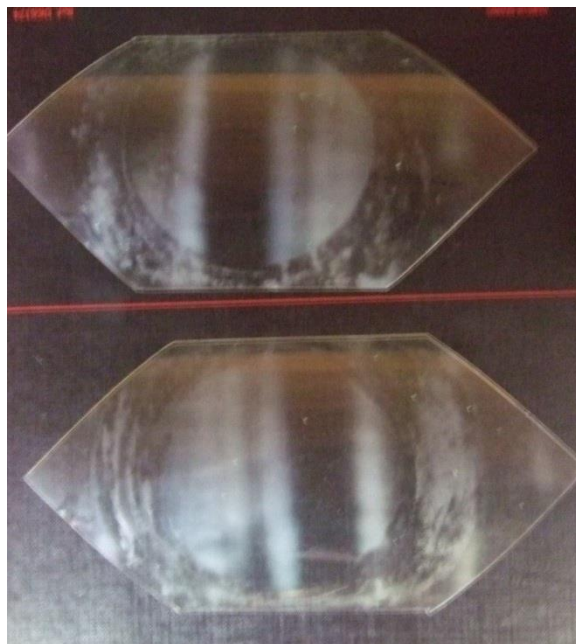


*Figure 4-9 Photograph of the samples of SiO<sub>x</sub> coating onto PET revealing hazy regions. The machine direction is vertical to the images*

The optical transmission was measured to be lower in the white hazy regions and the SEM analysis also shown a large difference in topographies between the yellow areas (centre) and the white regions. The difference in colour might be a difference in thickness of the film (which was not measured on the samples). It could also be due to a lack of uniformity of the injection of gases in the process zone through the gas bar. Indeed, these lines are corresponding with the direction of the injection. Further investigation would be required to understand and optimise gas flows and injection in order to confirm that the haze was caused by the direction of the gas injection.

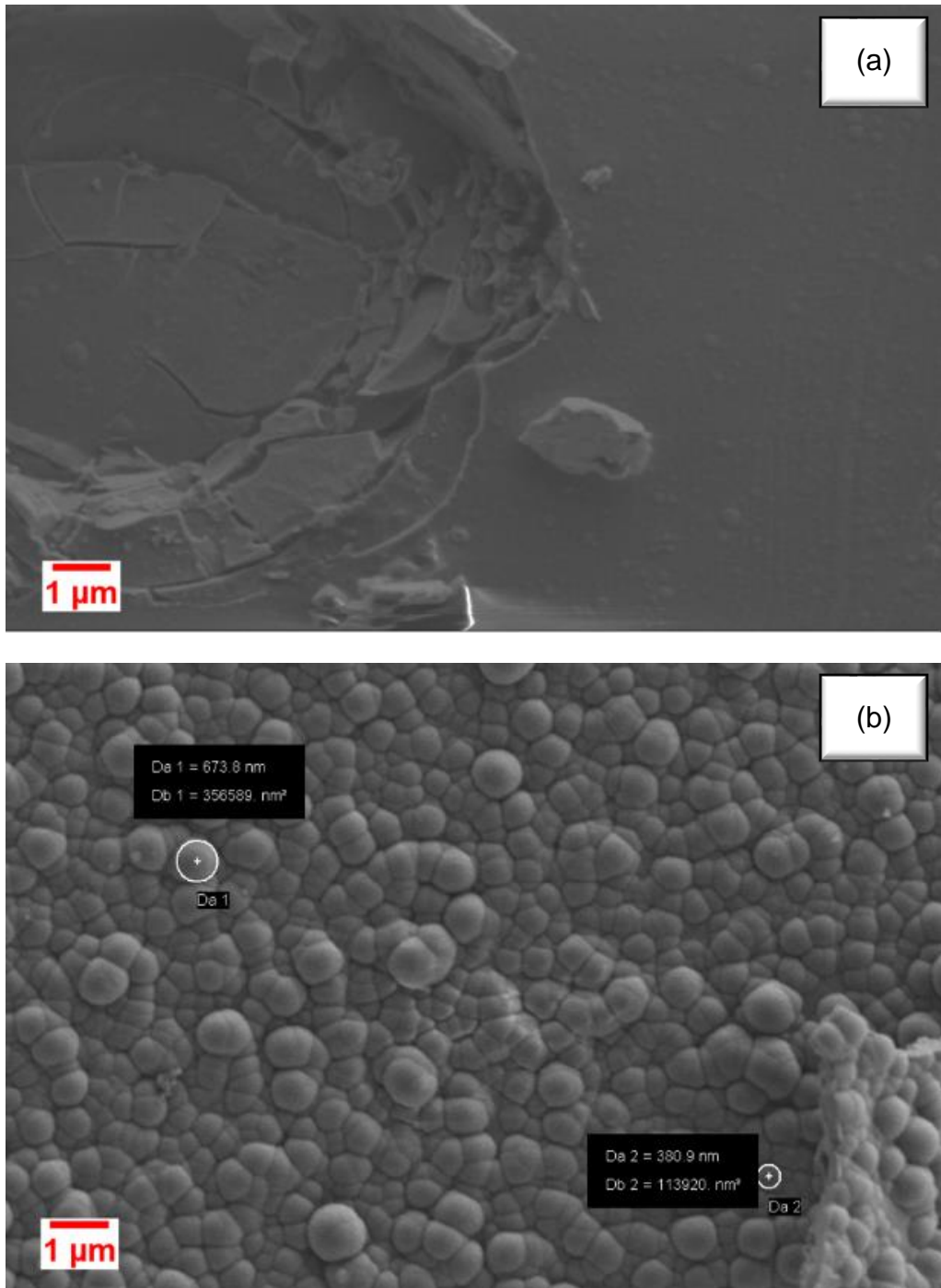


Figure 4-10 SEM micrographs of the dark side area of the coating (a) and the hazy white area of the  $\text{SiO}_x$  coated PET (b).

Micrograph (a) shows a 6μm diameter crater. The surface around it seems relatively uniform and smooth. Other craters due to crack can be found on brittle  $\text{SiO}_x$  coatings, however this crater size is not frequent. This crater might have been caused by an external source and probably is not related to the

process. No clear evidence of its origin has been identified, but it could have been caused by a protruding filler particle from the contacting back surface of the next layer of film.

Micrograph (b) demonstrate that the hazy areas of the coating are very porous and has a granular morphology. The closed packed grain structure of the hazy line is nevertheless not surprising as several groups have found that it was typical for SiO<sub>x</sub> PECVD [41, 61, 94-96] coatings on plastic substrates.

On one hand, one can expect this type of morphology to be due to volume polymerisation in the plasma. This polymerisation in the plasma would change the growth mode. These phenomena have been reported by can be found in Felts et al.[97] and Denlier et al. [98]. However, the size of the grains suggests that instabilities (observed during the process run) of the plasma have enhanced the grainy structure.

The measured WVTR on this sample was high (0.1 g/m<sup>2</sup>/day) which suggests that moisture permeates very easily between the grains, especially when they are bigger (in comparison to the smaller grain observed in Figure 4-10).

### **4.3.2 Composition and stoichiometry**

XPS is a powerful tool to characterise the composition and stoichiometry of the samples. In order to do that, depth profiles have been run. As the samples were expected to have thickness above the usual thicknesses analysed by XPS (few hundred of nanometres vs few nanometres), the depths profiles were run overnight. In the first place, a low argon etch rate was used to penetrate the first few nanometres and acquire the surface spectra. Afterwards, a high etch rate was applied and run over a long period in order to reach and overcome the coating/PET interface.

As it is an expensive technique, a few samples were selected to highlight the effect of the process parameters on the final coating. More details on the samples can be found in Table 4-3. All the samples were analysed with the same argon etch rate.

Table 4-3 Summary of the main data of the samples analysed via XPS: Oxygen flow rate, WVTR, %transmission.

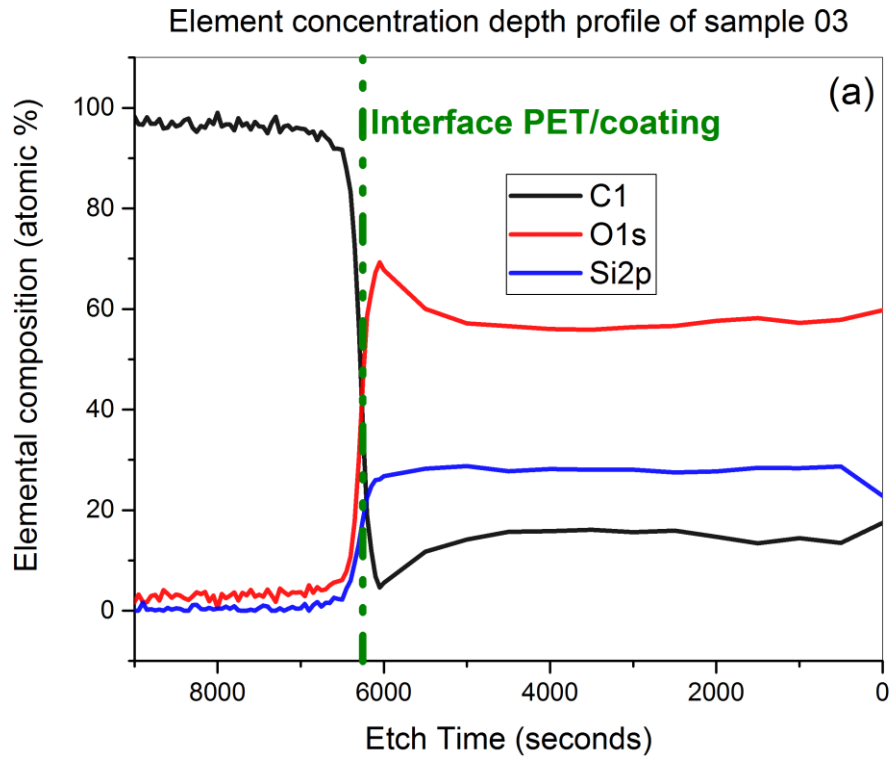
Identification	Oxygen flow rate (SCCM)	WVTR (g/m <sup>2</sup> /day)	%TR
Sample 01	550	0.100±0.0003	91
Sample 03	650	0.094 ± 0.001	87
Sample 09	350	0.092±0.004	83
Sample 10	250	0.057 ±0,004	79
Sample 11	150	0.058±0.003	72
Sample 12	50	0.065 ± 0.002	53

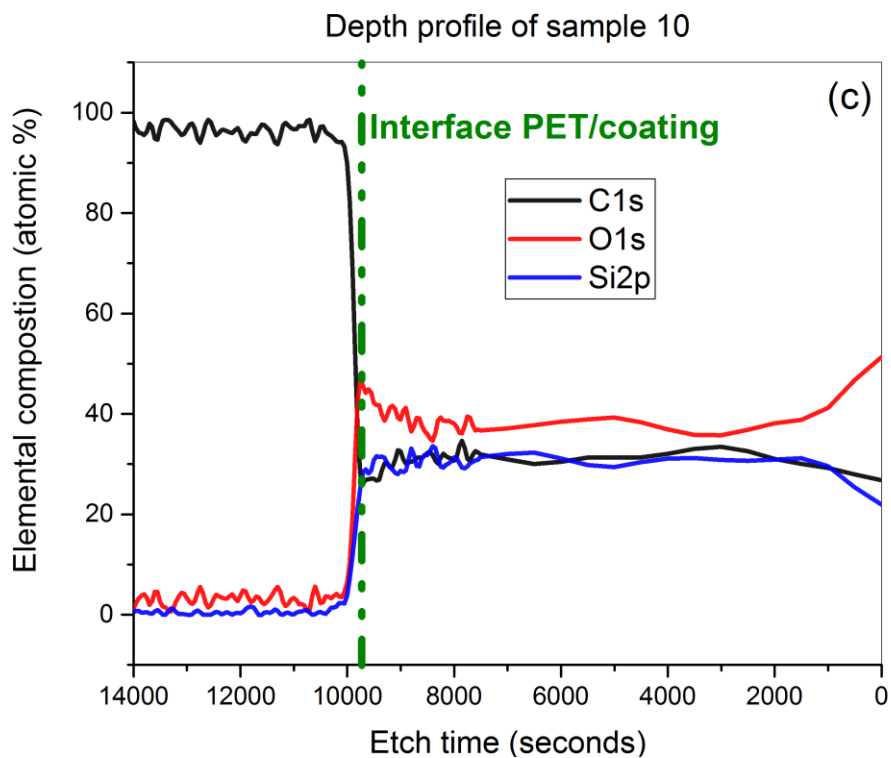
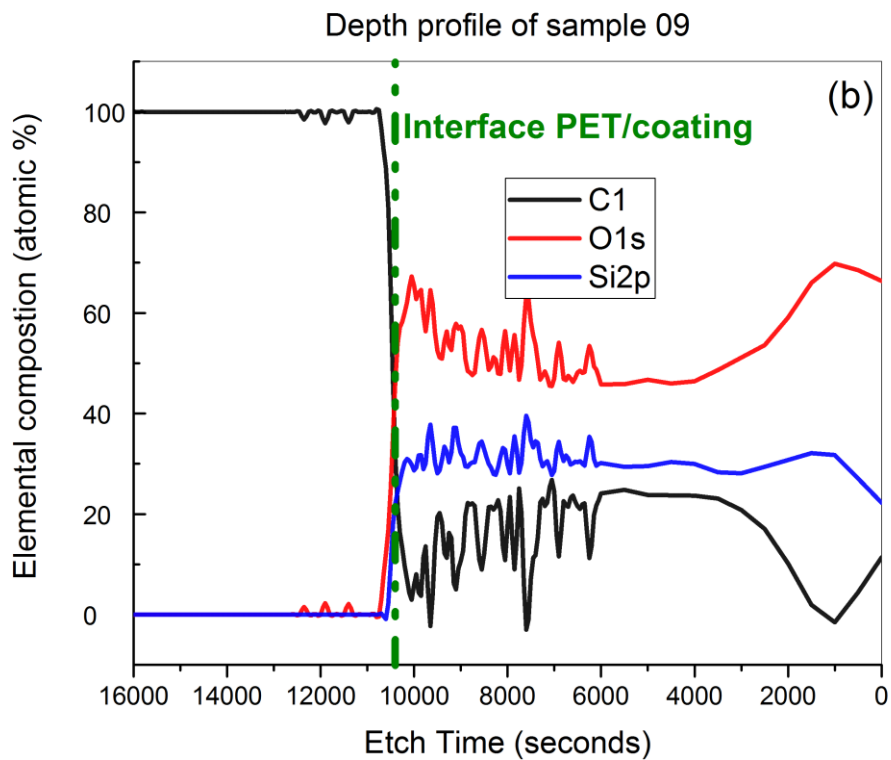
The samples chosen for analysis were obtained while using the same set of parameters and varying only the oxygen flow rates. The monomer flow rate was 133SCCM, the power: 1.2kW, and the line speed: 0.5m/min.

As expected, the XPS survey analysis highlighted the presence of oxygen carbon and silicon. The silicon and carbon coming from the HMDSO precursor and the oxygen being the reactive gas used to produce the coating. No other contaminant was found in either the coating or the substrate.

**Depth profiles of the samples**

This subsection presents the results of the XPS spectra of the samples mentioned in Table 4-3







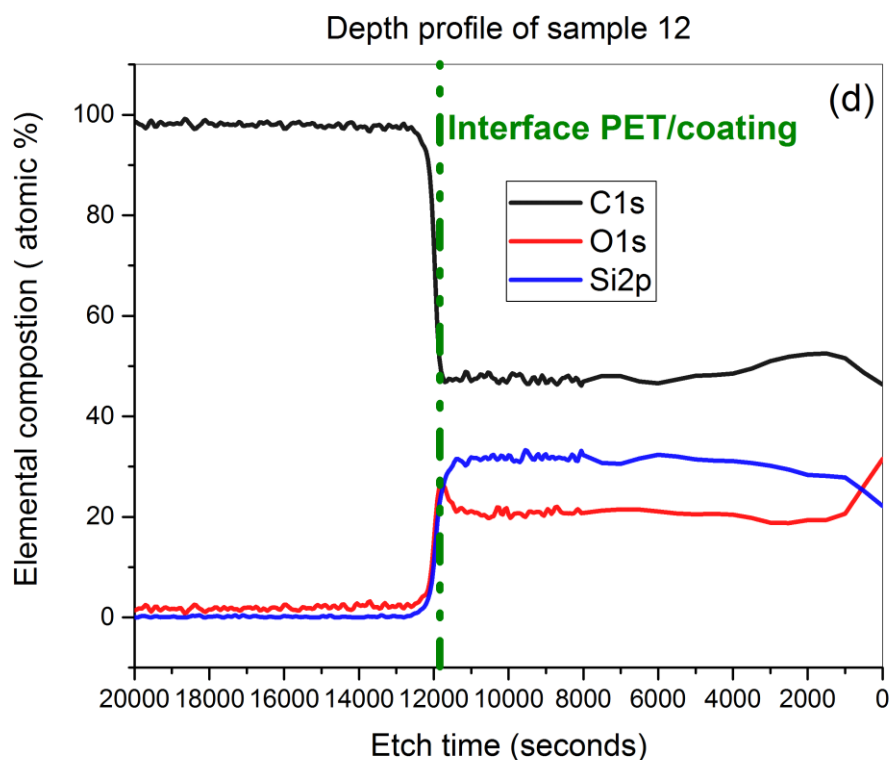


Figure 4-11 Depth profile of sample 03 (a), sample 09 (b), sample 10 (c), sample 12 (d). Black line for carbon content, red line for oxygen content and blue line for Si(2p) content.

#### 4.3.2.1 General observations

The first observation to be made is the constant atomic percentage of silicon when the oxygen flow varies, which is due to the monomer flow rate being kept constant. This indicates that at this monomer flow rate, the same amounts of Si atoms are removed from the HMDSO molecule even when the oxygen flow rate is low (50 SCCM). Then, it can be noticed that the content of oxygen and carbon in the coating varies with the oxygen flow rate. The atomic percentage of carbon increases when the oxygen flow rate decreases. In fact, when the oxygen flow rate increases, more oxygen can etch the carbon from the surface of the coating and replace it. The layer becomes then more oxidised and less organic.

In general, the composition is consistent within the depth of the sample but varies a lot at the outer surface (low etch time) as well as at the interface with the PET. The variation of the interface can be explained by the instabilities in the plasma on one side of the drum as the PET passes around it. Indeed, if the insulation on the left-hand side of the drum (entrance of the process zone) is failing, or when the plasma is unstable, the initial stages of growth are affected, therefore the first monolayers are not as consistent as they should be. This lack of consistency could result in a different structure (i.e. porosity) or a difference in composition due to a variation in the plasma composition.

### **4.3.3 Relationship between composition and WVTR**

In order to control the coatings, it appears relevant to understand the relationship between the composition of the barrier layer and the resulting barrier properties. This can be achieved by following the evolution of the barrier with the oxygen/HMDSO ratio and the evolution of the barrier with the composition of the film.

Figure 4-12 presents the relationship between the ratio oxygen:monomer and the Si/C/O content<sup>7</sup> in the coating as well as the relationship between the ratio oxygen:monomer and the WVTR.

---

<sup>7</sup> Determination of the atomic percentages was done by hand (taking the numbers from the most stable region of the spectra – middle region) and the error associated with the calculated measurement was less than 5%.

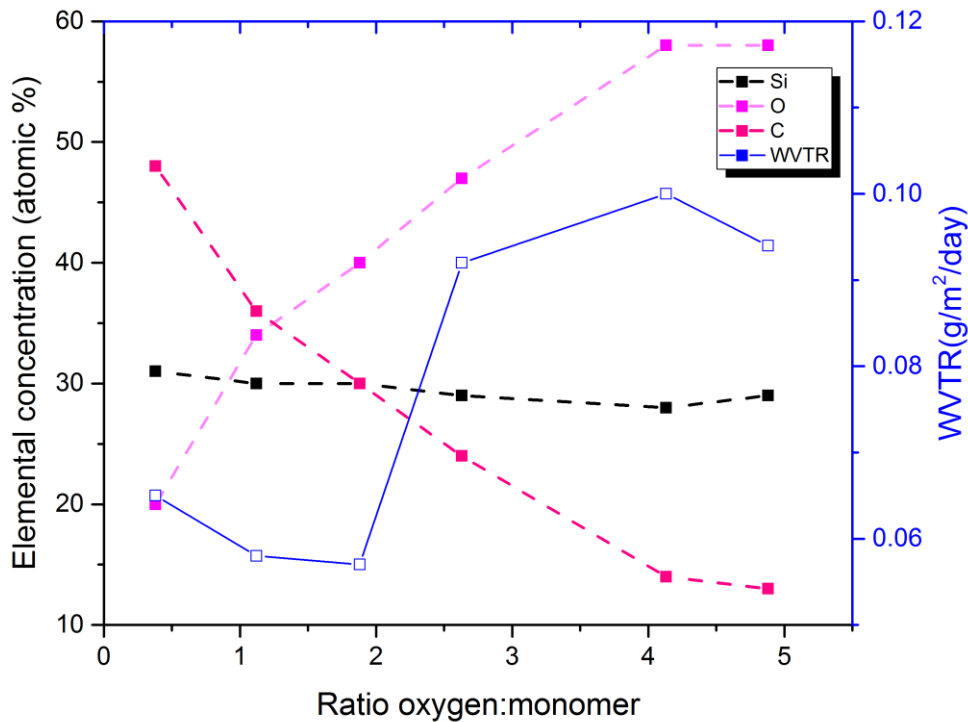


Figure 4-12 Evolution of the content of silicon, oxygen and carbon content in the coating with ratio oxygen:monomer

The carbon content in the film drops as the ratio oxygen:monomer is increased. On the other hand, the content of oxygen increases when the ratio increases. This behaviour can be explained by the increase of oxygen injected into the process, which increased the ratio of monomer broken down. The oxygen might also help etching the carbon away from the surface, preventing its incorporation in the coating. One can note the content in carbon and oxygen remain stable at high ratios (above 4). This might indicate that there are no remaining monomer molecules to be broken down and there is therefore an excess of oxygen in the chamber. Figure 4-12 also shows that the lower content of carbon and higher content of oxygen in the coating results in a higher WVTR ( $9.7 \times 10^{-2}$  g/m<sup>2</sup>/day). In general, the less carbon rich the coating is, the denser it is. These results are in good agreement with those obtained by Gunther et al. [39, 99, 100]. Although they worked with lower ratios (below 2), they identified similar trends in the coating composition and WVTR in

## 4 Initial Platform Assessment

relation to the ratio oxygen:monomer. Due to the limited number of samples that could be analysed the region of ratios between 3 and 4 could not be investigated

Table 4-4 summarises the composition and stoichiometry of each sample analysed and the corresponding oxygen:monomer ratio and oxygen flow rates used to produce the coatings concerned. All the data were taken at 5000 seconds etch time on the atomic percentage vs etch time graphs.

*Table 4-4 Summary of the composition and stoichiometry of the samples analysed by XPS (the composition is reported in atomic percentage (%) of each element Si, C, O)*

Sample	O <sub>2</sub> flow rate (SCMM)	Ratio O <sub>2</sub> /HMDSO	%Si	%O	%C	Stoichiometry	WVTR (g/m <sup>2</sup> /day)
Sample 01	550	4.13	28	58	14	SiO <sub>2.07</sub> C <sub>0.5</sub>	0.100± 0.0003
Sample 03	650	4.88	29	58	13	SiO <sub>2</sub> C <sub>0.44</sub>	0.094 ± 0.001
Sample 09	350	2.63	29	47	24	SiO <sub>1.62</sub> C <sub>0.82</sub>	0.092± 0.004
Sample 10	250	1.88	30	40	30	SiO <sub>1.3</sub> C	0.057 ±0,004
Sample 11	150	1.12	30	34	36	SiO <sub>0.64</sub> C <sub>1.58</sub>	0.058± 0.003
Sample 12	50	0.38	31	20	48	SiO <sub>1.13</sub> C <sub>1.2</sub>	0.065 ± 0.002

Table 4-4 reports that high ratios of oxygen monomer lead to low carbon and high oxygen compositions, which corresponds to a high rate of monomer decomposition in the plasma. Moreover, there seems to be a threshold in composition for a ratio greater than four. This behaviour could be due to an excess of oxygen in the plasma, at which point the point of monomer is insufficient and no further coating can be produced. At the same ratios, one can note that the carbon content in the coating is low and the coating is close to a stoichiometric  $\text{SiO}_2$ . It is thought that the residual carbon is etched away by the excess of oxygen.

Finally, the composition and WVTR results reported in Table 4-4 suggest that WVTR is minimised for low oxygen/high carbon compositions and that a quasi-stoichiometric  $\text{SiO}_2$  (with residual carbon) maximise the WVTR. This high carbon content is likely to result in a high thickness coating where the defects are covered as demonstrated by Howells et al.[90, 101]

#### 4.4 Defect observation (calcium test)

The calcium corrosion test from Oxford University was performed on SiO<sub>x</sub> coated sample (12\_10\_26\_05) for which the measured moisture vapour barrier was found to be 0.051±0.005g/m<sup>2</sup>/day and thickness is expected to be around 250 nm with a visible transmission of 81.28%. The process parameters used to obtain that sample are summarised in the table below.

*Table 4-5 Process parameters used to produce the coating tested on the calcium corrosion test.*

Process parameter	Value
Number of passes	3
Line speed (m/min)	1
Oxygen flow rate (SCCM)	550
Helium flow rate (SCCM)	133
Monomer flow rate (SCCM)	133
Argon in the GPE (SCCM)	180
Power (kW)	1.3
Voltage (V)	888
Current (A)	1.8
Magnetic array-to-drum distance (mm)	54

A 170µm thick layer of calcium was deposited onto the barrier-coated face of the sample, which was then encapsulated on a glass sheet (10mm x10mm) using UV curable epoxy as the sealant.

The whole stack was then exposed to moisture in a temperature-controlled atmosphere and photographs of the calcium coating were taken at regular

intervals. In the first instance, as the quality of the  $\text{SiO}_x$  barrier layer was not known, photos were taken every hour. After a couple of days, it appeared that this interval was too short to reveal any change, thus a photo was taken every 24 hours. Figure 4-13 shows the pictures taken at different exposure times of respectively 0 hour, 2 hours and 30 minutes, 26 hours and 365 hours.

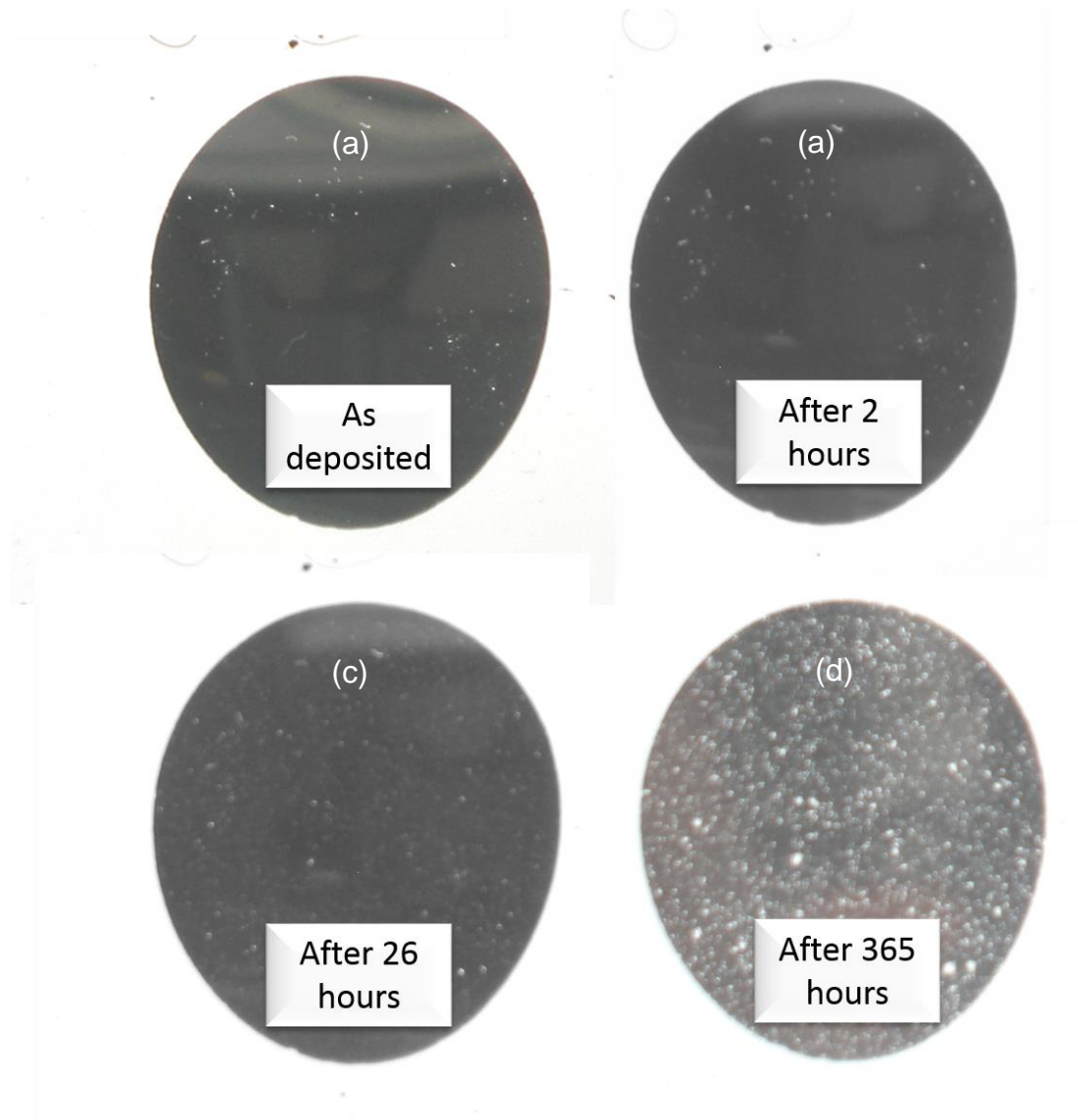


*Figure 4-13 Photos of calcium coating on top of the  $\text{SiO}_x$  coated samples taken after 0h, 2h, 26h, 365h exposure to 90% RH and temperature controlled atmosphere (37°C)*

These pictures show that the degradation of the calcium takes approximately 2 days.

On the photo taken straight after encapsulation, several holes (white dots) appear. It is more likely that those holes were initially present in the calcium layer and not in the  $\text{SiO}_x$  coating. This can be confirmed by the fact that these holes do not evolve and are not getting bigger with the exposure time. However, after a few hundreds of hours (photo (d) Figure 5-1) the calcium coating is covered with holes. These holes are located everywhere on the patch and seem to have the same size. Thus, the barrier is proved porous. Although, the calcium layer has degraded with exposure to moisture, it has not completely failed. Further analysis on the distribution of the holes can be done. Another point to be noticed is the two bubbles in the epoxy that are creating a leak, which could lead to degradation of the outside edge of the circular pattern.

As the calcium test is a not a standardised method, it is difficult to compare these results with the limited results on  $\text{SiO}_x$  coatings (onto plastic substrates) in the literature. However, similar work has been carried on at Oxford University on  $\text{AlO}_x$  coatings. The results obtained are very interesting, because they show that the defect through which the moisture permeates are not the same in  $\text{AlO}_x$  sputtered coatings and  $\text{SiO}_x$  PECVD coatings (for similar thicknesses). Indeed, the test revealed a small amount of large holes in the  $\text{AlO}_x$  coating, and a quicker failure of the calcium coating.[102]

### **4.5 Conclusion on the initial platform development**

The initial characterisation of the platform to produce  $\text{SiO}_x$  barrier coatings was achieved despite several stability and repeatability issues. This work led to some early findings. At first, several defects such as craters, roughness and lack of uniformity (i.e. hazy coating) were observed and identified as barrier limiting factors. These defects could be observed at micro level but also at a macro level via the calcium test. They appeared as pinholes and were covering the whole coating's surface.

As far as the process parameters were concerned, it appears that the ratio oxygen:monomer was affecting both the composition and WVTR of the



coating. WVTR was found to be minimised for low oxygen/high carbon compositions (ratios oxygen:monomer lower than 2). In addition, in carbon and a stoichiometric SiO<sub>2</sub> resulted in a higher WVTR. Therefore, a non-stoichiometric SiO<sub>2</sub> coating with a high level of residual carbon provided better barrier performances (around  $5 \times 10^{-2}$  g/m<sup>2</sup>/day).

## **5 PLATFORM CHARACTERISATION**

Note: All the results presented in this chapter have been measured on samples generated throughout the PhD project.

In this chapter (Chapter 5), the reference sample was chosen from the available data at the time of the study, for it exhibited the lowest WVTR to date for a single pass coating. The process associated with this sample are reported in Table 5-1

*Table 5-1 Process parameters used for the reference sample in the initial platform characterisation study*

Parameter	Value
Number of passes	1
Substrate speed (m/min)	0.5
Oxygen flow rate (SCCM)	1100
Helium flow rate (SCMM)	100
Monomer flow rate (SCMM)	159
Argon flow rate (SCCM)	110

### **5.1 Surface coating properties: topography**

An initial assessment of the coatings indicated that they were all semi-transparent with optical densities in the range 0.040 (91.2 % transmission in the visible range) to 0.090 (81.3 % transmission). The more detailed SEM topographical analysis of the films revealed the packed grainy structure of the PECVD SiO<sub>x</sub> coatings, which has already been observed by several groups [92, 103]. Figure 5-1 compares the electron microscope images of coatings produced with different input power levels.

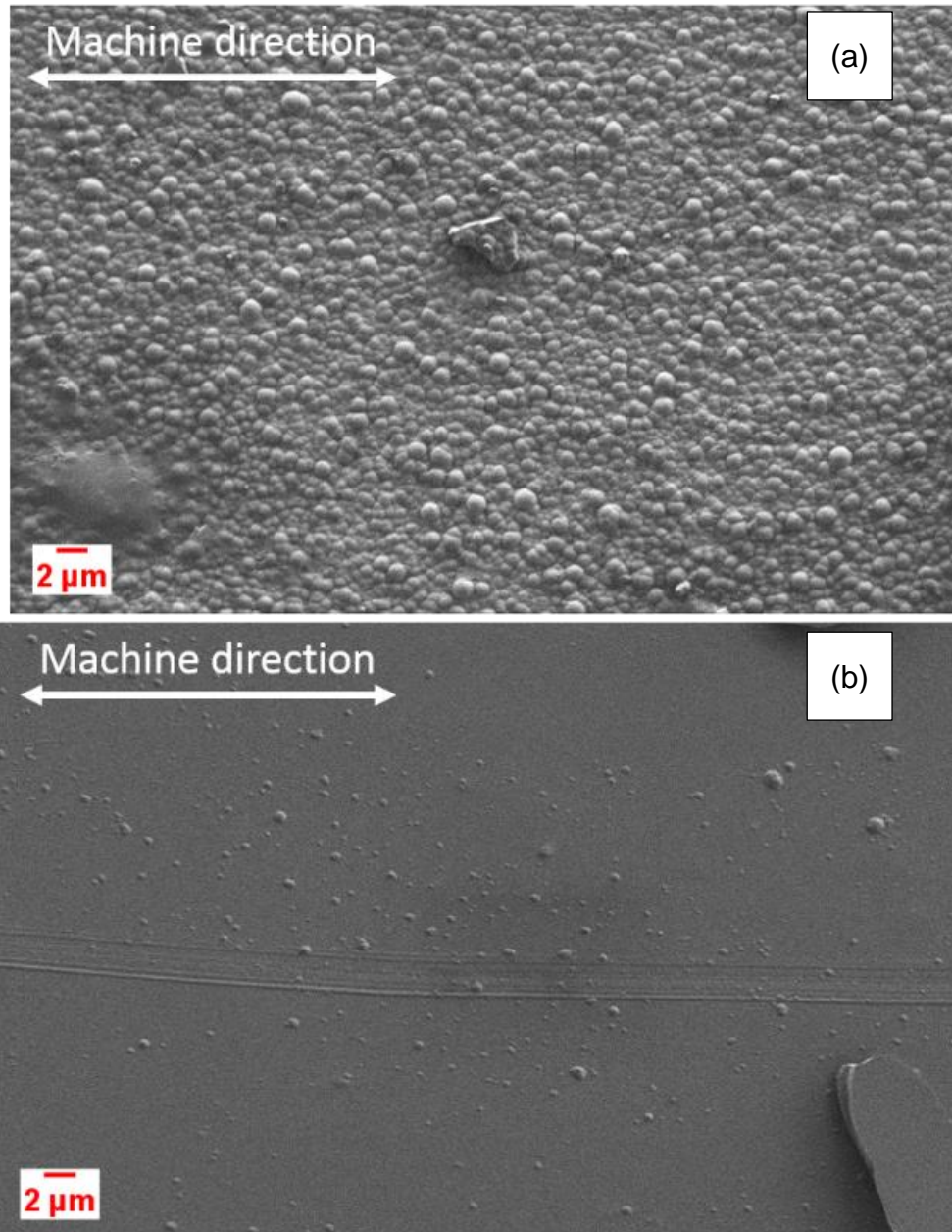


Figure 5-1 SEM micrographs of the coating deposited using the same parameters except input power. Sample a:  $P=1.1\text{kW}$ , sample b:  $P=1.6\text{kW}$ . The ratio oxygen: monomer for both samples was 6. The WVTR rates for the samples (a) is,  $0.230\text{ g/m}^2/\text{day}$  and sample (b)  $0.053\text{ g/m}^2/\text{day}$ .

## 5.2 Influence of power on coatings and barrier performances

It is clear from Figure 5-1 that increasing the power level has produced a significantly smoother surface (Figure 5-1 (b)) to the coating, although some scratches in the machine direction are visible on the surface of this coating

(these scratches might be inherent to the substrate and might have been conformally coated). The WVTR rates for samples a and b, mentioned in this figure were, respectively, 0.230 g/m<sup>2</sup>/day and 0.053 g/m<sup>2</sup>/day. The former result may well be related to the presence of cracks, pinholes and open porosity in the lower power coating, providing a preferential path for water vapour molecule permeation[59, 104].

To a first approximation, increasing the plasma power appears to have resulted in a smoother, denser, conformal coating with better water barrier performance. This assumption matches Bieder et al's assumption that increasing the power leads to an increase in ion bombardment, which increases the surface diffusion (of the chemical species) and reduces the voids. Therefore, with the coating being denser, the permeation is limited[88]. A more intense substrate ion bombardment at higher power also suppresses the development of rough structures by creating nucleation sites for arriving coating fragments, eroding surface roughness peaks, and overcoming shadowing effects by migration[104].

Figure 5-2 shows the WVTR measured for coatings produced with varied input powers (all the other parameters kept constant) and the associated barrier improvement factor.

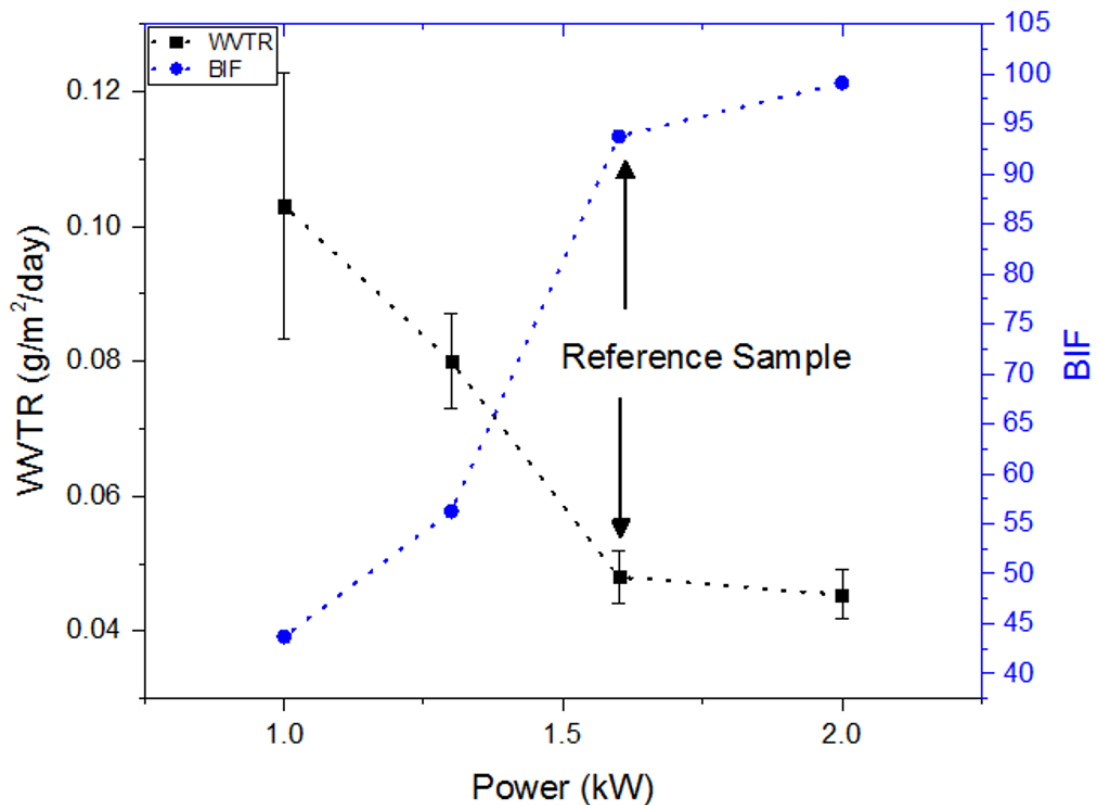


Figure 5-2 Graph showing the relationship between the input power and the WVTR/BIF

A clear trend seems to be drawn as far as the relationship between input power and WVTR is concerned. The WVTR improves (i.e. reduction in transmission rate) with increasing input power, indeed there is a barrier improvement of 2.5 times over the range of powers studied here. This was related earlier to an improvement in film structure observed at higher powers.

### 5.3 Barrier performances and coating thickness

The relationships between water barrier performance and coating thickness, oxygen:monomer flow rate ratio, web speed and plasma power have all been investigated. Coating thickness was found to vary between 250 nm and 950 nm (which equates to dynamic deposition rates in the range 127 to 425 nm·m<sup>-1</sup>·min<sup>-1</sup>). Thickness is decreasing with increasing oxygen:monomer flow rates (Figure 5-4), WVTR decreases when thickness increases (between 200nm and 800nm, which is in agreement with literature (Figure 5-4) [71, 105]. One can also notice that when thickness increases to above 900nm, the WVTR

increases again, which could be explained by the apparition of stress and defects (such as pinholes and cracks) in the coating as it was reported by Felts et al[97].

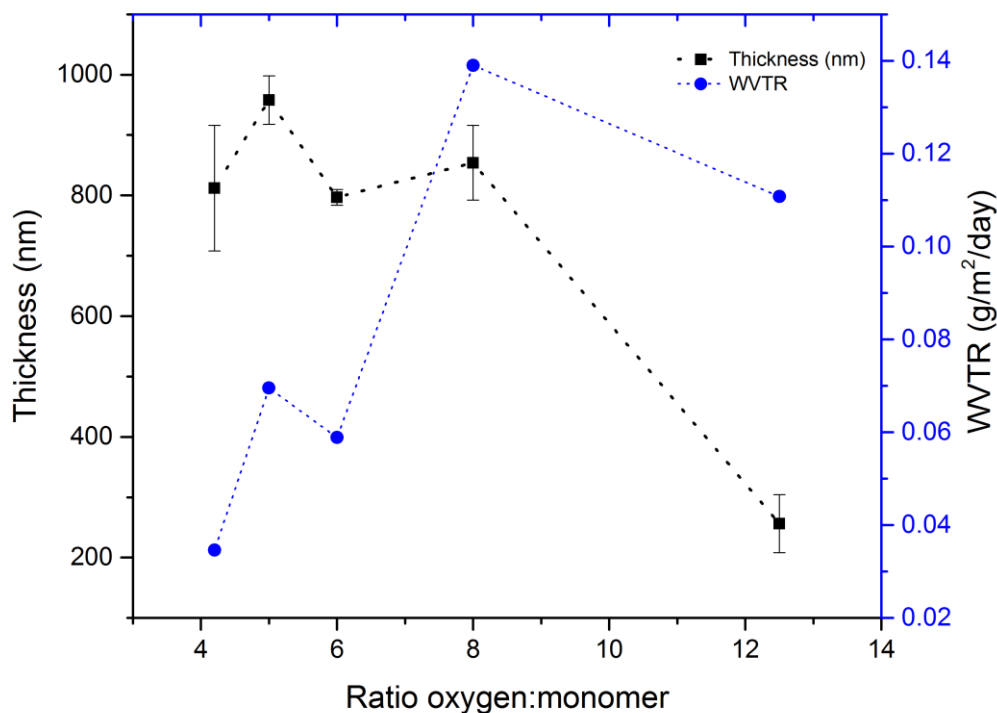


Figure 5-3 Graph showing the relationship between WVTR and ratio oxygen:monomer and associated barrier improvement factor when the oxygen flow rate remains constant (1100 SCCM) and the oxygen flow rate is varied from 88 to 264 SCCM.

Another set of experiments has been carried out whereby the oxygen flow rate was varied (from 1100 to 200 SCCM) whilst the monomer flow rate was kept constant at 179 SCCM. The trend is relatively similar and shown in Figure 5-4. This can be compared to the initial study of the WVTR in relation with the ratios. If one compares both sets of results, the trends appear similar. Indeed, in the range of ratio between 2 and 4 there is an increase in WVTR. This suggests that, despite the slight variations in WVTR, the coatings produced were relatively reproducible.

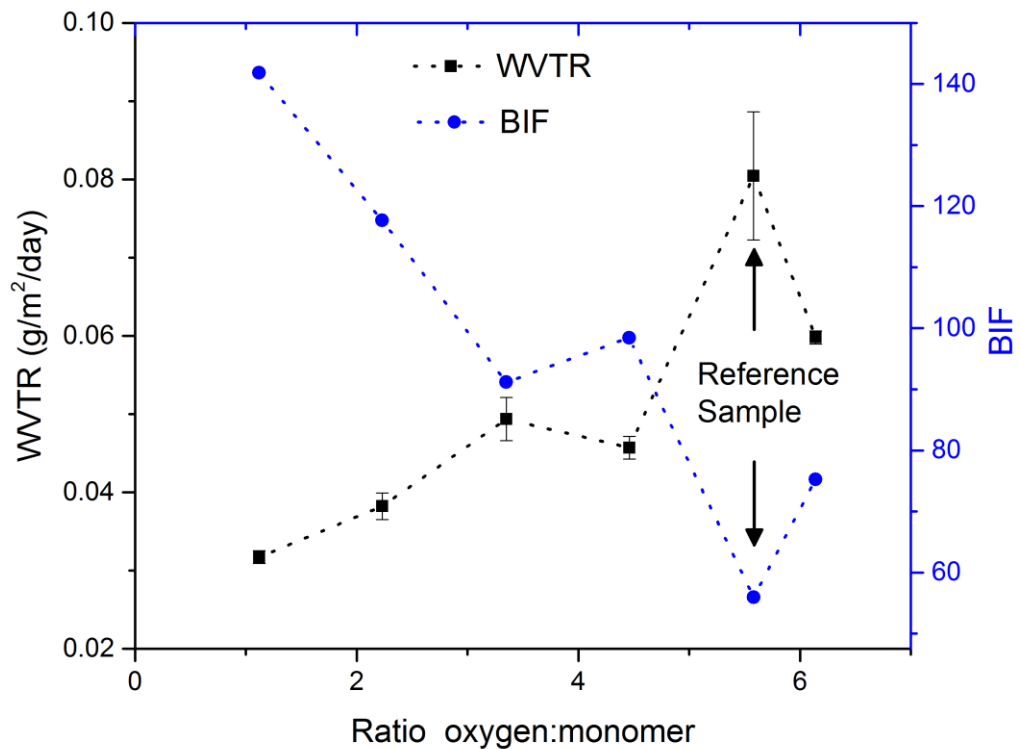


Figure 5-4 Graph showing WVTR and associated BIF as a function of the ratio oxygen:monomer. In this case the monomer flow rate was kept constant at 179SCCM and the oxygen flow rate was varied from 200SCCM to 1100 SCCM.

WVTR have been compromised with increasing the oxygen:monomer flow rate ratio, i.e. the best barrier results are found at lower flow rates of oxygen. As mentioned above, this promotes a more organic nature to the coating. In addition, it has been observed elsewhere that films deposited under high oxygen-to-HMDSO flow rate ratios showed an increased surface roughness and a more brittle nature[63, 88]. Another key parameter in the understanding and optimisation of the process and the coatings is the input power used to create and sustain the plasma, as discussed in Section 4.2[50, 60].



### 5.3.1 Relationship between web-speed and barrier performances

Finally, the web speed is also an interesting parameter as it affects the dwell time (exposure time of the substrate to the plasma) and the deposition rate. Figure 5-5 is a plot of the variation in WVTR as a function of web speed.

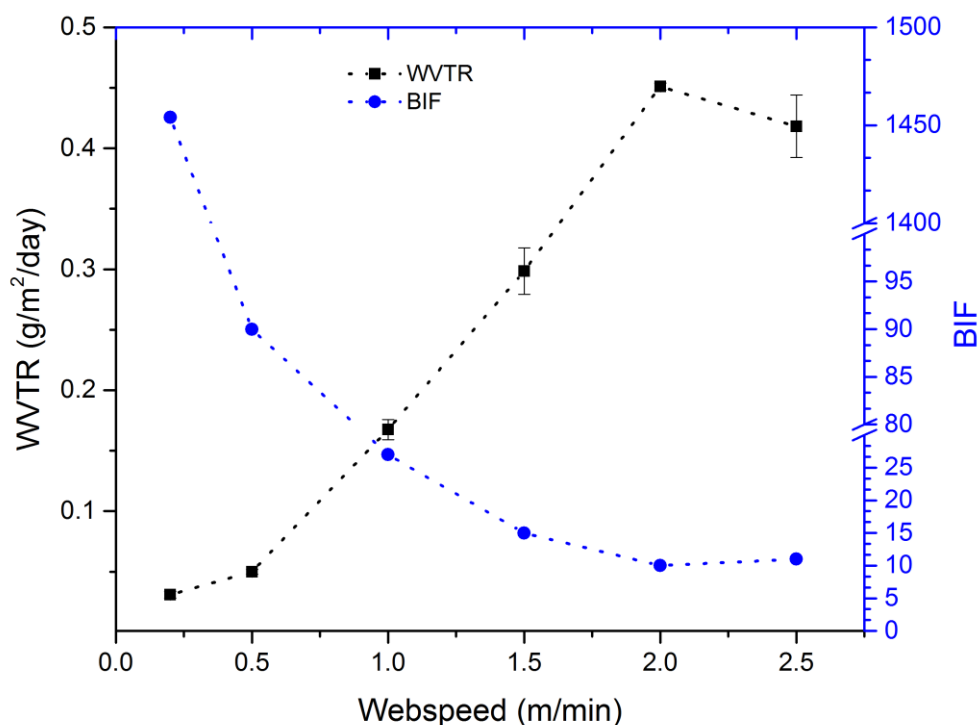


Figure 5-5 Graph showing the relationship between the web speed and the WVTR/BIF

The WVTR increased (barrier deteriorated) with web speed, with a maximum transmission rate at a speed of 2 m/min. This result is in good agreement with the data published by Okimoto on SiO<sub>x</sub> coated PEN[106]. This may be related to a reduction in coating thickness at higher web speeds as associated reduction in ion bombardment from the plasma affecting film growth, but no clear correlation with thickness has been observed at this stage.

### 5.3.2 Barrier performance with elongation

During coating, laminating and post vacuum coating conversion, the films are subject to repetitive strain (due to handling and processing). This can induce

defects and potentially compromise the barrier performance. Thus, barrier retention on strain (or flex-durability) can be investigated to determine the effect of this repetitive strain on the barrier properties of the film.

In order to assess the variation in barrier properties while handling the film (e.g. winding, tensions, etc.) tensile tests were performed on a roll of coated film. Strains between 0.5% and 5% were applied. The water vapour barrier was measured after relaxation.

Plots of WVTR and BIF versus applied (then released) strain are shown in Figure 5-14, for the SiO<sub>x</sub> coated PET.

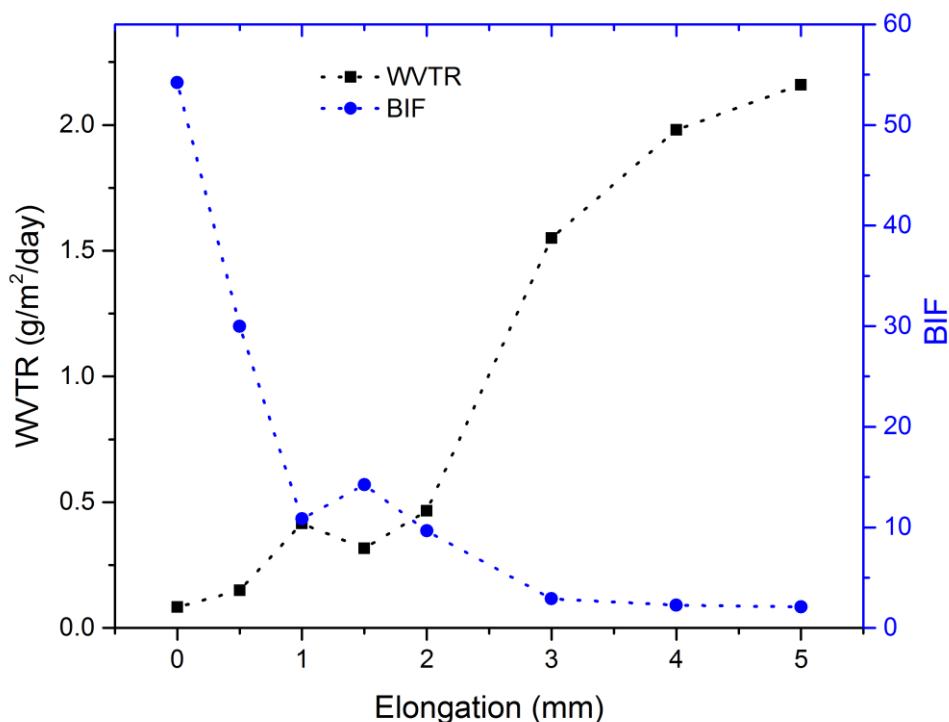


Figure 5-6 Graph illustrating the change in barrier induced by elongation of the coated film in the machine direction. WVTR measured after relaxation.

These results indicate that the WVTR increases during deformation of the polymer. These results are in agreement with the work done by Rochat et al[107] and Leterrier et al[108]. They reported that the first wrinkles appear at

3% strain on their 10 nm PECVD SiO<sub>x</sub> coating and assumed that there was no fracture of the coating at this stage, which could explain the preservation of the barrier properties. When the strain applied reached 5%, though, the first cracks (combined with the previous wrinkles created) started to appear, causing a loss in barrier.

However, in the case of this study, it was noticed that the loss in barrier occurs before 5%, which can be attributed to the higher expected thickness of the coating (a few hundred nm) and the different density of antiblock particles (to be determined). Indeed, it is also known that the crack onset (or coating resistance) decreases as thickness increases. In addition, the presence of additives in the substrate and exposed at the surface, causes a decrease of the crack onset strain of 25% (reported for thin coatings[107]). Thus, in the case of the results related to Figure 5-6, it can be thought that the combined effect of the additives and the thickness on the mechanical properties of the coating lead to a lower crack onset strain than those reported in the literature. The comparison of thin and thick coating mechanical properties is valid because of the influence of the first layer mechanical properties on the overall properties[107]. Although Rochat et al. didn't report any barrier values, Felts[97] reported that for a similar strain, the impact on the oxygen barrier is more important for thicker coatings.

Regarding the rate at which the WVTR of the coating degrades after the onset of cracking, Felts[71] assumed it is related to the relative adhesion between the coating and the first layer of the SiO<sub>x</sub> coating. This adhesion is, indeed, highly dependent on the surface properties of the substrate (roughness, defects, available bonds) that could be further investigated via atomic force microscopy/white light profilometry (roughness), SEM (defect density), Fourier transform infrared spectroscopy (for chemical bounds), etc.

No cracks were found on the samples using an SEM, or using a light microscope under 5% strain. However, the observation was made after the samples had relaxed and it is possible that the cracks have relaxed. Modelling of the cracking mode and the influence of the defects is also possible and has

been reported by Howells and Yang[101] . Further detail on the modelling of the barrier degradation with strain can be found in the work done by Yanaka et al.[104].

### **5.4 Summary and conclusion**

Single layer transparent SiO<sub>x</sub> barrier coatings have been deposited onto commodity grade PET substrates using the PECVD method in a pilot scale roll-to-roll coater. The coatings were found to have a grainy structured surface. The composition of the coatings varied with the oxygen:monomer ratio, with high oxygen flow rates resulting in coatings with close to stoichiometric SiO<sub>2</sub> compositions, whereas low oxygen flow rates produced more organic coatings with a higher carbon content. From an initial assessment of the influence of process parameters on the water barrier performance, it was found that low WVTR values were promoted by low oxygen:monomer flow rate ratios, low web transport speeds and high plasma discharge powers. Nevertheless, it was noted that the process was becoming unstable for higher input powers. Further investigation will be carried out on the physical and chemical nature of the coatings in order to gain a better understanding of the permeation mechanisms and to optimise the PECVD process and obtain barrier levels closer to the application's requirements.

## **6 PLATFORM DEVELOPMENT AND OPTIMISATION**

Understanding the deposition process and identifying stable operating conditions is a key step in order to achieve the level of barrier targeted. The work reported in the previous chapter lead to the conclusion that the best barrier performances that the original method could deliver with the original ingredients, recipes and substrate was in the low  $10^{-2}\text{g/m}^2/\text{day}$ . This figure is related to a single layer of  $\text{SiO}_x$  deposited onto  $120\mu\text{m}$  PET Jindal J500.

Although this result would be acceptable for other applications such as food packaging that require less severe levels of barrier ( $10^{-1}\text{g/m}^2/\text{day}$ ), the target aimed for the final protective coating product to be suitable for electronic encapsulation is in the  $10^{-6}\text{g/m}^2/\text{day}$  range. Therefore, some modification and optimisation of the methods were needed. Several options were considered and are detailed in this chapter.

### 6.1 Investigation of $\text{CO}_2$ injection

$\text{O}_2$  is very commonly used as reactive gas for its high reactivity with other species and easy decomposition (into atomic oxygen) in plasmas.  $\text{CO}_2$ , however, has shown some potential to facilitate the growth of the first Si-H/ $\text{SiO}_x$  layers deposited by PECVD (by promoting etching of the surface)[109] and is known to be a suitable treatment for improving the adhesion of metal barrier coatings (through surface chemistry modification of the PET under  $\text{CO}_2$  exposure)[108]. Thus, there was an interest in investigating the effect of injecting  $\text{CO}_2$  into the plasma on the moisture barrier and coating properties. Moreover,  $\text{CO}_2$  when broken down into CO by interactions with electrons and ions of sufficient energy, is very stable in PECVD plasmas[110], due to its high bond energy (11.2 eV). This could imply that the use of  $\text{CO}_2$  could improve the stability of the plasma.

#### 6.1.1 Methods and materials

The pilot roll-to-roll coater was used in normal conditions to deposit the coating onto a  $120\mu\text{m}$  PET substrate. However, the gas line usually used to feed helium into the chamber was connected to a  $\text{CO}_2$  tank instead.

Table 6-1 summarises the different process parameters used for the different trials that were carried out with CO<sub>2</sub> injection.

*Table 6-1 Process parameter used to deposit SiO<sub>x</sub> onto 120µm thick PET with and different flow rates of CO<sub>2</sub>*

Parameter	Reference run	Value (Trial 1)	Value (Trial 2)	Value (Trial 3)
Line speed (m/min)	1	1		
Monomer flow rate (SCCM)	179	179		
Oxygen flow rate (SCCM)	1100	1100	1000	700
CO <sub>2</sub> flow rate (SCCM)	0	100	200	500
Helium flow rate (SCCM)	100	no		
Argon flow rate through GPE (SCCM)	100	100		
Power (kW)	1.6	1.6		

All the samples were produced during one campaign over a day.

## 6.1.2 Results

### 6.1.2.1 Surface topography

In general, the SiO<sub>x</sub> coatings revealed the same granular (finer granular structure for the background) textures as found for reference sample films.

However, increasing the flow rate of CO<sub>2</sub> appears to increase the brittleness of the coatings, as illustrated in Figure 6-1.

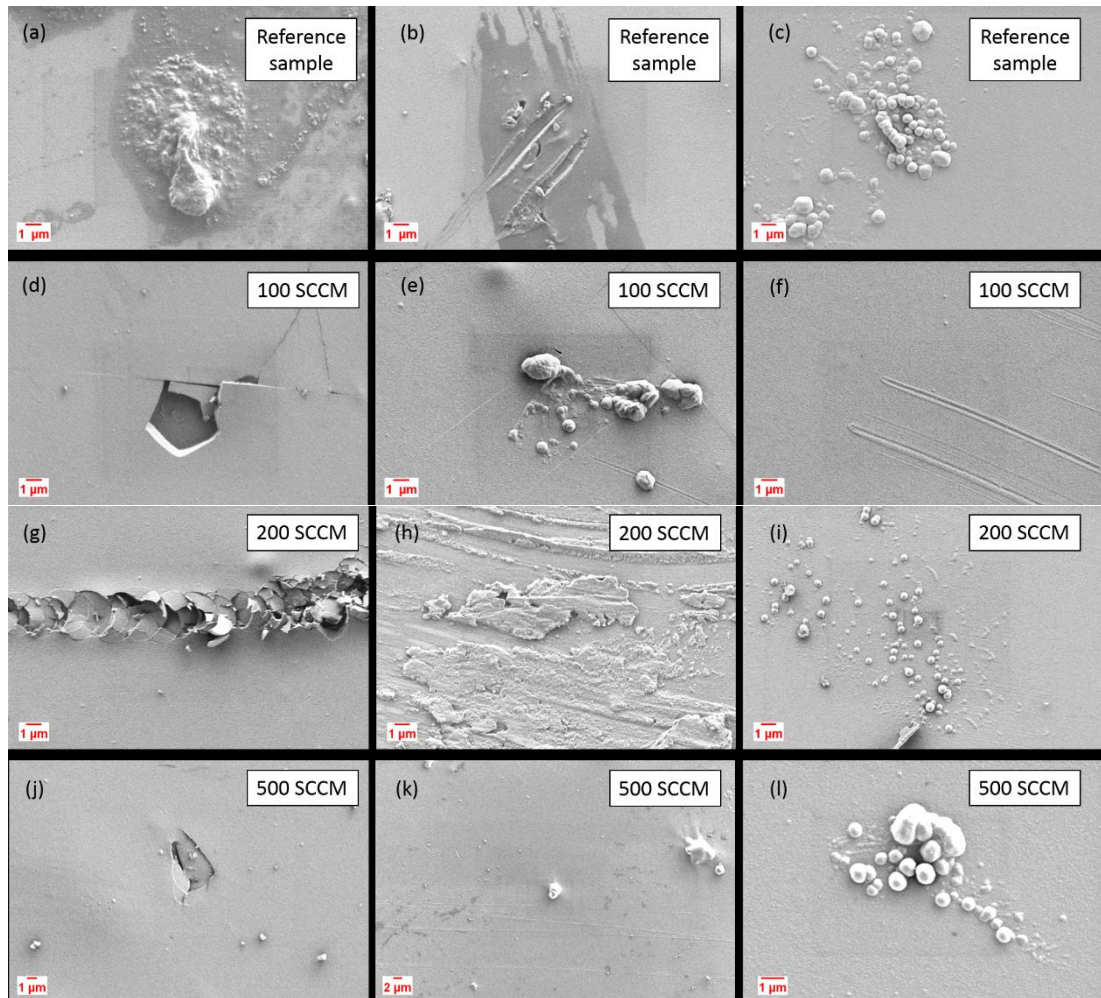


*Figure 6-1 SEM images showing surface features of SiO<sub>x</sub> coated polymer films deposited through plasma containing 100SCCM, 200SCCM and 500SCCM of CO<sub>2</sub> in comparison to the reference sample*

The brittleness could be explained by a potential increase in carbon content in the coating, which is known to degrade the mechanical properties of SiO<sub>2</sub> coatings[111]. Jeong et al[112] have established that replacing O<sub>2</sub> by CO<sub>2</sub> in the mixture increased the carbon content and decreased the density of the SiOCH coating. Furthermore, at low CO<sub>2</sub> content (100SCCM) the surface



seemed to have been sprayed and “melted” in some places[113]<sup>8</sup>, creating discolouration (Figure 6-1b) and an agglomeration of particles (Figure 6-1c). This effect does not appear to be enhanced by further addition of CO<sub>2</sub>. However, these discoloured zones seemed to be more prone to damage due to scratches. Indeed, the scratches appear to be wider in the coloured area.

Some grains and defects can be observed on all of the samples including the reference sample (Figure 6-1 a,b,c,i and l). This type of defect has already been observed on regular SiO<sub>x</sub> coatings and might be due to volume polymerisation. It appears that the discoloured area (Figure 6-1b) is softer than the rest of the coating which caused the scratches to be wider than usual (1µm wide on Figure 6-1b against <500nm wide on Figure 6-1f). However, the scratches might have been caused by debris causing damages to the substrate in the unwind roll as it is unwound.

One can also note that the coating seems to be more and more brittle as the crack become more serious when the flow rates increased from 100SCCM (Figure 6-1d) to 200SCCM (g). Moreover, Figure 6-1h shows some delamination of the coating, which might be due to a lack of adhesion. However, according the micrograph in Figure 6-1j), the coating appears less brittle when the flow rate is increased to 500SCCM.

### **6.1.2.2 Barrier properties**

Barrier performance was measured with the Systech 7001, using a cycle of 45 minutes without zeroing. Table 6-2 reports the barrier performances of the samples produced with injection of CO<sub>2</sub> alongside the reference sample.

---

<sup>8</sup> These damages might be due to local plasma arcs which tend to be very hot local points. At these locations, there might also be some electrolytic oxidation with the residual water in the chamber which creates the roughness/granules.

*Table 6-2 Moisture barrier performance results comparing the barrier performance of the reference samples with helium and the samples produced with the injection of CO<sub>2</sub>*

<b>CO<sub>2</sub> Flow rate (SCCM)</b>	<b>Barrier (g/m<sup>2</sup>/day)</b>	<b>BIF</b>
<b>Reference run with Helium</b>	0.073 ± 0.003	62
<b>100</b>	0.079 ± 0.003	57
<b>200</b>	0.060 ± 0.019	76
<b>500</b>	0.119 ± 0.009	38

The barrier performances seem to remain similar to the reference run for a low CO<sub>2</sub> flow rate. However, when increasing the CO<sub>2</sub> flow rate to 200SCCM it appears that the barrier properties are improved, with the WVTR slightly decreasing. Nevertheless, when the CO<sub>2</sub> flow rate is increased to 500SCCM, the WVTR dramatically increases by a factor about two; thus, a high CO<sub>2</sub> flow rate does not seem to be beneficial for the barrier performances. One can note, however that the data is slightly scattered which make it difficult to draw any firm conclusions.

Howells[101] has shown that high carbon contents in the coating promote excellent mechanical properties such as adhesion and crack onset strain (the coating is more ductile, therefore the first cracks occurs at higher strain). The high carbon content may also increase the thickness and defect coverage, which creates a more tortuous path for moisture to permeate through the material. The higher carbon content can be due to the unreacted monomer incorporated in the coating. This is further confirmed with the decrease in water vapour transmission rate observed in Table 6-2 for high flow rates of CO<sub>2</sub>. Therefore, a higher amount of carbon might have been incorporated in the coating. This hypothesis is confirmed by the FTIR analysis (as described in the following section in Figure 6-2), which revealed that the content of carbon in

the coating increases when the flow rate of CO<sub>2</sub> is slightly increased from 100 to 200SCCM. On the other hand, when the CO<sub>2</sub> flow rate is increased further to 500SCCM, the WVTR doubles which tends to highlight a threshold of flow rate for which the content of carbon might be too high and does not compensate for the lack of monomer that can be broken down.

Moreover, the drop in moisture barrier properties at high CO<sub>2</sub> flow rate can be associated with the increase of Si-OH bonds in the coating revealed in the FTIR analysis (presented below in Figure 6-2). According to Kim et al. [114] the adsorption of moisture on a surface is proportional to the concentration of Si-OH bonds.

### 6.1.2.3 Surface roughness

The topography of the three samples (produced with different CO<sub>2</sub> flow rates) was found to be similar. Therefore, the roughness could be estimated using the parameters R<sub>a</sub> and R<sub>q</sub>, respectively describing the average roughness and the mean square of the roughness. The measured roughness of all samples was in the same range and highly affected by the presence of antiblock particles. The antiblock particles are between 1µm and 2µm in diameter and their distribution on the surface is under 11 particles/345µm<sup>2</sup> (counted on an SEM micrograph). As a reference, the uncoated substrate R<sub>q</sub> value was measured to be 82 nm on an 800x800µm<sup>2</sup> image.

*Table 6-3 Measured R<sub>a</sub> and R<sub>q</sub> roughness parameters for the different samples deposited with 100SCCM, 200SCCM and 500SCCM flow rate of CO<sub>2</sub>, the reference sample and the PET substrate.*

Sample	R <sub>a</sub> (nm)	R <sub>q</sub> (nm)
Sample 100 SCCM	55	82 ± 14
Sample 200 SCCM	48	72 ± 16

Sample 500 SCCM	55	84 ± 7
Reference sample	57	80 ± 11
PET	50	82 ± 9

#### 6.1.2.4 Coating composition

FTIR analyses reveal similar spectra for the samples produced with 100 and 200SCCM of CO<sub>2</sub> as shown in Figure 6-2. The trace for the sample produced at 500SCCM shows some variation as detailed below.

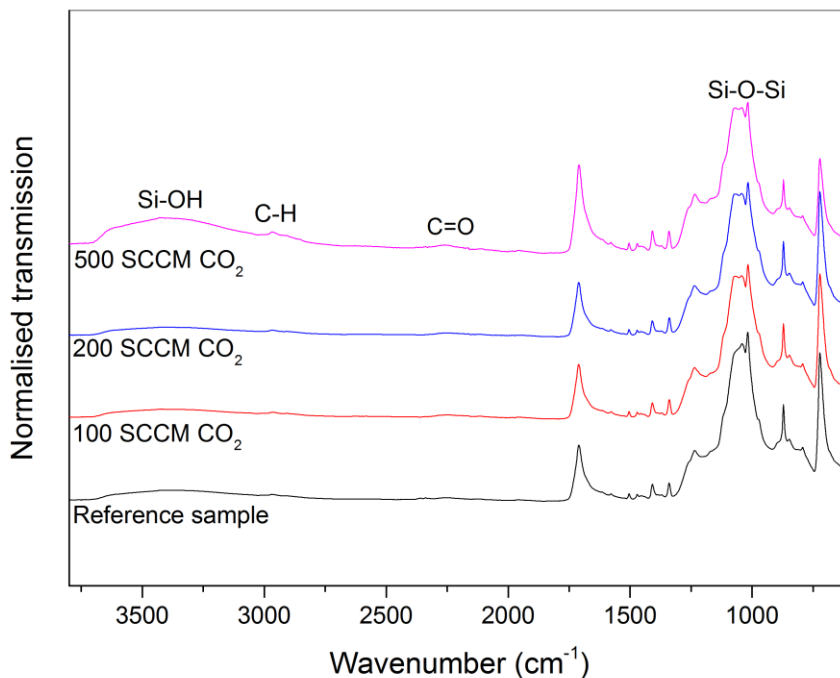


Figure 6-2 FTIR spectra of coated films produced with 100, 200 and 500SCCM of CO<sub>2</sub> injected into the plasma and the spectrum of the reference sample.

Two areas are of interest in these spectra. Firstly, the area of 800-1200 cm<sup>-1</sup> that contains some characteristic peaks of the SiO<sub>2</sub> coatings, secondly the area between 2300 and 4000 cm<sup>-1</sup> that contains complementary information about the coating.

No conclusion can be drawn from the observation of the peaks in the area 800-1200 $\text{cm}^{-1}$  as there is no obvious difference in the shapes or intensity of the peaks for the different samples.

However, a noticeable difference, appears between the high flow rate (500SCCM) and all the other samples in the region 2300-4000 $\text{cm}^{-1}$ .

As the  $\text{CO}_2$  flow rate is increased, other peaks appear, such as, C=O (in  $\text{CO}_2$ ) at 2252 $\text{cm}^{-1}$ , and C-H (in  $\text{CH}_3$ ) at 2969 $\text{cm}^{-1}$ [50]. These peaks demonstrate that the coating is becoming richer in carbon. The  $\text{CO}_2$  band is likely to be related to carbon trapped in the voids of the  $\text{SiO}_x$  [115]. Even though one could see the trend of the coating becoming more carbon rich, it can't be quantified by FTIR. Indeed, it appears that the content of carbon is very close to the detection limit of the equipment.

Other interesting features can be observed in the 2000 to 4000 $\text{cm}^{-1}$  area of the spectra. Firstly, the hydrogen bonded to the OH band, around 3400 and the adjacent peak at 2969 $\text{cm}^{-1}$  become more intense as the  $\text{CO}_2$  flow rate is increased. This can be explained by the incomplete oxidation of the Si due to partial decomposition of the HDMSO[114], and adsorption of water onto the surface[116].

In conclusion, within the detection limit of the FTIR, no major variation in composition was observed between the reference sample and the samples produced with injections of 100SCCM and 200SCCM of  $\text{CO}_2$ . Only when the  $\text{CO}_2$  flowrate was increased to 500SCCM, can one suggest there is more carbon incorporated in the coating.

### **6.1.2.5 Mechanical hardness**

The hardness of the coatings was assessed in order to understand the effect of the injection of  $\text{CO}_2$  on the coating properties. The pencil test was used based on ASTM D336305. Table 6-4 summarises the results of the hardness tests performed on samples produced with various amount of  $\text{CO}_2$  injected in the plasma.

*Table 6-4 Results of hardness tests performed on samples produced with different flow rates of CO<sub>2</sub> (pencil hardness decreases from 6H to F). The values presented are an average of the measurements carried out on 5 samples*

Sample	Cut	Gouge
Sample 1 – 100 SCCM	5H	H
Sample 2 – 200 SCCM	4H	2H
Sample 3 –500 SCCM	4H	F
Reference sample	3H	F

According to Quinn et al.[117], hardness and brittleness are related, in that that brittleness is a combination of (fracture) toughness, hardness, stiffness and elasticity. Consequently, a material that is hard, therefore rigid, will resist the load and the load will not be distributed throughout the material during indentation. This high concentration of stress in one point results in cracks.

However, these results go against George et al.'s findings[118], who found that increasing the oxygen ratio had a beneficial impact on hardness. Indeed, the results in Table 6-4 indicate that increasing the CO<sub>2</sub> content (therefore decreasing the pure O<sub>2</sub> flow rate) seems to decrease the cut hardness (i.e. a harder pencil is needed to cut the sample produced at 100SCCM of CO<sub>2</sub> than to cut the sample produced at 500SCCM of CO<sub>2</sub>) but increases the gouge hardness (i.e. a harder pencil-2H – is required to gouge the surface of sample 2, than the first pencil that gouges the surface of sample 1 –F). Nevertheless, there does not seem to be a significant variation in hardness between the reference sample and sample 3.

## 6.2 Conclusion

SiO<sub>x</sub> coatings have been produced using a plasma enhanced chemical vapour deposition method with a roll-to-roll coater. The study demonstrated that the addition of CO<sub>2</sub> into the plasma didn't affect the roughness or morphology of the coatings. On one hand, at low CO<sub>2</sub> flow rates (100 and 200SCCM); the

hardness of the coatings was increased. Those coatings were, therefore, more brittle, which lead to cracks, that are more serious on the surface of the coating. Despite the enhancement of brittleness, the WVTR appeared to decrease with the slight increase of CO<sub>2</sub> low rate to 200SCCM.

On the other hand, a significant increase of the CO<sub>2</sub> flow rate to 500SCCM caused the WVTR to double and reach 0.12g/m<sup>2</sup>/day. This could potentially be attributed to an increase of carbon content in the coating. Further coating and plasma composition analysis are required to confirm the trend observed by FTIR. Nevertheless, the coating's hardness seems to decrease at this high flow rate.

### 6.3 Investigation of injection of argon and oxygen through GPE

#### 6.3.1 Methods and materials

Another option to increase the amount of reactive species is to increase the concentration of atomic oxygen in the plasma[1]. Indeed, oxygen is injected as an O<sub>2</sub> molecule and is dissociated in the plasma in order to release some oxygen atoms that react with the silicon atoms contained in the monomer to create the SiO<sub>2</sub>-glass like coating. As O<sub>2</sub> is injected separately from the other gases into the chamber, it only dissociates through collisions with Ar and potentially [71] He. However, the machine design allows the O<sub>2</sub> to be injected through the gas purge electrode (GPE) as well. Therefore, the reference run was carried with O<sub>2</sub> and argon injected simultaneously through the GPE. Table 6-5 summarises the process parameters used.

*Table 6-5 Process parameters used to produce and the sample with injecting the O<sub>2</sub> and Ar through the GPE.*

Parameter	Value
Line speed (m/min)	1
Monomer flow rate (SCCM)	179
Oxygen flow rate (SCCM)	1100
Argon flow rate (SCCM)	120
Helium flow rate (SCCM)	150
Power (kW)	1.6

The flow rates were kept the same and the reference sample was produced immediately before the actual experiment in order to be able to compare the sample produced with the reference sample. This allows variability in the process from one day to another to be excluded.



### 6.3.2 Barrier properties

Barrier performances were measured on the Systech 7001 using a 45 minutes cycle and no re-zeroing. The results are reported in Table 6-6

*Table 6-6 Barrier performance of the reference run and sample produced with feeding the oxygen through the GPE*

<b>Sample</b>	<b>WVTR (g/m<sup>2</sup>/day)</b>	<b>BIF</b>
<b>Reference sample</b>	0.073 ± 0.001	62
<b>Test sample</b>	0.074 ± 0.034	61

The results show a limited impact of the injection of argon and oxygen through the GPE. Further investigations are required to understand the ineffectiveness of mixing the gases prior to injection in the plasma.

#### 6.4 Study on the effect of the power delivery type

As the plasma discharge is critical to the film growth, it was thought useful to investigate other means of driving the plasma than the original 40kHz bipolar power supply. It is well established that pulsing the discharge can raise the plasma (electron) temperature and, therefore create species that are more reactive. It is also an alternative to deposit more conformal and pore filling coatings[119]. Thus, an alternative power supply, which can deliver a range of driving voltage waveforms was trialed. To allow comparison between the current and voltage waveforms that were investigated, the outputs from the original PSU (Advanced Energy PEII) are shown below. This supply delivers a sinusoidal current wave and monopulse square voltage between -800 and 0V.

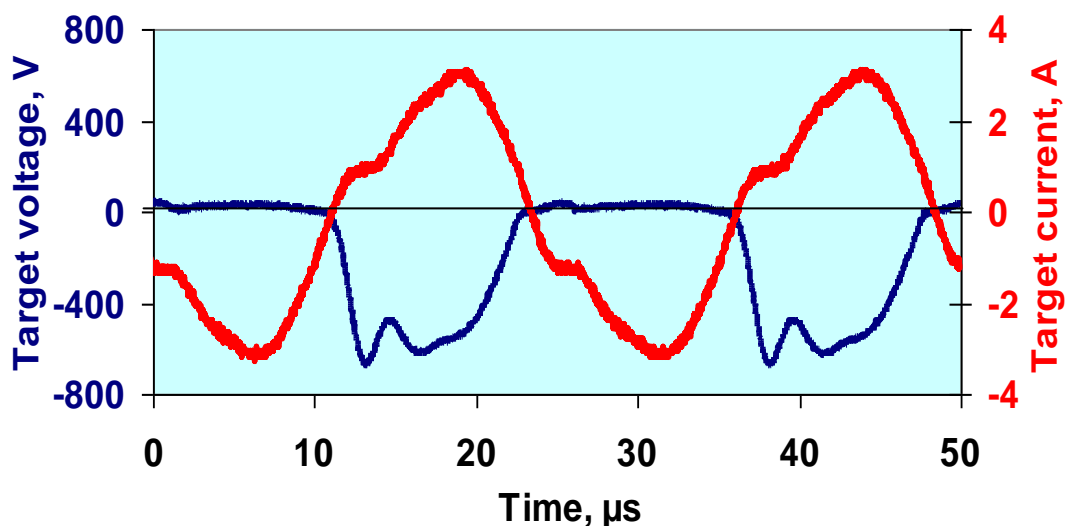


Figure 6-3 Waveform recorder on the advanced energy power supply unit.

One can observe a slight delay in reaching the intensity peak. Moreover, due to the sharp form of the top of the sinusoidal, the duration of the peak current is quite short (under  $2\mu\text{s}$ ), whereas with the square wave the current is maintained at the peak level over a longer period of time (around  $8\mu\text{s}$ ). This longer period of peak current was thought to be a factor that could promote and increase the reaction rate in the plasma-

### 6.4.1 Material and methods

The power supply unit used for this work was a TruPlasma Bipolar 4040.



*Figure 6-4 Picture of the 4040 TruPlasma power supply unit*

The module presented in Figure 6-4 allows power delivery in these mode: full-mode, bi-pulse mode, trapeze mode). Preliminary trials showed that the trapeze and bi-pulse modes were not suitable for the particular PECVD process used on the pilot coater presented in Figure 6-4. Various modes (full-mode, trapeze, bi-pulse) are available through this unit, however both trapeze and bi-pulse resulted in high instabilities of the plasma and impossibility to deposit coating (the cause of this incompatibility has not been identified).

An oscilloscope was connected to the PSU in order to monitor the waveforms and potential instabilities.

### 6.4.2 Initial work

The drum and GPE (both electrodes in the circuit) both have different resistances with respect to the ground. This caused the plasma to be unstable and enter the winding zone, which should not happen, as the pressure is lower in the winding zone than in the process zone. Therefore, an optimisation of the power was needed. Table 6-7 contains the different values tested.

Table 6-7 Power equalisation parameters investigated in full mode

Power delivered to the GPE (%)	Power delivered to the drum (%)	Process stability
50	50	Plasma arcs
75	25	Plasma arcs
25	75	Plasma stable

Even though adjusting the power, as presented in the table, helped to stabilise the process, other settings need to be adjusted, such as the ignition voltage (ignition is the short intensity peak present at the beginning of the graph that has a high intensity and short duration to ignite the plasma).

### 6.4.3 Full-mode

#### 6.4.3.1 Description of the mode

In full mode (full power mode), the delivery can be regulated by power or voltage. For the purpose of comparison with the reference runs, it was chosen to work with a fixed power. Therefore, the device itself adjusted the voltage and current. However, the equipment has a limit of +/- 1000V.

In practice, the full mode delivers a square shaped wave that is symmetrical, as shown in Figure 6-5. A rectangular wave allows the user to generate the maximum power (full power mode) in a pulse (in comparison to the maximum power available with sinusoidal waveforms). Full mode is commonly used for sputtering because it allows the user to power both cathode and anode, as opposed to the monopulse mode.

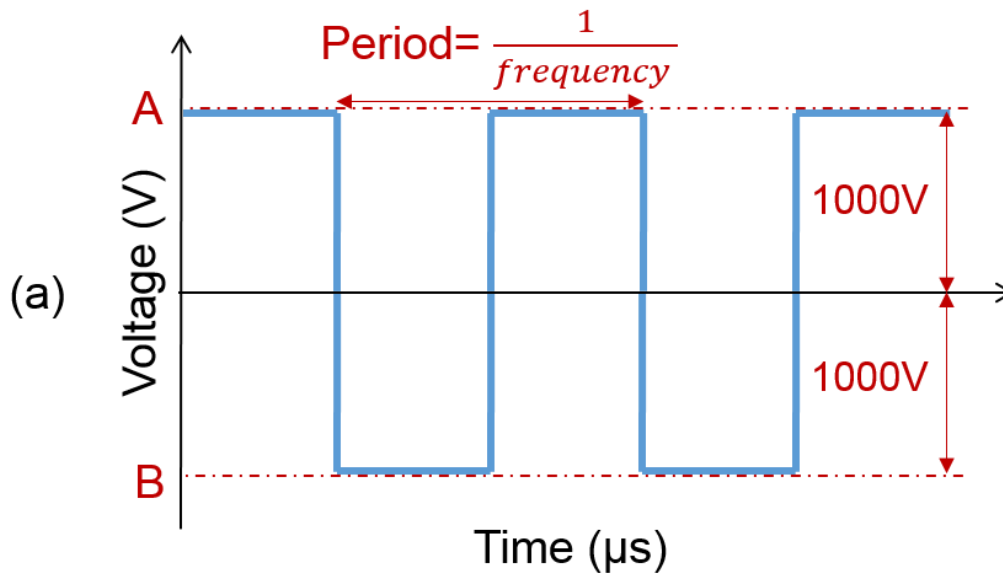


Figure 6-5 Graph representing the waveform of delivered by the PSU in Full-Mode

#### 6.4.3.2 Trials

In the first place the reference  $\text{SiO}_x$  run parameters were chosen to be run in full mode and in AC mode with the original Advanced Energy power supply unit (Section 3.1) to have a direct comparison and reference sample. Other frequencies were then tested in the range of frequencies available. Table 6-8 summarised the electrical parameters used to carry out the different investigation trials in full mode.

Table 6-8 Main electrical parameters used during the investigation of PECVD deposition in full mode with the 4040 PSU

Trial	Frequency (kHz)	Power (kW)	Current (A)	$U_{\text{rms}}$ (V)
1 (Sample 1)	40	1.6	2.8	900
2 (Sample 2)	60	1.6	2.8	910
3 (Sample 3)	80	0.9	2.2	1000

The aim was to produce samples with the same input power of 1.6kW as it showed better results in term of barrier performance on the final coatings. However, it was impossible to generate a stable plasma at 80kHz and, at this frequency; the power supply unit automatically adjusted the power down to 0.9kW to keep the voltage at the maximum level of 1000V.

### **6.4.3.3 Results**

#### **General comments**

The full mode appeared to provide a stable plasma, however it was impossible to ignite a plasma in the de-stick zone simultaneously. In full mode, the user can change the frequency from 40 to 80 kHz in 20 kHz steps. In the first place, 40 kHz was used to allow comparison with the normal working conditions of the coater. The plasma did not seem to stabilise and was jumping into the de-stick zone. The plasma in the process zone was switching off quickly and flickering throughout the run. The process specialist from Huttinger explained that it could be due to a wrong power balance between the drum and GPE (two electrodes). This balance was automatically set up by the PSU to 50%/50%. As it was not appropriate, other balances were tried and it appeared that applying 75% power on the drum and 25% on the GPE provided the most stable plasma. (Considering the capabilities of the PSU - 25 to 75% is the range available)

The plasma was much more stable and not jumping into the de-stick zone anymore. This set point was then kept constant for all the full mode trials and three samples were produced.

#### **Electrical parameters**

The electrical parameters of the system were monitored during the trials using an oscilloscope. This allowed the parameters to be adjusted if instabilities were observed. Some screenshots of the waveforms were recorded to understand the process.

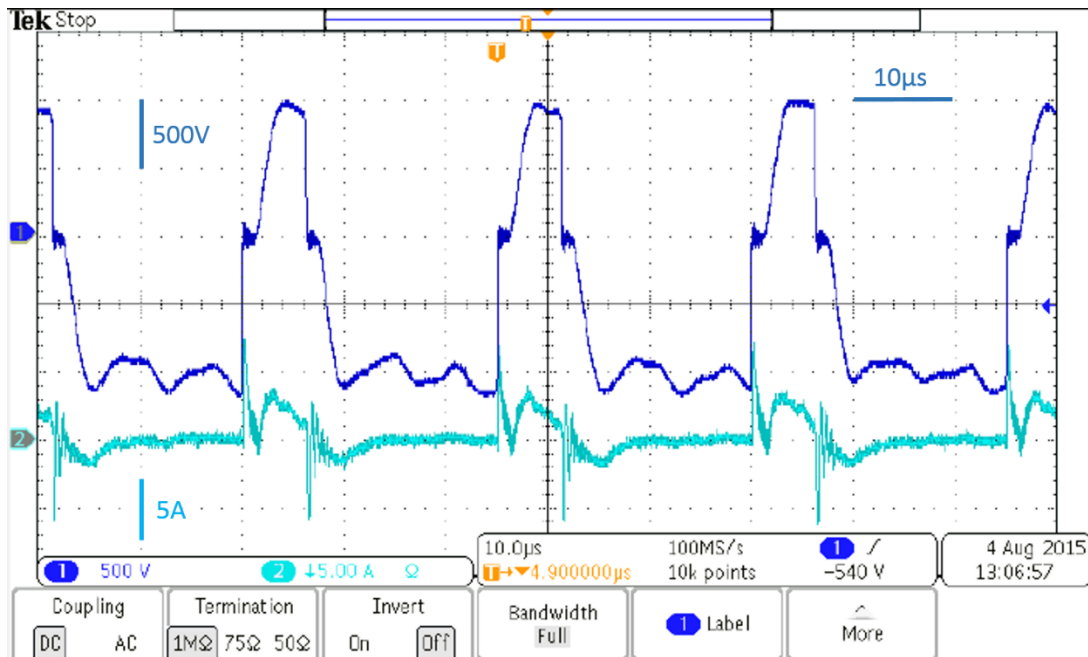
**Full Mode**

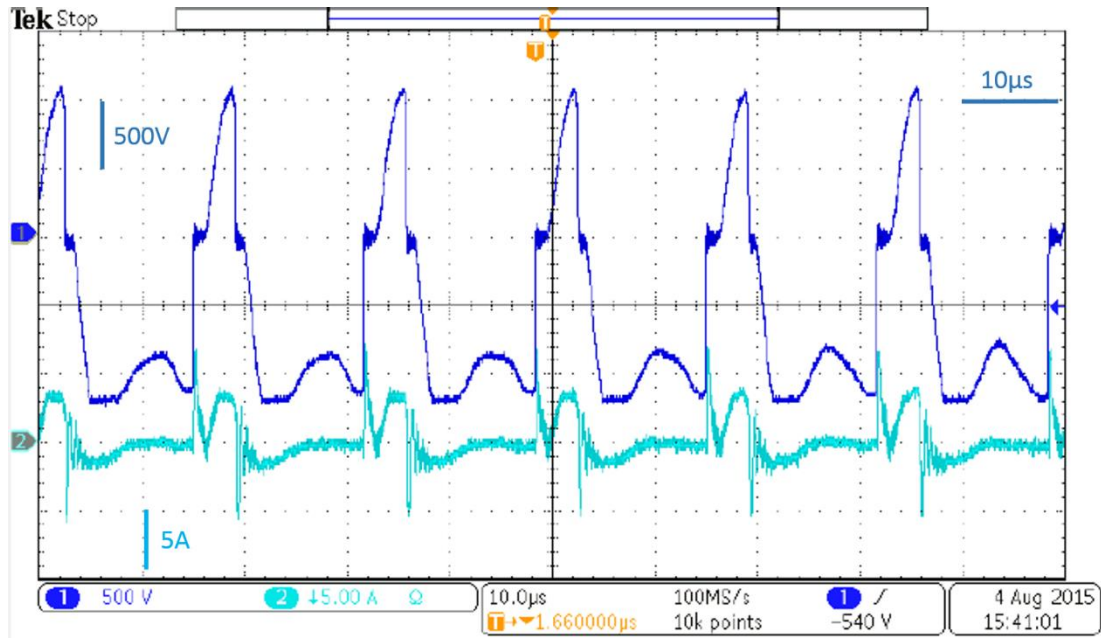
Figure 6-6 Screenshot showing waveform delivered by the PSU during the trial carried out at 40 kHz ( $U=960V$ ,  $I= 3A$ )

Figure 6-6 shows the waveform recording during the first trial in full mode. The top wave (dark blue) represents the voltage evolution over time and the bottom wave (light blue) represents the evolution of the measured current over time. It can be noted that the voltage wave is similar to the theoretical square wave expected in full mode. However, it appeared that there is a short break time between pulses. This break time has been measured to be approximately  $1.240\mu s$  before the pulse and  $1.040\mu s$  after the pulse. According to the plasma specialist[120] this break could be due to the configuration of the machine and the high difference in size between the two electrodes. Indeed, when tested on their CVD system, breaks did not appear.

- Full mode 60kHz

The waveform recorded during the second trial in full mode, as shown in Figure 6-7, exhibit a shorter peak time as expected. The break time between pulses appeared to be reduced as well in comparison to the break time observed at 40 kHz/1.6kW shown in Figure 6-6. As before, the top wave (dark blue)

represents the voltage evolution over time and the bottom wave (light blue) represents the evolution of the measured current over time.



*Figure 6-7 screenshot of the waveform recorded when running the power supply unit in Full mode at 60 kHz and 1.6kW*

Full mode, F= 80 kHz, 0.9kW, P=0.9kW,  $I_{rms} = 2.2$  A,

The waveforms were not recorded during the last trial in full mode at 80kHz.

Other modes have been investigated without success as the plasma was very unstable and no coating could be deposited.



#### 6.4.4 Barrier performances

The moisture barrier performances of the samples produced using the full mode are reported in Table 6-9.

*Table 6-9 Barrier performances of the coating deposited in full-mode at 4 kHz, 60kHz and 80kHz . Reference sample (AC Advanced Energy power supply unit)*

Sample	Frequency (kHz)	WVTR (g/m <sup>2</sup> /day)	BIF
Sample 1	40	$2.40 \times 10^{-1} \pm 0.01$	18
Sample 2	60	$2.15 \times 10^{-1} \pm 0.07$	21
Sample 3	80	$2.0 \pm 1.69$	2.2
Reference sample	40	<b>0.07</b>	62

According to the measured WVTR, increasing the input generation frequency to 60kHz has a moderate beneficial impact on the barrier properties, compared to operating at 40 or 80 kHz. Nevertheless, the barrier levels are still several times lower than the reference sample that can be produced with the standard AC 40kHz power supply unit. It is necessary to add that a thickness interference effect was noticed on the roll of samples produced at 40kHz. It was thus difficult to extract exploitable and representative samples for barrier measurement. This also can explain the variation in barrier performances. A change in coloration was also noticed on the samples produced with higher frequency. The coating appeared to become lighter in colour (from light brown to yellow) as the frequency was increased. This point needs further investigation to understand the link between the frequency and the coloration. From an industrial point of view, this method of production did not pass the qualification as a viable and suitable method as it proved to be difficult to control the process and sample quality.

### 6.4.5 Conclusions from the study

Coatings have been produced using an alternative method of delivering power through the electrodes. The aim was to assess the effect of pulsed AC delivery on the moisture barrier. A TruPlasma Bipolar 4040 was used as the alternative power supply tool. One of the key findings was the importance of balancing the power between the drum and the GPE (two electrodes) in order to sustain a stable plasma for a long period. The optimised balance was found to allow 75% of the power to go through the drum and 25% remaining power to go through the GPE. This optimised balance was attributed to the large difference in size between the two electrodes. It was found that only the full mode could be used on the particular roll-to-roll PECVD platform. Three frequencies were experimented with (40, 60, 80kHz) in this particular mode. It appeared that the WVTR was increased by a factor of almost three by using the 40kHz full mode as opposed to the standard 40kHz delivery, which means that the moisture barrier degraded. Moreover, within the same alternative delivery mode, there was a dramatic increase (by a decade) of WVTR when the frequency was increased to 80kHz. This could be attributed to the machine not being able to adapt to high frequencies. In conclusion, the alternative power delivery mode used in this study was not suitable and did not prove to be an effective method to enhance the barrier properties of the SiO<sub>x</sub> coating on PET.

## 6.5 Investigation of double sided coatings

Wuu et al.[121] demonstrated that a double sided SiO<sub>2</sub> (100 nm on each side) on polyethylene sulfonate reduced the WVTR by a factor three (from 0.31 to 0.1g/m<sup>2</sup>/day). This enhancement of the moisture barrier properties was attributed to the creation of a more tortuous pass for moisture. Indeed, the defects created in the coating (as deposited) on each sides of the substrate are not aligned and randomly located. Therefore, the path of moisture out of the coated material through the defect is not linear but rather more tortuous.

In light of this work, similar experiments were conducted at BML, whereby the PET substrate was coated on both sides. The same process parameters as were used for the reference sample were used for each side of the substrate: power, web speed, flow rates, etc. Table 6-10 presents the moisture barrier performances measured for both the double-sided samples in comparison to the reference sample.

*Table 6-10 Barrier performances of double sided coatings (Sample 01 and sample 02) compared to the reference sample*

Sample	WVTR (g/m <sup>2</sup> /day)	BIF
Sample 01	0.025	178
Sample 02	0.007 ± 0.001	643
Reference sample	0.045 ± 0.001	99

It appears clear that depositing a coating on both sides of the substrate is beneficial for the moisture barrier levels. Indeed, the WVTR had been reduced by a factor of at least two when a coating is applied on both sides. The moisture barrier on sample 02 indicated that WVTR is closer to the detection limit of the

barrier measurement equipment<sup>9</sup>. Therefore, the author would argue the accuracy of the value and consider it as a very low WVTR (lower than  $10^{-2}$  g/m<sup>2</sup>/day). A more thorough assessment of the barrier measurement showed that the measurement of low WVTR were not repeatable. It was noted that under  $10^{-2}$ mbar (which is very close to reading limit of the equipment  $5 \times 10^{-3}$ g/m<sup>2</sup>/day) the reading varied between  $5 \times 10^{-2}$ g/m<sup>2</sup>/day and a zero reading. This could be due to the accuracy of the sensor in the lower part of the measurement range. The accuracy could explain the difference in barrier performances.

---

<sup>9</sup> An assessment of the equipment has demonstrated that WVTR was not measured accurately in the lower end of the scale (under 0.01g/m<sup>2</sup>/day). The measurements were not repeatable.

### 6.6 Investigation of different substrates

The influence of the substrate quality on the ultimate barrier properties of the products is a controversial topic. Although PET substrates are relatively inexpensive, their semi-crystalline and rough nature can limit the moisture barrier properties. This has been studied and it was demonstrated that both the roughness and the presence of antiblock particles lead to low adhesion and strain induced micro/nano defects (cracks, porosity)[86, 108, 122]

Further investigations have shown barrier levels on PEN substrates [101, 105] in the region of low  $10^{-4}$ g/m<sup>2</sup>/day.

Therefore, an investigation was carried out to determine whether the method used by the industrial partner was sensitive to the substrate type. In order to achieve that, coatings were applied to different PEN substrates and the barrier properties and coatings properties were studied.

#### 6.6.1.1 Polymer substrates

The aim was to compare the role of the substrate type (i.e. treatment, planarization, thickness, etc.) on the moisture barrier of SiO<sub>x</sub> (PECVD) coated samples.

Various substrates were supplied by DuPont Teijin Films in A4 sheet format. Table 6-11 states the films that have been used and their main properties. All the base films exhibit a very high transparency (above 90% transmission of light in the visible).

Table 6-11 Summary of the technical data of the substrates used for the study

Type	Name	Thickness	WVTR (g/m <sup>2</sup> /day)	Comment
PEN	Teonex PQA1	125	1.35 <sup>10</sup>	One side planarised (coated)
	Teonex Q65HA	125	2	one side treated for adhesion (heat stabilised)
	Teonex Q65FA	125	1.3	Heat stabilised
PET	Melinex ST504	125	4	Plain surface and adhesion treated side
Standard PET	Standard substrate	120	4.5	Reference substrate, non planarised, non- treated

#### 6.6.1.2 Deposition method and details

SiO<sub>x</sub> deposition was carried out by PECVD on the pilot roll-to-roll coater (in Bobst Manchester Limited). The A4 sheets were spliced into the carrier web (125µm PET Jindal J500). This allowed coatings to be deposited on both the carrier web and on the A4 DuPont Teijin Films samples using the same

<sup>10</sup> Measured in BML (the other information come from the technical data sheet provided by DTF)

conditions. Table 6-12 indicates which side of the DuPont Teijin Film substrates was coated

*Table 6-12 Table indicating which side was coated for each DTF film used*

<b>Base substrate</b>	<b>Coated side</b>
<b>Teonex PQA1</b>	Planarised side
<b>Teonex Q65HA</b>	Adhesion side
<b>Teonex Q65FA</b>	Heat stabilised PEN
<b>Melinex ST504</b>	Adhesion side

The Teonoex PQA1 is claimed to be a smooth defect-free polyethylene naphthalate (PEN) material suitable for electronic applications. One side is planarised and the other is not treated.

Teonex® Q65HA is highly transparent and smooth surface substrate that is pre-treated for adhesion on one side. This side was chosen as the side to be coated. DTF states it is tailored for flexible electronics applications (OLED, PV cells) and has excellent heat stability.

TEONEX® Q65FA is a highly transparent heat stabilised unfilled polyethylene PEN. One side is heat stabilised and the other one has no treatment.

It was particularly difficult to obtain a stable micrograph as the surface was charging under the effect of the SEM's electron beam. This effect was more difficult to overcome on the planarised side (side A).

The Melinex® ST504[123] is a crystal clear, high gloss, heat stabilized polyester film. DuPont Teijin states that it can be overprinted with a wide range of solvent-based graphic inks and varnishes, silver conductive and dielectric inks. It is ideally suited for graphic and certain circuitry layers in membrane touch switches. Melinex® ST504 is pre-treated on one side to promote

adhesion. SEM micrographs were taken on both sides of the substrate prior to coating; they are presented in Figure 6-8.

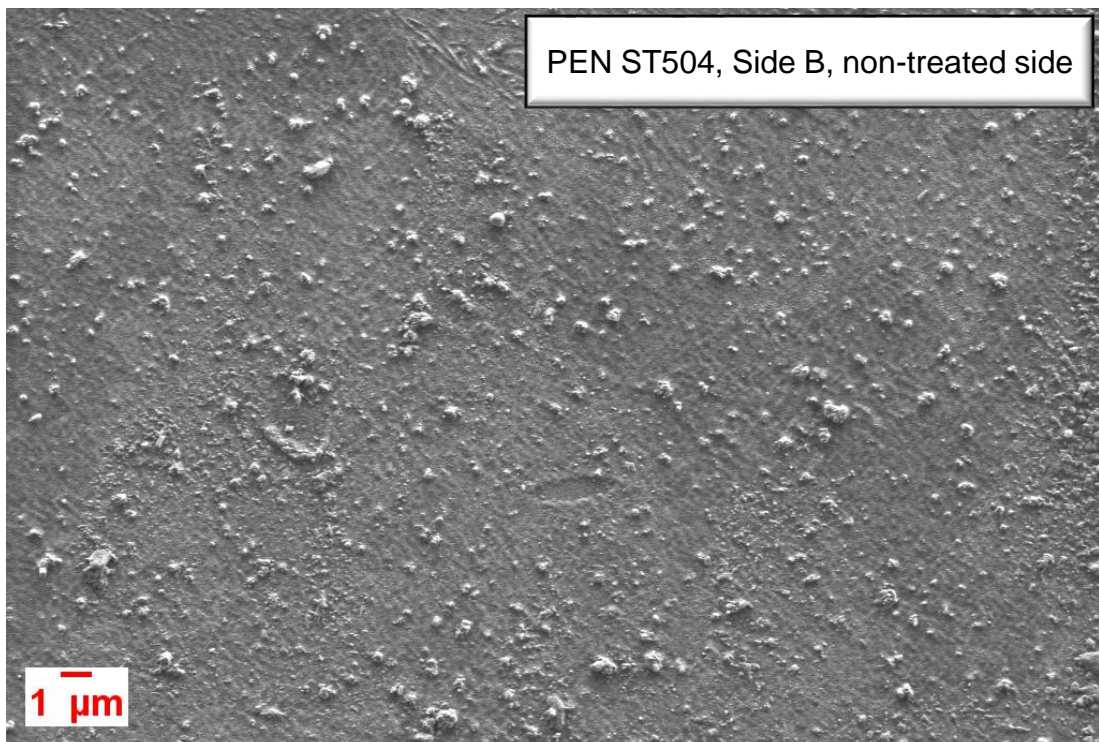
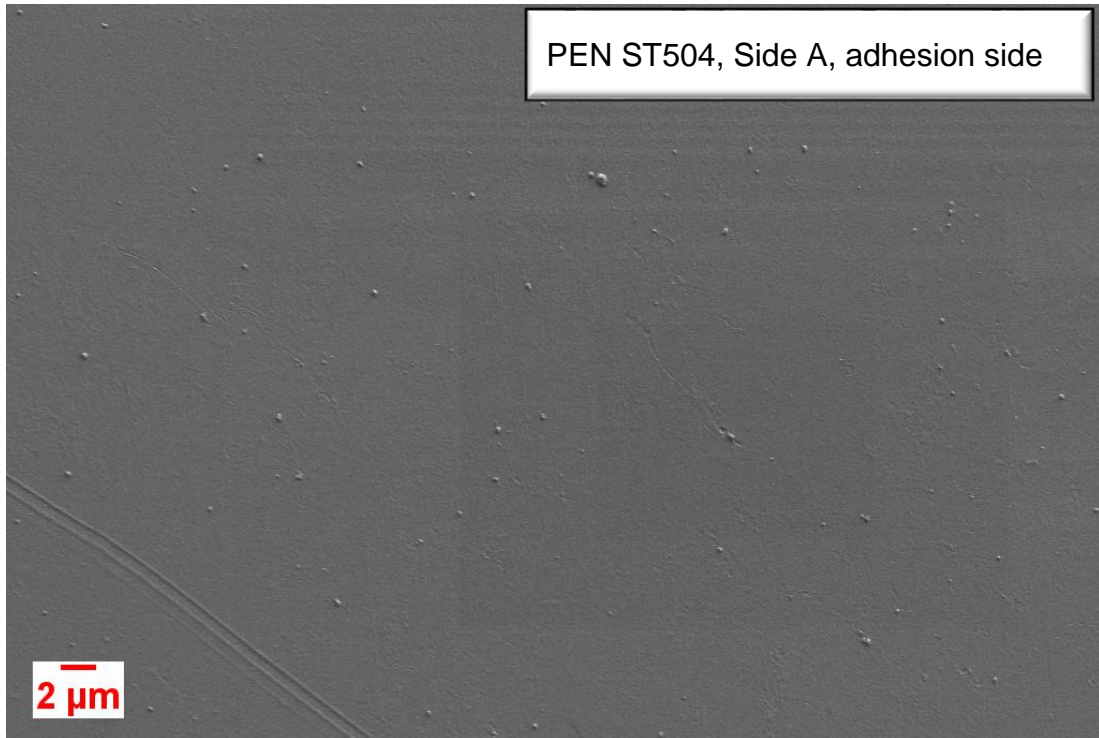




*Figure 6-8 SEM micrographs of the surface of the substrate DuPont Teijin Film ST504, Side A is the planarised side B and Side B is the surface treated for adhesion*

Figure 6-8 shows that the adhesion side (Side A, to be coated with SiO<sub>x</sub>) of the substrate appear relatively uniform and smooth except certain damaged rough regions. In comparison, the other side of the material presents particles and a high apparent roughness.

### **6.6.2 Coating topography**

SEM investigations were carried out on some of the coated materials to understand the impact of the substrate's surface properties on the topography of the coating.

It was found that the coating was deposited relatively conformally to the morphology of the substrates surface.

Figure 6-9 shows micrographs of the planarised and non-treated side of the substrate PQA1 and the SiO<sub>x</sub> coating deposited onto on the planarised side.

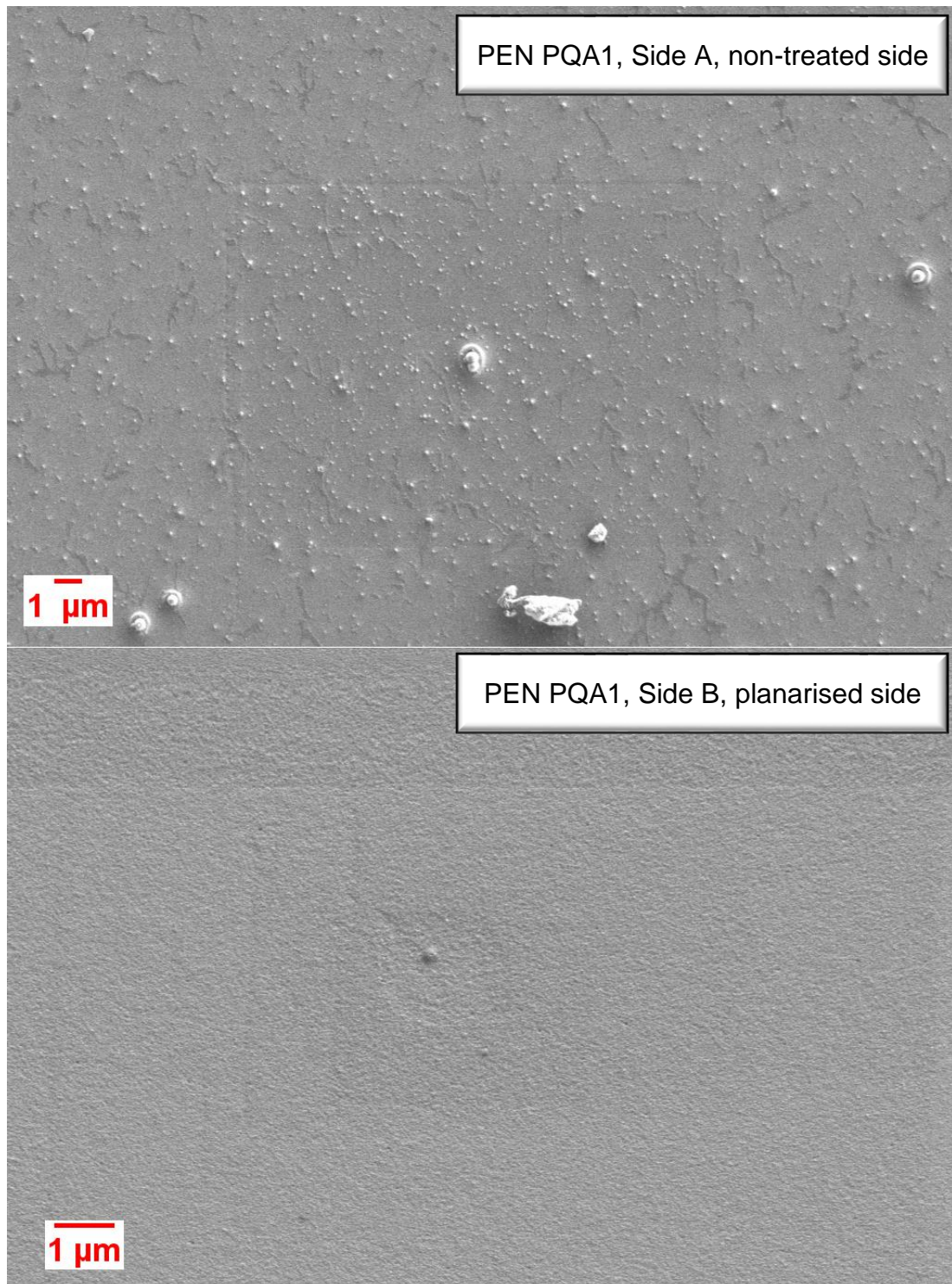


*Figure 6-9 SEM micrographs of both sides (coating on planarised side A) and non-planarised (Side B) of the base substrate PQA1 and the coating deposited on the planarised side.*

It clearly appears that the planarised side is smoother and more uniform which leads to uniform coating. However, it seems like the coated material presents

more rounded particles of various sized on the surface. These particles might originate from several sources:

- the monomer that reacted in the gas phase and deposited as such on the be contamination during handling of the film that was coated in the process
- particles that migrate from the bulk of the substrate
- contamination transferred from the back of the substrate ( the A4 sheets were not cleaned before they were spliced up in the coater

The analysis of these particles was difficult to the size of the probe (in the SEM) resolution was around  $2\mu\text{m}$ .

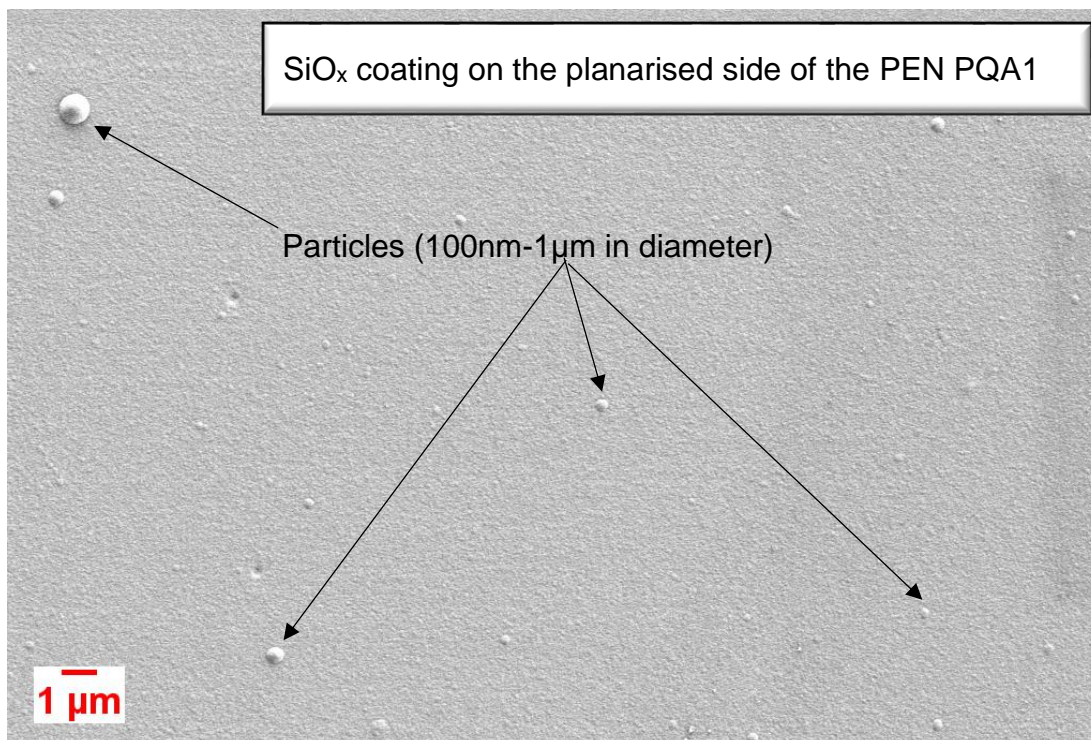


*Figure 6-10 SEM micrograph of the SiO<sub>x</sub> coating applied onto the planarised base substrate (Side A coated)*

If one considers the adhesion treated side of the substrate PEN PQA1 coatings are consistent from one substrate to another, it is expected that the resulting topography of the coated material should be relatively conformal to that of the base substrate. This appeared to be true from the coating deposited on adhesion side of the Teonex® Q65HA as shown in Figure 6-11.

On the other hand, it has been observed that the coating deposited on the adhesion side of the PEN Q65HA (Figure 6-11) is apparently rougher than on the PQA1 (Figure 6-10) and has a granular aspect.



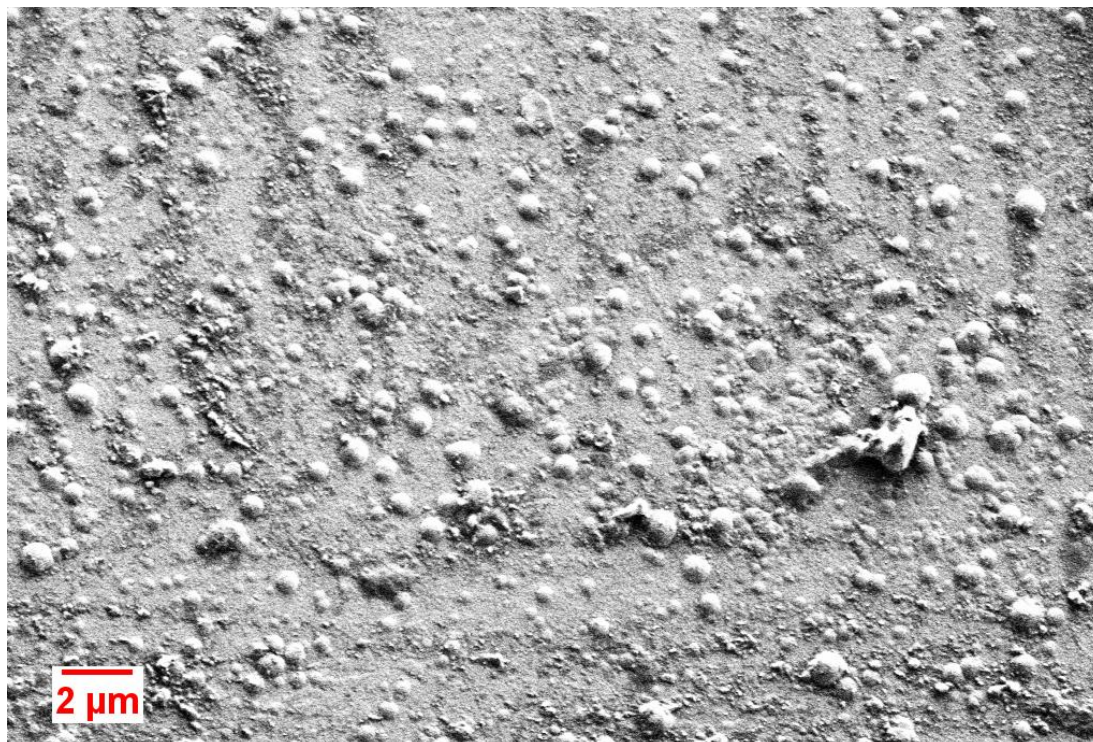


*Figure 6-11 SEM micrograph of the SiO<sub>x</sub> coating deposited onto the Teonex® Q65HA*

The particles present on the surface seem to have similar sized and distribution in Figure 6-10 to that of the adhesion side of the substrate (similar to the surface presented in Figure 6-8, except that their number is higher on the coating than on the base substrate). This apparent roughness and defects are a potential barrier performance-limiting factor. The origin of this roughness has not been identified, but one can think that the chemical (not disclosed by the manufacturer) used to treat this side of the substrate might interact with the SiO<sub>x</sub> and create a different solid phase on the surface. This could explain the slight discolouration.

### **6.6.3 Barrier performances**

Barrier performances were measured with the Systech 7001 at 90% RH, and 37.8°C. Table 6-13 summarises both WVTR measured on the DTF coated substrates and the associated barrier improvement factors. This table also contains barrier data of the reference SiO<sub>x</sub> coatings deposited onto the commodity grade PET.

Table 6-13 Barrier performances and barrier improvement factor of the coated PEN films (DTF) and the commodity grade PET

Substrate	WVTR (g/m <sup>2</sup> /day)		BIF
	Substrate	SiO <sub>x</sub> /substrate	
PEN Q65FA	1.3	$2.34 \times 10^{-2} \pm 0.0036$	55
PEN PQA1	1.35	$2.1 \times 10^{-2} \pm 0.006$	28
PEN Q65HA	2	$3.7 \times 10^{-2} \pm 0.029$ <sup>11</sup>	63
PET ST504	4	$3.8 \times 10^{-2} \pm 0.0$	104
120µm PET Jindal	4.5	$5.2 \times 10^{-2} \pm 0.00$	85

In the first place, it can be noted that the barrier performances (WVTR only) are enhanced when using a planarised or treated film rather than a plain non-treated substrate (PET). The best barrier performances are obtained for the coating deposited on the adhesion side of the Q65FA and the planarised side of the PQA1. The barrier levels of coated PENs are relatively similar once the error is considered. Therefore, it is difficult to attribute the barrier enhancement to the planarisation of the substrate.

However, the barrier improvement factors, which indicate the relative performance of the overall sample in comparison with the base substrate, tend to show that the barrier performances have been further enhanced in the case of the ST504 in comparison to the standard PET.

<sup>11</sup> Error is less than 0.002, same for PET.

The highest BIF is obtained on the coated ST504 film, which exhibit similar base film barrier properties as the commodity grade PET (i.e.  $\approx 4 \text{ g/m}^2/\text{day}$ ).

### **6.6.4 Summary of the study**

Silicon oxide moisture barrier layers have been deposited onto various PEN/PET substrates in order to assess the influence of the substrate type and quality on the final barrier performances of the material.

The early results shown an enhancement of the barrier when the coating is deposited onto a planarised or/and treated surface of PEN in comparison to the commodity grade PET. The WVTR is decreased by a factor two and more when the coating is deposited onto a planarised or treated surface. The lowest WVTR measured was  $2.1 \times 10^{-2} \text{ g/m}^2/\text{day}$  on the planarised substrate (PQA1). The best improvement of barrier as comparison with base substrate WVTR was achieved with the ST504 when the coating was deposited on the surface treated for adhesion.

Altogether, it appeared that optimising the quality of the surface onto which the coating is deposited is necessary to reach another level of barrier than that reached on the standard PET.

### **6.7 Investigation of design of the machine**

Modifying or optimising the process can also be done by tailoring the design of the machine. Indeed, it has been proven in plasma processing that the design might be critical to the efficiency[111]. Different aspects can be considered from the position of different elements like the magnetic array, to the cleanliness of the environment[111]. Some of these areas have been investigated and the results are reported in this section.

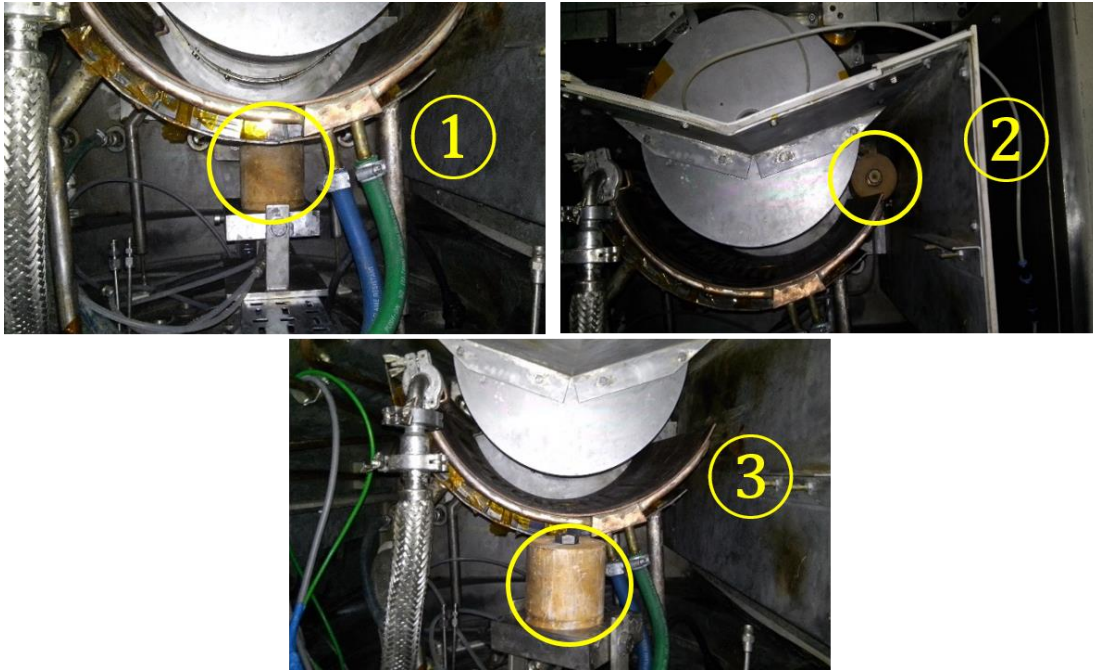
#### **6.7.1 Internal parameters: modification of the GPE position**

##### ***Experimental details***

The first element that was looked at was the gas purge electrode, which delivers the argon in to the chamber. It was thought that bringing the GPE closer to the drum would be beneficial for stability and densification of the plasma.

Therefore, samples were produced with the GPE in three different locations in the chamber. Due to a limited amount of space in the process zone and the relatively big size of the GPE, only three positions were possible. These locations of the GPE are circled in Figure 6-13





In addition, detailed in Figure 6-12.

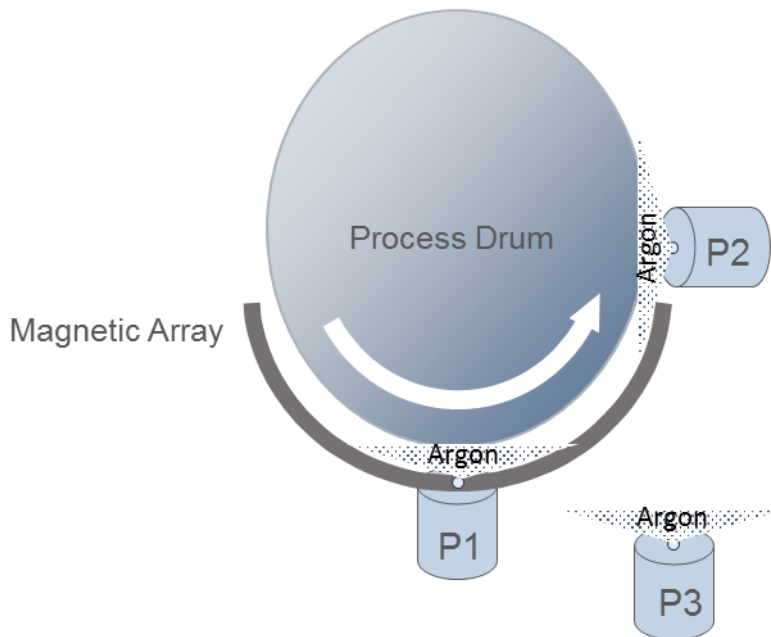
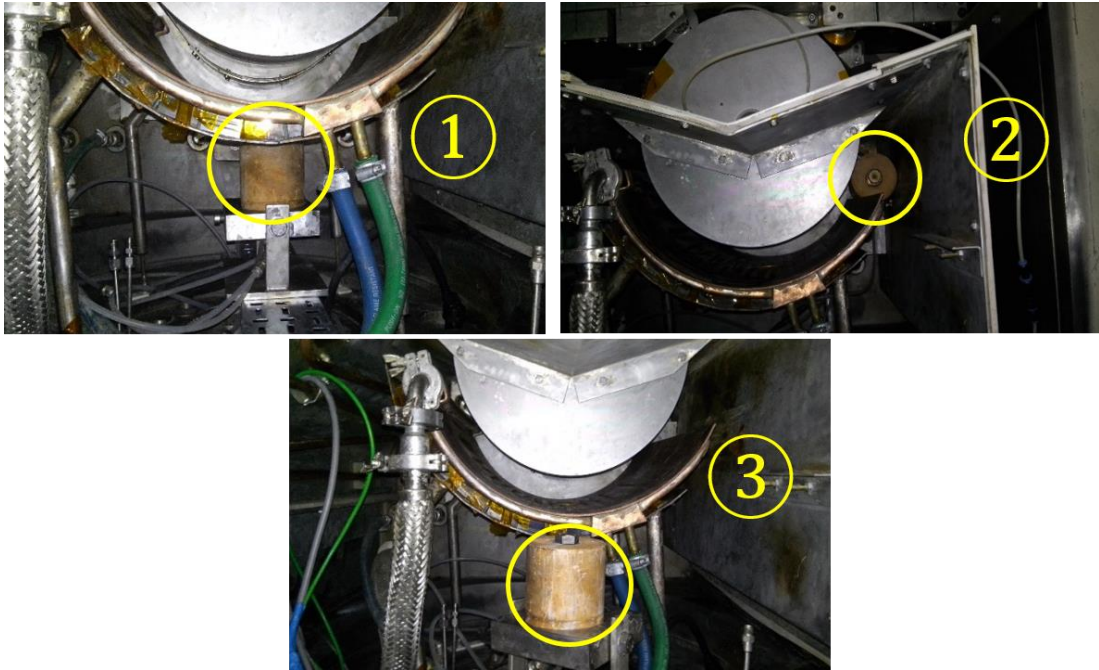


Figure 6-12 Schematic showing the three GPE experimental positions



*Figure 6-13 Photograph showing the location of the GPE on the process zone for different experiments. Positions referred as 1, 2 and 3.*

Table 6-14 Detail of the locations number and name

Location number	Location name
P1	Under the magnetic array
P2	Drum exit position
P3	Bracket door

### **Barrier properties**

Table 6-15 shows the WVTR measured for the samples that were produced using the GPE respectively under the magnetic array, at the exit on the drum, and in bracket of the process zone door.

Table 6-15 Barrier performances of coatings produced with various GPE positions

Position	WVTR (g/m <sup>2</sup> /day)	B.I.F
P1 (under mag array)	0.09 (0.088)	48
P2 (drum exit position)	0.08	54
P3 (bracket door)	0.08 ± 0.02	53

According to the measurements, the position has a limited effect on the barrier. These measurements are within the error of the barrier equipment; therefore, no conclusion can be drawn. Nevertheless, the plasma appeared more stable (fewer arcs) when the GPE was located under the magnetic array. This configuration was therefore adopted as a new standard for the all the trials. (results from Chapter 5 and 6).

### 6.7.2 External parameters: dust and cleanliness management

#### *Experimental details*

Contamination occurring in the process can compromise the integrity of the barrier layer [63]. This is mainly due to the debris giving rise to pinholes in the coating. [124] One of the main consequences of contamination on the substrates is the decrease in adhesion of the coating on the substrate. Contamination can come from grease, dust and dirt[125].

In the case of PECVD vacuum processes, it has been noticed that the main source of contamination was dust, especially when the coater is in a factory environment without an air cleaning system. In order to address the dust contamination, the simplest method was to remove the contamination from the substrate prior to coating.

Different rollers were implemented in different areas of the coater. One roller (provided by System Division Incorporation, SDI) was placed close to the drum on the side of the film to be coated prior to plasma exposure (Figure 6-14).

The roll was taken out in between runs to be cleaned with a tacky roller.



*Figure 6-14 Roller located before the drum to clean the substrate before being exposed to the plasma.*

The second set of cleaning rollers is constituted of a Teknek elastomer rubber and an adhesive roller (the product name is Simco-Ion's and was commercialised by Teknek[126] to be used to clean and eliminate particles larger than 300nm. It was located in the rewind zone prior to the roll of coated film (Figure 6-15) in order to remove the contamination prior to rewinding the film. In this case, a tacky roller meets the polymer substrate, the debris stick to the roller and are removed from the surface. A second high-tack roller is used to remove the debris from the first tack roller. The tack rollers are silicone-free hence they will leave no residue on the substrate.



*Figure 6-15 Cleaning rollers positioned in the rewind zone before the rewind roller.*

### 6.7.2.1 Barrier performances results

Table 6-16 presents the moisture barrier performances measured on samples produced using the dust management rollers mentioned above as compared to the samples produced without the cleaning system.

It appears that moisture barrier is decreased (WVTR increased) when using dust-cleaning rollers. This effect could be explained by smaller particles being imparted on the coating by the tacky roller that was located prior to the drum due to insufficient cleaning (after a certain length of coating). The tacky roller would then be increasing the contact with these particles with the coating, and therefore creating pinholes. Moreover, the set of tacky roller could be better position behind the substrate on the uncoated face in order to remove the debris and contamination on this side of the material which were likely to damage the coated surface of the following rewind layer (backside)[127, 128].

*Table 6-16 Barrier performances of samples produced without the dust cleaning rollers (Coating 01) and with the dust cleaning rollers (Coating 02)*

Sample	WVTR (g/m <sup>2</sup> /day)	BIF
Coating 01	$3 \times 10^{-2} \pm 0.012$	168
Coating 02	$5 \times 10^{-2} \pm 0.002$	82

### 6.7.3 Conclusion of the study

As a step to control the process, it was necessary to understand the impact of some internal and external factors on the coatings and process.

As far as internal parameters are concerned, the main area of improvement being the plasma, different GPE positions were trialled to improve the plasma stability and density. The main results showed that WVTR was not sensitive to the position of the location of the GPE inside the process zone.

Among the available external variables, dust and contamination are known to be critical for nanosized coatings. One way to control and manage dust in the industry is to use adhesive roller to clean the web prior and post coating. This method of cleaning has been experimented by implementing a roller before the drum and a roller in the rewind zone (prior to rewind roller). At first glance, the WVTR seemed to increase from  $3 \times 10^{-2} \text{ g/m}^2/\text{day}$  to  $5 \times 10^{-2} \text{ g/m}^2$  with the addition of an adhesive roller. These results could be attributed to the tacky roller removing coated material which would then damage the following surface in contact with the tacky roller if the cleaning of the tacky roller is not efficient enough. This coated material could be covered with some coated oligomer with poor adhesion to the bulk of the coating.

## **7 TOP COATS AND HYBRID COATING**



### ALD top coats

Atomic layer deposition is a method used to deposit highly dense and conformal coatings onto highly textured substrates that can contain features with high aspect ratios. This method is precise and can be used to fill nanopores. Therefore, it was thought to be the adequate technique to densify the porous  $\text{SiO}_x$  coating. Moreover, several groups have managed to produce high barrier/low WVTR coating on polymer substrates using ALD[129]. It can also be used to produce an inorganic  $\text{Al}_2\text{O}_3$  layer constituting the inorganic/organic multi-barrier coating [13, 130][129]. ALD also fits perfectly into the scope of flexible electronics as it is a suitable technique to produce flexible solar cells a reporter by van Delft and co-workers.[131]

#### 7.1 Experimental details

ALD is based on self-limiting surface chemical reactions. This is achieved by growing a monolayer of  $\text{Al}_2\text{O}_3$  using the precursors  $\text{Al}(\text{CH}_3)_3$  and  $\text{H}_2\text{O}$  by a simple ligand exchange mechanism.

The following sketches illustrate the mechanisms of the different steps occurring in ALD of  $\text{Al}_2\text{O}_3$ .

Prior to any coating, the surface is functionalised and covered by the adsorption of layer of hydroxyl species, OH (ads.) is illustrated in Figure 7-1.

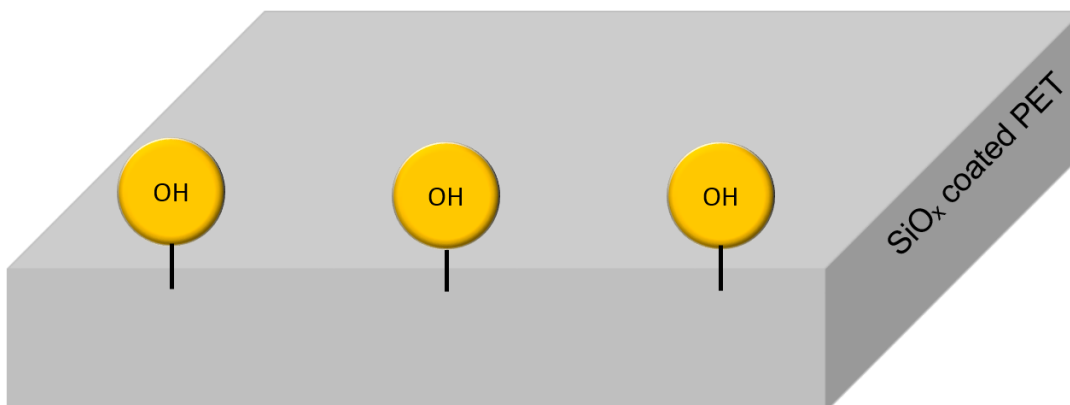


*Figure 7-1 Schematic representing the surface prior to ALD when the OH are adsorbed onto the surface*

The first half-cycle consists in introducing the aluminium based monomer precursor. It will absorb  $\text{Al}(\text{CH}_3)_3$  (ads) onto the surface as illustrated in the sketch in Figure 7-2.

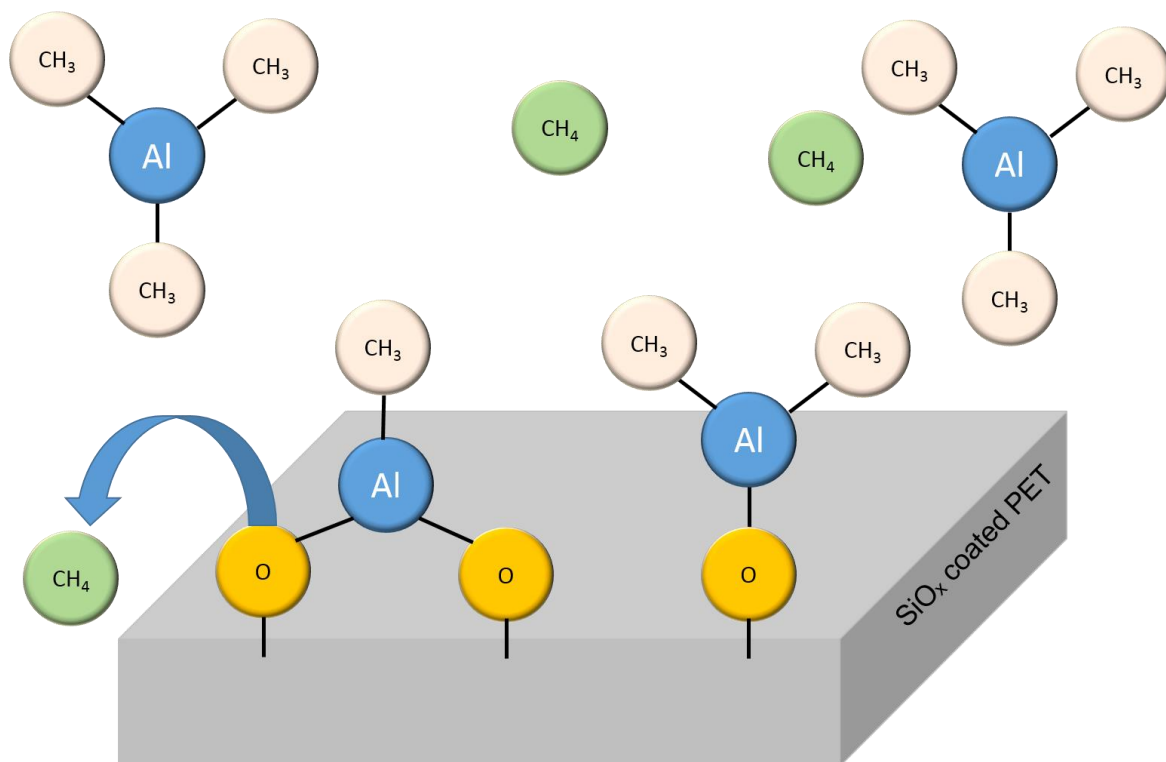


Figure 7-2 Schematic and equation describing the reaction occurring during the first half-cycle of the deposition of  $\text{Al}_2\text{O}_3$  via ALD

The adsorbed layer of  $\text{Al}(\text{CH}_3)_3$  prevents more  $\text{Al}(\text{CH}_3)_3$  from adsorbing, which is a key step in the self-limiting growth mechanism.

The sample is then purged to flush away any excess of  $\text{Al}(\text{CH}_3)_3$ . This is achieved by introducing more of the first precursor into the chamber (Figure 7-2). Following the purge, the sample is ready for the second half of the ALD cycle whereby  $\text{H}_2\text{O}$  is introduced to react with the adsorbed  $\text{Al}(\text{CH}_3)_3$  and form the  $\text{Al}_2\text{O}_3$  layer.

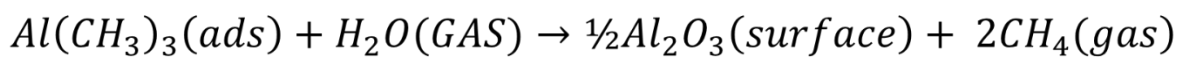
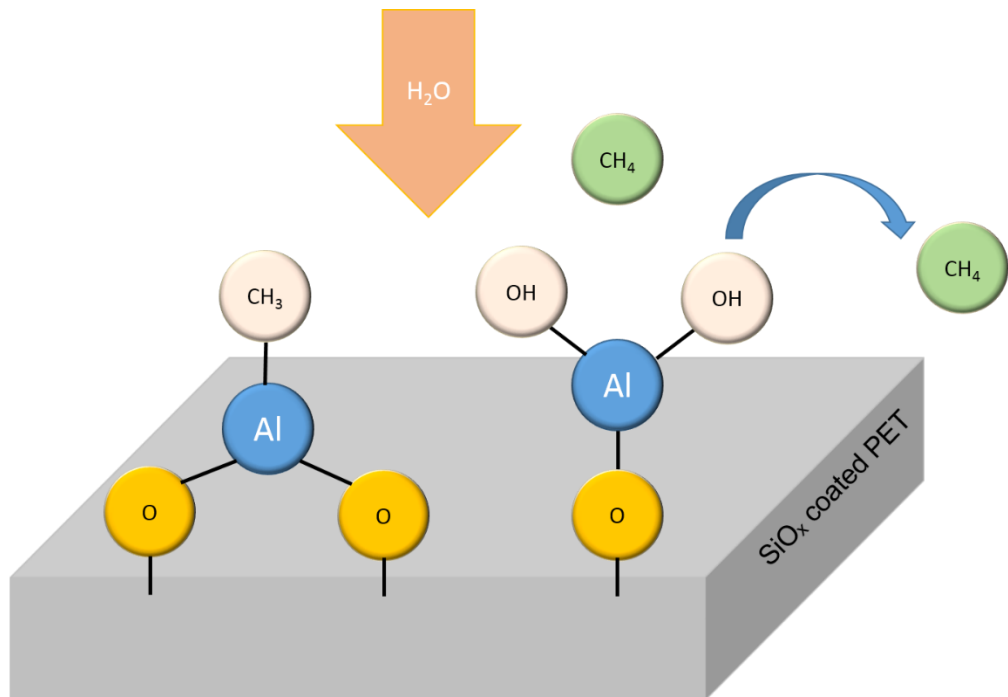


Figure 7-3 Sketch and equation illustrating the second part of the half cycle of deposition of  $Al_2O_3$  by ALD

An additional final purge step is often added to pump away the remaining unreacted TMA molecules. (Incorporation of TMA, because two molecules of TMA won't react together).

## 7.2 Results

The sample coated was chosen for its high WVTR, to evaluate whether the topcoat would provide further barrier improvement. The process parameters will not be reported.

A layer of  $Al_2O_3$  was applied onto  $SiO_x$  coated 120 PET (10cm<sup>2</sup> samples). The moisture barrier proper was measured prior and post topcoat and are reported in Table 7-1.

## 7 Top Coats and Hybrid Coating

---

Table 7-1 Barrier performances of the SiO<sub>x</sub> coating with and without Al<sub>2</sub>O<sub>3</sub> topocoant

Sample	WVTR (g/m <sup>2</sup> /day)
SiO <sub>x</sub> /PET	0.15
AL <sub>2</sub> O <sub>3</sub> /SiO <sub>x</sub> /PET	Above detection limit (displaying 0)

The topcoated samples exhibited lower WVTR than the detection limit (within the error) than the SiO<sub>x</sub> coating alone. This first result, needs, however to be confirmed.

According to the results presented above ALD topcoat is an adequate technique to be used to further enhance moisture barrier properties and should therefore be used in complement to PECVD.

## **8 CONCLUSIONS AND OUTLOOK**

The work presented in this thesis investigates and discusses the deposition of transparent  $\text{SiO}_x$  moisture barrier coatings onto polymer films (with the focus placed on BO-PET web) for electronic encapsulation. The coatings were produced on an industrial pilot-scale roll-to-roll coater using the plasma enhanced chemical vapour deposition method.

The coated films, as well as the uncoated substrates, were characterised in terms of barrier performance, surface topography, coating composition, coating adhesion, coating thickness and optical properties, using a range of analytical techniques. Furthermore, the effects addition  $\text{CO}_2$  as a reactive gas, alternative AC square wave power delivery, dust management via the implementation of adhesive rollers, varying the substrate type and acrylate and  $\text{Al}_2\text{O}_3$  ALD topcoats on the barrier properties of the  $\text{SiO}_x$  barrier layer were investigated.

The water vapour transmission rate of the  $\text{SiO}_x$  coated polymer films are on the coating structure, i.e. the coating's porosity; the less porous the  $\text{SiO}_x$  coating, the better will be the resulting barrier performance. The porosity could originate from polymerisation occurring in the gas phase instead of at the surface of the substrate. This type of polymerisation was found to happen at low input power and high oxygen:monomer ratios. The investigation of the surface topography at different magnification levels revealed that for all film substrates the  $\text{SiO}_x$  barrier layer replicated the underlying plain film surface topography, including defects, such as antiblock articles. The coating composition in the case of  $\text{SiO}_x$  layers was determined to be predominantly affected by the oxygen:monomer ratio. Indeed, a stoichiometric  $\text{SiO}_2$  with residual carbon could be produced at a ratio of about 2. The numerous small defects, such as pinholes observed by calcium test, were identified as barrier limiting factor. They confirm the high porosity of the coating.

As mean to address the porosity, pore filling by ALD topcoat and defect coverage with double-sided coating were attempted. Both methods resulted in a significant improvement in barrier performances, whereby the WVTR was beyond measurement limit (measuring 0) on the  $\text{Al}_2\text{O}_3/\text{SiO}_x$  coating and in the

between  $2 \times 10^{-3}$  and  $7 \times 10^{-3} \text{g/m}^2/\text{day}$  for the double-sided coating. Acrylate topcoat were also investigated and the WVTR was not increased on the topcoated  $\text{SiO}_x$  barrier layer, most likely due to a lack of adhesion of the acrylate topcoat on the  $\text{SiO}_x$  coating.

As the lowest WVTR obtained in standard process conditions was  $5 \times 10^{-2} \text{g/m}^2/\text{day}$  on BO-PET, several other routes were taken in order to reach the WVTR target. One route consisted in injecting  $\text{CO}_2$  into the chamber along with  $\text{CO}_2$  along with  $\text{O}_2$ . Injecting  $\text{CO}_2$  had a very limited impact on the barrier as the WVTR was only slightly decreased for low  $\text{CO}_2$  flow rates. Moreover, such deposition conditions seemed to have increased the brittleness of the coating leaving serious cracks on the surface. High content of  $\text{CO}_2$  caused the increase of WVTR by a factor two.

$\text{SiO}_x$  coatings on different polymer substrate with planarised and adhesion treated layers showed a decrease in WVTR by a factor two in comparison to the same barrier layer deposited on the standard PET. The change in surface topography and the absence of antiblock particles on the surface of the surface led to better growth of the coating and a more uniform coating.

Several other changes were made on the platform in order to stabilise the process, which could have led to more repeatable and consistent results. For instance, the position of the counter electrode was altered to increase the density of the plasma. The magnetic array was baffled to isolate the plasma and adhesive rollers were implemented to improve the cleanliness of the substrate prior to deposition and that of the coating prior to rewinding. WVTR has been found to be relatively insensitive to the counter electrode position and the implementation of the adhesive roller but very sensitive to the confinement of the plasma in between the magnetic array and the drum.

### 8.1 Future work

With respect to future work, several areas of improvement are identified.

In the first place, a systematic and quantitative study of the WVTR would be needed to confirm the early results. In order to do that, the various trials should be repeated and analysed before drawing any definite conclusions.

Then, it would be very useful to collect some data on the actual composition of the plasma during the process to clarify the deposition mechanisms and identify the changes occurring in the plasma during instabilities or unexpected events such as arcing. This would lead to a better understanding of the defects observed on the coating (i.e. pigmentation, volume polymerisation, porosity, dark and clear regions). The basic experiments could, then, be repeated and analysed from the plasma chemistry point of view. On the other hand, physical aspects of the plasma could be altered to enhance and densify it. In this case, altering the design, number or type of magnets (i.e. stronger magnets, such as rare earths) could be investigated. Additional GPEs in the shape of a GPE bar could be implemented to provide a wider and uniform stream of ionised gases from the counter electrode. Infrared heaters are also an interesting element to add at the entrance of the process zone in order to desorb the potential moisture trapped in the substrate. This moisture might have an effect on the nucleation of the coating on the substrate.

The chemical route could also be explored. For instance, other monomers could be used. Amongst the possible chemicals could be hydrophobic monomers such as PCF6 and metacrylated silanes.

On the coating analysis side of the work, a more comprehensive research is to be carried out on the suitable method to measure thickness offline, in order to include this very important property in the understanding of moisture barrier performances. Alongside this work, complementary defect analysis is to be carried out either via etching or calcium test to reveal the defects in the coatings that let the moisture permeate. A more comprehensive study of the size and distribution of defects on various samples would help clarify the



relationship between the coating properties and the process parameters and therefore would further optimise the process. On this aspect, a complementary study of the porosity could be carried out. However, one would have to first optimise the X-Ray Reflectivity or ellipsometry technique in order to make it applicable for coatings on PET substrates. Alternatively, coatings could be applied to thin glass in order to have a first rough measurement of the porosity. Additional substrate could be tested such as fluorinated polymers and PES as they have been reported as suitable for high barrier  $\text{SiO}_x$  coatings due to their chemistry.

As far as the work on reactive gases is concerned, further experiments are needed to understand in depth the effect of  $\text{CO}_2$  on the barrier and coating properties. At this stage, several experiments with various amount of  $\text{CO}_2$  between 200 and 500SCMM might be required to clarify and identify the trend. Alternative reactive gases such as nitrogen could also be added to the mixture in appropriate quantities.

Finally, additional work on the topcoats is required in order to understand the lack of adhesion of acrylate topcoat on  $\text{SiO}_x$ . Alternatively, acrylates could be applied as first layer.  $\text{SiO}_x$  sputtered layers could also be deposited as seeding layers prior to depositing the PECVD coatings

---

## 9 REFERENCES

1. R S A. Kelly. *Development of clear barrier films in europe.* in *Proceedings of the 36<sup>th</sup> Annual Technical Conference of the Society of Vacuum Coaters.* 1993.
2. S. Garner, G. Merz , J. Tosch, J. Matusick, X. Li , D. Marshall, C. Chase, J. Steiner, D. Yopez, J. Switzer, and P. Moschak, *Flexible glass substrates for continuous manufacturing,* in *2011Flex 10th annual conference.* 2011, FlexTech Alliance: Phoenix, AZ.
3. C. F. Struller, *Next generation vacuum deposited AlO<sub>x</sub> clear barrier coatings for flexible food packaging materials. (PhD Thesis).* 2013, Manchester Metropolitan University: Manchester.
4. A. W. Smith, N. Copeland, D. Gerrerd, and D. Nicholas. *PECVD of SiO<sub>x</sub> barrier films.* in *Proceedings of the 45<sup>th</sup> Annual Technical the Society Vacum Coaters.* 2002. Lake Buena Vista, Florida.
5. P. F. Carcia, R. S. McLean, M. H. Reilly, M. D. Groner, and S. M. George, *Ca test of Al<sub>2</sub>O<sub>3</sub> gas diffusion barriers grown by atomic layer deposition on polymers.* Applied Physics Letters, 2006. 89(3): p. 1 -3.
6. U. Moosheimer, H.-C. Langowski, and A. Melzer. *Permeation of oxygen, water vapor and aroma substances through vacuum web coated film.* in *Proceedings of the 43<sup>rd</sup> Annual Technical Conference of the Society of Vacuum Coaters.* 2000. Denver, CO.
7. B. M. Henry, J. A. Topping, A. Searle, H. E. Assender, C. R. M. Grovenor, M. Creatore, and M. C. M. van de Sanden. *Barrier properties of transparent multilayer films.* in *Proceedings of the 50<sup>th</sup> Annual Technical Conference of the Society of Vacuum Coaters.* 2007. Louisville, KY, USA.
8. J. S. Lewis and M.S. Weaver, *Thin-film permeation-barrier technology for flexible organic light-emitting devices.* IEEE Journal of selected topics in quantum electronics, 2004. 10(1): p. 45-57.
9. S. Hashmi, *Comprehensive materials processing,* ed. C.J.v. Tyne. Vol. 1. 2014, Golden, CO: Elsevier Science
10. A. M. Bagher, *Comparison of organic solar cells and inorganic solar cells.* International Journal of Renewable and Sustainable Energy, 2014. 3(3): p. 53-58.
11. J.-M. Nunzi, *Organic photovoltaic materials and devices.* Comptes Rendus Physique, 2002. 3(4): p. 523-542.
12. J. Singh, *Semiconductor devices: basic principles.* 2007: John Wiley & Sons.
13. H. Klumbies, *Encapsulations for organic devices and their evaluation using calcium corrosion tests (PhD thesis).* 2013, Technischen Universität Dresden: Institut für Angewandte Photophysik Fakultät Mathematik und Naturwissenschaftender.

## Appendix D Investigation of Thickness

---

14. M. I. Ahmed, A. Habib, and S. Sa. Javaid, *Perovskite solar cells: Potentials, challenges, and opportunities*. *International Journal of Photoenergy*, 2015. 2015 p. 1-13.
15. E. Bovill, *The air stability and operational lifetime of organic photovoltaic materials and devices (PhD thesis)*. 2015, University of Sheffield: Sheffield.
16. M. Kempe, *Modeling of rates of moisture ingress into photovoltaic modules*. *Solar Energy Materials and Solar Cells*, 2006. 90(16): p. 2720-2738.
17. C. Bilen. *Degradation behaviours of organic solar cells*. 2016 Date accessed: 19/05/2016]; Available from: <https://www.newcastle.edu.au/research-and-innovation/centre/coe/research/organic-solar-cells/chhinder-bilen-project-overview>.
18. Chaolysti Management Consulting. *The new mexico solar tour: Part 1 - panel degradation cannot lie, so plan smart*. Date accessed: 02/06/16]; Available from: <http://www.chaolysti.com/blog/travel/the-new-mexico-solar-tour-part-1>.
19. L. Olsen, S. Kundu, and G. Graff, *Barrier coatings for thin film solar cells*, in *National Center for Photovoltaics and Solar Program Review Meeting*. 2010, National Renewable Energy Laboratory: Pacific Northwest National Laboratory, Richland, Washington.
20. A. W. Czanderna *Encapsulation of PV modules using ethylene vinyl acetate copolymer as a pottant: A critical review*. *Solar Energy Materials and Solar Cells*, 1996. 43: p. 101-181.
21. J. Pern, *Module encapsulation materials, processing and testing*, in *Asia-Pacific Partnership International PV Reliability Workshop*. 2008: Shanghai, China.
22. A. Zielnik, *Validating photovoltaic module durability*. 2013, Atlas Material Testing Technology, Amtek Corporation.
23. K. Ghaffarzadeh, *OLED lighting opportunities 2015-2025: Forecasts, technologies, players full analysis including materials, manufacturing costs, modules and LED competitive assessment*. 2014, IDTechEx.
24. R. Meerheim, B. Lussem, and K. Leo, *Efficiency and stability of p-i-n type organic light emitting diodes for display and lighting applications*. *Proceedings of the IEEE*, 2009. 97(9): p. 1606-1626.
25. J. Lewis, *Material challenge for flexible organic devices*. *Materials Today*, 2006. 9(4): p. 38-45.
26. H. Zervos, *Barrier layers for flexible electronics 2015-2025: Technologies, markets, forecasts*. 2014, IDTechEx.

## Appendix D Investigation of Thickness

27. M. Pfeiffer, K. Leo, X. Zhou, J.S. Huang, M. Hofmann, A. Werner, and J. Blochwitz-Nimoth, *Doped organic semiconductors: Physics and application in light emitting diodes*. *Organic Electronics*, 2003. 4(2-3): p. 89-103.
28. K.L. Choy, *Chemical vapour deposition of coatings*. *Progress in Materials Science*, 2003. 48(2): p. 57-170.
29. A.C. Jones and M.L. Hitchman, *Chemical vapour deposition: precursors, processes and applications*. 2009, Cambridge: Royal Society of Chemistry.
30. W.G. Breiland, P. Ho, M.L. Hitchman, and K.F. Jensen, *Analysis of chemical vapor deposition processes*, in *Chemical Vapor Deposition* M.L.a.J. Hitchman, K. F., Editor. 1994, Academic Press London: London
31. J.R. Creighton and J.E. Parmeter, *Metal CVD for microelectronic applications: An examination of surface chemistry and kinetics*. *Critical Reviews in Solid State and Materials Sciences*, 1993. 18(2): p. 175-237.
32. B.D. Fahlman, *Recent advances in chemical vapor deposition*. *Current organic chemistry*, 2006. 10(9): p. 1021-1033.
33. H.O. Pierson, *Handbook of chemical vapor deposition: principles, technology, and applications*. 1999, Norwich, N.Y: Noyes Publications.
34. S.G. Walton and J.E. Greene, *Chapter 2 - Plasmas in deposition processes*, in *Handbook of Deposition Technologies for Films and Coatings (Third Edition)*, P.M. Martin, Editor. 2010, William Andrew Publishing: Boston. p. 32-92.
35. M. Gilo. *Low-reflectance, durable coatings for infrared lenses*. 2013 Date accessed: 20/12/2014]; Available from: <http://spie.org/newsroom/4581-low-reflectance-durable-coatings-for-infrared-lenses>.
36. J.-O. Carlsson and P.M. Martin, *Chapter 7 - Chemical vapor deposition*, in *Handbook of Deposition Technologies for Films and Coatings (Third Edition)*, P.M. Martin, Editor. 2010, William Andrew Publishing: Boston. p. 314-363.
37. L. Martinu, O. Zabeida, and J.E. Klemberg-Sapieha, *Chapter 9 - Plasma-enhanced chemical vapor deposition of functional coatings*, in *Handbook of Deposition Technologies for Films and Coatings (Third Edition)*, P.M. Martin, Editor. 2010, William Andrew Publishing: Boston. p. 392-465.
38. R. Wolf and A.C. Sparavigna, *Role of plasma surface treatments on wetting and adhesion*. *Engineering*, 2010. 2(6): p. 397-402.
39. S. Günther, M. Fahland, J. Fahlteich, B. Meyer, S. Straach, and N. Schiller, *High rate low pressure plasma-enhanced chemical vapor deposition for barrier and optical coatings*. *Thin Solid Films*, 2013. 532: p. 44-49.
40. L. Bárdoš, H. B. *Thin film processing by radio frequency hollow cathodes*. *Surface and Coatings Technology*, 1997. 97(1-3): p. 723-728. B e r g ,
41. A.S. Da Silva Sobrinho, M. Latrèche, G. Czeremuskin, J.E. Klemberg-Sapieha, and M.R. Wertheimer, *Transparent barrier coatings on polyethylene*

## Appendix D Investigation of Thickness

---

- terephthalate by single- and dual-frequency plasma-enhanced chemical vapor deposition. Journal of Vacuum Science and Technology, 1998. 16(6): p. 3190-3198.*
42. M. Deilmann, S. Theiß, and P. Awakowicz, *Pulsed microwave plasma polymerization of silicon oxide films: Application of efficient barriers on polyethylene terephthalate. Surface and Coatings Technology, 2008. 202(10): p. 1911-1917.*
  43. D.-S. Wu, *Transparent barrier coatings for flexible organic light-emitting diode applications. Chemical Vapor Deposition, 2006. 12(4): p. 220–224, April.*
  44. H. Adam. *Fundamentals of vacuum technology. 2007* Date accessed: 03/11/2016]; Available from: [http://www3.nd.edu/~wzech/Resources LEYBOLD FUNDAMENTALS.pdf](http://www3.nd.edu/~wzech/Resources_LEYBOLD_FUNDAMENTALS.pdf).
  45. J.F. Shackelford, *Gas solubility in glasses – principles and structural implications. Journal of Non-Crystalline Solids, 1999. 253(1-3): p. 231-241.*
  46. K. Cooksey, K.S. Marsh, and L.H. Doar, *Predicting permeability & transmission rate for multilayer materials. Food Technology, 1999. 53(9): p. 60-63.*
  47. R.M. Barrer, *Diffusion in and through solids. 1941, London: Cambridge University Press.*
  48. C.E. Rogers, *Permeation of gases and vapours in polymers, in Polymer permeability, J. Comyn, Editor. 1985, Chapman & Hall: London. p. 11-73.*
  49. L.K. Massey, *Permeability properties of plastics and elastomers - A guide to packaging and barrier materials. 2<sup>nd</sup> ed. 2003, Norwich, NY: William Andrew Publishing/Plastics Design Library.*
  50. L. Korner, *Diffusion barrier coatings for polymer containers processed by plasma enhanced chemical vapor deposition (PhD Thesis). 2010, ETH Zurich: Switzerland.*
  51. O. Miesbauer, M. Schmidt, and H.-C. Langowski, *Stofftransport durch Schichtsysteme aus Polymeren und dünnen anorganischen Schichten (Mass transport through layer systems consisting of polymers and thin inorganic coatings). Vakuum in Forschung und Praxis, 2008. 20(6): p. 32-40.*
  52. G.L. Robertson, *Food packaging: Principles and practise. 2<sup>nd</sup> ed. 2006, Boca Raton, FL: CRC press, Taylor and Francis Group.*
  53. H. Chatham, *Oxygen diffusion barrier properties of transparent oxide coatings on polymeric substrates. Surface and Coatings Technology, 1996. 78(1-3): p. 1-9.*
  54. W. Prins and J.J. Hermans, *Theory of permeation through metal coated polymer films. The Journal of Physical Chemistry, 1959. 63(5): p. 716-720.*

## Appendix D Investigation of Thickness

---

55. W. Decker and B. Henry, *Basic principles of thin film barrier coatings*. 45th Annual Technical Conference Proceedings, Society of Vacuum Coaters, 2002: p. 492-502.
56. H.-C. Langowski, *Stofftransport durch polymere und anorganische Schichten (Transport of Substances Through Polymeric and Inorganic Layers)*. *Vakuum in Forschung und Praxis*, 2005. 17(1): p. 6-13.
57. M. Elrawemi, BluntLiam, L. Fleming, D. Bird, D. Robbins, and F. Sweeney, *Modelling water vapor permeability through atomic layer deposition coated photovoltaic barrier defects*. *Thin Solid Films*, 2014. 570(Part A): p. 101-106.
58. H. Yasuda and T. Hirotsu, *The effect of glass transition on gas permeabilities*. *Journal of Applied Polymer Science*, 1977. 21(1): p. 105-112.
59. A.P. Roberts, B.M. Henry, A.P. Sutton, C.R.M. Grovenor, G.A.D. Briggs, T. Miyamoto, M. Kano, Y. Tsukahara, and M. Yanaka, *Gas permeation in silicon-oxide/polymer (SiO<sub>x</sub>/PET) barrier films: role of the oxide lattice, nano-defects and macro-defects*. *Journal of Membrane Science*, 2002. 208(1-2): p. 75-88.
60. Y.G. Tropsha and N.G. Harvey, *Activated rate theory treatment of oxygen and water transport through silicon oxide/poly(ethylene terephthalate) composite barrier structures*. *The Journal of Physical Chemistry B*, 1997. 101(13): p. 2259-2266.
61. A.S. da Silva Sobrinho, G. Czeremuszkina, M. Latrèche, and M.R. Wertheimer, *Defect-permeation correlation for ultrathin transparent barrier coatings on polymers*. *Journal of Vacuum Science & Technology*, 2000. 18(1): p. 149-157.
62. A. Grüniger and P. Rudolf von Rohr, *Influence of defects in SiO<sub>x</sub> thin films on their barrier properties*. *Thin Solid Films*, 2004. 459(1-2): p. 308-312.
63. A.G. Erlat and R.J. Spontak, *SiO<sub>x</sub> gas barrier coatings on Morphology and gas transport considerations*. *J. Phys. Chem. B*, 1999. 103(29): p. 6047-6055.
64. H.-C. Langowski, *Permeation of gases and condensable substances through monolayer and multilayer structures, in Plastic packaging - Interactions with food and pharmaceuticals*, O.G. Piringer and A.L. Baner, Editors. 2008, WILEY-VCH Verlag: Weinheim. p. 297-347.
65. T. Hirvikorpi, M. Vähä-Nissi, A. Harlin, and M. Karppinen, *Comparison of some coating techniques to fabricate barrier layers on packaging materials*. *Thin Solid Films*, 2010. 518(19): p. 5463-5466.
66. M.D. Groner, S.M. George, R.S. McLean, and P.F. Carcia, *Gas diffusion barriers on polymers using Al<sub>2</sub>O<sub>3</sub> atomic layer deposition*. *Applied Physics Letters*, 2006. 88(5): p. 051907.
67. J.C. Sellers, *The disappearing anode myth*. *Vakuum in Forschung und Praxis*, 1998. 10(3): p. 193-196.

## Appendix D Investigation of Thickness

---

68. M.T. De Meuse, *Biaxial stretching of film: Principles and applications*. 2011: Woodhead Publishing Limited.
69. J. Murphy, *Additives for plastics handbooks*. 2001, Oxford (UK): Elsevier Science Limited.
70. A. Parashar, S. Kumar, J. Gope, C.M.S. Rauthan, P.N. Dixit, and S.A. Hashmi, *Influence of argon dilution on growth and properties of hydrogenated nanocrystalline silicon films*. *Solar Energy Materials and Solar Cells*, 2010. 94(5): p. 892-899.
71. S.-R. Kim, M.H. Choudhury, W.-H. Kim, and G.-H. Kim, *Effects of argon and oxygen flow rate on water vapor barrier properties of silicon oxide coatings deposited on polyethylene terephthalate by plasma enhanced chemical vapor deposition*. *Thin Solid Films*, 2010. 518(8): p. 1929-1934.
72. M.W. Beckman, *The effects of low pressure helium ion bombardment on hydrogenated amorphous silicon (PhD thesis)*. 2008, Iowa State University.
73. ASTM International, *ASTM F1249 - 13 Standard test method for water vapor transmission rate through plastic film and sheeting using a modulated infrared sensor*. 2013, ASTM International: West Conshohocken, PA.
74. Systech Illinois, *Model M7001 / M7011 water vapour permeation analyzer. Operators manuals. Version 3.2 1*. 2013, Systech Instruments Limited.
75. K. Evans. *Technical article: oxygen permeability of contact lens materials and testing standards*. 2011 Date accessed: 24/10/2014]; Available from: [http://www.systechillinois.com/en/oxygen-permeability-of-contact-lens-materials-and-testing-standards\\_363.html](http://www.systechillinois.com/en/oxygen-permeability-of-contact-lens-materials-and-testing-standards_363.html).
76. ASTM International, *ASTM F392 / F392M-11, standard practice for conditioning flexible barrier materials for flex durability*. 2011, ASTM International: West Conshohocken, PA.
77. R. Volk, *Rauheitsmessung - theorie und praxis*. 2005, Berlin - Wien - Zürich: Beuth Verlag.
78. Mocon Incorporation, *AQUATRAN® Model 2 High sensitivity coulometric water vapor transmission rate test system*. 2014, Mocon Incorporation.
79. Macbeth corporation, *QUANTALOG® color transmission densiometer*, D.o.c. corporation, Editor.: Newburgh, N. Y.
80. K.L. Mittal, *Adhesion measurement of thin films*. *Electrocomponent Science and Technology*, 1976. 3: p. 21-42.
81. D.M. Brewis and D. Briggs, *Industrial adhesion problems*. 1985: Wiley.
82. P. Fink-Jensen, *Hardness testing of organic coatings* *Pure and Applied Chemistry*., 2009. 10(3): p. 239-292.

## Appendix D Investigation of Thickness

---

83. D. Briggs, *X-ray photoelectron spectroscopy (XPS)*, in *Handbook of Adhesion*, J.W. Sons, Editor. 2005: Chichester. p. 621-622.
84. B.C. Smith, *Fundamentals of Fourier transform infrared spectroscopy*. 2<sup>nd</sup> ed. 2011, Boca Raton, FL: Taylor & Francis.
85. B. H. Stuart, *Infrared spectroscopy: Fundamentals and applications*. 2004, Chichester: John Wiley & Sons.
86. P. Fayet, B. Jaccoud, R. Davis, and D. Klein, *Effect of anti-blocking particles on oxygen transmission rate of SiO<sub>x</sub> barrier coatings deposited by PECVD on PET films*. 48th Annual Technical Conference Proceedings, Society of Vacuum Coaters, 2005: p. 237-240.
87. G. Rochat, Y. Leterrier, P. Fayet, and J.A.E. Månson, *Influence of substrate additives on the mechanical properties of ultrathin oxide coatings on poly(ethylene terephthalate)*. *Surface and Coatings Technology*, 2005. 200(7): p. 2236-2242.
88. A. Bieder, *PECVD of SiO<sub>x</sub> films from oxygen and hexamethyldisiloxane in a double source reactor*. 2006, ETH Zurich: Switzerland.
89. A. Gruniger, *Deposition of SiO<sub>x</sub> diffusion barriers on flexible packaging materials by plasma enhanced chemical vapor deposition*. 2004, ETH Zurich: Switzerland.
90. D.G. Howells, B.M. Henry, J. Madocks, and H.E. Assender, *High quality plasma enhanced chemical vapour deposited silicon oxide gas barrier coatings on polyester films*. *Thin Solid Films*, 2008. 516(10): p. 3081-3088.
91. L. Qi, C. Zhang, and Q. Chen, *Properties of Plasma Enhanced Chemical Vapor Deposition Barrier Coatings and Encapsulated Polymer Solar Cells*. *Plasma Science and Technology*, 2014. 16(1): p. 45-49.
92. A.S. da Silva Sobrinho, J. Chasle, G. Dennler, and M.R. Wertheimer, *Characterization of defects in PECVD SiO<sub>2</sub> coatings on PET by confocal microscopy*. *Plasma Processes and Polymers*, 1998. 3(4): p. 231-247.
93. B.M. Henry, A.G. Erlat, C.R.M. Grovenor, C.S. Deng, A.G.D. Briggs, T. Miyamoto, N. Noguchi, T. Nijima, and Y. Tsukahara, *The permeation of water vapor through gas barrier films*. 44th Annual Technical Conference Proceedings, Society of Vacuum Coaters, 2001: p. 469-475.
94. A.S. da Silva Sobrinho, G. Czeremuskin, M. Latrèche, G. Dennler, and M.R. Wertheimer, *A study of defects in ultra-thin transparent coatings on polymers*. *Surface and Coatings Technology*, 1999. 116-119: p. 1204-1210.
95. P.-z. Yang, L.-m. Liu, J.-h. Mo, and W. Yang, *Characterization of PECVD grown porous SiO<sub>2</sub> thin films with potential application in an uncooled infrared detector*. *Semiconductor Science and Technology*, 2010. 25(4): p. 045017.



## Appendix D Investigation of Thickness

---

96. Q. Lei, *Properties of Plasma Enhanced Chemical Vapor Deposition Barrier Coatings and Encapsulated Polymer Solar Cells*. **Plasma Science and Technology**, 2014. 16(1): p. 45-49.
97. J.T. Felts. *Thickness effects on thin film gas barriers: Silicon-based coatings*. in *Proceedings of the 34th Annual Technical Conference of the Society of Vacuum Coaters*. 1991.
98. G. Dennler, *Growth Modes of SiO<sub>x</sub> Films Deposited by Evaporation and Plasma-Enhanced Chemical Vapor Deposition on Polymeric Substrates*. **Plasmas and Polymers**, 2003. 8(1): p. 43-59.
99. N. Schiller, S. Straach, S. Günther, A.L. Quiceno, A.G. Contreras, R. Ludwig, and G. Hoffmann, *Innovative clear barrier technology for the packaging industry*. **AIMCAL Fall Technical Conference**, 2008.
100. S. Gunther, *High Rate, Low Pressure PECVD for Barrier and Optical Coatings in 2016 Web Coating & Handling Conference Europe - AIMCAL*. 2012: Prague.
101. D.G. Howells, B.M. Henry, Y. Leterrier, J.A.E. Manson, J. Madocks, and H.E. Assender, *Mechanical properties of SiO<sub>x</sub> gas barrier coatings on polyester films*. **Surface and Coatings Technology**, 2008. 202(15): p. 3529-3537.
102. V. Tobin, *Roll-to-roll deposition of highly flexible organic-inorganic barrier layers for printed electronics and photovoltaics (DPhil thesis)*. 2016, University of Oxford.
103. A. Barranco, J. Cotrino, F. Yubero, J.P. Epsinos, and A.R. Gonzalez-Elipea, *Room temperature synthesis of porous SiO<sub>2</sub> thin films by plasma enhanced chemical vapor deposition*. **Journal of Vacuum Science**, 2004. 22(4): p. 1275-1284.
104. M. Yanaka, B.M. Henry, A.P. Roberts, C.R.M. Grovenor, G.A.D. Briggs, A.P. Sutton, T. Miyamoto, Y. Tsukahara, N. Takeda, and R.J. Chater, *How cracks in SiO<sub>x</sub>-coated polyester films affect gas permeation*. **Thin Solid Films**, 2001. 397(1-2): p. 176-185.
105. H. Tamagaki, T. Okimoto, Y. Kurokawa, and T. Segawa. *Transparent high barrier coating on polymer web by PE-CVD roll coater*. in *Proceedings of the 53<sup>rd</sup> Annual Technical Conferenc of the Society of Vacuum Coaters*. 2010. Orlando, FL,.
106. T. Okimoto, *Barrie properties of high barrier coating on plastic substrate by PECVD roll coater/*, in *Society of Vacuum Coaters*. 2011: Chicago. p. 580-583.
107. G. Rochat and P. Fayet, *Characterization of mechanical properties of ultra-thin oxide coatings on polymers by uniaxial fragmentation tests*. **Journal of Adhesion Science and Technology**, 2012. 26(20-21): p. 1-12.
108. Y. Leterrier, *Durability of nanosized oxygen-barrier coatings on polymers*. **Progress in Materials Science**, 2003. 48(1): p. 1-55.

## Appendix D Investigation of Thickness

---

109. O. Gabriel, S. Kirner, M. Klick, B. Stannowski, and R. Schlatmann, *Plasma monitoring and PECVD process control in thin film silicon-based solar cell manufacturing*. EPJ Photovoltaics, 2014. 5(55202): p. 55202.
110. S. Calnan, O. Gabriel, I. Rothert, M. Werth, S. Ring, B. Stannowski, and R. Schlatmann, *Influence of chemical composition and structure in silicon dielectric materials on passivation of thin crystalline silicon on glass*. ACS Appl Mater Interfaces, 2015. 7(34): p. 19282-94.
111. R. S. A. Kelly. *Development of aluminium oxide clear barrier films*. in *Proceedings 37th Annual Technical Conference of the Society of Vacuum Coaters*. 1994. Society Vac. Coaters.
112. K.-H. Jeong, S.-G. Park, and S.-W. Rhee, *Nanocomposite low-k SiCOH films by plasma-enhanced chemical vapor deposition using vinyltrimethylsilane and CO<sub>2</sub>*. Journal of Vacuum Science & Technology B: Microelectronics and Nanometer Structures, 2004. 22(6): p. 2799.
113. K.H. Kale and S.S. Palaskar, *Plasma enhanced chemical vapor deposition of tetraethylorthosilicate and hexamethyldisiloxane on polyester fabrics under pulsed and continuous wave discharge*. Journal of Applied Polymer Science, 2012. 125(5): p. 3996-4006.
114. Y.S. Kim, *Plasma-enhanced chemical vapor deposition of SiO<sub>2</sub> thin films at atmospheric pressure by Using HMDS/Ar/O*. J. Korean Phys. Society, 2008. 53(2): p. 892-896.
115. J.A. Theil, *Carbon content of silicon oxide films deposited by room temperature plasma enhanced chemical vapor deposition of hexamethyldisiloxane and oxygen*. Journal of Vacuum Science & Technology A: Vacuum, Surfaces, and Films, 1994. 12(4): p. 1365.
116. R. Reuter, *Silicon-oxide-like thin film deposition from hexamethyldisiloxane by means of non-equilibrium atmospheric pressure plasmas: The role of oxygen and surface reactions (PhD thesis)*. 2012, Ruhr-Universität Bochum: Bochum. p. 128.
117. J.B. Quinn. *Hardness and Brittleness of Ceramics*. in *Proceedings of the 20th Annual conference on composites, advanced ceramics, materials, and structures—a: Ceramic engineering and science*. 2008. John Wiley & Sons, Inc.
118. M. George, *Deposition of silicon oxide, silicon nitride and silicon carbide thin films by new plasma enhanced chemical vapor deposition source technology*, in *2007 USA Fall Technical Conference- AIMCAL*. 2007: Fountain Hills , Arizona. p. 1-12.
119. H. Pedersen, *A novel high-power pulse PECVD method* Surface & Coatings Technology, 2012. 206(22).
120. W. Gajewski, *Qualification tests TruPlasma Bipolar 4040 (G2) BOBST Manchester Ltd*. 2015, TruPlasma, Triumph Hutinger

## Appendix D Investigation of Thickness

121. D.S. Wu, *Properties of SiO<sub>2</sub>-like barrier layers on polyethersulfone substrates by low-temperature plasma-enhanced chemical vapor deposition*. *Thin Solid Films*, 2004. 468 p. 105- 108.
122. Y. Leterrier. *Durability of thin PECVD SiO<sub>x</sub> coatings on polymer films*. in *Proceedings of 41<sup>st</sup> Annual Technical Conference of the Society of Vacuum Coaters*. 1998. Boston, MS.
123. DuPont Teijin Films. *Datasheet MELINEX® ST504* Date accessed: 18/07/2016]; Available from: <http://www.dupontteijinfilms.com/FilmEnterprise/Datasheet.asp?Result=Print&ID=269&Version=US>.
124. H.L. Brown, *The properties and performance of moisture/oxygen barrier layers deposited by remote plasma sputtering (PhD thesis)*. 2015, University of Surrey: Faculty of engineering and physical sciences.
125. The Adhesive and Sealant Council Incorporation. *Surface Treatment*. 2009 Date accessed: 03/11/2016]; Available from: [http://www.adhesives.org/docs/default-document-library/surfaceprep\\_adhesives-org.pdf?sfvrsn=0](http://www.adhesives.org/docs/default-document-library/surfaceprep_adhesives-org.pdf?sfvrsn=0).
126. Simco-Ion. *Teknek Elastomer Rollers - Product Overview*. 2016 11/07/2016]; Available from: <https://www.simco-ion.com/Products/TeknekContactCleaners/ContactCleaningRollersAdhesives/TeknekElastomerRollers.aspx>.
127. S. Louch, S. Edge, M. Hodgson, and K. Luxmore, *Transparent conducting oxides on polymer webs*. 52nd Annual Technical Conference Proceedings, Society of Vacuum Coaters, 2009: p. 746-750.
128. Mark Hodgson, *Cleaning of Polyester Films Prior to Vacuum Coating*, in 2010 Fall Technical Conference. 2010, AIMCAL: Naple, CA.
129. P. Chen, T. Mitsui, D.B. Farmer, J. Golovchenko, R.G. Gordon, and D. Branton, *Atomic layer deposition to fine-tune the surface properties and diameters of fabricated nanopores*. *Nano Letters*, 2004. 4(7): p. 1333-1337.
130. T. Bulow, H. Gargouri, M. Siebert, R. Rudolph, H.H. Johannes, and W. Kowalsky, *Moisture barrier properties of thin organic-inorganic multilayers prepared by plasma-enhanced ALD and CVD in one reactor*. *Nanoscale Res Lett*, 2014. 9(1): p. 223.
131. J.A.v. Delft, D. Garcia-Alonso, and W.M.M. Kessels, *Atomic layer deposition for photovoltaics: applications and prospects for solar cell manufacturing*. *Semiconductor Science and Technology*, 2012. 27(7): p. 074002.
132. K.L. Mittal, *Adhesion measurement: Recent progress, unsolved problems, and prospects*, in *Adhesion measurement of thin films, thick films, and bulk coatings*, K.L. Mittal, Editor. 1978, American Society for Testing and Materials (ASTM): Philadelphia, PA. p. 5-17.

## Appendix D Investigation of Thickness

---

133. K.L. Mittal, *Adhesion measurements of films and coatings: A commentary*, in *Adhesion measurements of films and coatings*, K.L. Mittal, Editor. 1995, VSP: Utrecht. p. 1-13.
134. A. Pizzi and K.L. Mittal, *Handbook of adhesive technology, revised and expanded*. 2003: Taylor & Francis.
135. C. Elsner, *Photoinitiator-free plasma-induced polymerization and microstructuring of acrylate based coatings on 3D substrates*. *Macromolecular Materials Engineering*, 2009. 294: p. 422-431.
136. F. Hochart, J. Levalois-Mitjaville, and R. De Jaeger, *Application of a cold plasma process for polymerization and copolymerization of fluorinated and hydrogenated (meth)acrylates*. *Polymer*, 2000. 41(9): p. 3159-3166.
137. ASTM International, *D3359-09e2, standard test methods for measuring adhesion by tape test*. 2009, ASTM International: West Conshohocken, PA.

**A. APPENDICES**

## **Appendix A      Investigation of Thickness**

This part of the appendices reports the work done on developing a method that allows easy, reliable and repeatable measurement of the thickness of SiO<sub>x</sub> coatings on thick PET substrates. This has proved to be challenging and difficult to achieve, due to the nature of the samples.

The samples studied were SiO<sub>x</sub> type coatings deposited by plasma enhanced chemical vapour deposition onto 120µm PET (Provided by Jindal).

The samples have been produced using different process parameters, therefore their thicknesses vary. To understand and optimise the process the information about the thickness of the deposited layer is essential. However, it appeared that some conventional methods commonly used in the industry (i.e. X-Ray Fluorescence) were not suitable for measurement of SiO<sub>x</sub> thickness (i.e. variation in composition and artefact of measurement due to antiblock particles).

Some methods and techniques already exist to measure the thickness of organic/inorganic coatings on plastic polymers. Some of these techniques are used online during the deposition process (i.e. crystal quartz) while others are used offline to measure the thickness after deposition (ellipsometry, etc) and some combine online and offline (step edge and profilometry measurement).

Several samples were measured to evaluate the applicability of the methods. The first sample studied was a sample of which thickness was measured at BML using XRF. In addition, the aim was to compare the physical thickness and the chemical thickness to determine whether XRF was a fit for thickness measurement. This sample will be called sample A.

Then as the project progressed and a reference sample was produced, it was decided to use this reference sample (sample B) as a comparison point for thickness measurement (comparison with other samples A to H and comparison between techniques). Along the way, other samples were

measured to confirm that the technique could be used on the whole range of samples.

Different techniques were assessed. Among those were measurement of step edge via interferometry, cross section observation obtained via microtome or ultramicrotome sectioning, embedding and mechanical polishing of the sample and ion milling.

### **Step edge and profilometry/interferometry**

Interferometry and profilometry both require the user to create a step edge in the coating. This is done by placing a piece of Kapton® tape on the substrate prior to deposition. This strip of tape will obstruct deposition creating an area where there is no coating. The difference in height between the coated and uncoated area is measurable and represents the coating's thickness.

Profilometry is widely used to measure the step edge created on surfaces in order to get a direct measurement. This technique is mainly based on exploiting the mechanical contact between the tip and the sample to detect and measure the height of the step edge. This method may alter the sample morphology if the tip is harder than the coating. Interferometry relies on light interferences as detailed in Section 3.4.1.

A batch of samples from trial campaigns was considered. The image obtained via white light interferometry is presented in Figure A-1.

## Appendix D Investigation of Thickness

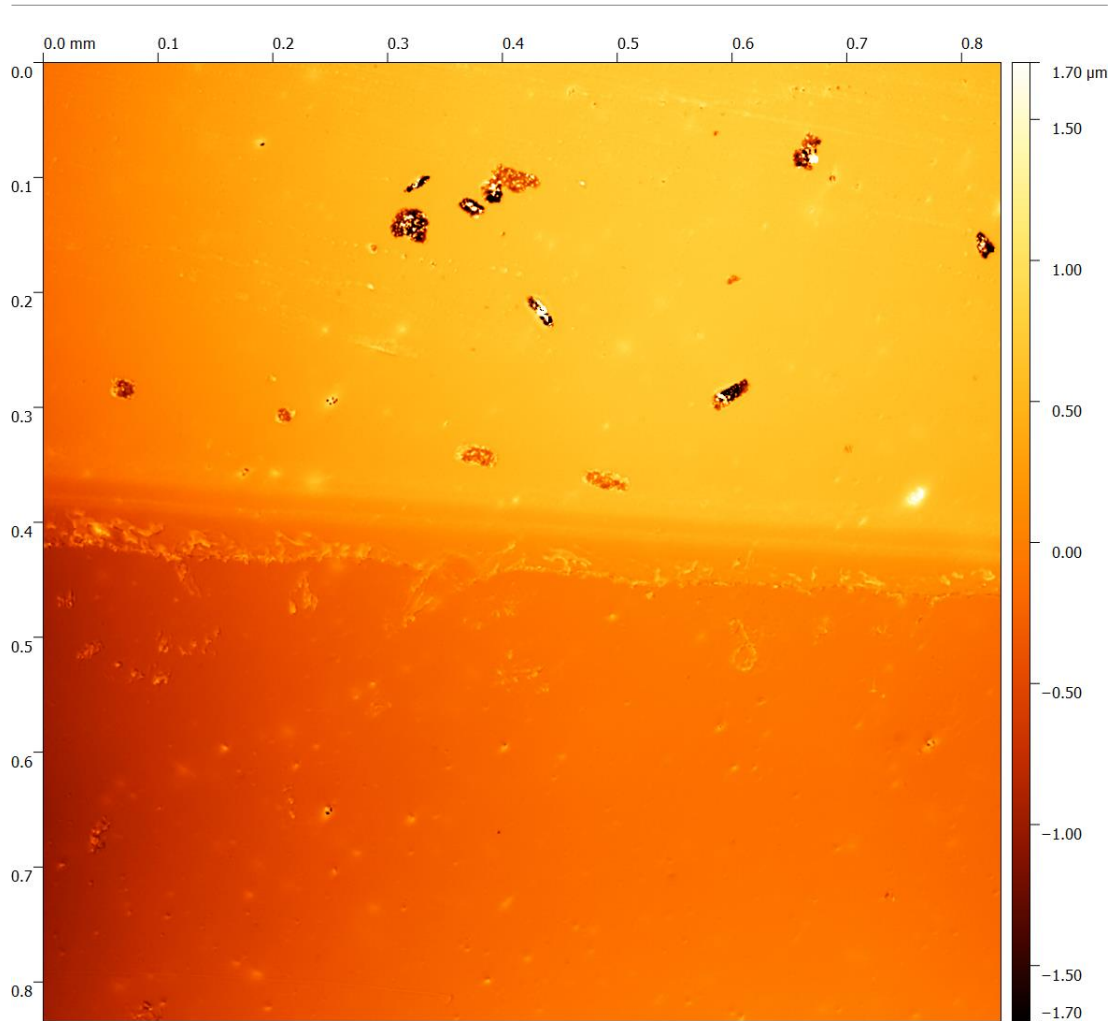


Figure A-1 White light interferometer scan of the stepedge created on the  $\text{SiO}_x$  coating onto PET for thickness measurement

On each scan, the mean plan was subtracted from the measurement, then the 2D profile was extracted using the Gwydion software, and the heights of the two plateaux of the profile were measured (Figure A-2 Screenshot of the tools used in the Gwydion software to measure the profile along the step edge). The difference between those heights is the coating thickness. This was done on five different images (different areas), the measurements were then averaged.



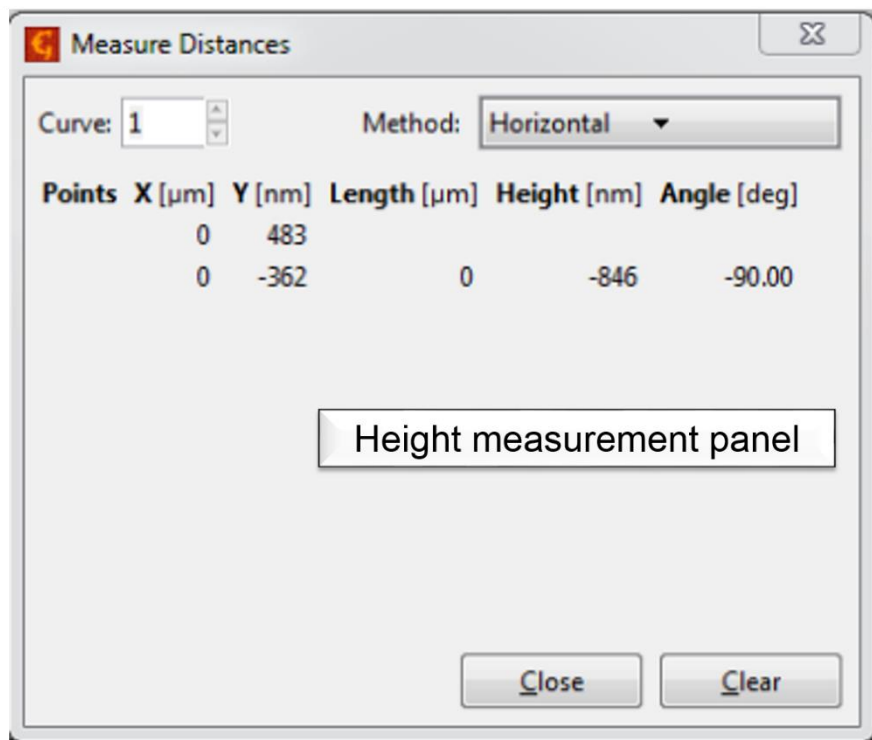
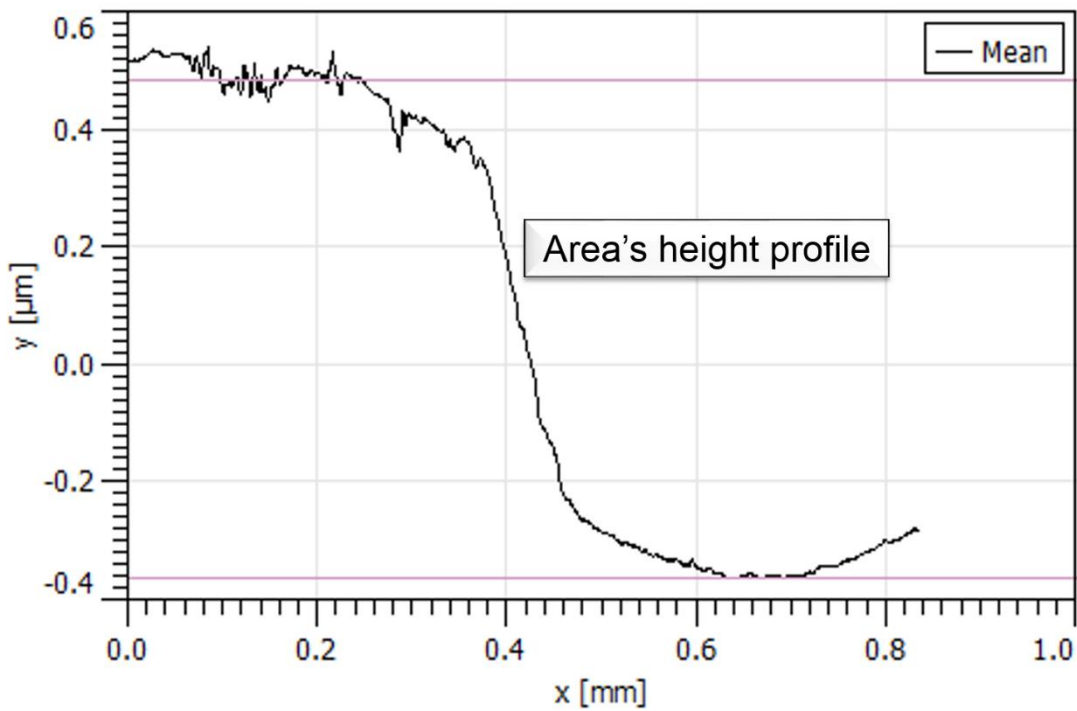


Figure A-2 Screenshot of the tools used in the Gwydion software to measure the profile along the step edge

### **Microtome**

A microtome is a tool that can be used to cut very thin slices, so-called sections. This is a step in the preparation of samples for electron microscopy (TEM or SEM) or optical microscopy.

Several types of microtome techniques were available in MMU.

A rotational manual (RM) simple microtome and a cryomicrotome were available. Therefore, cross-sections of frozen samples (-50°C) were performed with the cryomicrotome. Raw and embedded samples were sectioned with the rotational microtome.

A microtome is used to cut extremely thin slices of material (a couple of tens of nm). It is commonly used to prepare samples for transmission light (i.e. optical microscope) or electron radiation (SEM or transmission electron microscopy) analysis. Steel, glass or diamond knives can be used depending on the grade of microtome used. Throughout the work, access was given to a manual rotary Leica RM, with suitable steel blades.

Several methods can be used to cross section samples with a standard Microtome.

The samples can be sectioned either in their raw form or frozen (embedded in a special cryomaterial). Both raw and frozen samples sectioning were trialled and will be detailed in the following section of the appendices.

### **Cryomicrotomy**

Cryomicrotomy is commonly used to slice tissues and a special cryomicrotome (Figure A-3) is required to freeze the samples prior to sectioning.

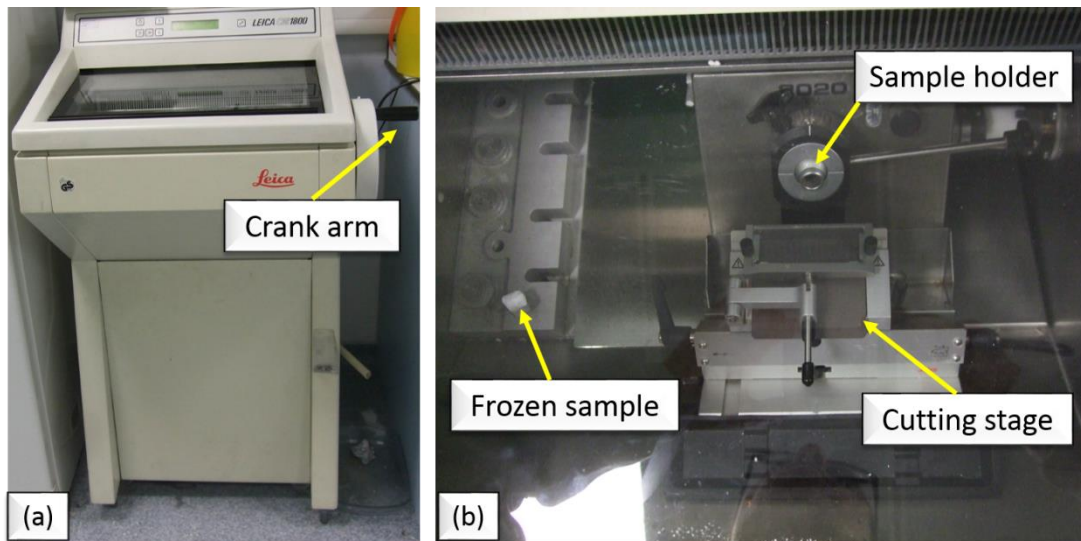


*Figure A-3 Photograph of the cryo microtome LEICA CM 1800(a) and inside of the microtome (b, used to cut the sections.*

Samples were embedded in optimised cutting tissue material (OCT) using Richard-Allan Scientific™ Neg-50™ embedding medium and frozen at  $-35^{\circ}\text{C}$  for 40 minutes. The mould containing the embedded sample was then stuck to the sample stage using Shandon™ Cryomatrix™. The sample was positioned, as shown in Figure A-4, in order to optimise the relative orientation of the sample with the cutting. The sample and cutting stage make an angle of  $45^{\circ}$ , which is optimum in microtomy to avoid damage and cut with precision. The low edge of the sample needs to be as parallel as possible to the edge of the blade. 50nm slices were cut and stuck onto microscope glass slides for transmission microscope and SEM stubs for electron microscopy.

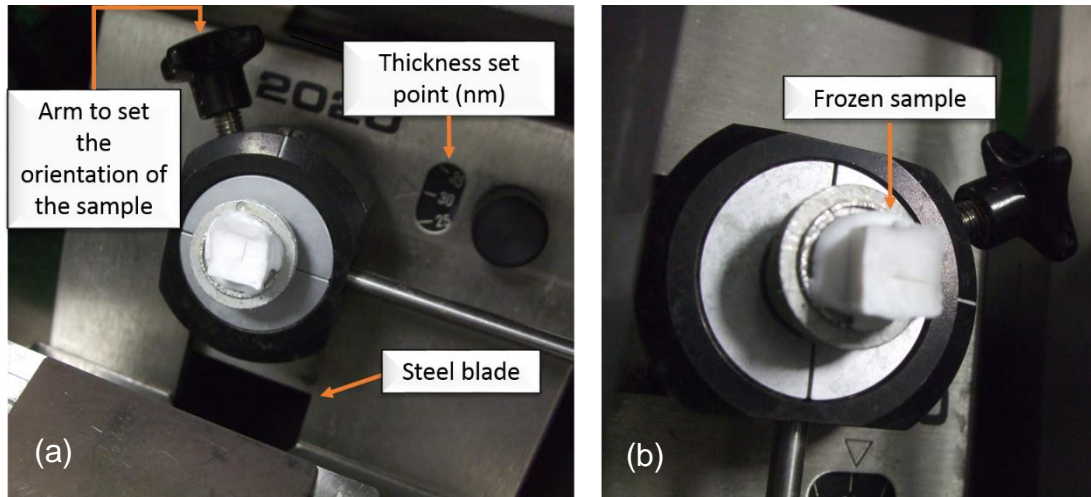


*Figure A-4 Configuration and positioning of the frozen sample prior to cutting the slice.*

Picture (a) in Figure A-4 shows the sample embedded in OCT and frozen just above the steel blade prior to sectioning. The arm is used to set the orientation of the samples and the thickness of slices is set with a gauge on the right-hand side of the sample holder. Picture (b) in Figure A-4 is a closer photograph of the embedded sample.

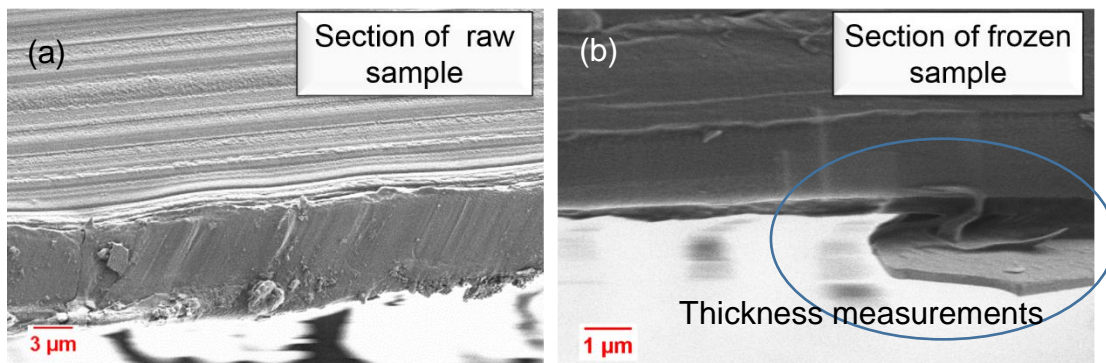
The sample was held in a cubic holder, frozen at  $-50^{\circ}\text{C}$  for 12h, and cut with the same equipment using a manual speed control and an angle for  $45^{\circ}$ . The blade was a standard steel blade commonly used to cut tissues.

Figure A-5 shows the SEM image of the cross section obtained prior to freezing the sample. At low magnification it appears that, the coating can be distinguished. However, when the magnification is increased to  $\times 16\text{k}$  it can be noted that the PET substrate has been “crushed over” by the blade. The bottom of the sample indicated that the blade has damaged the sample.

This can be explained by the competition between the hard blade and the combination of a flexible substrate and brittle/hard coating.

Moreover, on PECVD  $\text{SiO}_x$  samples, the thickness is not expected to exceed  $2\mu\text{m}$  and if it is assumed that the bottom of the image represents the coating, the coating would in that case be about  $6.9 \pm 0.45\mu\text{m}$  thick.

Comparing the images obtained with a raw sample (micrograph (a)) and frozen/embedded sample (micrograph (b)) presented in Figure A-5, it appears that the sample needs support to stay stable and not move. Indeed, during cutting it was noticed that the raw (not embedded) sample (corresponding to micrograph (a) in Figure A-5) was wobbling around the vertical axis, which could explain the piece of material damaged at the bottom of Figure A-5 (b).



*Figure A-5 SEM micrographs of the cryosection and raw section of the reference sample.*

This work gave some evidence that support was needed for the sample.

A simpler approach based on using metal plates to hold the sample in place on a SEM stub was attempted. With this approach, the sample wobbling around the vertical axis could not be avoided as a piece of material was left above the metal plates for sectioning. This piece was, therefore, not held in place and compromised repeatability and quality sectioning. Several height measurements were done with Gwydion on the bottom piece of coating which is circled in Figure A-5 and the thickness was found to vary from 300nm to 1μm. The scattered measurements were attributed to the difficulty of limiting charging and the fact that the coating flake was not perfectly square to the blade (90° angle). There might also be a natural variation in the coating thickness but this is not expected to be more than 10% along the sample. On the raw sample the measured thickness would be about 6μm, if one considered that the coating is the thick part at the bottom of image (a) in Figure A-5. This is not realistic for such coatings and it was therefore concluded that

what appeared to be the coating might just be a portion of the substrate that was bending over as the blade was cutting through it. This seems plausible as it could be seen by eyes that the sample was slightly bending as the blade was cutting through.

### Rotational microtome

A simpler way to create a cross section is to use the rotational microtome.

The Leica RM2235, presented in Figure A-6, is a rotational manual microtome that can be used to section samples, embedded and raw.

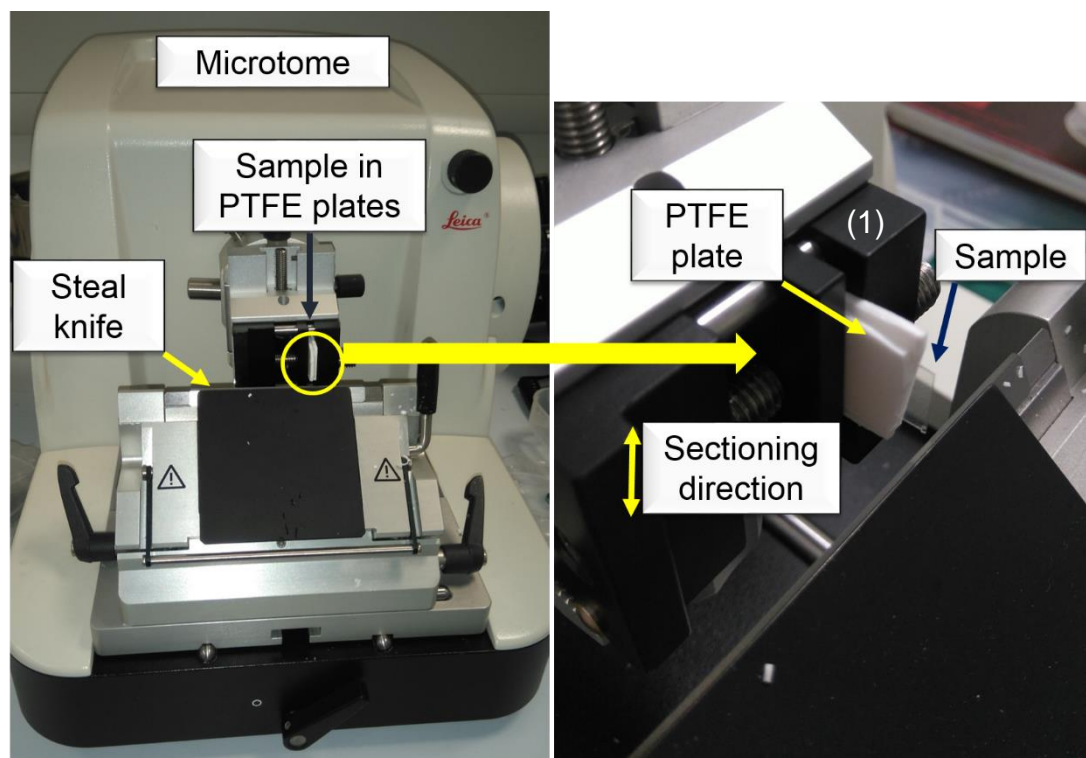


Figure A-6 Photograph of microtome Leica RM2235 and the additional stage used to section the samples in order to measure the coatings' thickness.

An additional tool (1) was implemented to hold samples in between two PTFE plates in the microtome without embedding. The moving stage containing the sample was moved up and down above the knife (the slice thickness was not relevant so was kept constant to 50 $\mu$ m). A slice of adhesive tape was stuck

onto the sample to get a slice and then stuck to a microtome stub for SEM observation.

### **Ultramicrotome**

Another method that has proved suitable for certain  $\text{SiO}_x$  coatings and  $\text{AlO}_x$  coatings[3] is ultramicrotomy.

Ultramicrotomes work on the same principles as rotational microtomes, but they allow much thinner sections to be cut (~50nm). The precision is higher, and it possible to section plastics and ceramics easily as an ultramicrotome is equipped with a glass knife or diamond knife. According to DiAtom, the very close mechanical properties of the diamond and the silicon oxide coating makes it a suitable and adequate tool to perform the cross section effectively.

In this work, two different types of ultramicrotomy were investigated. The first one was simple sectioning without embedding the sample and the second one was cryo-ultramicrotomy.

### **Ultramicrotomy with vibrating blade**

Ultramicrotomy was performed on a Leica UC7(Figure A-7)that is a vibrating microtome. The slices are cut by vibrating a blade, allowing the resultant cut to be made with less pressure than would be required for a stationary blade. The thickness varies from 30nm to 150nm.

This method was performed by DiAtom in Switzerland who are specialists in production of glass knives for microtomes. According to them, glass knives are more appropriate to cutting  $\text{SiO}_x$  coatings as the coating and the knife would have similar hardnesses.





*Figure A-7 Photograph of the ultramicrotome used at DiAtom to create cross sections of the SiO<sub>x</sub> coatings.*

The operator used the following procedure

- clamping the sample in a sample holder
- trimming with a trim 45 diamond blade, leaving only a few microns foil plus the SiO<sub>2</sub> coating
- sectioning with an ultrasonic knife, resonance frequency 23.7kHz, Amplitude 10V, feed 70nm<sup>12</sup>, sectioning speed 0.3mm/sec. The clearance angle was set at 10° (most commonly 6°).

The samples analysed on the SEM were cross sections mounted on a special vertical stub as illustrated in the schematic in Figure A-8

---

<sup>12</sup> Diatom recommended 30nm section for brittle material.



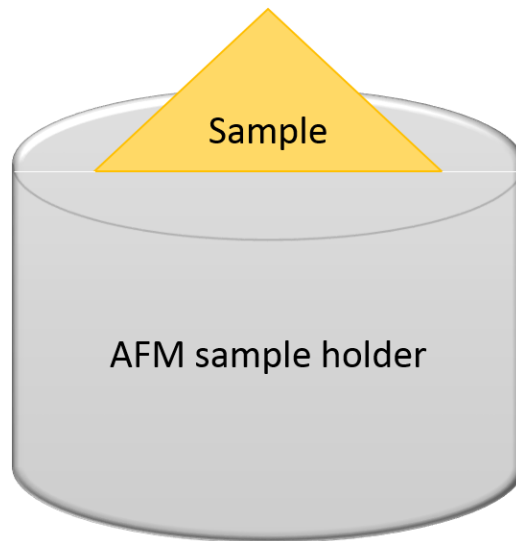


*Figure A-8 Schematic showing the sample held in AFM sample holder after cross sectioning with the ultramicrotome and vibrating knife.*

### **Cryo ultramicrotomy**

All the sample preparation was done by ISS Group Services Ltd. The samples were cut using an RMC PT-PCZ ultramicrotome with CR-X cryo-sectioning system equipped with a diamond knife. Both the sample and knife were cooled to  $-25^{\circ}\text{C}$  and the samples seemed to cut well resulting in mirror-polished surfaces.

Figure A-9 presents the micrographs of one sample that was sectioned using the two variations of the ultramicrotomy technique (room temperature and cryo ultramicrotomy).

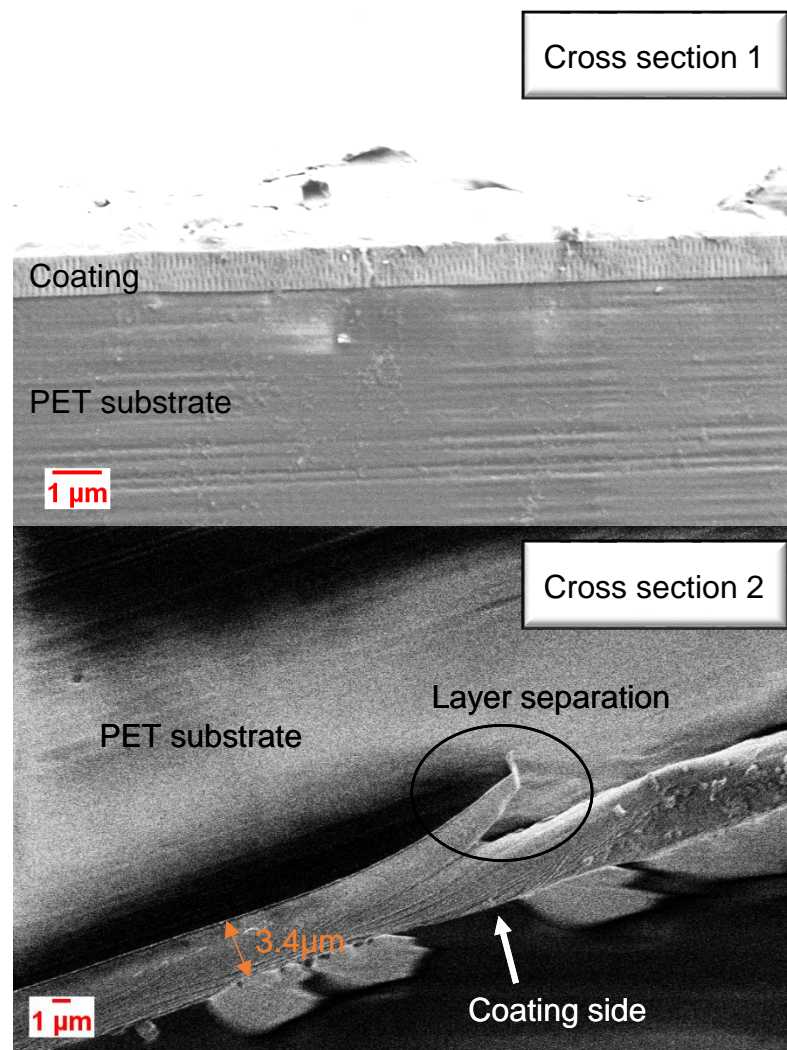


Figure A-9 SEM micrograph of the same sample. Cross section 1 was done by ultramicrotomy with vibrating knife and cross section 2 was done by cryo ultramicrotomy.

Cross sections (Figure A-9) reveals that the two techniques did not produce the same quality of samples. It is hard to clearly identify the coating on cross section 2 whereas it the coating is obvious and easy to measure. One could thin that the bottom part of cross section 2 is the actual coating. However, the layer separation identified on the micrograph was relatively similar to the macro bending and “curling” of the PET observed in room temperature microtomy. Moreover, the average thickness of the bottom section of the micrograph is around  $3.4 \pm 0.3 \mu\text{m}$ , which is not realistic for this type of coating and is higher than the thickness measured on cross section 1 ( $777 \pm 21 \text{nm}$ ).

To summarise, room temperature ultramicrotomy was more suitable for cross sectioning in the case of this sample. A few other samples were sectioned using these two techniques and it seemed like cryo ultramicrotomy was not a good fit for any of the samples (difficult to clearly identify the coating on the final samples).

Detailed thickness measurements and comparisons between techniques are reported in Table A-1.

### **Ion milling**

Ion milling is an etching technique whereby beam of inert gas I accelerated towards a material in order to remove some of the material away to some desired depth. Ion milling is operated in vacuum (typically  $10^{-4}$ Torr) where the mean free path (average distance an atom ion or molecule can travel before collision with another particle that will modify its direction to some degree). Ion milling was performed with the device shown in Figure A-10.



*Figure A-10 Photograph of PECS II ion milling device used in the work(Gatan).*

The sample holder is illustrated in Figure A-11 and the principle of the technique is illustrated in the schematic in Figure A-12

A U-shaped region is created under the effect of the ion beam (Figure A-12). The thickness was measured in this region of the sample.

The samples were cut into 1cm<sup>2</sup> square and stuck to a metal sample holder with a conductive glue.

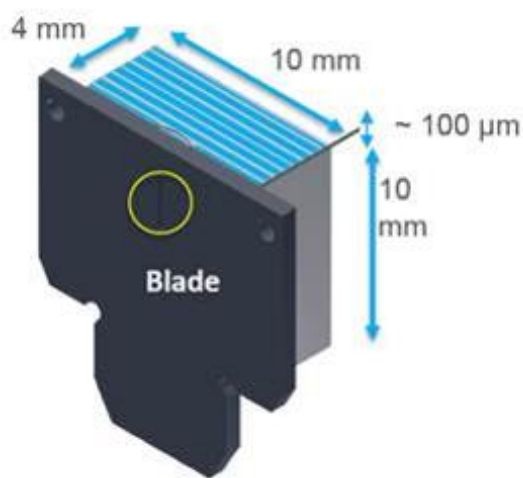


Figure A-11 Schematic showing the sample holder used for ion milling.

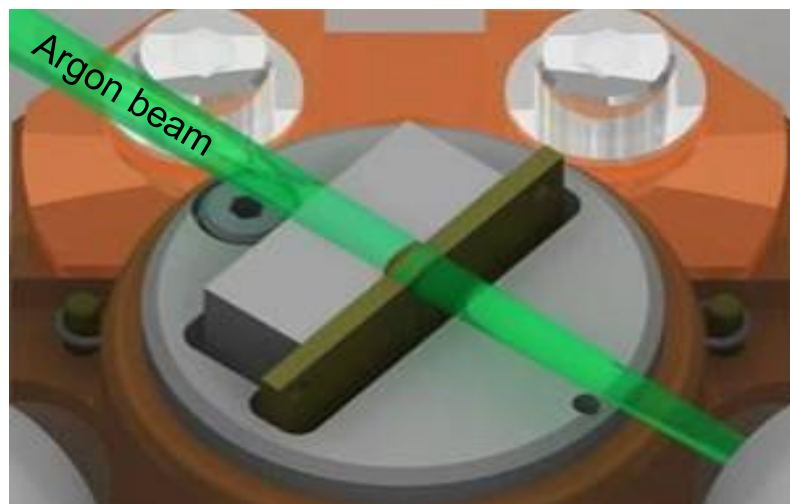


Figure A-12 Schematic showing the sample inserted in the ion milling device and the argon ion beam hitting the top surface of it.

Several series of parameters were trialled in order to avoid overheating of the samples. The final parameters were as follow:

- Beam accelartion voltage: 4kev,
- Gun angle 0°,
- Temperature: -40°C,
- Duration: 120 minutes

Figure A-13 show the SEM micrographs of the region that was etched. The top region of the sample can be identified as being the coating as it seems to have delaminated from the substrate under etching.

The thickness measured on the SEM micrograph of the etched area Figure A-13 was  $310 \pm 20\text{nm}$ . This figure is very different from the thickness that could be measured on an ultramicrotome cryo-section of the same sample that revealed an apparent coating that is  $525 \pm 18\text{nm}$ .

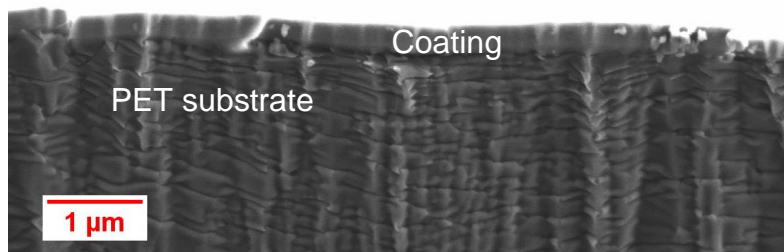


*Figure A-13 SEM micrograph othe sample treated via ion milling.*

Further experiments would we needed to understand the scattered data. One can think that some of the coating might have been etched away by the argon beam. This would be plausible if one considered that, the cohesion of the layer is not good enough. However, the most probable reason for the difficult to measure thickness following ion milling is the charging occurring at the surface of the coating, which seemed more intense than on other samples.

### Embedding and polishing

Another method was developed to measure the thickness. This method consists in embedding the sample (Figure A-14) in a two-part epoxy and polish it to a fine grain in order to reveal the surface of the coating. It is used in metallography to reveal phases.

A strip of sample was held in place in a metal clip (Figure A-14) and embedded in epoxy. The embedded sample was then polished with paper of different grades (from 600 $\mu\text{m}$  to 2400 $\mu\text{m}$  silicon paper) and finished with 3m and 2 $\mu\text{m}$  diamond polishing obtain a smooth surface and clear interface between coating, substrate and epoxy. The polishing was performed by hand and the samples were cleaned and ultrasonic ethanol bath in between each step). The quality of the polished surface was initially evaluated with optical microscope before the samples were analysed with the SEM.

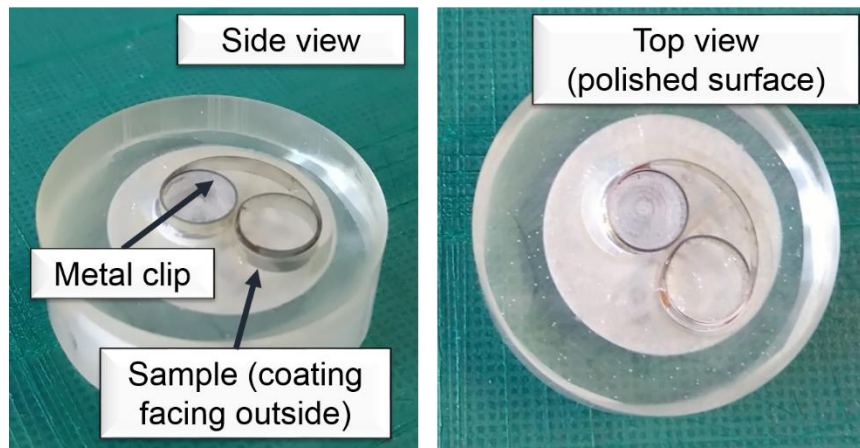


*Figure A-14 Embedded sample to be polished to reveal the interface between coating and substrate.*



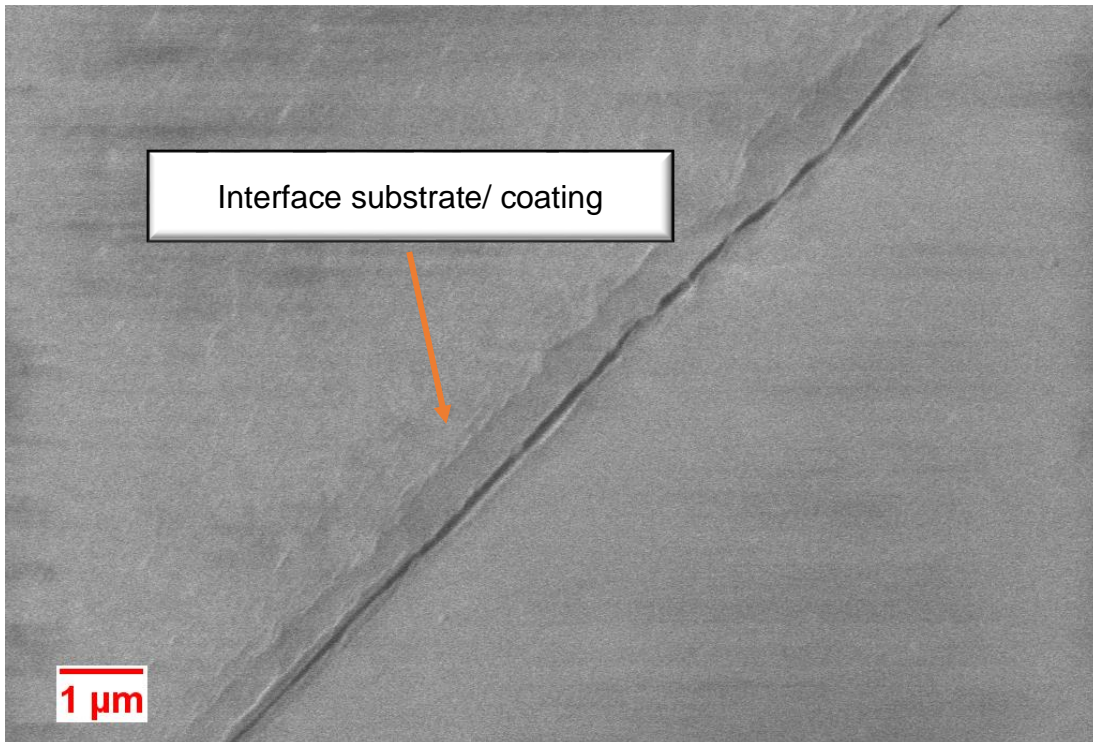


*Figure A-15 SEM micrographs showing of a sample after embedding and mechanical polishing.*

It is difficult to identify areas as actual interface between the coating and the substrate. However, if one considers that the slight difference in contrast in the micrograph indicated the presence of the coating, then the thickness of that coating is measured to be  $630 \pm 50\text{nm}$ . For this sample, it does not match which thicknesses measured after ion milling  $310 \pm 20\text{nm}$  and cryo ultramicrotomy  $525 \pm 18\text{nm}$ . These results are very scattered because the identification of the coating relies on subjective criteria and interpretation.

### **Comparison between techniques**

Table A-1 reports the various thickness measurements that were made possible with the techniques mentioned in Appendices A. the data shows a variability in the measured thickness that is both depended on the samples and on the technique. However, the thicknesses of sample N and Q have good consistency across the techniques, which is a starting point. Further

investigations would be needed in order to understand what made the sample not suitable for given techniques. (Mechanical properties might be the main impact factor)

In conclusion, the difficulty to find a common, repeatable technique to measure the thickness of SiO<sub>x</sub> technique was one of the major limiting element in the interpretation of the barrier performances. Indeed, barrier performances are known to be linked to thickness. Similarly, the thickness is directly impacted to the process parameters. Therefore, all interpretation is diffusely t without knowing exactly without a doubt what the thickness is.



## Appendix A Investigation of Thickness

*Table A-1 SiO<sub>x</sub> coating thickness measurements. Comparison of thicknesses measured using different techniques.*

Sample	WLI	Room temperature microtome	Ultramicrotome	Embedding + polishing	Ion milling
A	797 ± 13.6	776.9 ± 20	Not processed	Not measurable	Not measured
B	256 ± 47.8	Not suitable			
C	854 ± 62.3				
D	958 ± 39.7				
E	812 ± 104				
F	No step edge available		775 ± 21.4**		
G			736 ± 71.7**		
H			Not processes		
I			253 ± 30.4**		
J			283 ± 47.4**		
K			449 ± 67.2	Not processed	
L		±	718 ± 86.3*		
M		520 ± 37.9	681 ± 51.9*	681 ± 52	
N		583 ± 87	408 ± 27		
O		504 ± 37.8	Not processed	Not measurable	
P	504 ± 99.7				
Q			525 ± 18*	465 ± 43	310 ± 20

\* Samples prepared via cryo ultramicrotomy\*\* samples prepared at room temperature via ultramicrotomy

### **Conclusion**

It is clear from a work that the measurement of the thickness of SiO<sub>x</sub> coatings deposited by PECVD onto 120µm PET is not as straightforward as might be expected. Despite the easy breaking of some sample, the mechanical properties vary a lot from one sample to another.

Therefore, it is recommended for one sample to follow these steps:

Use microtomy and try to find areas where the coating has come off, if none can be found, the sample can be embedded and polished. However, it can be long and tedious

## **Appendix B Study of the morphology with the atomic force microscope**

A study of the morphology of the SiO<sub>x</sub> coating deposited with injection of CO<sub>2</sub> (refer to Section 6.1) was conducted with the aim of evaluating the suitability of the technic for such sample and the potential measurement of roughness.

All the micrographs were acquired externally at NTMDT by Dr Ashvin. The analysis was also done there.

The system used was the Solver Nano from NTMDT as shown in Figure A-16. The calibration of the system was confirmed to be less than 2% error (which is the tolerance of the calibration grating used). The system was used in closed loop. The sensor height data and the phase data were recorded. The AFM was used in semi-contact mode (intermittent contact/tapping). All the scans reported in this section have been carried out at angle of 0° unless stated differently. The topography and phase scan are presented after treatment of the image consisting of removing the mean plan.



*Figure A-16 Picture of the Solver Nano on a table top active vibration isolation system use for the study of prophology.*

The phase data was also recorded. The probe used was the AppNano ACT. Any vibration that can affect the measurements were isolated thanks to the NTMDT tabletop Active damping system. A Solver Nano Bungee system was also used to confirm that some features observed were not produced by environmental noise. However, all the data used in this report are with the active tabletop vibration isolation system.

The samples mentioned in section 6.1 were analysed. For further details on process parameters, the reader should refer to the data presented in that section.

- Sample 03: reference sample,
- Sample 02: 100SCCM CO<sub>2</sub>,
- Sample 03: 200SCCM CO<sub>2</sub>,
- Sample 04: 500SCCM CO<sub>2</sub>,
- 120µm PET substrate.

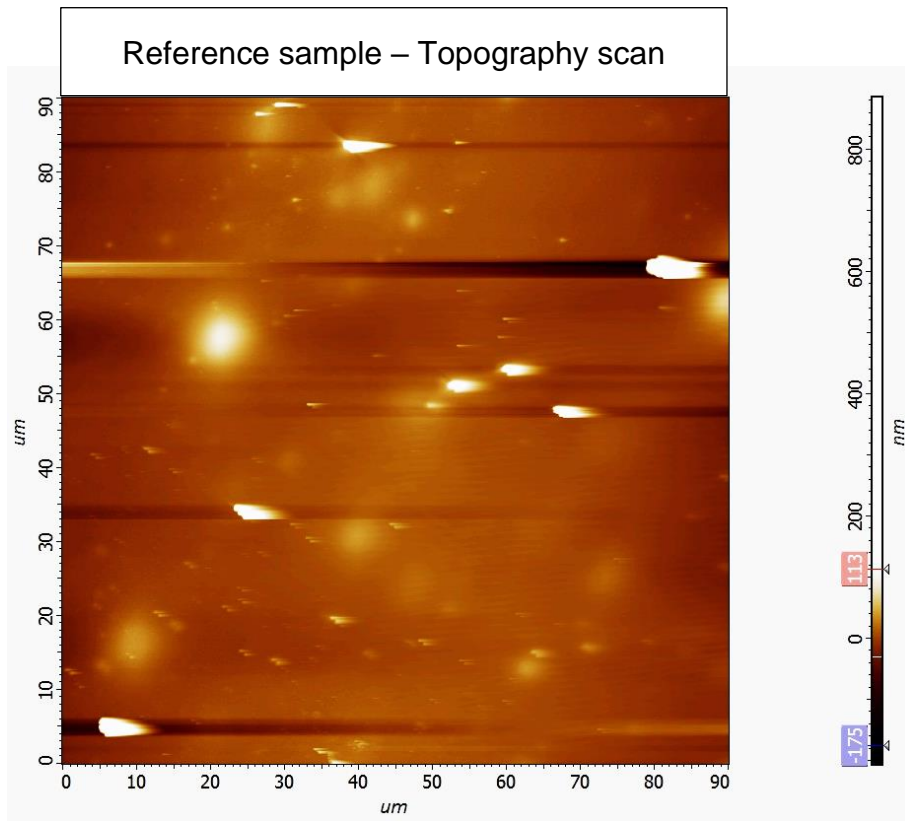
An internal reference sample (from the company) was first used to set the device up and check it was measuring properly

For all samples, where possible three different area sizes were chosen to evaluate the accuracy to which the AFM could probe the surface. These sizes were as follow:

- 90µm x 90µm,
- 20µmx 20µm,
- 5µmx 5µm.

### **Reference sample**

Figure A-17 shows both the topography and phase scan performed on the reference sample on a 90µmx90µm area.



Reference sample – Phase scan

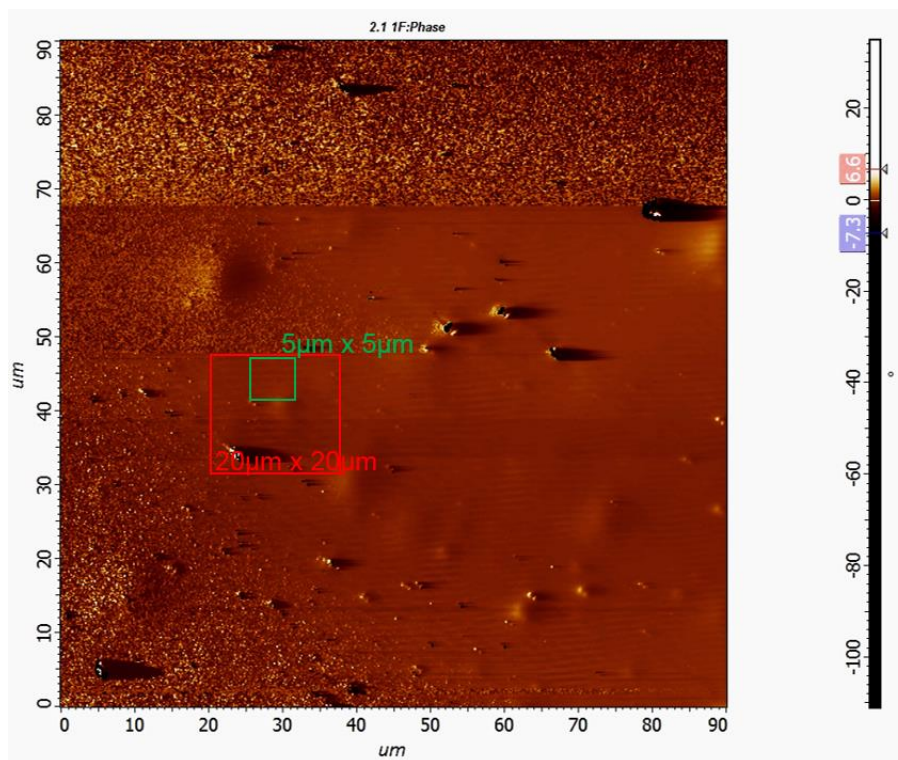


Figure A-17 AFM scan of the reference  $\text{SiO}_x$  sample. Scan size  $90\mu\text{m} \times 90\mu\text{m}$ . The top image is the topography scan and bottom image is the phase scan.

There are several large features from  $100\text{nm}$  to  $450\text{nm}$ . This makes tracking rather difficult. In the flatter regions, we can still see striped structures. The left lower half of the image appears to contain some artefacts caused by a double tip. As we scan from down upwards in this image, we no longer see this effect in the upper half of the image. Some debris must have adhered to the tip causing double tip effect. Those debris were subsequently brushed off as the tip collided with another large feature. However, the phase image in figure 2-3 highlight the grainy/noisy aspect of the surface on the lower left. This suggests that the material on the lower left may be different/have a different structure compared to that on the right. The large peak at vertical position about  $68\mu\text{m}$  affects the probe in such a manner that the phase image is completely grainy.

Additional scans were performed in smaller  $20\mu\text{m} \times 20\mu\text{m}$  (in the position of the red square) and a smaller  $5\mu\text{m} \times 5\mu\text{m}$  square in approximately the position

of the green square for further investigation. Both the scans are presented in Figure A-18.

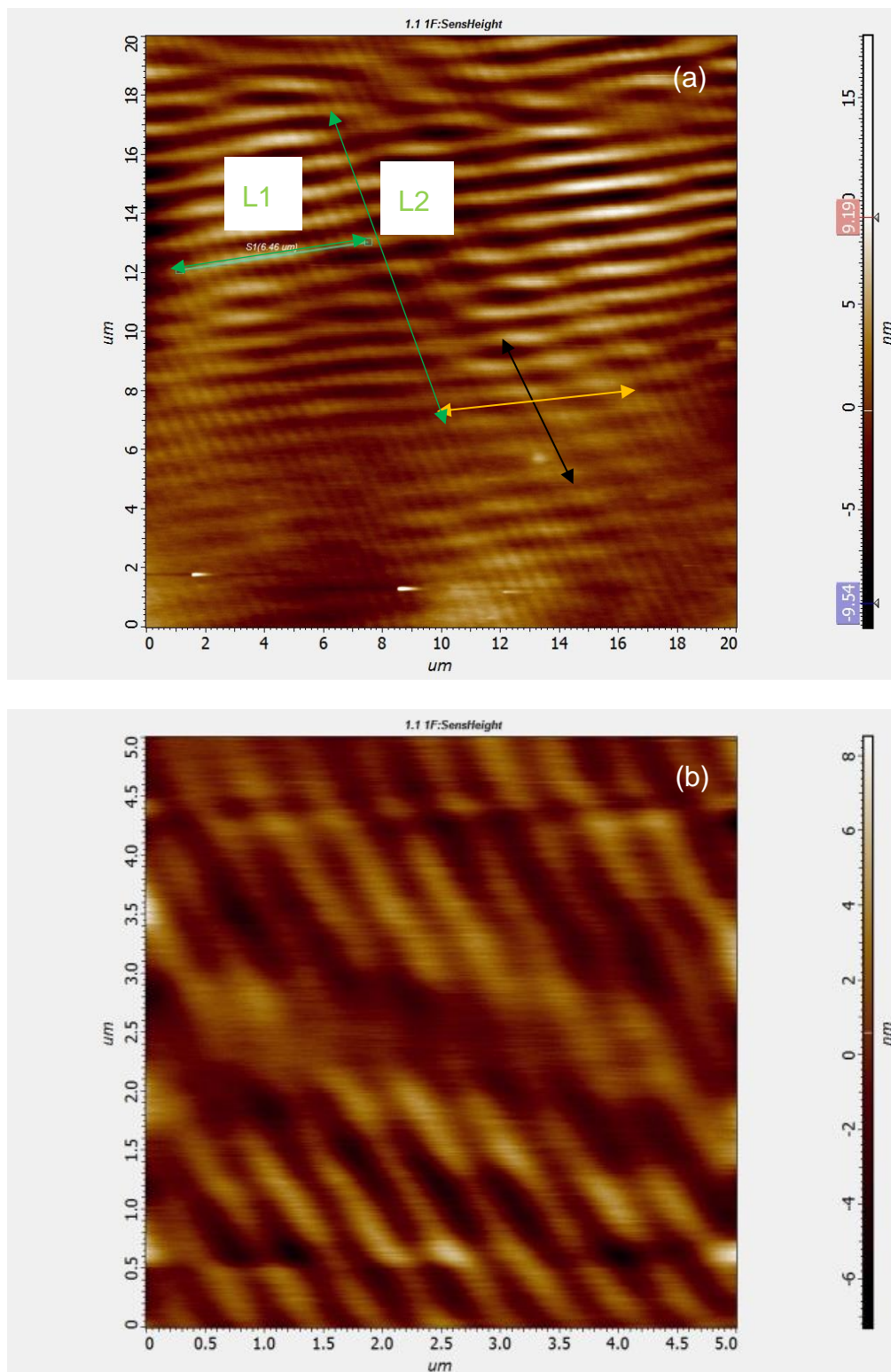


Figure A-18 AFM scan of the topography of the reference  $\text{SiO}_x$  sample. Scan size  $20\mu\text{m} \times 20\mu\text{m}$  (a) and  $5\mu\text{m} \times 5\mu\text{m}$  (b). The length of line L1 is  $6.46\mu\text{m}$  and the length of line L2 is  $9.80\mu\text{m}$ .



In the top half of the 20 $\mu$ m $\times$ 20 $\mu$ m, one can observe a row-like superstructure (A) in an almost vertical direction indicated by the black arrow with a periodicity of approximately 500nm. Adjacent rows undulate in groups of 6-8 (B) along the direction of the yellow arrow such that the height of the rows vary 1nm to 6nm. Along the direction of the rows (indicated by the black arrow), the superstructure has an additional undulating wave-like formation(C) with a periodicity of 950nm. The overall structure looks like a superstructure of rows superimposed on rows of oval shaped clusters in some areas.

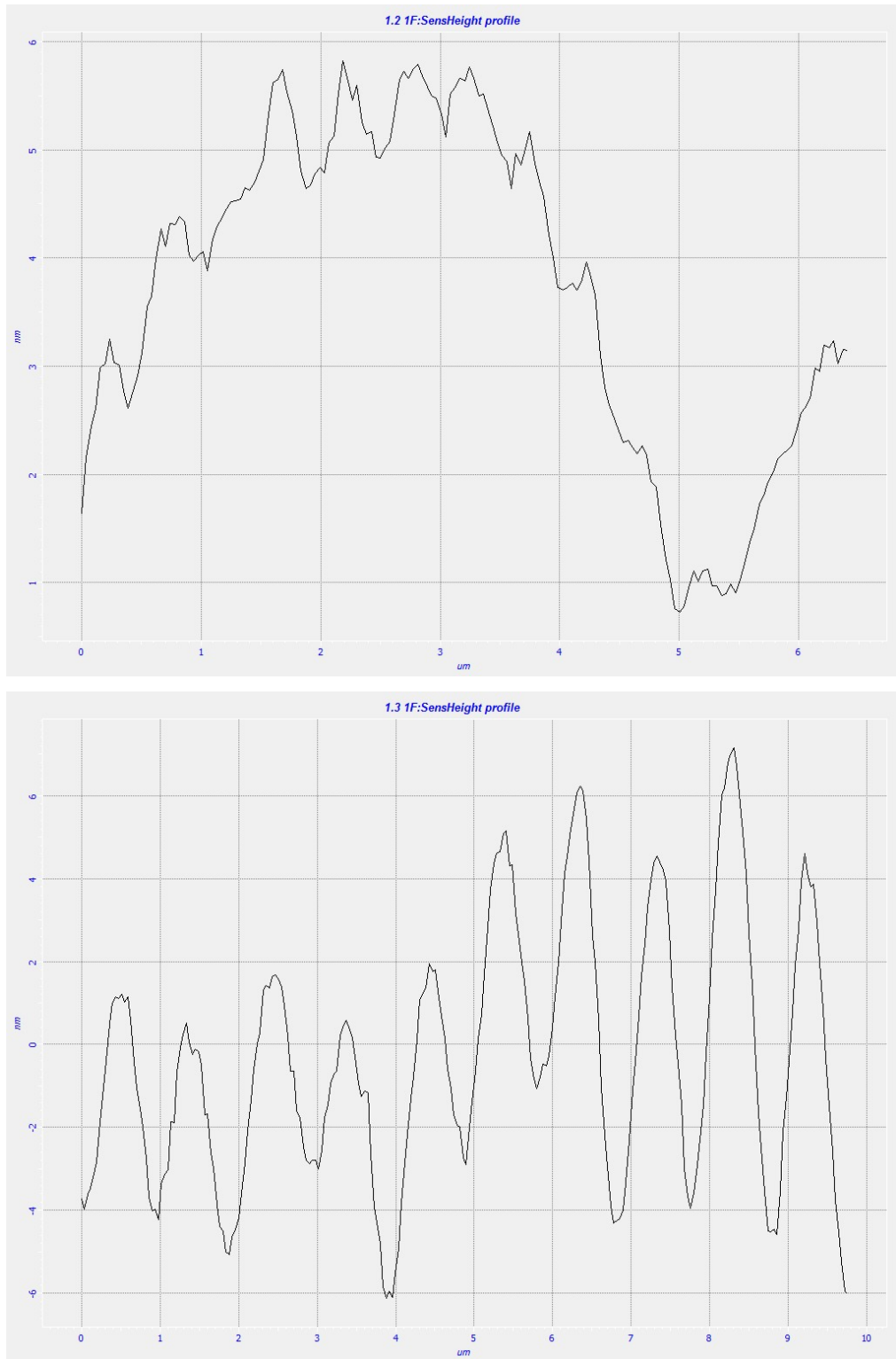
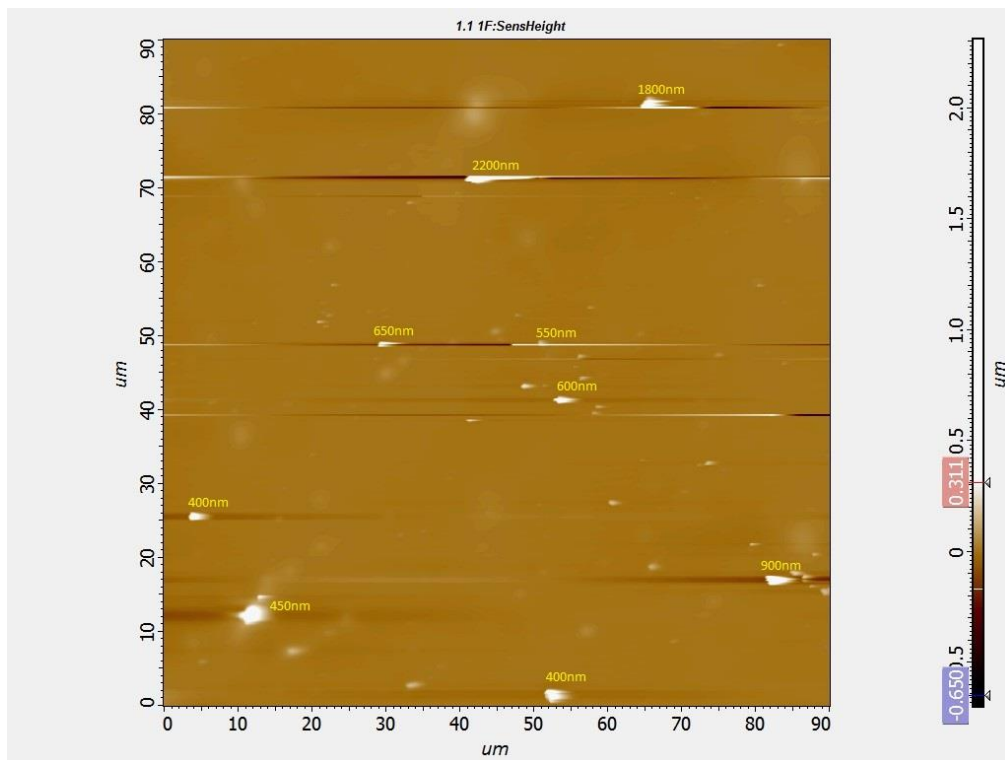


Figure A-19 Profiles measured along the green lines S1 (top image) and S2 (bottom image) shown in Figure A-18.

Figure A-19 shows that there is a certain waviness on a sub-micron level. This waviness is more pronounced in the vertical direction. The height of the peaks varies between 0.1nm and approximately 7nm. This confirms that the waviness is not artefact but might be coming from the coating itself. The resolution in these images is too low to derive any additional information.

### Sample 02 - 100SCCM of CO<sub>2</sub>

The topography and phase scans of the second sample are presented in Figure A-20.



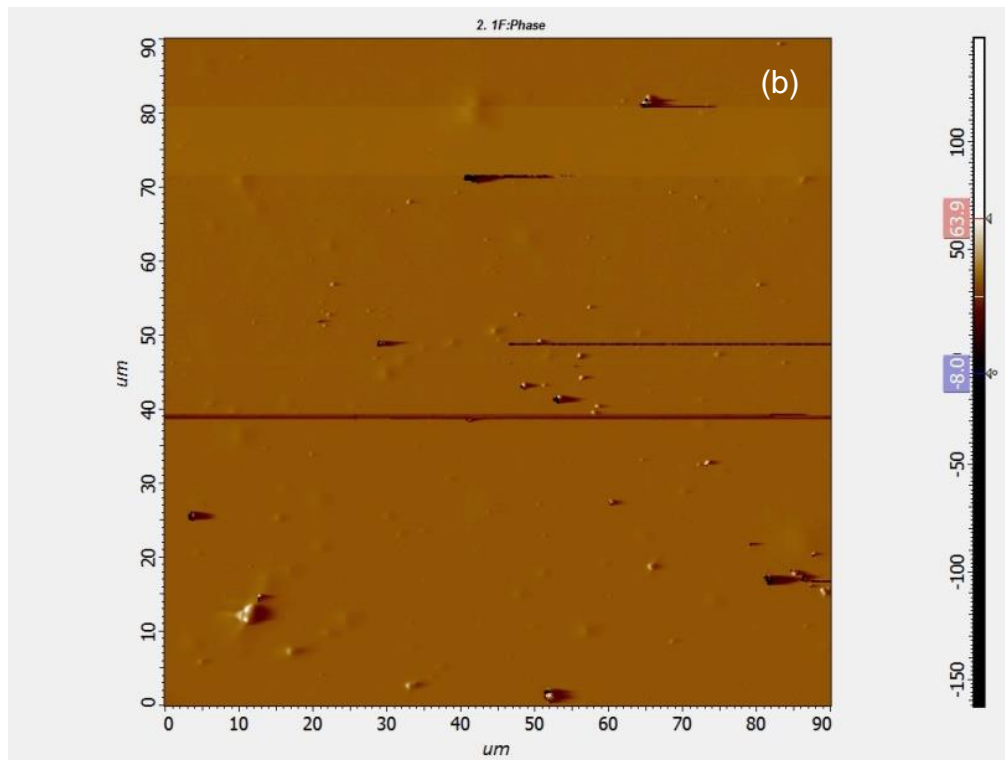
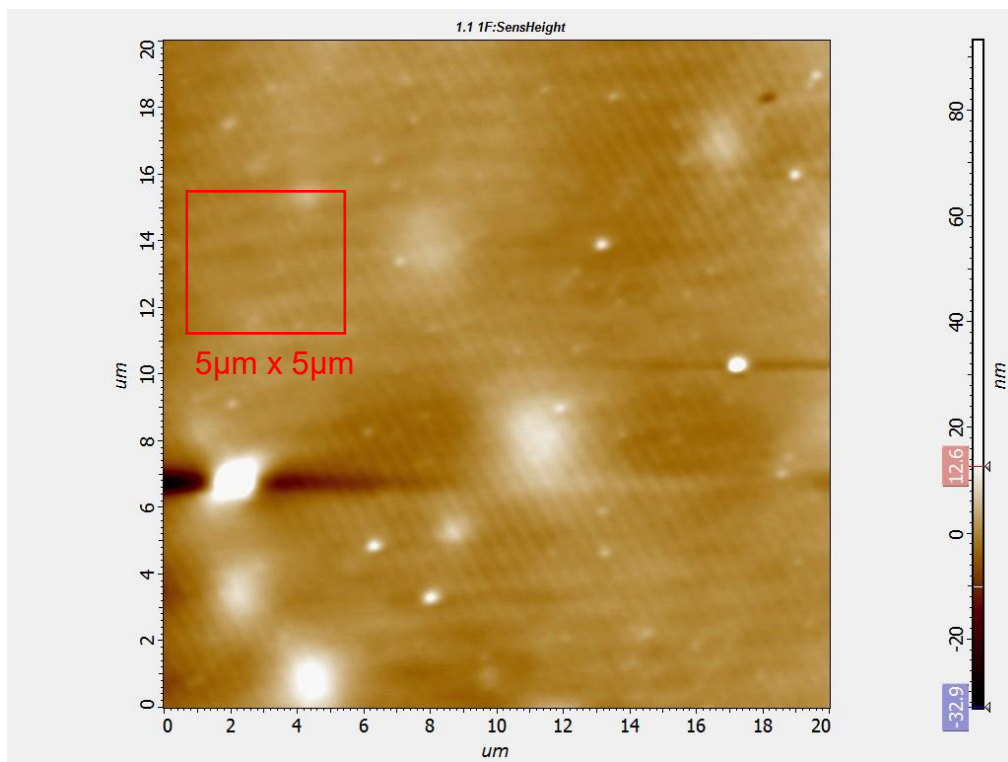


Figure A-20 AFM topography (a) and phase (b) scan of the  $\text{SiO}_x$  sample deposited with injecting 100SCCM of  $\text{CO}_2$  into the plasma. Scan size  $90\mu\text{m} \times 90\mu\text{m}$ .

Numerous sharp features that are between 100 and 230nm in height appear on the surface. The phase scan reveals a difference in contrast between some of the features suggesting that they may be of different material/contaminants. Some of them are likely to be the antiblock particles and others some contamination, the nature of which must be determined (i.e. dust).



*Figure A-21 AFM topography scan of topography the SiO<sub>x</sub> sample deposited with injecting 100SCCM of CO<sub>2</sub> into the plasma. Scan size 20µm x 20µm. Scan taken in flat region away from the very large particles.*

The surface presents a lot of particles less than 40nm in height but there are a few as tall as 80nm even in the flatter regions. In the background, a row like superstructure is superimposed on the wave like formation. Those features are similar to the waves observed on the reference sample (Figure A-18).

An additional 5µm x 5µm scan taken in the position of the red square is presented in Figure A-22.

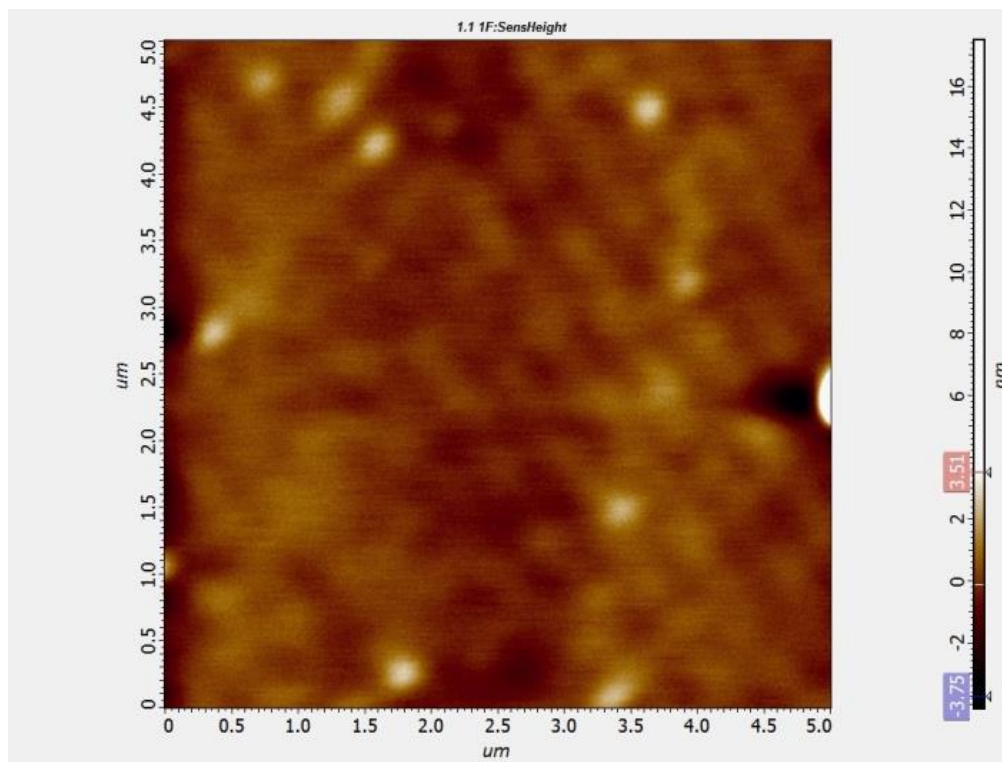


*Figure A-22 AFM topography scan of the SiO<sub>x</sub> sample deposited with injecting 100SCCM of CO<sub>2</sub> into the plasma. Scan size 5μm x 5μm.*

Despite the poor resolution due to blunt/damaged tip, it is possible to make out that the heights of the rows mostly vary between 1nm and 2nm in heights and 400-600nm wide. The bright spots are 4nm to 6nm in height. One can clearly see the grainy structure of the sample on the topography scan in Figure A-22.

**Sample 03 - 200 SCMM of CO<sub>2</sub>**

The first scan presented in Figure A-23 is a topography scan of a 90µm x 90µm sized area.

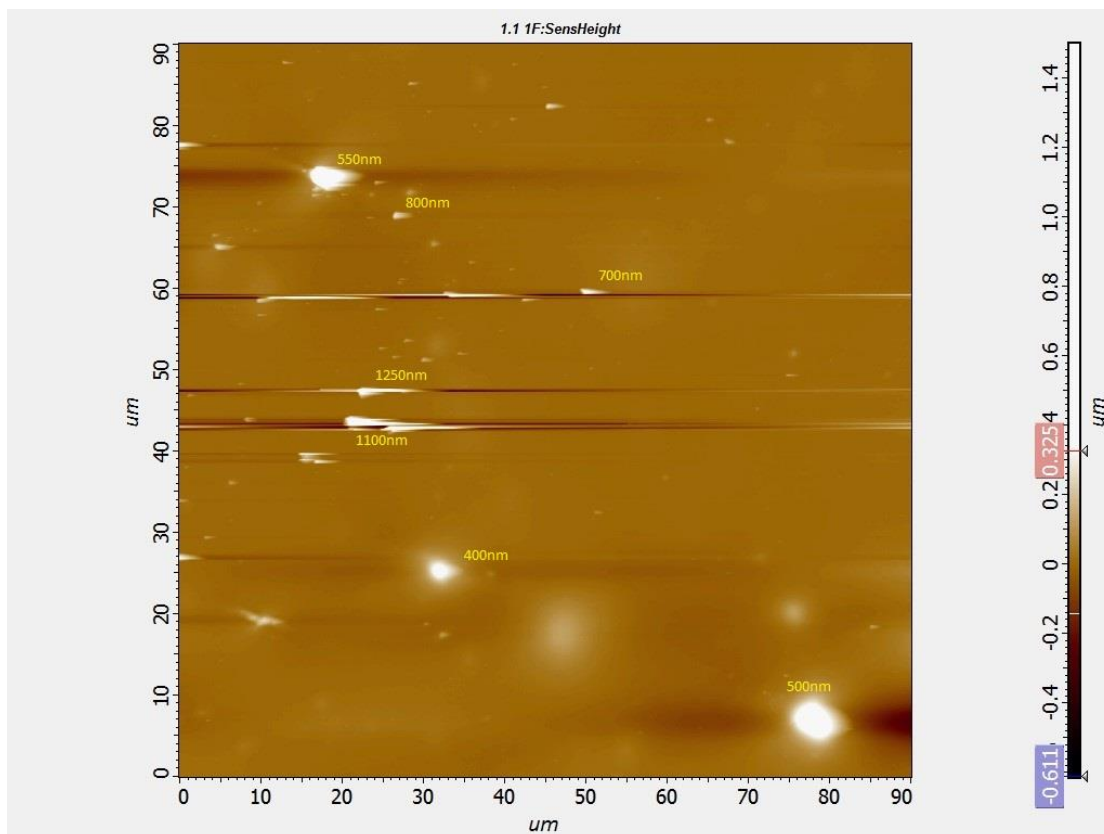


*Figure A-23 AFM topography scan of topography the SiO<sub>x</sub> sample deposited with injecting 200SCCM of CO<sub>2</sub> into the plasma. Scan size 90µm x 90µm. The particles height is annotated next to them.*

One can see the presence of numerous particles on the surface with sizes varying between 1µm and 5µm. there is also a variation on the height of those particles (between 400nm and 1.1µm). Those particles could be contamination, as the antiblock are not expected to be larger than 1µm in diameter. Those contaminants can also be identified more clearly on a 20µm x 20µm scan as shown in Figure A-24.

The absence of the wavy structure can be noted in the flat regions. The phase scan shown the same features and is therefore not presented here.



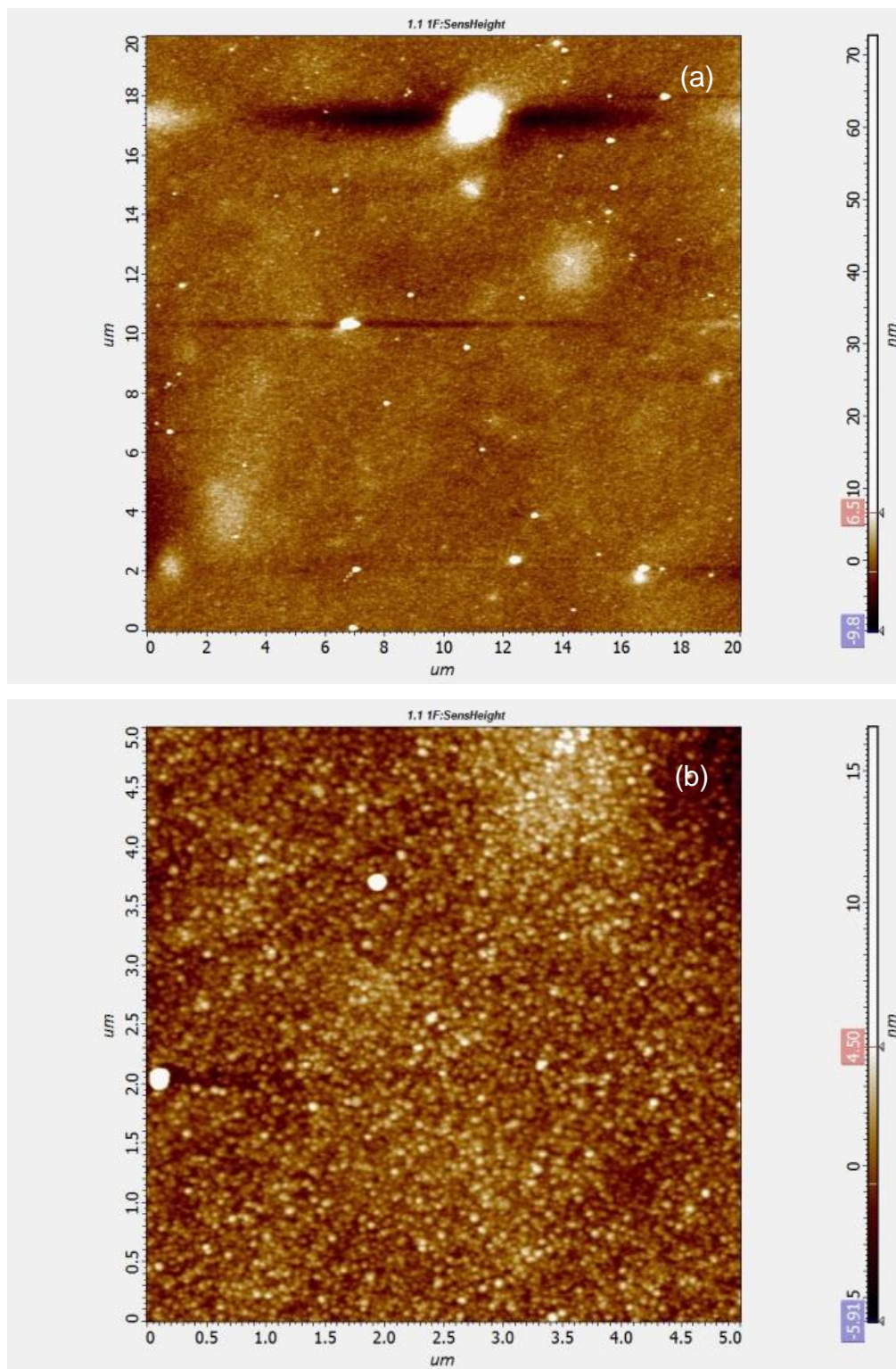


Figure A-24 AFM topography scan of topography the  $\text{SiO}_x$  sample deposited with injecting 200SCCM of  $\text{CO}_2$  into the plasma. Scan (a) is  $20\mu\text{m} \times 20\mu\text{m}$  in size and scan (b) is  $5\mu\text{m} \times 5\mu\text{m}$  in size .



Both scans in Figure A-24 confirm the absence of row-like and wave-like structures in the flatter regions. In addition, the smaller scan (5 $\mu\text{m}$  x 5 $\mu\text{m}$ ) exhibits the grainy aspect of the surface.

**Sample 04 - 500SCCM of CO<sub>2</sub>**

The 90 $\mu\text{m}$  x 90 $\mu\text{m}$  and 20 $\mu\text{m}$  x 20 $\mu\text{m}$  topography scans of the sample produced with 500SCCM of CO<sub>2</sub> are presented in Figure A-25.

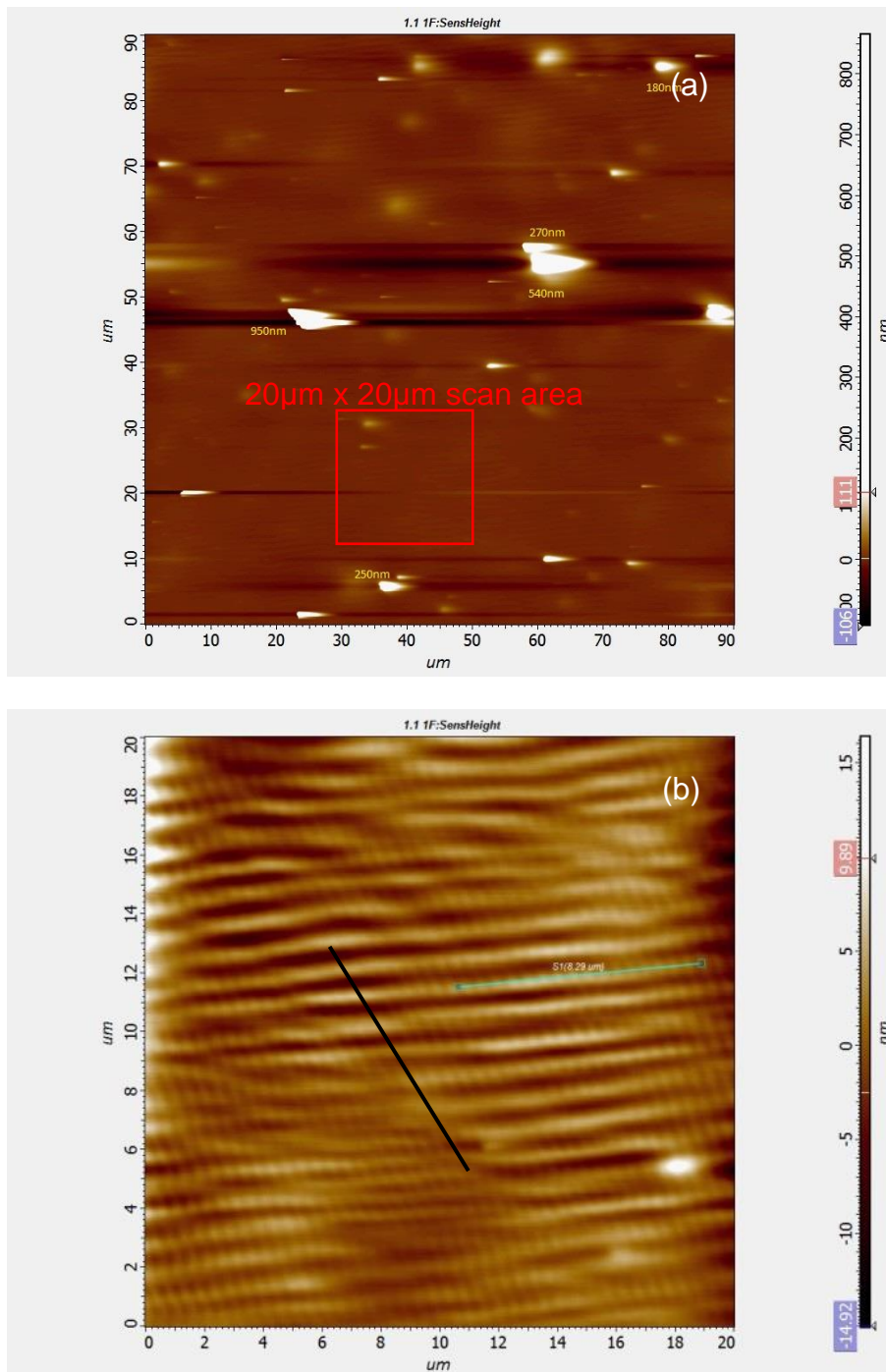


Figure A-25 AFM topography scans of SiO<sub>x</sub> sample deposited with injecting 200SCCM of CO<sub>2</sub> into the plasma. Scan (a) is 90 $\mu\text{m}$  x 90 $\mu\text{m}$  in size and scan (b) is 20 $\mu\text{m}$  x 20 $\mu\text{m}$  and was taken in the square area highlighted in Scan (a).

The wavy structure is observable in both directions (black and green lines). However, the waviness in the direction of the green line is more likely to be a periodic artefact as the periodicity is very small, very well defined and clear. In the case of scanning artefact, they will not rotate as the angle of scan is changed. Therefore, in the case of this series of samples, one can be confident that the structure observed in the direction of the dark line is coming from the sample.<sup>13</sup>

The waviness is confirmed in the 5 $\mu\text{m}$ x5 $\mu\text{m}$  scan shown in Figure A-26.

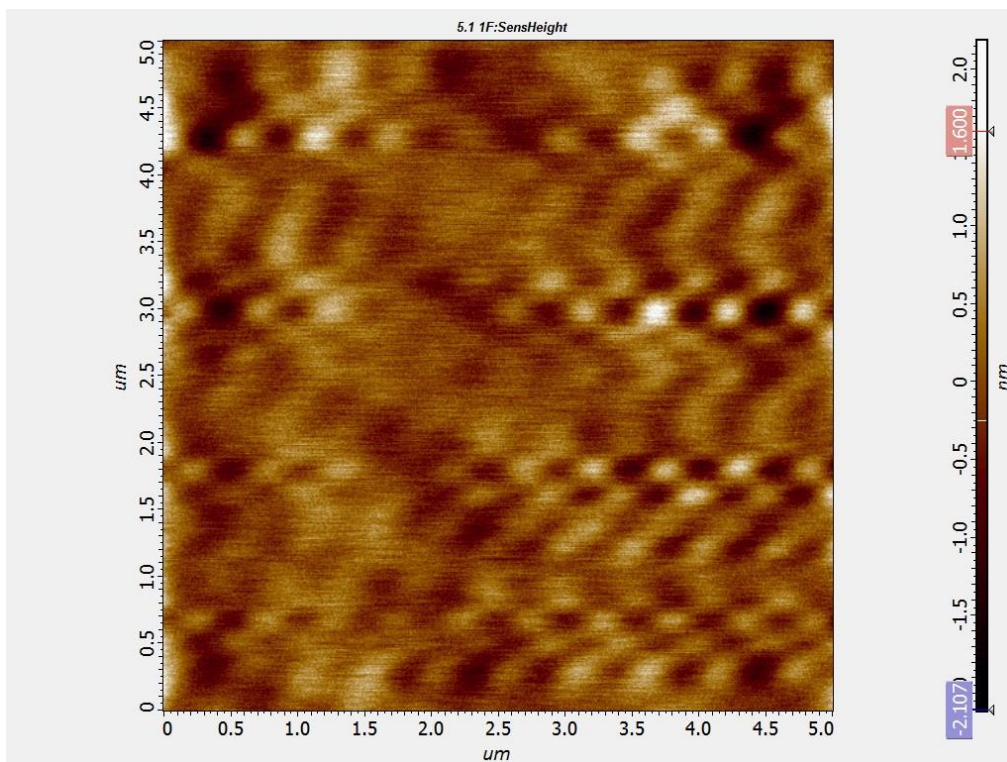
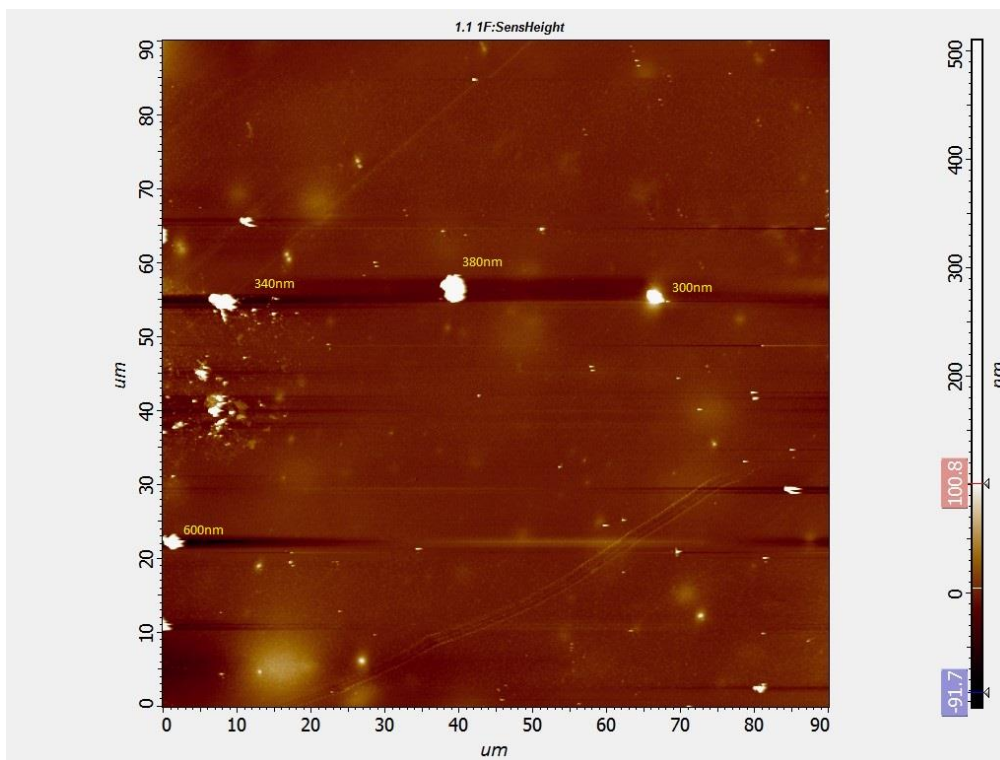


Figure A-26 AFM topography scans of SiO<sub>x</sub> sample deposited with injecting 200SCCM of CO<sub>2</sub> into the plasma. Scan size is 5 $\mu\text{m}$  x 5 $\mu\text{m}$  in size.

<sup>13</sup> Noise can also produce periodic artefacts. These will not rotate as scanning angle is rotated. Changes in the frequency of noise will cause changes but here one sample has not shown these structures, which means they are likely to be genuine.

In order to understand the variation in surface topography of the coated samples the substrate's surface was also analysed. Figure A-27 shows the 90µm x 90µm topography scan.



*Figure A-27 AFM topography scan of the surface of the 120 µm thick PET bare substrate on which the SiO<sub>x</sub> coatings have been deposited.*

Some particles can be observed on the PET substrate that were observed on the coating. It is more likely that they are contamination rather than particles embedded in the substrate (such as antiblock).

The periodic wave-structure observed on the coated samples cannot be seen on the substrate at this scan size. However, when performing the phase scan of a smaller region 5µm x 5µm in a flat region, the wave-structure appears clearer as shown in Figure A-28.



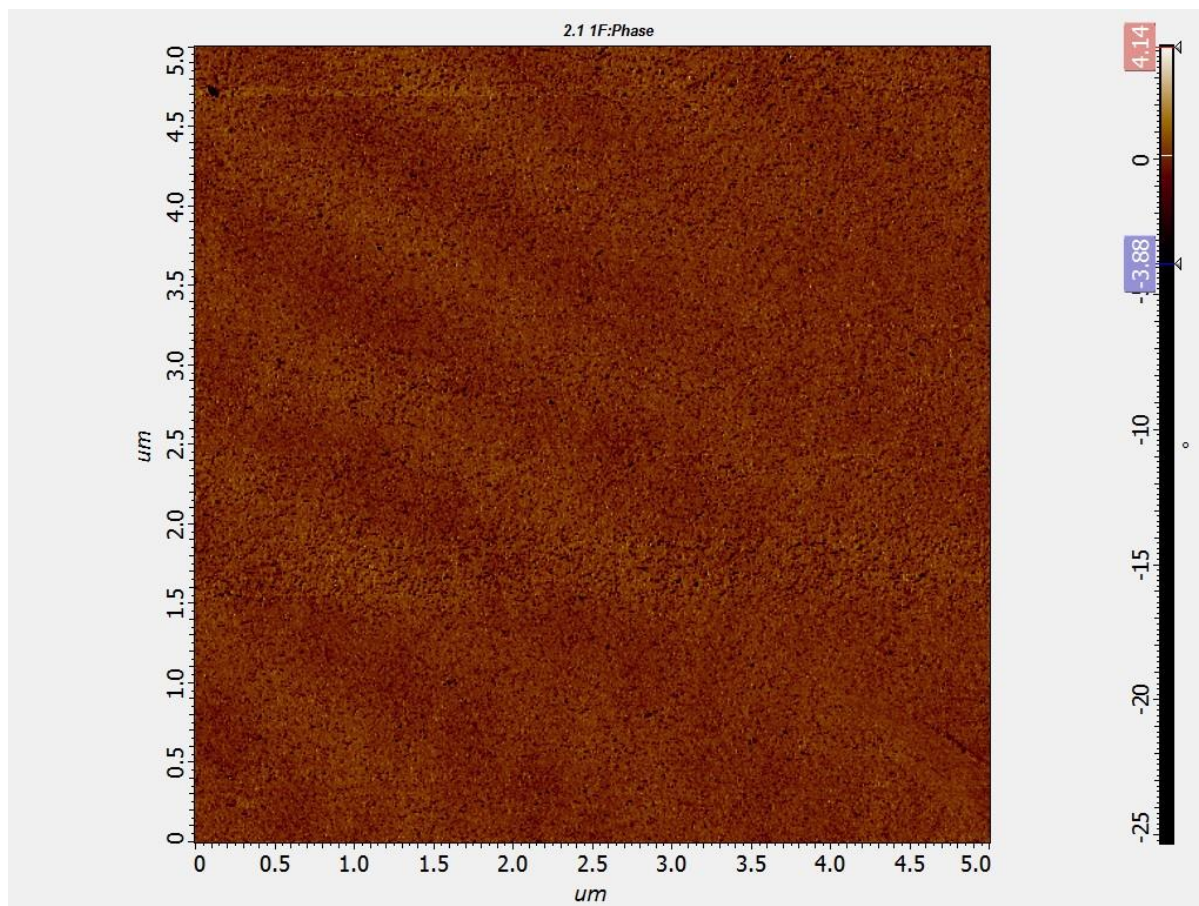


Figure A-28 AFM phase scan of the surface of the 120 $\mu\text{m}$  thick PET bare substrate on which the  $\text{SiO}_x$  coatings have been deposited. Scan size 5 $\mu\text{m}$  x 5 $\mu\text{m}$ .

Both the small and big waves can be seen. Considering this scan and the previous scans of the coatings, it is confirmed that the substrate has a wavy substructure and that the silicon oxide coating conforms to this structure. On the other hand, this substructure appears to be more pronounced on the coated substrate. One explanation for that effect could be that the contact with the rollers in the roll-to-roll coater amplifies the waves.

Despite the difficulty in tracking due to the presence of large particles, and the wave-like structure some roughness data can be reported as an overview. The roughness data provided by the company does not include the roughness of the PET and is reported in Table A-2.

*Table A-2 Roughness measurement done on the 20 $\mu$ m x 20 $\mu$ m and 5 $\mu$ m x 5 $\mu$ m topography scans of each sample (reference sample, produced with 100SCCM, 200SCCM, 500SCCM of CO<sub>2</sub> injected into the plasma)*

Sample	20 $\mu$ m x 20 $\mu$ m scan		5 $\mu$ m x 5 $\mu$ m scan	
	R <sub>a</sub> (nm)	R <sub>q</sub> (nm)	R <sub>a</sub> (nm)	R <sub>q</sub> (nm)
<b>Reference sample</b>	1.9	2.5	1.8	1.4
<b>Sample 01 (100SCCM CO<sub>2</sub>)</b>	1.8	3.5	0.4	0.6
<b>Sample 02 (200SCCM CO<sub>2</sub>)</b>	1.2	2.5	0.9	1.3
<b>Sample 03 (500SCCM CO<sub>2</sub>)</b>	14	16	0.3	0.4

The roughness data shows inconsistency when measured on the larger areas (20 $\mu$ m x 20 $\mu$ m) as the probe is encountering the various particles and contaminants. Therefore, only the 5 $\mu$ m x 5 $\mu$ m scans are to be discussed. On the 5 $\mu$ m x 5 $\mu$ m areas, the influence of the particles is minimised as it is possible to select an area that doesn't have any of them. The limited roughness data shows that a very high (500SCCM) flow rate of CO<sub>2</sub> injected into the plasma is beneficial for the roughness as the average roughness is decreased by a factor almost two when the flow rate is increased from 100 to 500 SCCM. The higher roughness measured on sample 03 could be explained by the difficulty of tracking due to the presence of particles.

In conclusion, the AFM study of the roughness and morphology of the SiO<sub>x</sub> coated samples proved difficult due to the particles present on the surface that make the tracking difficult and therefore reduce the scan resolution. Smaller areas can be scanned more easily (5 $\mu$ m x 5 $\mu$ m) and show some wave-like structure. This substructure is most likely come from the underlying substrate structure and defects. A more throughout analysis is needed to confirm this structure.

## **Appendix C Study of adhesion**

### **Motivation**

The reliability of a thin film as a moisture and oxygen barrier is influenced by several factors related either to the coating itself or the environment or stresses that the coating might be exposed to over its lifetime, processing and conversion. Poor adhesion can cause delamination of the coating, or extreme wear, which should be avoided in the case of protective coatings. [80, 81]

According to the American Society for Testing and Materials (ASTM D907), adhesion is “the state in which two surfaces are held together by interfacial forces”.

Further theoretical explanation can be found in the following references [80, 132-134]

The peel test is one of the methods widely used in the measurement of adhesion for metalised thin films and was available to the author. In the case of metalised films the test is performed on a structure that is close to the actual final packaging application of the film, for comparison purposes. This involves laboratory lamination of the coating[3]. At first, the same lamination method was used on SiO<sub>x</sub> PECVD coating, in order to assess the suitability of the technique for this particular material. Lamination is a standard method used by the industrial partner (BML) to prepare AlO<sub>x</sub> and Al coatings to prepare the samples for adhesion testing. Therefore, it was interesting to determine the suitability of the technique for standardising the method to all the samples produced in the company.

### Methods and materials

In order to measure the adhesion, the film sample was first laminated to a CPP<sup>14</sup> sheet using a 2-component high performance PU adhesive (Rock-Paint RU-77, the hardener, H-7; supplied by DNP), a solvent-based adhesive lamination (with ethyl acetate) and 4g/m<sup>2</sup> (dry) of the adhesive. The mixture was applied to the SiO<sub>x</sub> surface with an RDS wire bar 12 to reach an approximate wet film thickness of 27.4µm. The dilution used was EA/RU-77/H7 = 30/10/1, i.e. 15 % solids). Lamination was conducted with a rubber roller (by hand). This method allows the final sample structure: PET/silicon oxide/adhesive/CPP to be formed. This final test sample was left to cure in an incubator for 24h at 55 – 57 °C.

Prior to the peel test, the samples were cut to 15 mm strips (standard for this peel test method). The PET side of the laminate was stuck down on an aluminium plate with double-sided adhesive tape. The CPP film was peeled off (with the coating) at a speed of 50 mm/min (peeling in machine direction of CPP and metallised PET), as shown schematically in Figure A-29.

---

<sup>14</sup> 70µm CPP film (corona side was facing the adhesive; film sheets supplied by DNP)



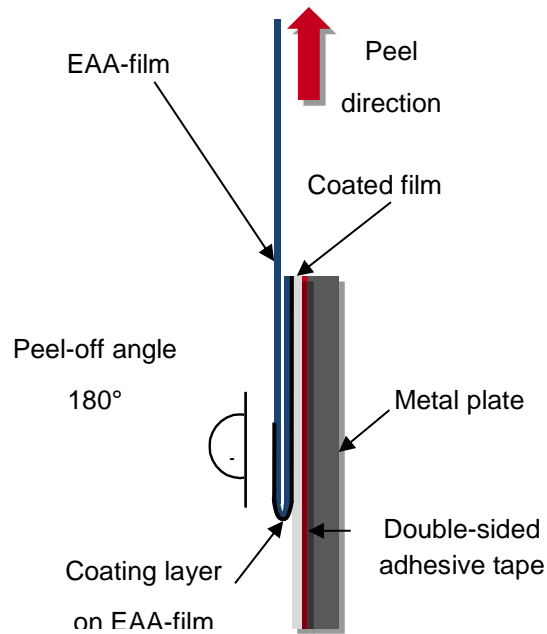


*Figure A-29 Cross-sectional view of sample during peel test (from [3])*

## Results

The initial test was performed on a 850nm thick sample. The laminated layer was peeled off at speed of 5mm.min. The result of the test is presented in Figure A-30

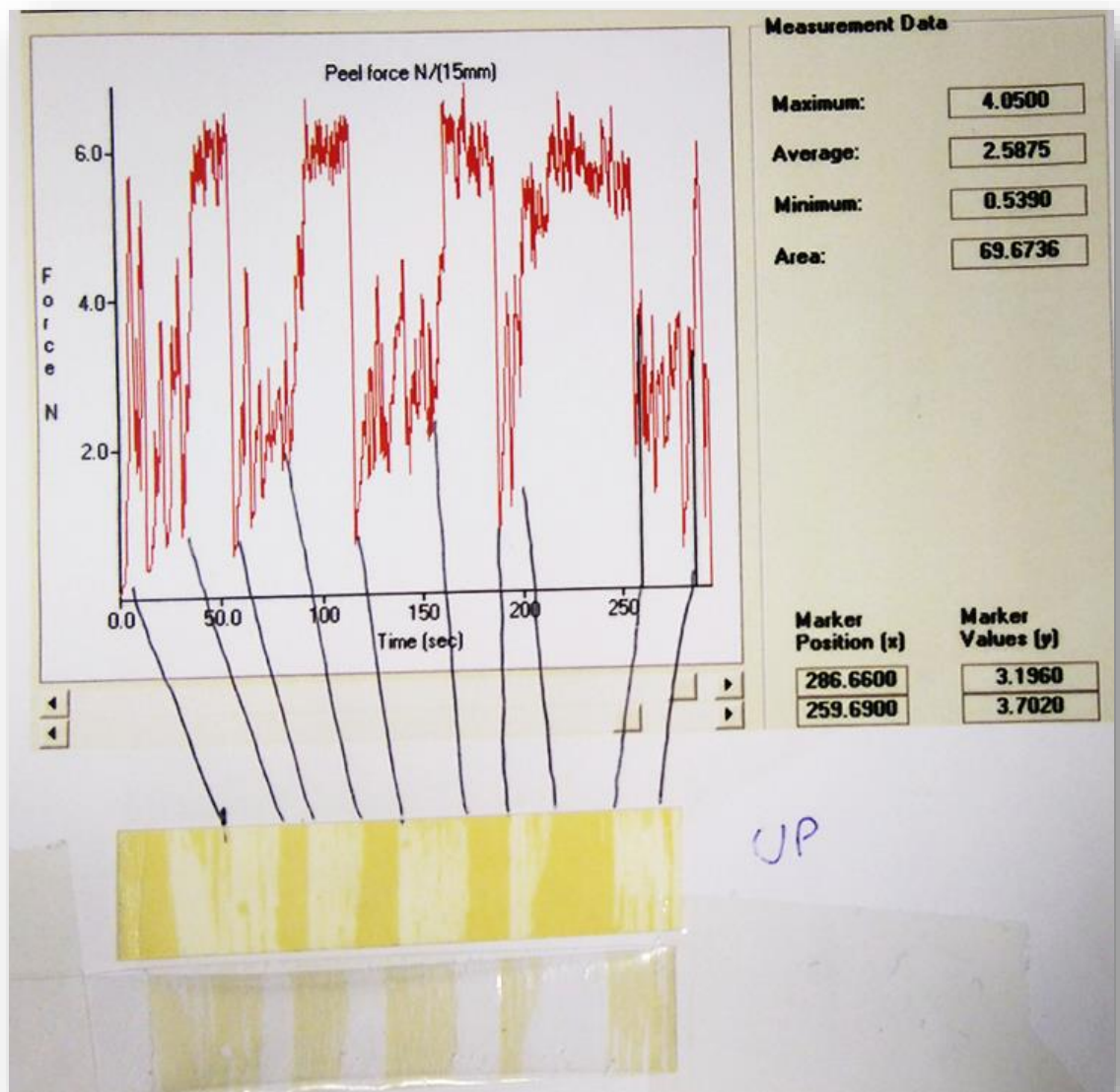


Figure A-30 Photograph showing results of the test on Sample A. Graph associated with the physical sample after the peel test.

It appears that the coating has been peeled off in certain areas and has not been peeled in other areas. This might be due to a higher adhesion of the coating to the PET substrate or might be an effect of the thickness of the coating. Further investigation is needed to understand the failure mode (cohesive failure in the thickness or adhesive failure in the interface).

### **Summary and conclusion**

Adhesion of SiO<sub>x</sub> PECVD samples was measured using a hand lamination technique in conjunction with a 180° peel test.

It appeared that the method was not appropriate for the type of coating as full removal of the coating was not achieved in all cases. Moreover, the laminate CPP strip seemed to be stretched (this might be due to the adhesion between the CPP and the adhesive being the higher than that of the adhesive to the SiO<sub>x</sub>).

On another note, another issue with peel test of SiO<sub>x</sub> coatings is the difficulty to evaluate full removal in the case of lighter coatings.

## **Appendix D      Study of plasma cure of acrylate**

### **Motivation**

Plasma curing consists of placing the product to cure in a plasma. This plasma is created from a carrier gas such as nitrogen. The reactive species created in the excitation process of the carrier gas (electron, ions, radicals<sup>15</sup> and photons) are all transferred to the liquid phase (acrylic monomer) and contribute to initiating the polymerisation.

Different groups have investigated plasma curing of acrylates. Elsner et al. recently found that a nitrogen medium frequency plasma could allow an acrylic coating to cure without the need to include a photoinitiator in the formulation[135]. They managed to cure up to 98% of thick (15 microns) TRPGDA coatings on glass. They explained that the cure is mainly made possible by the creation of photons in the range of 220nm wavelength; these photons are generated by the emission of non-oxygenated species.

Plasma polymerisation has been proven to be achievable for various acrylates and methyl acrylates polymers[136]. It was therefore interesting for the industrial partner to develop a method to cure acrylate coatings using a plasma.

---

<sup>15</sup> A radical is a specie that contains one or more unpaired electrons. Reactions between radicals involve the movement of single electrons. Single, radical electrons are usually represented by a dot (•).

### **Methods and materials**

Plasma curing was investigated on the pilot PECVD coater.

Several multifunctional monomers were tested among which was the SR399 from Sartomer.

The initial work was done on AlO<sub>x</sub> coated PET. The main aim was to determine whether the plasma created on the machine would provide sufficient cure and adhesion to the coating.

### **Results**

The main findings in this work were that it was possible to cure the surface of the topcoat; however, adhesion was poor for most of the acrylates/photoinitiator mixture. In this case low adhesion was demonstrated by performing the tape test according to the standard ASTM D3359.[137] tape test.

A typical result is presented in Figure A-31.

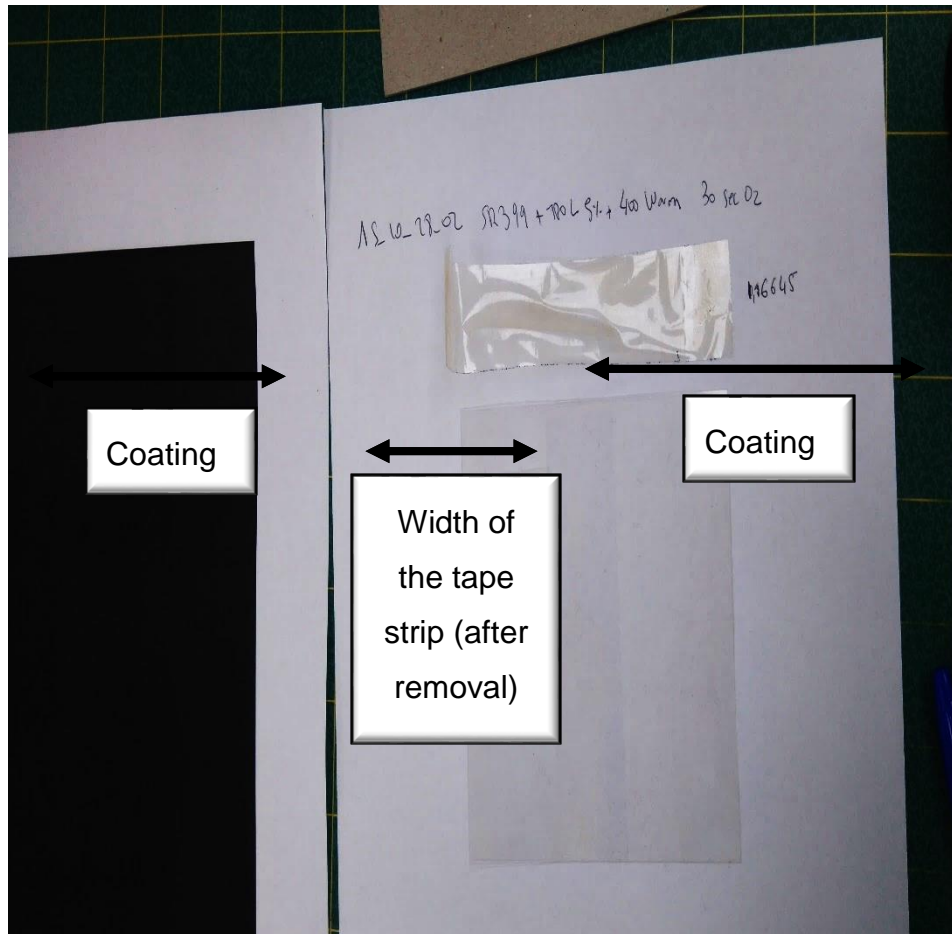



Figure A-31 Photograph of the acrylate (SR399+3% TPO-L) coated sample ( $\text{AlO}_x$  coated 120 $\mu\text{m}$  PET).

## Appendix E Substrate information

	<b>HEAD OFFICE:</b> Plot No. – 12, Sector B1, Local Shopping Complex, Vasant Kunj, New Delhi - 110 070 (INDIA). Tel: 0091-11-26139256 – 265, Fax: 0091-11-26125739 Web site: www.jindalpoly.com					
	<b>TECHNICAL SPECIFICATION SHEET (J-500)</b>					
<p><b>DESCRIPTION:</b> J500 is Transparent, Co extruded high clarity film having smooth surface, excellent clarity and good handling property</p> <p><b>APPLICATIONS:</b> High clarity film suitable for metallisation, holographic, high quality lamination and other general application.</p> <p><b>SALIENT FEATURES:</b></p> <ul style="list-style-type: none"> <li>• High clarity and Transparency</li> <li>• High surface gloss</li> <li>• Excellent Machinability</li> <li>• Excellent Mechanical Properties</li> <li>• Excellent Dimensional Stability</li> </ul>						
<b>TECHNICAL DATA</b>						
Properties	Test method	Unit	J-500			
<b>PHYSICAL</b>						
Thickness	ASTM D-374	Micron (Gauge)	23 (92)	36 (144)	50 (200)	
Yield	JPFTM	m <sup>2</sup> /kg (in <sup>2</sup> /lb)	31 (21800)	19.8 (13900)	14 (10000)	
<b>OPTICAL</b>						
Haze	ASTM D-1003	%	1.4	1.4	1.5	
Total luminous transmittance	ASTM D-1003	%	90	90	90	
<b>MECHANICAL</b>						
Tensile strength (Min)	MD	ASTM D-882	Kg/cm <sup>2</sup> (psi)	1900 (27000)	1900 (27000)	1900 (27000)
	TD	ASTM D-882	Kg/cm <sup>2</sup> (psi)	1800 (25600)	1800 (25600)	1800 (25600)
Elongation (Min)	MD	ASTM D-882	%	90	90	90
	TD	ASTM D-882	%	85	85	85
Coefficient of friction (Side-A / B) (Max)	St	ASTM D-1894	-	0.60	0.60	0.60
	Dy	ASTM D-1894	-	0.50	0.50	0.50
<b>THERMAL</b>						
Shrinkage (Max) (150 <sup>o</sup> C / 30 min)	MD	ASTM D-1204	%	2.80	2.80	2.80
	TD	ASTM D-1204	%	0.40	0.40	0.40
<b>SURFACE</b>						
Wetting tension (Min)	ASTM D-2578	Dyne / cm	44	44	44	
<p>The values given in this technical datasheet are typical performance data and are believed to be accurate. These are given in good faith but it is for the customer to satisfy of the suitability for its own particular purpose. JINDAL POLY FILMS LIMITED suggests the customer to confirm these values and product compatibility prior to their use and the company offers neither guarantee nor accepts any responsibility for the fitness of the product for any particular use.</p>						
JPFTM: JINDAL POLY FILMS TEST METHOD, MD: MACHINE DIRECTION, TD: TRANSVERSE DIRECTION						
<b>WORKS:</b> 28 - KM, Stone, Nashik - Igatpuri Road, Village : Mundegaon, Maharashtra Phone : + 91 2553 229100, 231002 / 3 / 5 Fax: + 91 2553 231004						

## **Appendix F      Public engagement and publications**

### **Oral presentations and posters**

- Management Meeting (annual update) presentation, Bobst Manchester Limited, February 2014
- Oral, MMU Research Symposium, September 2014 “ Transparent High Barrier for electronic encapsulation”
- Poster, Institute of Physics Early Career Research Meeting, Loughborough University, April 2016 (Best poster prize winner)



**Non-peer reviewed publications:**

N. Kaabeche, P. Kelly, L. Harland, N. Copeland, *Transparent High Barrier Coating for electronic encapsulation*, Proceedings of the 58<sup>th</sup> Society of Vacuum Coaters, Santa Clara, 2015

N. Kaabeche, P. Kelly, L. Harland, N. Copeland, *Development of PECVD moisture barrier coatings for electronic encapsulation*, Proceedings of the 59<sup>th</sup> Society of Vacuum Coaters, 2016 (in press).

### Transparent High Barrier Coating for Electronic Encapsulation

N.M. Kaabeche<sup>1</sup>, P.J. Kelly<sup>1</sup>, L. Harland<sup>2</sup>

<sup>1</sup>Surface Engineering Group, Manchester Metropolitan University, Manchester, United Kingdom

<sup>2</sup>Bobst Manchester Ltd., Lancashire, United Kingdom

---

#### ABSTRACT

Barrier coatings for use in electronic applications (such as flexible displays, digital paper, lighting, OLEDs and solar cells) are designed to protect the device from environmental influence, especially the permeation of oxygen and water vapour that can cause malfunctions. In addition, the barrier coatings must remain transparent and flexible. In this project, silicon oxide barrier layers were deposited onto a commodity grade bi-oriented polyethylene (BO-PET) via plasma enhanced chemical vapour deposition, using a pilot scale roll-to-roll coater. The aim was to optimise the deposited coatings by understanding the effect of the deposition parameters on the water vapour barrier properties and the physical and chemical properties of the coatings.

#### INTRODUCTION

Electronic devices and printed circuits are very sensitive to moisture. The ingress of moisture into the device is a potential source of corrosion, which decreases the efficiency and causes malfunctions [1]. In order to protect the product, it can be encapsulated with impermeable materials; ideally the whole encapsulate should not let more than  $10^{-3}$  g/m<sup>2</sup>/day of moisture permeate [2]. Glass substrates provide an excellent barrier, but they are expensive to produce, heavy and prone to damage due to lack of mechanical ductility. Consequently, development is underway for high barrier transparent coatings on polymeric substrates to provide a cheaper, lighter and more flexible alternative to glass. However, these materials are in general more permeable than glass and a functional film needs to be applied onto them to decrease the overall water vapour transmission rate. SiO<sub>x</sub> (silicon oxide) coatings deposited onto polymeric web by techniques, such as plasma enhanced chemical vapour deposition (PECVD), appear to offer a solution as they exhibit good optical properties over the solar spectrum, excellent resistance to mechanical stress and good stability and durability with exposure to UV radiation and extreme climates [2]. These properties are crucial to ensure a long service life for the device.

The barrier performance of SiO<sub>x</sub> coatings are, in general, dependant on the composition and the structure of the coatings [3-5]. For example, it is reported that oxygen migrates through voids, defects and pores in the coatings. However, although oxygen permeation mechanisms have been well investigated with regard to PECVD SiO<sub>x</sub> coatings [6], permeation of water vapour remains difficult to understand, due to the potential physical and chemical interactions of moisture vapour with the coatings. [5, 7]. Multi-layer coatings have been investigated as a means of increasing barrier, but this also increases the complexity and cost of the process.

In this project, single layer PECVD SiO<sub>x</sub> coatings were deposited onto commodity grade substrates with the aim of developing a lower cost solution. This paper will therefore report on the study of the moisture barrier performances of PECVD SiO<sub>x</sub> coatings with regard to their physical and chemical properties and the deposition process parameters.

#### EXPERIMENTAL

##### Substrate Materials and Monomer

The substrate used was a 120 μm thick commodity grade (PR/P/U type) polyethylene terephthalate (PET) provided by Jindal Poly Films Limited. This film is not an optical film, but it exhibits high optical transmission in the visible range and a moisture barrier of 4 g/m<sup>2</sup>/day. The effective coating width was 150 mm. Hexamethyldisiloxane (HMDSO) was used as the monomer precursor and oxygen was used as the main reactive gas for the production of SiO<sub>x</sub> coatings.

##### Coating Process

The polymer films were coated via PECVD using a pilot-scale roll-to-roll coater at Bobst Manchester Ltd. Further details of the coater are available in previous publications [8]. The plasma was generated by capacitively coupling medium frequency (e.g. 40kHz, Advanced Energy PEII) power between a glycol cooled rotating cylinder electrode, part of the web transport system, and a counter electrode. Input power, web transport speed, oxygen and monomer flow rates were varied.

This vacuum process was carried out at pressures in the  $10^{-2}$  mbar (1 Pa) range and is assisted by a magnetic array located under the process cylinder. As the plasma forms in this region between the magnetic array and the web as it travels around the drum, this is referred to as the process zone.

Single layer silicon oxide coatings were deposited onto the moving web by introducing the vaporised monomer and the reactive gas (oxygen) into the process zone. Inert gases such as helium and helium are used for cleaning and purging purposes. Argon, especially prevents the counter electrode from being coated with the insulating coating. The influence of several parameters on the barrier performances of the coating was investigated. This paper will focus on the following parameters: input process power, ratio of reactive gas flow rates (ratio oxygen: monomer flow rates) and the web speed.

### Analytical Techniques

Barrier properties, in terms water vapour transmission rates (WVTR), were determined in accordance with ASTM F 1927 and ASTM F 1249/ISO 15106-3 using a Mocon Permatran-W 3/33 and Systech Illinois 7001. Test conditions were 37.8°C and 90 % relative humidity.

For topographical examination, a Zeiss Supra 40VP field emission gun scanning electron microscope (FEG-SEM) was used to acquire images of the uncoated and silicon oxide coated film surfaces at an acceleration voltage of 0.5 kV. In order to avoid masking any surface detail, no conductive layer was applied to these insulating samples prior to analysis.

The composition and stoichiometry of the coatings were assessed using X-ray photoelectron spectroscopy (XPS) in a Thermo Fisher Scientific (East Grinstead, UK) Theta Probe spectrometer. XPS spectra were acquired using a monochromated Al K $\alpha$  X-ray source ( $h\nu = 1486.6$  eV). An X-ray spot of  $\sim 100$   $\mu\text{m}$  radius was employed. XPS depth profile data

was acquired using the monochromated Al K $\alpha$  X-ray source, while sample etching was achieved using an argon (Ar) ion gun operated at 3 kV and delivering  $\sim 1\mu\text{A}$  of Ar $^+$  etch current. The etch area was  $\sim 1.5 \times 1.5$  mm $^2$  and an etch time of 500s (initial) and 50s (through the SiO/PET interface) was employed. The Ar ion gun was fixed at an angle of 45° to the sample surface.

Coating thickness was measured by using the Zygo white light interferometer (using a step edge created with polyimide Kapton™ tape as a mask). The Gwyddion software was then used to generate the thickness profiles. Several profiles were measured along the step edges in order to provide an average thickness.

In order to assess the variation in barrier properties while handling and converting the film (e.g. winding, tensions, etc.) tensile tests were performed on a roll of coated film and the base substrate. Strains between 0.5 and 5 % were applied using a Hounsfield H10KS universal mechanical testing machine with QMat software. The water vapour barrier on a sample taken in the middle of the stretched area was measured after relaxation.

## RESULTS AND DISCUSSION

### Surface Topography

An initial assessment of the coatings indicated that they were all semi-transparent with optical densities\* in the range 0.040 (91.2 % transmission in the visible range) to 0.090 (81.3 % transmission). The more detailed SEM topographical analysis of the films revealed the packed grainy structure of the PECVD SiO $_x$  coatings, which has already been observed by several groups [9, 10]. Figure 1 compares the electron microscope images of coatings produced with different input power levels. It is clear from this figure that increasing the power level

\*Measured with MacBath TD931

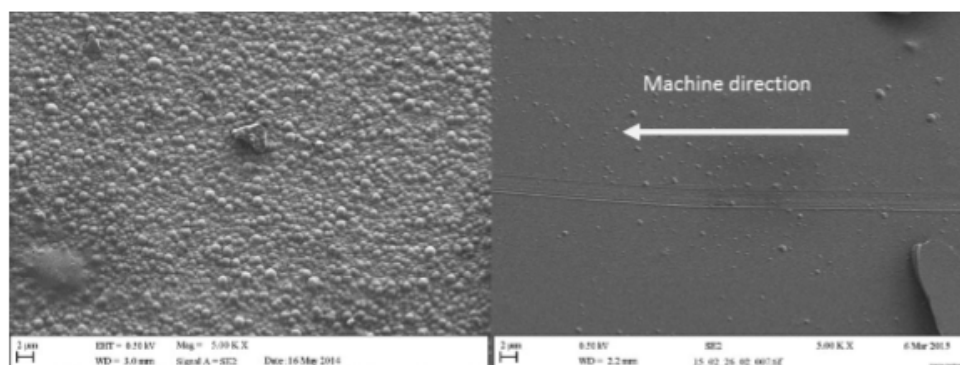


Figure 1: Scanning electron microscope image (SEM) of the surface of a coating produced using: a power set-point of 1.1kW and monomer flow rate ratio of 6 (left) and a power set point of 1.6kW and the same monomer ratio of 6 (right). All the other parameters are the same for both coatings.

has produced a significantly smoother surface to the coating, although some scratches in the machine direction are visible in the surface of the coating deposited at a higher power.

The WVTR rates for the samples mentioned in this figure were, respectively, 0.230 g/m<sup>2</sup>/day and 0.053 g/m<sup>2</sup>/day. The former result may well be related to the presence of cracks, pinholes and open porosity in the lower power coating, providing a preferential path for water vapour molecule permeation [6, 11]. Thus, to a first approximation, increasing the plasma power appears to have resulted in a smoother, denser, conformal coating with better water barrier performance. This matches Bieder et al.'s. assumption that increasing the power leads to an increase in ion bombardment, which increases the surface diffusion (of the chemical species) and reduces the voids. Therefore, with the coating being denser, the permeation is limited [12]. More detailed consideration of the influence of process parameters on the coatings is given in the following sections.

### Surface Chemistry

When producing SiO<sub>x</sub> coatings by the PECVD method, some parameters are known to be critical and influence the deposition process and to some extent the barrier performance [4, 13-15]. The oxygen and monomer flow rates, often grouped and expressed as a ratio, are one of the main parameters driving the process. The effect of the oxygen:monomer ratio on the composition of the SiO<sub>x</sub> coating was determined using XPS and the results are presented in Table 1.

At the highest flow rate of oxygen tested here, the coating is close to stoichiometric SiO<sub>2</sub>, with residual carbon in the deposited film. As the oxygen flow rate is reduced at a constant flow rate of HMDSO, the silicon content in the coating increases, as does the carbon content for the majority of samples tested here. It has been found elsewhere that, at high oxygen flow rates, the coating has an inorganic character and tends to be brittle, whereas at lower oxygen flow rates the coatings are more organic in nature with a higher carbon content, because

byproduct gases do not form completely and cannot be vented away [7, 14].

### Relationships Between Barrier Performance, Film Properties and Process Parameters

The relationships between water barrier performance and coating thickness, oxygen to monomer flow rate ratio, web speed and plasma power have all been investigated. Coating thickness was found to vary between 250 nm and 950 nm (which equates to dynamic deposition rates in the range 125 to 425 nm·m<sup>-1</sup>·min<sup>-1</sup>), with thickness decreasing with increasing oxygen:monomer flow rates, but there was no apparent trend between thickness and barrier. This is surprising as barrier is generally found to increase with thickness [13, 14]. The lack of a correlation here may be due to the small data set and difficulties in accurately measuring coating thickness. Further investigations will be carried out in the future.

Figure 2 shows the variation of the water vapour barrier as a function of the oxygen:monomer ratio. In this case the ratio has been increased by increasing the oxygen flow rate at a constant flow rate of monomer.

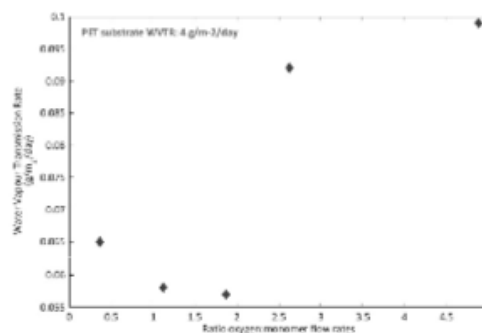


Figure 2: The variation in water vapour transmission rate with the oxygen-to-monomer flow rate ratio. (all the other process parameter were kept constant).

Table 1: summary of the composition and stoichiometry properties of samples produced with different ratio oxygen/HMDSO flowrates, based on 133 sccm of HMDSO.

Identification	O <sub>2</sub> flow rate (cm <sup>3</sup> /min)	Ratio oxygen:HMDSO	Si (%)	O (%)	C (%)	stoichiometry
Sample 03	650	4.88	29	58	13	SiO <sub>2</sub> C <sub>0.45</sub>
Sample 09	350	2.63	32	45	23	SiO <sub>2.04</sub> C <sub>0.72</sub>
Sample 10	250	1.87	30	40	30	SiO <sub>1.33</sub> C <sub>1</sub>
Sample 11	150	1.12	36	34	30	SiO <sub>0.94</sub> C <sub>0.83</sub>
Sample 12	50	0.37	47	32	21	SiO <sub>0.68</sub> C <sub>0.45</sub>



WVTR have been compromised with increasing the oxygen-to-monomer flow rate ratio, i.e., the best barrier results are found at lower flow rates of oxygen. In fact, the transmission rate almost double as the ratio is increased from 2 to 2.5. As mentioned above, this promotes a more organic nature to the coating. In addition, it has been observed elsewhere that films deposited under high oxygen-to-HMDSO flow rate ratios showed an increased surface roughness and a more brittle nature [12, 16].

Another key parameter in the understanding and optimisation of the process and the coatings is the input power used to drive the plasma. Indeed, this can be considered as the energy used to create the reaction [4, 5]. Figure 3 shows the WVTR measured for coatings produced with varied input powers (all the other parameters kept constant) and the associated barrier improvement factor.

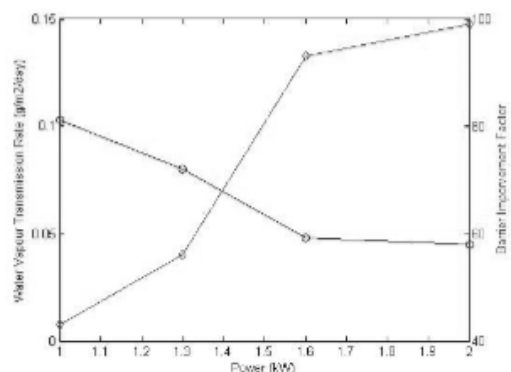


Figure 3: Plot of the evolution of the barrier with the input power for 4 set points 1 kW, 1.3 kW, 1.6 kW, 2 kW. All the other parameters have been kept constant.

A clear trend seems to be drawn as far as the relationship between input power and WVTR is concerned. The WVTR improves (i.e. reduction in transmission rate) with increasing input power, indeed there is a barrier improvement of 2.5 times over the range of powers studied here. This was related earlier to an improvement in film structure observed at higher powers. This result is in agreement with the work done by Bieder et. al. with RF PECVD [12], where they also found that increasing the power level delivered to the plasma improved the WVTR. A more intense substrate ion bombardment at higher power suppresses the development of rough structures by creating nucleation sites for arriving coating fragments, eroding surface roughness peaks, and overcoming shadowing effects by migration [11].

Finally, the web speed is also an interesting parameter as it affects the dwell time (exposure time of the substrate to the

plasma) and the deposition rate. Figure 4 is a plot of the variation in WVTR as a function of web speed.

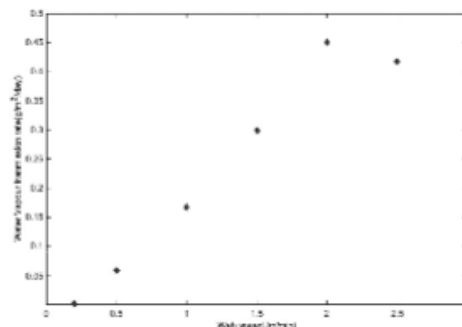


Figure 4: Water vapour transmission rate as function of the substrate (web) speed. All other parameters kept constant.

It can be seen that the WVTR increased (barrier deteriorated) with web speed and peaks at a speed of 2 m/min. This result is in good agreement with the data published by Okimoto on SiO<sub>x</sub> coated PEN [14]. This may be related to a reduction in coating thickness at higher web speeds, but no clear correlation with thickness has been observed at this stage.

#### Barrier Performance with Elongation

During coating, lamination and post vacuum coater conversion, the films are subject to repetitive strain (due to handling and processing). This can induce defects and potentially compromise the barrier performance. Thus, barrier retention on strain (or flex-durability) can be investigated to determine the effect of this repetitive strain on the barrier properties of the film. Figure 5 shows the change in barrier induced by elongation of the coated film in the machine direction.

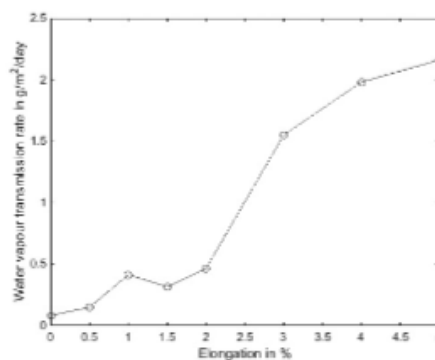


Figure 5: Plot of the variation of the water vapour transmission rate with the elongation of the SiO<sub>x</sub> coated samples. The estimated thickness of the tested samples is 800 nm.

These results indicate that the WVTR increases during plastic deformation of the polymer. These results are in agreement with the work done by Rochat et. al. [17] and Leterrier et. al. [18]. They reported that the first wrinkles appear at 3 % strain on their 10 nm PECVD SiO<sub>x</sub> coating and assumed that there was no fracture of the coating at this stage, which could explain the preservation of the barrier properties. However, when the strain applied reached 5 %, the first cracks (combined with the previous wrinkles created) started to appear causing a loss in barrier.

Regarding the rate at which the WVTR of the coating degrades after the onset of cracking, Felts [15] assumed it is related to the relative adhesion between the coating and the first layer of the SiO<sub>x</sub> coating. This adhesion is, in turn, highly dependent on the surface properties of the substrate (roughness, defects, available bonds) that could be further investigated via atomic force microscopy/white light profilometry (roughness), SEM (defect density), Fourier transform infrared spectroscopy (for chemical bounds), etc.

No cracks were found on the samples, which had been strained up to 5 %, using a SEM, or using a light microscope. However, the observations were made after the samples had relaxed and it is possible that the cracks have relaxed. Modelling of the cracking mode and the influence of the defects is also possible and has been reported by Howells and Yang [19]. Further detail on the modelling of the barrier degradation with strain can be found in the work of Yanaka et al. [11].

### SUMMARY AND CONCLUSIONS

Single layer transparent SiO<sub>x</sub> barrier coatings have been deposited onto commodity grade PET substrates using the PECVD method in a pilot scale roll-to-roll coater. The coatings were found to have a grainy structured surface. The composition of the coatings varied with the oxygen:HMDSO ratio, with high oxygen flow rates resulting in coatings with close to stoichiometric SiO<sub>2</sub> compositions, whereas low oxygen flow rates produced more organic coatings with a higher carbon content. From an initial assessment of the influence of process parameters on the water barrier performance, it was found that low WVTR values were promoted by low oxygen:monomer flow rate ratios, low web transport speeds and high plasma discharge powers. Nevertheless, it was noted that the process was becoming unstable for higher input powers.

Further investigation will be carried out on the physical and chemical nature of the coatings in order to gain a better understanding of the permeation mechanisms and to optimise the PECVD process and obtain barrier levels closer to the applications requirements.

### ACKNOWLEDGEMENTS

The authors would like to thank Dr Steve Hinder at the University of Surrey, UK, for conducting the XPS analysis of our samples.

### REFERENCES

1. B. Ketola, "The role of encapsulant moisture permeability in the durability of solar photovoltaic modules", Michigan, USA: Dow Corning Corporation. (2010).
2. S. Seethamraju, "Encapsulation for Improving the Efficiencies of Solar Cells.", Materials and Processes for Solar Fuel Production, 2014. 174(1).  
[http://dx.doi.org/10.1007/978-1-4939-1628-3\\_2](http://dx.doi.org/10.1007/978-1-4939-1628-3_2)
3. Chatham, H., "Oxygen diffusion barrier properties of transparent oxide coatings on polymeric substrates.", Surface and Coatings Technology, 1996. 78(1-3): p. 1-9.  
[http://dx.doi.org/10.1016/0257-8972\(95\)02420-4](http://dx.doi.org/10.1016/0257-8972(95)02420-4)
4. Korner, L., "Diffusion Barrier Coatings for Polymer-Containers processed by Plasma Enhanced Chemical Vapor Deposition.", Thesis, 2010, ETH Zurich.
5. Tropsha, Y.G. and N.G. Harvey, "Activated rate theory treatment of oxygen and water transport through silicon-oxide/poly(ethylene terephthalate) composite barrier structures.", Journal of Physical Chemistry B, 1997. 101(13): p. 2259-2266.  
<http://dx.doi.org/10.1021/jp9629856>
6. Roberts, A.P., et. al., "Gas permeation in silicon-oxide/polymer (SiO<sub>2</sub>/PET) barrier films: Role of the oxide lattice, nano-defects and macro-defects.", Journal of Membrane Science, 2002. 208(1-2): p. 75-88.  
<http://dx.doi.org/10.1021/jp9629856>
7. Elrawemi, M., et. al., "Modelling water vapor permeability through atomic layer deposition coated photovoltaic barrier defects." Thin Solid Films, 2014. 570(Part A): p. 101-106.
8. A.W. Smith, N. Copeland, D. Gerrerd, and D. Nicholas, "PECVD of SiO<sub>x</sub> Barrier Films." 45<sup>th</sup> Annual Technical Conference Proceedings of the Society of Vacuum Coaters, p. 525, 2002.
9. da Silva Sobrinho, A.S., "Characterization of Defects in PECVD SiO<sub>2</sub> Coatings on PET by Confocal Microscopy." Plasma and Polymers, 1998. 3(4): p. 231-247.  
<http://dx.doi.org/10.1023/A:1021854805605>

## Appendix F Public Engagement

---

10. A. Barranco, "Room temperature synthesis of porous  $\text{SiO}_2$  thin films by plasma enhanced chemical vapor deposition." *Journal of Vacuum Sciences*, 2004, 22(4). <http://dx.doi.org/10.1023/A:1021854805605>
11. Yanaka, M., et al., "How cracks in  $\text{SiO}_2$ -coated polyester films affect gas permeation". *Thin Solid Films*, 2001, 397(1-2): p. 176-185. [http://dx.doi.org/10.1016/S0040-6090\(01\)01473-0](http://dx.doi.org/10.1016/S0040-6090(01)01473-0)
12. Bieder, A., "PECVD of  $\text{SiO}_2$  films from oxygen and hexamethyldisiloxane in a double source reactor." 2006, ETH Zurich: Switzerland. <http://dx.doi.org/10.1016/j.surfcoat.2005.03.044>
13. Kim, S.-R., et al., "Effects of argon and oxygen flow rate on water vapor barrier properties of silicon oxide coatings deposited on polyethylene terephthalate by plasma enhanced chemical vapor deposition". *Thin Solid Films*, 2010, 518(8): p. 1929-1934. <http://dx.doi.org/10.1016/j.tsf.2009.07.147>
14. H. Tamagaki, T. Okimoto, and T. Segawa, "Transparent High Barrier Coating on Polymer Web by PE-CVD Roll Coater," *53<sup>rd</sup> Annual Technical Conference Proceedings of the Society of Vacuum Coaters*, p. 553, 2010.
15. E. Finson and J. Felts, "Transparent  $\text{SiO}_2$  Barrier Coatings: Conversion and Production Status," *37<sup>th</sup> Annual Technical Conference Proceedings of the Society of Vacuum Coaters*, p. 139, 1994.
16. Erlat, A.G., et. al., " $\text{SiO}_2$  gas barrier coatings on polymer substrates: Morphology and gas transport considerations." *The Journal of Physical Chemistry B*, 1999, 103(29): p. 6047-6055. <http://dx.doi.org/10.1021/jp990737e>
17. Rochat, G. and P. Fayet, "Characterization of mechanical properties of ultra-thin oxide coatings on polymers by uniaxial fragmentation tests.", *Journal of Adhesion Science and Technology*, 2012, 26(20-21): p. 2381-2392. <http://dx.doi.org/10.1163/156856111x599517>
18. Y. Leterrier, et. al., "Durability of thin PECVD  $\text{SiO}_x$  coatings on polymer films," *41<sup>st</sup> Annual Technical Conference Proceedings of the Society of Vacuum Coaters*, p. 429-433, 1998.
19. Howells, D.G., et. al., "Mechanical properties of  $\text{SiO}_2$  gas barrier coatings on polyester films". *Surface and Coatings Technology*, 2008, 202(15): p. 3529-3537. <http://dx.doi.org/10.1016/j.surfcoat.2007.12.030>

**Conference Presentations:**

N. Kaabeche, P. Kelly, L. Harland, N. Copeland, *Transparent High Barrier Coating for electronic encapsulation*, Presentation at 58<sup>th</sup> Annual Technical Conference of the Society of Vacuum Coaters, Santa Clara, USA, 2015

N. Kaabeche, P. Kelly, L. Harland, N. Copeland, *Development of PECVD moisture barrier coatings for electronic encapsulation*, Presentation at 59<sup>th</sup> Annual Technical Conference of the Society of Vacuum Coaters, Indianapolis, USA, 2016.